University of Sheffield

Engineering and Physical Sciences Research Council

RAIL SAFETY AND STANDARDS BOARD

Rough Surface Contacts, Third-Body Layers and the Wheel-Rail Interface

---

Harry Shackleton

Thesis

iT-CDT Centre for Doctoral Training in Integrated Tribology

February 2024

Prof Roger Lewis

‘Something unknown is doing we don’t know what.’

Sir Arthur Eddington

Abstract

Understanding and managing adhesion at the wheel-rail interface is paramount to the safe running of a railway. Anything that increases or decreases the level of traction/adhesion is therefore of interest to the industry. Various third-body layers (3BLs) contribute to the levels of traction, be it leaves in autumn or lubricants applied at curves. Surface roughness is known to affect friction, however it is poorly understood when paired with 3BLs. High surface roughness occurs on wheels and rails following rail grinding and wheel turning procedures. How this surface roughness evolves after these reprofiling procedures is not yet known.

The aim of this thesis is to better understand surface roughness at the wheel-rail interface with and without 3BLs present. To do this the high pressure torsion (HPT) rig was employed to simulate the the tribology at the wheel-rail interface. Surface roughness was applied to the HPT specimens and measured using surface roughness replicas and an Alicona microscope. Water, grease and leaves were applied to the interface to better understand what effect these 3BLs would have on the traction. In addition to this, the HPT specimens were instrumented with ultrasonic sensors which would measure the interfacial stiffness in-situ during a test. Following this the extended creep-force (ECF) model was parameterised with the outputs from the HPT tests to predict full-scale outcomes when surfaces are both rough and contaminated with 3BLs. These predictions were then validated using the full-scale wheel-rail rig at the University of Sheffield.

A link between surface roughness and the traction coefficient when running-in was found for dry contacts. Post grinding roughness levels were found to reduce down to near run-in after just a few equivalent train passes. High levels of roughness reduced the impact of friction lowering 3BLs. Leaf layers slowed the rate at which roughness decreases. The ECF model parameterisation was successful and good agreement was found between the ECF and the HPT results. The ECF was able to predict full-scale outcomes with a fair degree of accuracy especially for the dry, water and leaf cases. A link was found between interfacial stiffness and surface roughness for dry contacts, meaning that surface roughness may be remotely measurable in real-time using ultrasonics. The ultrasonic sensors were also able to detect the presence of 3BLs, but not the distinguish the type of 3BL.

Acknowledgments

This thesis is dedicated to Mr Richard Kay.

Contents

1 Introduction

Globally, travelling by rail is one of the most popular methods of transport thanks to its low environmental impact, low cost and short journey times compared with other modes of transport. Whilst this may be so, there are a great many challenges that must be overcome in order to have an efficient, reliable and safe railway network. One such challenge is low traction/adhesion at the wheel-rail interface. Traction/adhesion is defined as the tangential force along the rail between the wheel and the rail. Low adhesion at the wheel-rail interface is estimated to cost the UK rail industry around £300m per annum [1]. These less than ideal conditions result in longer braking distances and longer acceleration periods which can cause station overshoots and timetable delays. If adhesion is too high, especially during curves in the track, wheels and rails are subjected to high shear stresses which result in excessive wear [2] [3], higher energy consumption [4] and wheel climb induced derailments [5] [6]. Many aspects alter adhesion, from external contaminants such as water and leaves to the surface roughness of the wheel and rail [7] [8]. This makes predicting adhesion conditions challenging.

By improving our fundamental understanding of the wheel-rail interface, it is hoped that countermeasures can be introduced to mitigate these issues, namely our understanding of how roughness at the wheel-rail interface affects the traction/adhesion coefficient. Roughness of wheels and rails is not static but evolves over time, most notably when they are reprofiled during wheel turning and rail grinding [9]. The high resultant roughnesses from these processes are cause for concern, as they increase lateral flange forces and the likelihood of derailment through a process known as wheel climb. This high roughness quickly decreases as the wheels and rails are run-in, however further understanding of this roughness and the nature of its evolution over time is required in order to reduce or eliminate the number of wheel climb derailments.

Acquiring non-destructive interfacial measurements for opaque contacts has remained difficult for many years. Recently ultrasonic reflectometry has offered a solution, allowing us for the first time to see what is happening at the wheel-rail interface [10–13]. Interfacial stiffness can be measured directly using ultrasound which in turn could be related to the surface roughness. 3BLs such as water and leaves lubricate the interface, resulting in conditions of low adhesion, and are therefore of great concern to the UK rail industry. If these 3BLs are detectable with ultrasonics

this could be used to develop a 3BL detection sensor.

2 Thesis Aim and Objectives

Aim

- To improve our fundamental understanding of the frictional behaviour of rough surface interfaces with and without third-body layers present. This will be primarily in the context of the wheel-rail interface.

Objectives

- Study how roughness evolves at the wheel-rail interface.
- Use the High Pressure Torsion (HPT) test approach alongside ultrasonic reflectometry to measure interfacial stiffness and link this to roughness and friction.
- Consider what effect third-body layers (3BLs) have on the roughness evolution and friction at the wheel-rail interface.
- Parameterise the extended creep-force (ECF) with the HPT results to model the full-scale rough surface frictional behaviour with and without 3BLs present.
- Validate the ECF predictions by conducting full-scale tests under the same conditions as the HPT tests.

3 Literature Review

The purpose of this literature review is to highlight any existing theory and knowledge surrounding the wheel-rail interface. This includes our understanding of roughness, how roughness affects friction and how we might measure that roughness. This chapter also reviews how we might use ultrasound to measure conditions at the wheel-rail interface and finally what gaps are there in the theory that might steer this research towards novel conclusions.

3.1 An Overview of Friction

Tribology is the study of interacting surfaces in relative motion. Since so much in the world of science and engineering relies on the interaction of components, ways in which we can extend component life and increase performance are of great interest to industry. Friction is one of the principle areas of study within tribology as one third of purposely produced energy is lost due to friction. Frictional losses remain the primary energy loss that mechanical processes endure [14]. By reducing energy losses due to friction, mechanical systems could work more efficiently, thereby reducing their environmental impact whilst additionally saving customers and manufacturers money. The friction force (F) of a sliding contact is described by Equation 3.1:

$$F = \mu N \tag{3.1}$$

where μ is the friction coefficient and N is the normal force. At the wheel-rail interface the vehicle speed and the rotational speed of the wheel are not necessarily equivalent. The wheel can be in pure rolling, pure sliding or a mixture of both. When this contact is a mixture of sliding and rolling, i.e there is some slip, F is known as the tractive force and μ is known as the traction coefficient, however this is covered in more detail in Section 3.3.3. To understand friction we must first understand the way in which materials interact or contact mechanics as it is more commonly known. The earliest ideas on contact mechanics were laid down by Heinrich Hertz over 100 years ago [15]. Hertzian contact mechanics states that under loading, materials elastically deform to produce a contact patch of measurable area. This area depends on the material properties of the interacting materials, the load between them and their size. The shape of the contact patch depends

on the geometry of the interacting components. Different interacting geometries produce different contact patch shapes. Hertz theory works well for perfectly smooth surfaces, however with the introduction of surface roughness, elements of the contact such as the real contact area, pressure distribution and deformation deviate from the results obtained with Hertz theory.

In reality the surfaces of all real materials, no matter how apparently smooth, have microscopic asperities which interact when materials come into contact with one another. The friction between surfaces relies on the interaction of these individual asperities (see Figure 3.1). The contact can therefore be described by a series of discretely distributed contact areas, meaning the real contact area is far smaller than the nominal contact area.

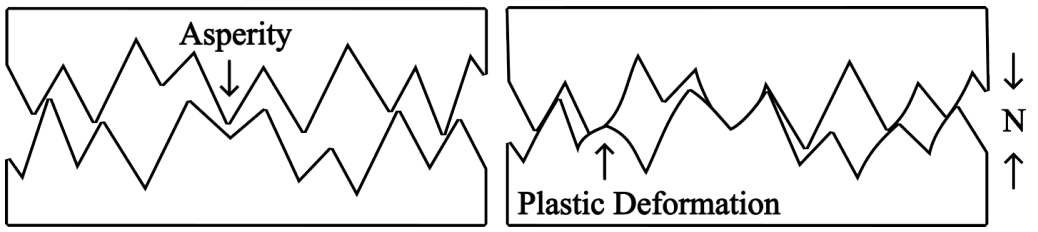

Figure 3.1: Surface asperities (left: before contact, right: under normal loading (N))

Historically, friction has been governed by three laws. These laws were founded on empirical observations and as such are not fundamental. For a dry sliding contact these laws were as follows:

- Friction force is proportional to normal load.
- Friction force is independent of the apparent area of contact.
- Friction force is independent of sliding velocity.

Subsequently more laws were added with advances in metrology so that the complete list was as follows:

- Friction force is proportional to normal load.
- Friction force is independent of the apparent area of contact.

- Friction force is independent of sliding velocity.
- Friction force is independent of surface roughness.
- Friction force is independent of temperature.

If we focus on metal-to-metal contacts, most metal-to-metal contacts agree with the first three laws for a dry sliding contact. They do not, however, when going from rest to sliding, nor do they for high relative velocities. Our current understanding of friction is based on the Bowden and Tabor model whereby all frictional effects take place at the micro (or asperity) scale [16]. The tangential force is comprised of two parts: the adhesion force and the ploughing force. The adhesion force depends on the real area of contact made by the interacting asperities and the ploughing force depends on the hardness of the two interacting materials, specifically the force required to force the harder material's asperities through the softer surface. For metal-to-metal contacts the asperity deformation is predominantly plastic which means it is proportional to load. An increase in normal load results in an increase in the number of asperities brought into contact with one another to support this increased normal load.

Since the ploughing component of the friction force depends on penetration depth, the majority of the summed friction force for metal-to-metal contacts depends predominantly on the adhesion component and is therefore largely proportional to normal load. This of course breaks down with the work hardening of asperities so they no longer behave plastically and for contacts with 3BLs present. Lubricated contacts also do not follow the standard laws of friction.

The role of surface roughness and its impact on friction is still not fully understood, not least due to the fact that there are many different ways to define it (see Section 3.2). Asperity shape, number and size all have roles to play as well as the more complex topographical concepts such as surface roughness directionality (surfaces that are not equal in roughness in all directions). Over modest temperature ranges the mechanical nature of most metal-to-metal contacts does not change. This means friction is independent of temperature, however, this is not the case for high temperatures. Therefore the laws for dry sliding friction are as follows:

- Friction force is NOT proportional to normal load.
- Friction force is NOT independent of the apparent area of contact.

- Friction force is NOT independent of sliding velocity.
- Friction force is NOT independent of surface roughness.
- Friction force is NOT independent of temperature.

Once again this only covers dry sliding contacts and not contacts that are going from rest to sliding or those with stick-slip regimes (see Section 3.3.3). These modified laws are largely unhelpful in explaining friction, but perhaps go some way to explaining why tribology is such a wide ranging field of research with such major real life implications. When the performance, efficiency and cost of tribological materials rely on such changeable laws, they present researchers and product manufacturers with a great deal to consider.

3.2 Roughness of Wheels and Rails

Roughness at the wheel-rail interface is of great concern to the rail industry as wheel and rail roughness affects interfacial traction/adhesion and noise production. It can also instigate wheel climb and in the worst cases cause derailments. Rail roughness is not static, but evolves over time. This evolution is most dramatic after reprofiling events such as rail grinding and wheel turning. Both these processes produce high roughness surfaces that are then run-in as the wheels and rails are used. It follows that to mitigate the negative effects roughness induces on track, we must first understand how roughness changes. Ultimately this will help us understand how roughness influences friction at the wheel-rail interface.

3.2.1 Defining Roughness

When it comes to defining roughness, there are a number of ways one can do this. The simplest way is to look at the average height of asperities over a specific length (L). The solution is the line roughness (R_a) and can be seen in Equation 3.2:

$$R_a = \frac{1}{L} \int_L |z(x)| \, dx \tag{3.2}$$

where $z(x)$ is the asperity height function of the surface. This gives the roughness of a line drawn across a flat surface [17]. Cylindrical coordinate systems can be used

to account for curved surfaces. Figure 3.2 shows the equivalent R_a value for a given surface profile.

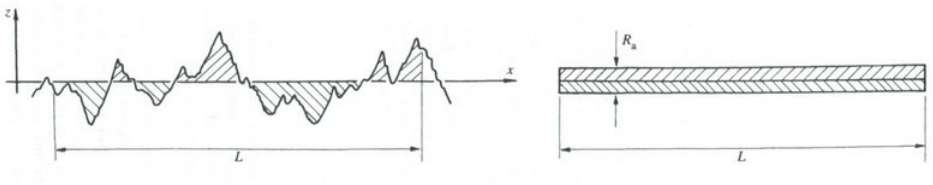

Figure 3.2: Line roughness R_a [17]

Since $z(x)$ is made up of peaks and troughs, it contains both positive and negative values, therefore the modulus of $z(x)$ is used in Equation 3.2 so as to obtain an average height of asperities regardless of their sign. Another way to achieve this is by taking the root mean squared (RMS) value of the asperity heights. The solution is the RMS line roughness (R_q) and is outlined in Equation 3.3:

$$R_q = \sqrt{\frac{1}{L}\int_L z^2(x)dx} \tag{3.3}$$

R_a and R_q do not provide us with the full picture of a surface's topography as completely different surfaces can have the same R_a or R_q value. Directionality also plays a part, whereby the roughness value in one direction across a surface may be completely different from that of another. Real surfaces are so complex that you would need an infinite number of discrete parameters to describe them fully, however the more parameters one uses the closer one can get to representing a surface. Line skewness (R_{sk}) is a parameter that determines the symmetry about the mean roughness line. A symmetrical height distribution has zero skewness [18]. Figure 3.3 shows two skewed rough profiles.

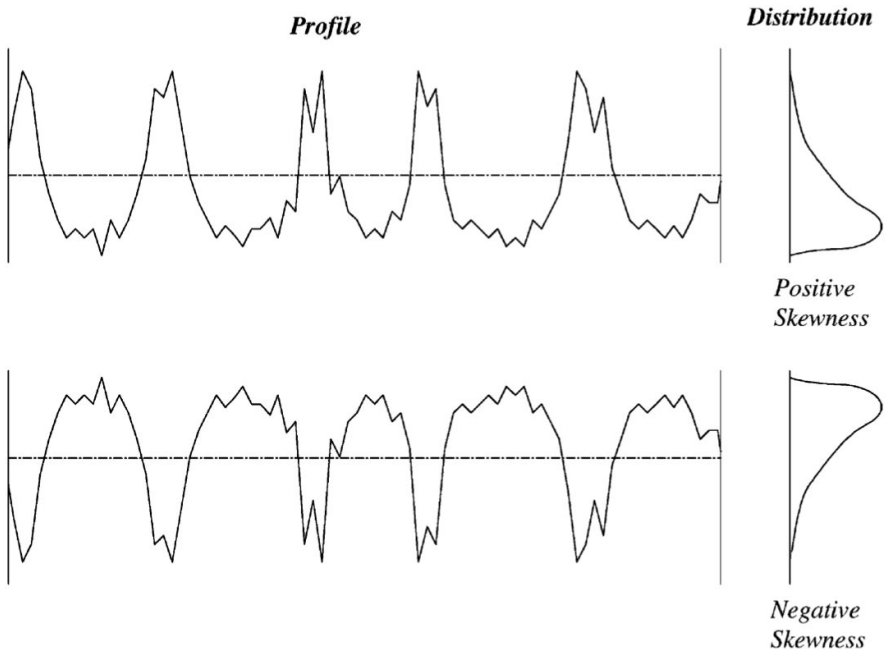

Figure 3.3: Line skewness (R_{sk}) and the amplitude distribution curve [18]

Line kurtosis (R_{ku}) describes the sharpness of the probability density profile as seen in Figure 3.4. When $R_{ku} < 3$ the distribution curve is platykurtoic, meaning it has a lower proportion of high peaks and low valleys. When $R_{ku} > 3$ the distribution curve is leptokurtoic, meaning it has a higher proportion of high peaks and low valleys [18].

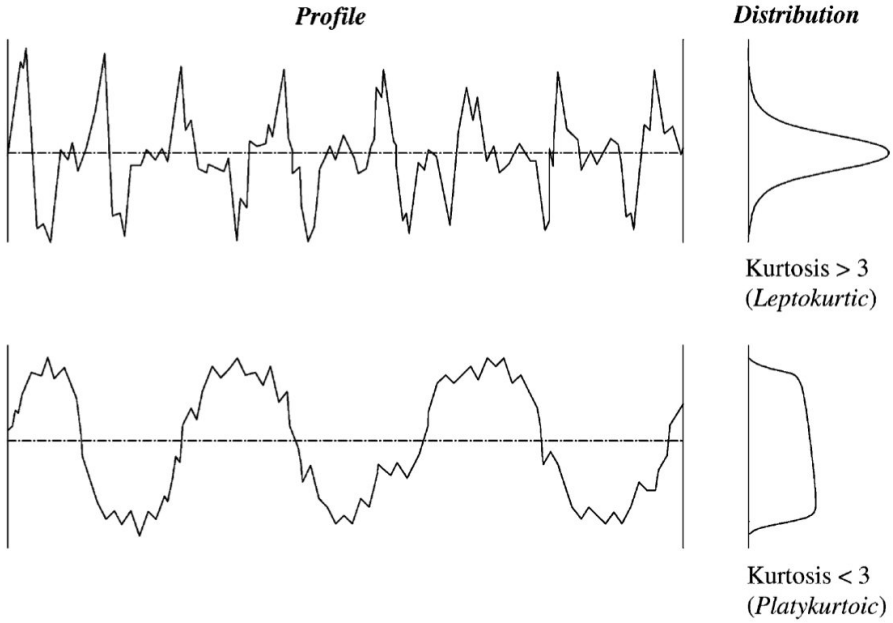

Figure 3.4: Line kurtosis (R_{ku}) and the amplitude distribution curve [18]

The surfaces in Figure 3.3 and 3.4 are visually completely different from one another, but could have similar R_a values. It is now thought that R_{sk} and R_{ku} could have a greater role to play than previously expected when linking surface roughness to friction [19] [20]. The surfaces present in tribological systems cannot be fully explained by just R_a, or any iteration thereof, therefore more knowledge of the surface topography is needed to fully understand the tribological processes involved.

Despite the complexity of all real surfaces, R_a values are commonly used to describe a material's roughness especially with respect to manufacturing processes where surface roughness is often encompassed in the term 'surface finish'. The R_a values for some common manufacturing processes can be seen in Figure 3.5. Whilst this may be useful from a manufacturing and materials selection perspective, a linear representation of roughness is often inappropriate from a tribological point of view as surfaces interact with one another through a three dimensional contact patch. The wheel-rail contact is generally observed to be elliptical (see Section 3.3.2) so a different approach is needed to account for three dimensional rough surfaces.

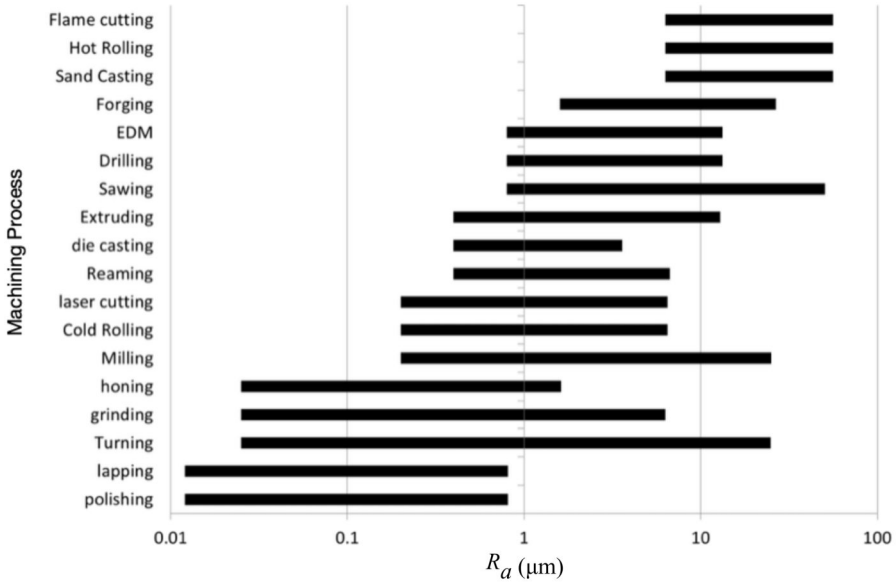

Figure 3.5: Typical R_a values associated with various machining processes [17]

An alternative method of calculating roughness is to calculate the average height of asperities over a specific area (A). This gives a more comprehensive measurement of roughness that accounts for roughness in both the x and y directions. Roughness can be highly directional so this method helps to eliminate possible miscalculations

due to this directionality. The solution can be seen in Equation 3.4:

$$S_a = \frac{1}{A} \int \int_A |z(x,y)| \, dxdy \tag{3.4}$$

This gives the surface roughness (S_a) of an area or the areal roughness as it is commonly called. Cylindrical coordinate systems can also be used to account for curved surfaces. The parameters included in Equation 3.4 are outlined in Figure 3.6. It stands to reason that determining S_a is computationally more difficult than computing R_a. S_a requires more complex measuring techniques and equipment (see Section 3.2.3), and since R_a is a more established/more easily obtainable roughness parameter, it is often quoted instead.

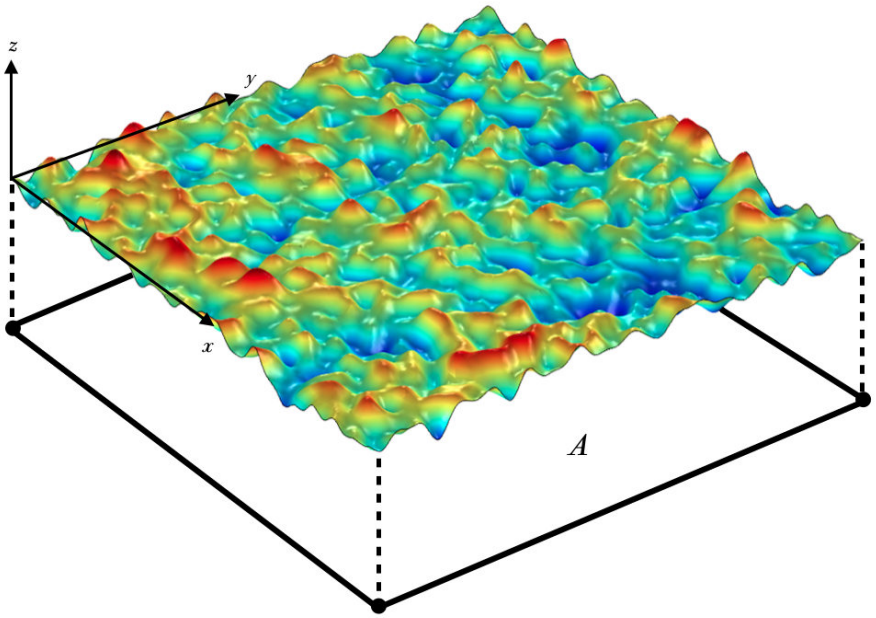

Figure 3.6: Surface roughness (S_a)

Like R_a, S_a has a RMS counterpart: the RMS surface roughness (S_q) which is outlined in Equation 3.5. In addition to S_a and S_q, surface skewness (S_{sk}) and surface kurtosis (S_{ku}) are also used when studying surface topography in three dimensions.

$$S_q = \sqrt{\frac{1}{A} \int \int_A z^2(x,y) dxdy} \tag{3.5}$$

Multiple industries and fields of research have contributed to the various defini-

tions of roughness over the years. Manufacturing and materials science use R_a as it is the easiest to measure. In the field of micrology, a science that deals with the handling and preparation of microscopic objects for study, it is the grade of abrasive paper used to polish a specimen that describes the resultant surface roughness. Whilst these methods may seem strange to a tribologist, they are adequate for their respective applications which are primarily concerned with tolerance and surface finish. These two definitions of roughness are for a single surface, however in tribology these surfaces interact with one another. When two surfaces come into contact the surface asperities plastically deform. Larger asperities are 'wiped away' and the surfaces begin to conform to one another, eventually resulting in a run-in state. Since both surfaces are changing, it can be useful to unify the two separate roughnesses as a single combined roughness. The RMS line combined roughness ($R_{q\sigma}$) and RMS surface combined roughness ($S_{q\sigma}$) have been defined by Equations 3.6 and 3.7 respectively:

$$R_{q\sigma} = \sqrt{R_{q1}^2 + R_{q2}^2} \tag{3.6}$$

$$S_{q\sigma} = \sqrt{S_{q1}^2 + S_{q2}^2} \tag{3.7}$$

Combining the component roughnesses in this way gives greater prevalence to specimens with high roughness than simply summing the component parts. This better represents surface interactions whereby large asperities penetrate the other surface. When the interface between two surfaces is lubricated, it is most likely that R_q will be used to describe roughness as it forms the basis of the lambda ratio (λ_r) (see Equation 3.8). Figure 3.7 shows two rough interfaces with RMS line roughnesses R_{q1} and R_{q2} separated by a fluid film of height h. Due to line roughness measurements being more common than surface roughness measurements, R_q is used when determining λ_r, however, R_q and S_q are interchangeable in the λ_r equation so long as the comparison used the same roughness parameter.

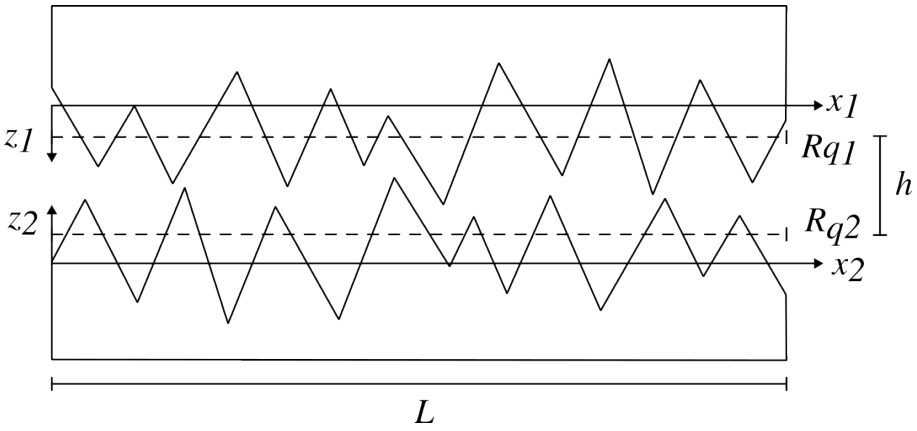

Figure 3.7: Lambda ratio schematic

$$\lambda_r = \frac{h}{R_{q\sigma}} \tag{3.8}$$

The lambda ratio describes the lubrication regime that a particular interface operates under. This is best visualised on a Stribeck curve (see Figure 3.8). The Hersey number is a dimensionless number that draws on the relative velocity and load the two surfaces are experiencing as well as the viscosity of the lubricant between them. The boundary regime describes interfacial contact where there is insufficient lubricant in the interface to avoid asperity interaction. The result is a high coefficient of friction. The mixed lubrication regime describes the predominant separation of surfaces by a lubricant film. There may still be contact given lower relative speeds and viscosities or higher loads. The hydrodynamic regime describes full surface separation by a lubricant film where there is no asperity contact. Clearly there is a sweet spot whereby components can operate with the lowest coefficient of friction thereby increasing their efficiency.

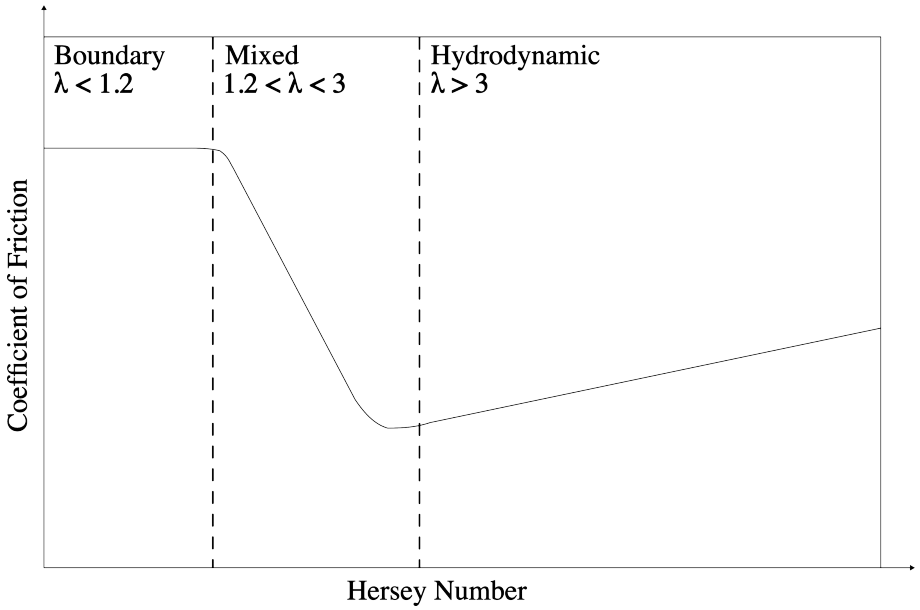

Figure 3.8: Stribeck curve

The Stribeck curve is useful when studying interfaces that are well lubricated and operating at elevated speeds such as bearings, however the majority of this work focuses on the boundary regime, where asperities are interacting with one another plastically and often without the presence of a lubricant. This is due to the relative component speeds and loads being too low for full separation. However by using the RMS values for line and surface roughnesses, comparisons can be made between interfacial contacts undergoing different lubrication regimes more readily.

One final parameter is surface conformity (S_c) which is a measure of the similarity of two surfaces with regard to surface roughness and is defined by Equation 3.9:

$$S_c = \left(1 - \frac{|S_{q1} - S_{q2}|}{|S_{q1} + S_{q2}|}\right) \times 100\% \tag{3.9}$$

This is an adaptation of the conformity equation used in the work of Wang et al. whereby instead of line roughness, surface roughness is used [21]. Highly conformal surfaces have more surface area in contact with one another which acts to increase friction. How we define roughness is a complex task that varies from definition to definition, therefore ballpark figures are really the best one can hope to achieve for a one-off measurement of roughness. Whilst how we define roughness and the method we choose to measure it (see Section 3.2.3) determines how rough something is, it is important to be consistent with your definition and measurement approaches when

studying roughness evolution. Given a consistent method, the changes in roughness should be accurate regardless of which method you use. ΔR_a, ΔR_q, ΔS_a and ΔS_q are all valid so long as like is being compared with like.

3.2.2 Separating Roughness from Waviness

Surfaces exhibit two kinds of topography: small-scale variations (Roughness) and large-scale variations (Waviness). This means that what is often described as 'roughness' is actually a combination of both roughness and waviness. These two characteristics are often studied separately. In order to do this, high and low pass filters are applied to surface profile measurements to separate small-scale and large-scale surface elements. Figure 3.9 shows this separation whereby an original roughness profile (a) is divided up into its constituent parts roughness (b) and waviness (c). The point at which these are separated is known as the cut-off wavelength (λ_c), which can vary depending on what is being measured and what is being used to measure it. These filters remove large variations in surface height creating a flat plain from which surface texture protrudes and recesses. This enables machining periodicity and other imposed large scale height variations to be eliminated from surface roughness measurements.

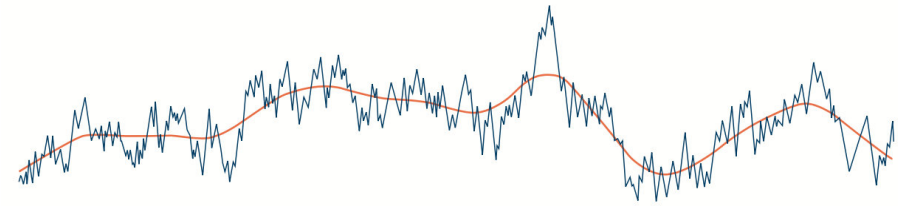

(a) Orignial profile

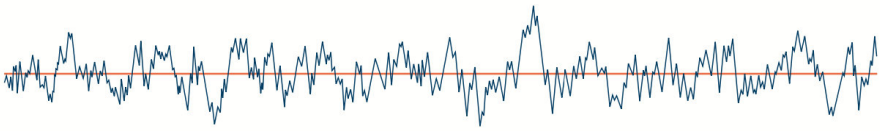

(b) Roughness profile

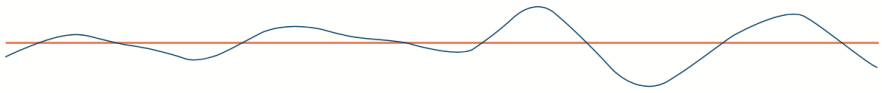

(c) Waviness profile

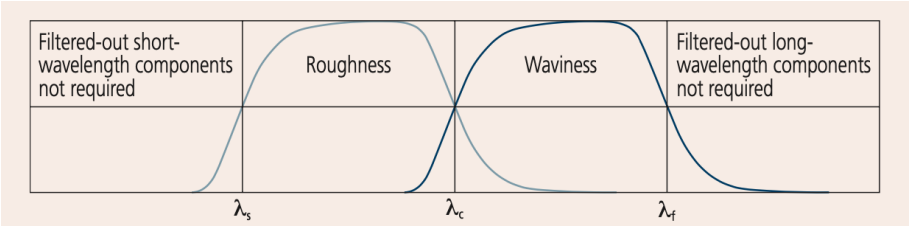

(d) Wavelength Filtering

Figure 3.9: Separating roughness and waviness profiles [22]

ISO standards 4287 and 4288 outline how to correctly measure roughness by applying an appropriate λ_c to the line/surface profile. Common λ_c values include 0.08mm, 0.25mm, 0.8mm, 2.5mm and 8mm. Selecting an appropriate λ_c depends on the roughness of the surface being measured. The catch-22 is that in order to measure a surface's roughness, you must first know how rough the surface is. With this is mind, a tailored surface roughness measurement process must be applied see Section 5.4.1.

3.2.3 Measuring Roughness

No engineering surface is geometrically perfect which means they all have a certain roughness. So how does one measure this roughness? A large proportion of this thesis will focus on the evolution of surface roughness over time and so a way to measure this roughness is required. Section 3.2 outlines how to produce the accepted line and surface roughness values R_a, R_q, S_a and S_q from a rough profile or surface area. Various measurement apparatus is available that produce the functions $z(x)$ and $z(x, y)$ in Equations 3.2, 3.3, 3.4 and 3.5. From this R_a, R_q, S_a and S_q can be calculated. The apparatus used for calculating these functions vary in accuracy and complexity.

Profilometry is the name given to the process of acquiring topographical data from a surface. This data includes the roughness, be it from a line trace or a three dimensional scan. Roughness measurements can be obtained through the use of profilometers. Profilometers can be further subcategorised into two main groups: contact and non-contact profilometers. Contact profilometers use a stylus (usually diamond) which is dragged across the surface of a material thereby following the profile of the surface. A schematic of a typical contact profilometer can be seen in Figure 3.10.

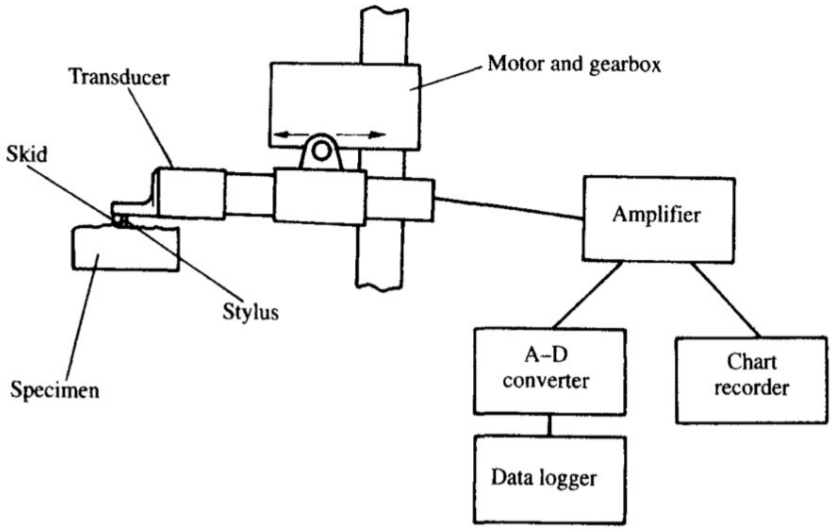

Figure 3.10: Contact profilometry equipment schematic [17]

Smaller styli and increased processing power have improved contact resolutions over the years, so much so that nanometer scale vertical and lateral resolutions are now

possible. Lateral resolutions depend on the stylus diameter, therefore lateral resolutions are typically lower than vertical resolutions. To produce a representative surface, the horizontal travel needs to be far greater than the vertical travel. Therefore vertical resolutions are typically around 20x that of horizontal resolutions [17]. Figure 3.11 shows how the greater vertical resolution and larger horizontal travel displays a more realistic surface roughness profile.

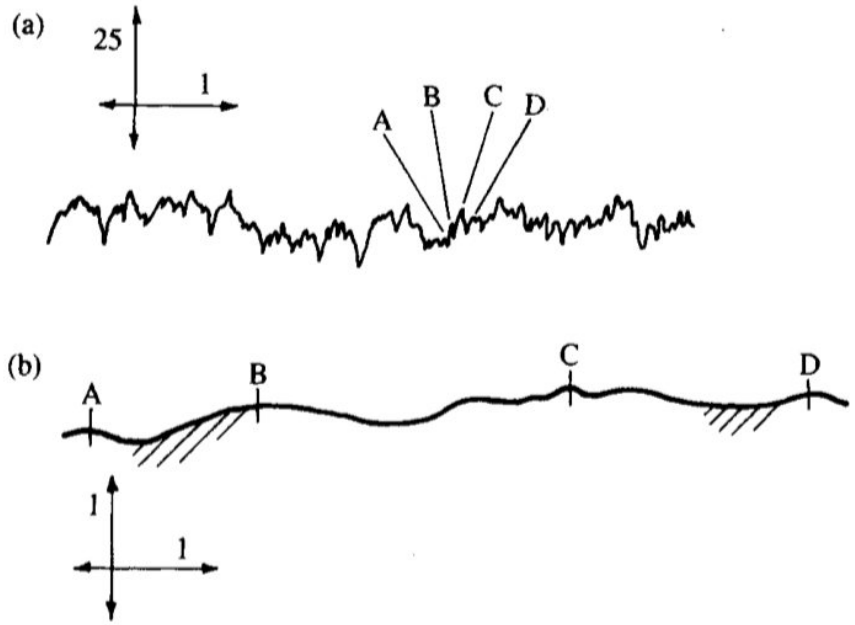

Figure 3.11: Vertical and horizontal resolution comparison [17]

Non-contact profilometers gather topological data using light. These all use a scanning optical head which is moved over the surface of a specimen and records the electromagnetic reflections. These reflections are then processed to create a 2D profile or 3D map of the surface. Figure 3.12 shows a non-contact optical profilometry device (Alicona microscope). The purpose of these non-contact methods are to not alter the surface profile physically by dragging a stylus across it and to map larger areas faster. Their resolution is limited by the spot size, but nanometer scale vertical and lateral resolutions are now possible given high magnification, although the measurement area also decreases. This means that an appropriate magnification factor should be selected based on the expected surface roughness of the specimen and the area you want to measure. Images can be stitched together to provide high resolution scans of larger areas, but this is a time consuming process and the resultant scan file sizes are large. Portable non-contact profilometers are also now available, which although cumbersome can measure surfaces directly. These can be

used to measure surfaces such as railheads in the field where moving the specimen is impossible. Optical scanning heads can also be attached to robotic arms, much like on coordinate measuring machines (CMM), to produce component scans and roughness measurements on complex components.

Figure 3.12: Non-contact profilometry equipment (Alicona Microscope)

Non-contact profilometry methods are now more frequently used than contact profilometry methods [23]. It is easier to scratch specimens with contact profilometers. These scratches permanently alter the surface topography. Alteration of the specimen is undesirable, especially when repeating roughness profile measurements during multi-cycle testing. As a rule of thumb, when the surface roughness is below $0.1\mu m$, contact measurement approaches should be used. Above this, non-contact approaches are more than adequate provided sufficient magnification. If the roughness is initially unknown, as is usually the case, a non-contact profilometer can be used prior to a contact profilometer to gain a better understanding of the topography. This is so as not to damage profilometer stylus or exceed the operating limit of the contact profilometer. Roughness profiles can now be acquired so quickly

with non-contact profilometers that it is these methods that are now used most frequently when measuring roughness or when preliminarily assessing a surface's topography [24].

It is worth noting a third type of profilometry: atomic force microscopy (AFM). This is a hybrid of both contact and non-contact profilometry methods. This form of profilometry is only used for measuring extremely smooth surfaces at the nm scale, and the lateral and vertical travel is highly limited so that only small area scans can be made [25, 26]. This makes this type of profilometer over sensitive for many standard roughness measurements, especially when considering the wheel-rail interface where roughness is measured in μm.

Specimens can either be measured directly or by making a cast of the specimen surface in a process known as replication. In this process a replication compound is coated over the surface and allowed to cure. Once cured and carefully removed from the surface, replicas can then be read with profilometers without effecting the real surface as much as directly measuring it. This can be useful if the overall specimen is too large to fit under a profilometer, a profilometer is not readily available or if you want a permanent record of a surfaces topography. Replication compounds are either one-part or two-part compounds. One-part compounds are easy to use, have short curing times (around 5 minutes) but produce replicas of lower resolution. Two-part compounds tend to produce higher resolution replicas, but have longer curing times (from 15 minutes up to 24 hours). They also require mixing in exact amounts which introduces additional errors that can effect repeatability [27]. Replication does not yield as accurate results as measuring the true surface because some topographical information is lost due to the limitations of the replication compound, and as the profile is removed from the true surface.

Broster produced some of the earliest work comparing replicas with true surfaces in 1972. Figure 3.13 shows a comparison between sawn brass and an epoxy resin replica of that same surface which was done using an analogue contact profilometer (Talysurf Model 3 Stylus Type) that used a $2.5\mu m$ diameter diamond stylus that was dragged over the surface. The physical stylus movements were then converted into an electrical signal much like on a record player. Once amplified, this signal was then graphically represented using a linear chart recorder. By applying different cut-offs, the $z(x)$ function produced was then numerically integrated to provide an R_a value. Note the reversed scale on (b) as a replica is a negative of the true surface. The y-axis is in μm and the length of the profile is around $2.5mm$. The two profiles

are relatively well matched, however replicas deviated from the true surface when replication took place outside of $0 - 40°C$ and were unable to be matched when the surfaces were smoother [28].

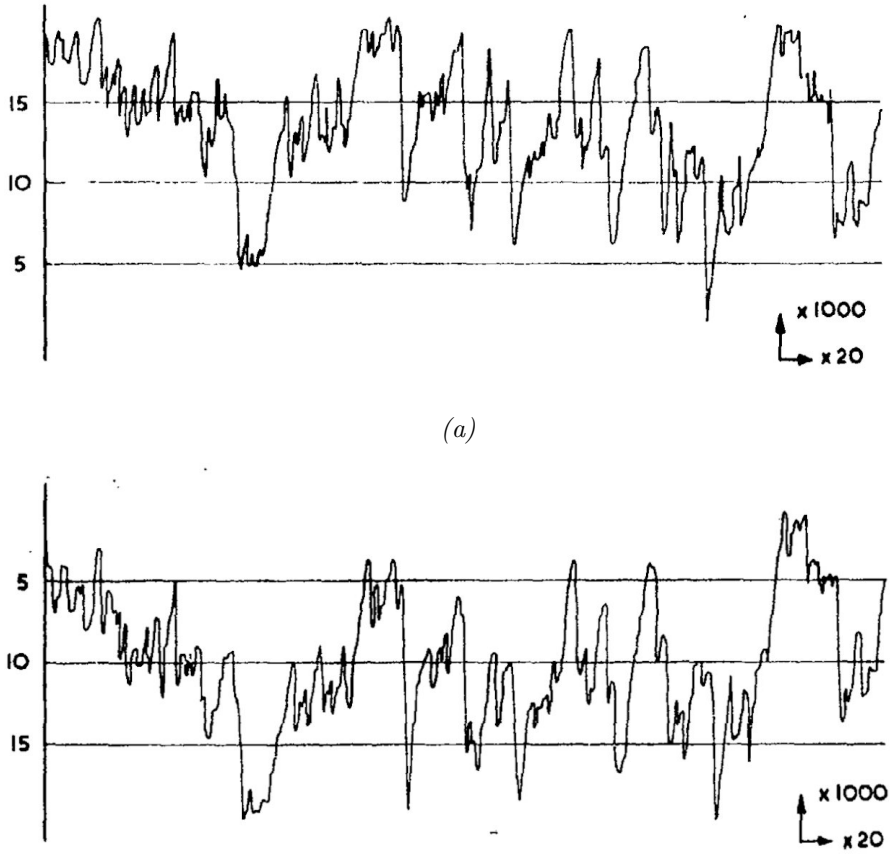

Figure 3.13: Comparison of the roughness profiles of (a) sawn brass (a) and (b) epoxy resin replica [28]

Since this study, specialised replication compounds have been developed such as the two-part resin Technovit 3040 and the one-part compound MICROSET 101RF, as well as more advanced 2D and 3D profilometers that produce far more accurate surface representations. Nilsson and Ohlsson found that replication errors exceeded 10% when $S_a < 0.3\mu m$. For reliable replication using one-part compounds the S_a roughness should be above $1\mu m$ and for two-part compounds the S_a roughness should be above $0.4\mu m$, which suggests that either of these type of compounds would be appropriate for wheel-rail surface replication. A modern comparison between a micromilled surface and a two-part replica is shown in Figure 3.14. The z-axis on the replica plot has been inverted to compare these two surface scans. The replica

shows good agreement for a surface $5X$ smoother than the surface in Figure 3.13 demonstrating the advancement in replication compound technology.

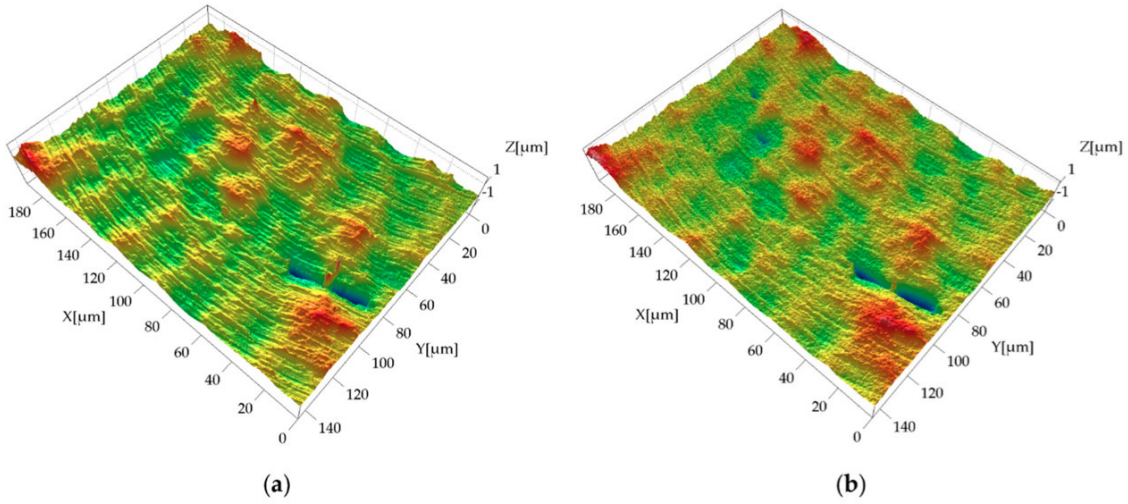

Figure 3.14: 3D comparison of the roughness profiles of (a) a micromilled surface and (b) an epoxy resin replica [29]

3.2.4 Variability of Wheel and Rail Roughness

As wheels and rails are used they wear away, deform or develop cracks. To combat this, reprofiling procedures are performed to both wheels and rails that both return these components back to the correct interfacial shape and remove subsurface cracks. The rail reprofiling processes are known as rail grinding or rail milling, and the wheel reprofiling process is known as wheel turning. Rail grinding and wheel turning are necessary parts of rail transport maintenance. Rail grinding is performed by a grinding train which travels along sections of track removing material from the railhead with numerous angled grinding stones. Wheel turning occurs on a lathe. As well as reprofiling the wheel, these lathes also act to reround the wheels which become out-of-round during service. Traditionally the entire wheelset must be removed from the train to work on the wheels, however more recently this can been done in-situ on mobile lathes. Both of these processes introduce roughness to these surfaces.

Rail grinding in particular poses a problem to industry as railway networks are often extensive and large amounts of material need to be removed quickly from the railhead. This means the material removal rate must be high which inevitably means a poor surface finish and high surface roughness. As rail networks are so extensive,

this rough surface is run-in using operational trains. Once run-in, the wheels and rails should have uniformly smooth surfaces of the desired profiles. There is a sweet spot from a maintenance perspective whereby crack propagation is in sync with the natural wear rate caused by traffic to reduce the impact of subsurface cracks [9].

The process whereby a rail goes from a freshly ground rail to working run-in rail is complex and happens over a relatively short space of time. Figure 3.15 shows the railhead roughness evolution for this process. It can be seen that ground rail in its pure form has a roughness that varies from $6 - 10\mu m$. After just the first day of traffic, this roughness decreased to around $1-2\mu m$. This drop in measured roughness is attributed to just 26800 ton of traffic. After 10 days or 259000 ton of traffic, there is relatively little change in roughness from the roughness measured after the first day [9]. Such a rapid change in roughness needs to be better understood, as do the effects of this roughness on traction/adhesion at the interface.

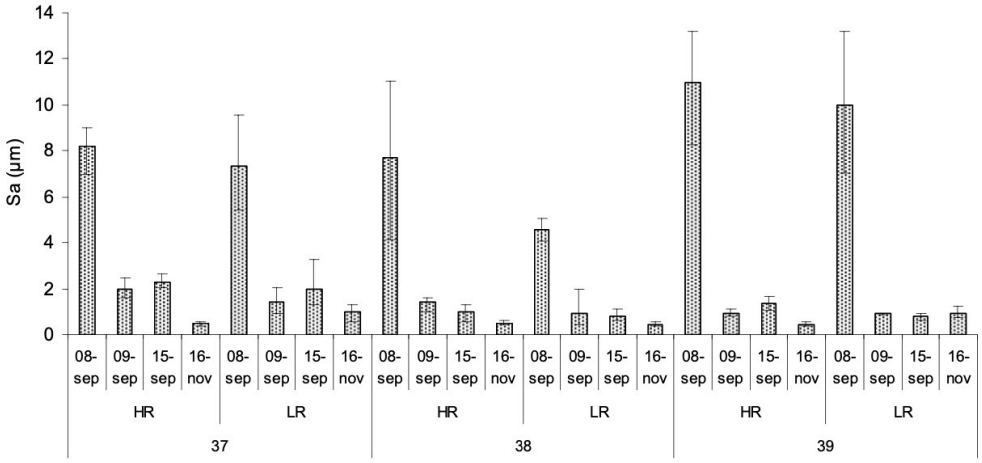

Figure 3.15: Running-in of ground rail [9]

3.3 The Wheel-Rail Interface

The wheel-rail interface is one of the most complex and studied interfaces in the field of tribology. The tribological behaviour at the interface is influenced by many factors which can all have significant effects on the durability and performance of the rail system. The nature of the wheel-rail contact is a fairly unique one due to the forces, geometries and environmental conditions involved.

3.3.1 Rail Regions

How the wheel and rail interact determines the forces, stresses and friction at the interface. A schematic of this interaction can be seen in Figure 3.16.

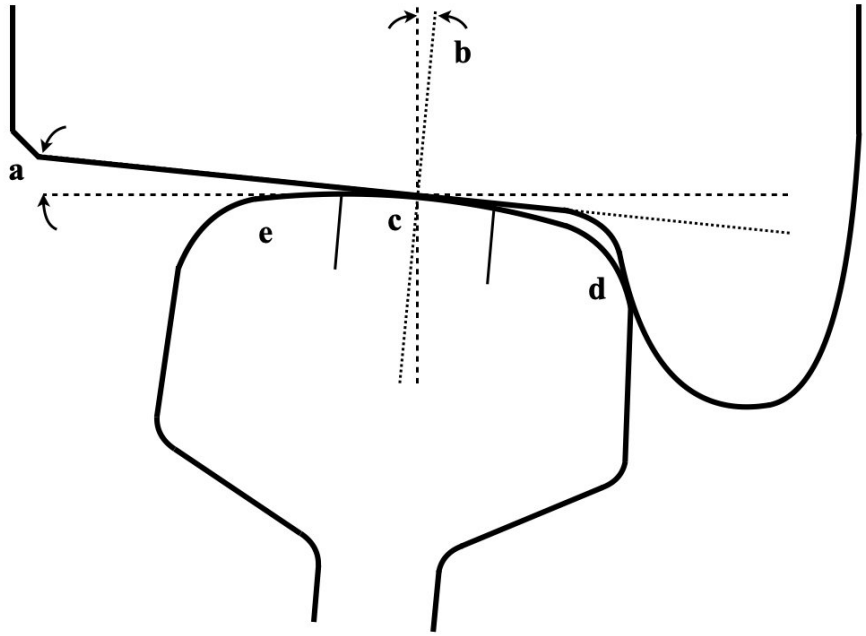

Figure 3.16: Schematic showing the profile of the wheel-rail contact: a) conical wheel profile; b) rail inclination; c) wheel tread-railhead contact; d) wheel flange-rail gauge contact; and e) undesirable region of contact

Figure 3.16 draws attention to several key features of the wheel-rail interface, firstly the conicity of the wheels which allow fo a variable effective wheel diameter. This allows a train to go round curves where the outermost (high) rail is longer than the innermost (low) rail. The wheel naturally drifts across the railhead to accommodate curves on the track. In doing so, the contact patch between the wheel and the rail moves about on the railhead. Railhead contact is the most common and occurs predominantly on well maintained straight sections of track. Due to the large railhead radius of this region, the contact patch is at its largest to accommodate the weight of the train and thereby reduce railhead stresses.

When going through curves, this type of contact often occurs with gauge-face contact

or wheel flange contact as it is more commonly known. The smaller radius of this rail region produces a smaller contact area, however, the lateral loads imposed on this region are usually smaller than those imposed by the weight of the train. When these lateral forces become too high, the lateral to vertical force (L/V) ratio becomes too high and can cause the wheel to climb over the rail resulting in derailment. The undesirable region of contact is the least common region and should not occur if the track and wheels are well maintained; it usually occurs due to incorrect track gauge and inclination or hollow wheels. Very high contact stresses are experienced in this region.

The scale at which trains operate presents a challenge to industry as whilst the wheel rotates presenting the same surface cyclicly, a specific section of rail is only in contact with the wheel once as a train travels from A to B. This means that the interface can have vastly different contact conditions at different points on a train's journey. The interface is effected by multiple contaminants or third-body layers (3BLs). Typical wheel-rail 3BLs include leaves, sand, water, oxides and friction modifiers. These are covered in more detail in Section 3.4.

3.3.2 The Contact Patch

The wheel-rail contact patch can be approximated by an ellipse in most cases (see Figure 3.17). An additional ellipse can occur if the flange is in contact with the rail gauge creating two points of contact. The high hardnesses of both the wheel and the rail as outlined in Table 3.1 mean the contact area is relatively small given the size of the components involved. Typical contact areas are in the region of $1cm^2$ which results in extremely high contact pressures (up to 1.5GPa in some cases) through each individual contact patch [30].

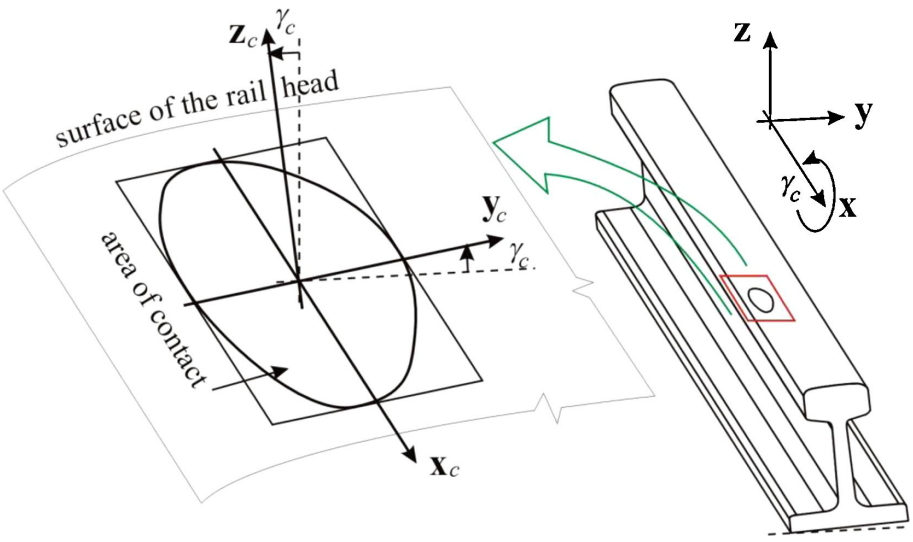

Figure 3.17: Schematic showing the wheel-rail contact patch [31]

3.3.3 Creep

For rolling contacts it may appear that the wheel is in a state of pure rolling however slip is often occurring at the interface due to the frictional conditions at the wheel-rail interface, this is represented by Figure 3.18.

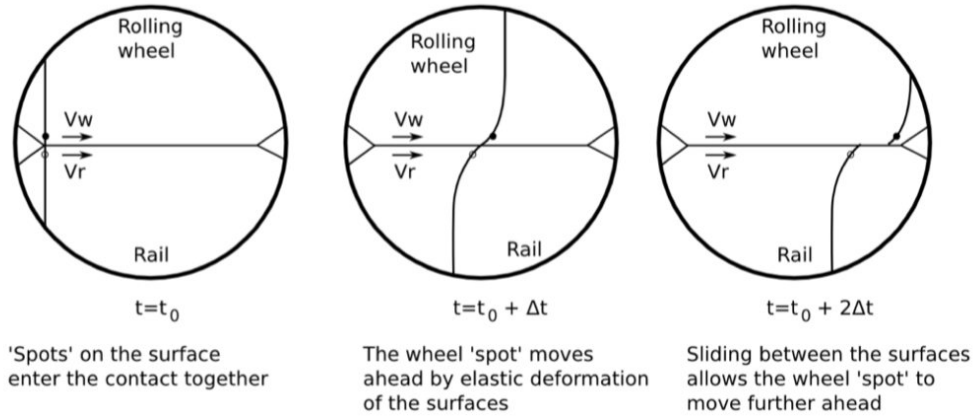

Figure 3.18: Graphical representation of slip [32]

In Figure 3.18 the wheel is rotating marginally faster than the distance it covers along the rail. The resultant wheel-rail contact patch will therefore be divided into slip and stick regions [33]. With increasing traction between the two surfaces, creep also rises which can be seen in Figure 3.19. When creep is represented as a percent-

age, it is known as creepage. High levels of slip result in excessive wear particularly for dry contacts.

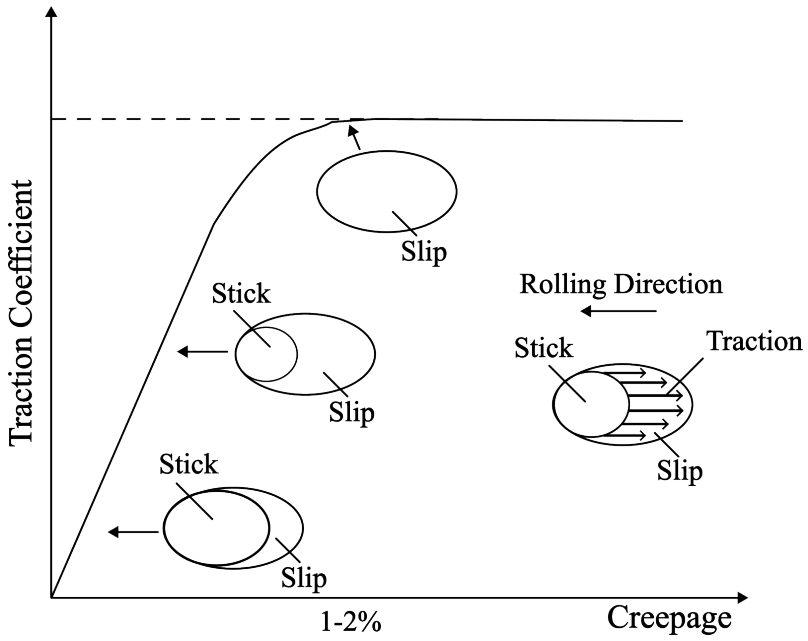

Figure 3.19: Stick-slip contact and their relationship with creep curves [34]

Creepage can occur as traction (during acceleration) or adhesion (during braking). The point at which a full slip scenario occurs (usually around 1-2% creepage) is known as the friction coefficient. Before this they are known as either the traction or adhesion coefficients. These are the same in essence, however they are given different names by industry to describe the two scenarios. In this work they are often used interchangeably. As creepage increases so does the traction coefficient until it reaches the limit (this depends on the loading and frictional conditions) and then remains constant at which point full sliding occurs. This is an idealised creep curve as traction at the interface can change when creepage is increased beyond 1-2%. This can be due to different factors such as lubrication regimes and thermal affects. It is worth noting that the creepage regime displayed here is along the length of the rail. Creepage also occurs across the rail most notably during bends in the track where there is a higher and lower rail.

3.3.4 Materials

Whilst both the wheel and rail are made from steel, there are a variety of steels used for the various wheel and rail types. Common industry standard wheel and rail steel grades in the UK are ER8 and R260 respectively, the material properties of which can be seen in Table 3.1. The 260 in this case refers to the Brinell hardness of the steel grade. Harder wheel and rail materials are available, however there is an increased cost associated with these high grade steels both in terms of manufacture and maintenance costs. For more information on hardness, see Section 3.3.5.

Steel Use	**Steel Grade**	**UTS** (MPa)	**Yield Stress** (MPa)	**Brinell Hardness** (HB)
Wheel	ER8	940	590	230-255
Rail	R260	880	420	260-300

Table 3.1: Approximate ER8 and R260 material properties [35] [36]

3.3.5 Hardness of Wheels and Rails

Hardness is defined as a material's resistance to localised plastic deformation. When wheels and rails are reprofiled, fresh 'soft' material is exposed which is then run-in by traffic. The stresses at the wheel-rail interface exceed the yield strength of the materials involved, and so the materials are plastically deformed when loaded. As more traffic passes over a section of rail, the rate at which the materials deform reduces i.e. the materials have become harder. The effect this has from a wear perspective is covered in more detail in Section 3.3.6. Hardness can be measured using hardness testers of which there are many. A few common tests are Brinell, Vickers and Rockwell hardness tests. These all use a specifically shaped indenter that pierces the material with a known load. The size of the indent tells you how hard the material is. Figure 3.20 shows a Rockwell hardness tester.

Figure 3.20: Rockwell hardness tester

Post grinding rail hardness on the railhead was found to increase from 280HB (Brinell Hardness) to 320HB after 50Mt of traffic [37]. The nature of work hardening means that the highest hardnesses were found below the surface where the highest stresses occur. When these rails were sectioned, the hardness 1.2mm below the surface was measured to be 380HB. Whilst these elevated hardnesses are the reason railways work at all, there are some implications of a harder less ductile material predominantly when it comes to wear. In addition, the discrepancy between the hardness of two contacting surfaces causes surfaces to interact differently and ultimately affects the way roughness evolves.

3.3.6 Wear Mechanisms of Wheels and Rails

Wear occurs on both wheels and rails and the amount of wear is usually quantified by the mass removal rate, however there are various types of wear that cause this mass to be removed. Rolling contacts such as those found at the wheel-rail interface exhibit a far lower resistance to motion than sliding contacts, however they require

comparatively hard surfaces. This increases the stress experienced in the wheel and rail [17]. Improvements in the material capabilities of wheels and rails have shifted research focus from a wear failure regime to a stress failure regime, whereby components are now more likely to fail due to fatigue than due to other failure mechanisms [38].

Rolling contact fatigue (RCF) is one such fatigue process caused by a near-surface alternating stress field. Counterintuitively the region of highest bulk stress lies just below the surface. This alternating stress field cyclicly loads the subsurface to extremely high stresses. Microcracks develop at inclusions or other inhomogeneities within this region of high alternating stress. These microcracks then propagate towards the surface. When enough of these cracks join together a piece of wheel or rail is removed from the surface in a process known as spalling [39]. This normally occurs with smooth contacts. Microcracks can also develop from the surface and propagate downwards in a process known as pitting. This normally occurs with rough contacts where the troughs between surface asperities act as stress-raisers [40]. Like spalling, these cracks join together with other cracks and material is removed. Both these processes can of course occur simultaneously, meaning the resultant wear is a combination of both surface and subsurface cracks. The presence of slip complicates matters further as material is simultaneously removed from the surface through oxidisation or delamination, meaning that given high slip rates, cracks can be worn away before they are able to propagate [40–42].

RCF is now the primary cause of failure for correctly set up wheel-rail systems and occurs most frequently at curves on the track. Over extended periods, plastic deformation causes permanent deformation through ratchetting (see Figure 3.21). Stage (a) represents elastic deformation. Scenarios (b) to (c) represent elastic and plastic shakedown. Materials plastically deform during the early cycles but then find a constant permanently deformed elastic steady state due to strain hardening of the materials involved. This region is desirable as materials accumulate protective residual stresses. Scenario (d) shows how repeated loading cycles beyond a material's yield strength cause incremental deformation over time. This undesirable process is known as ratchetting and can cause large plastic deformations over time [43].

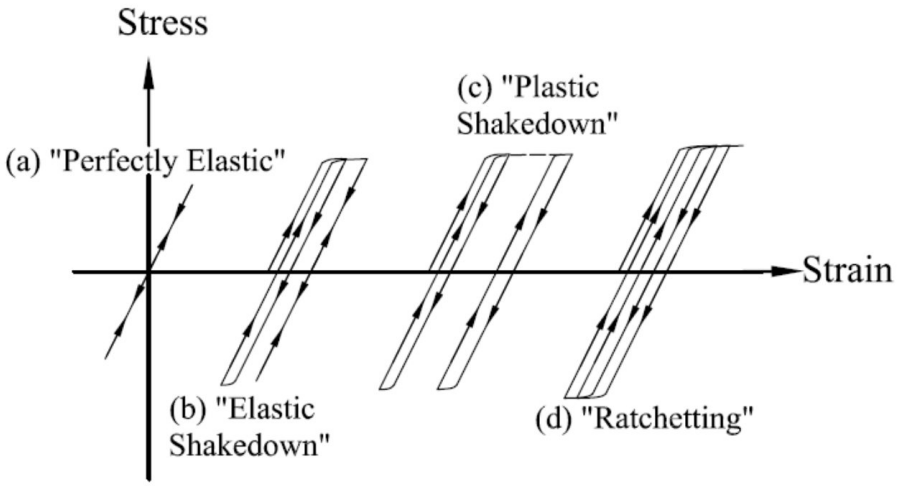

Figure 3.21: Plastic deformation hysteresis loop [43]

The subsurface plastically deformed layer that ratchetting produces can be seen in Figure 3.22. An oxide layer encases this deformed layer which eventually wears away through delamination.

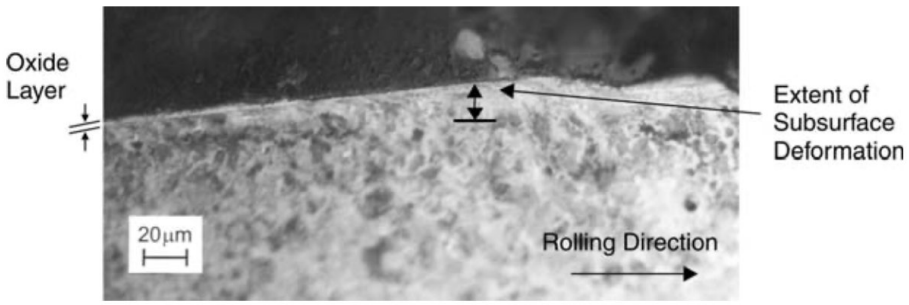

Figure 3.22: Subsurface plastically deformed layer (1.5GPa slip = 0.2%) [44]

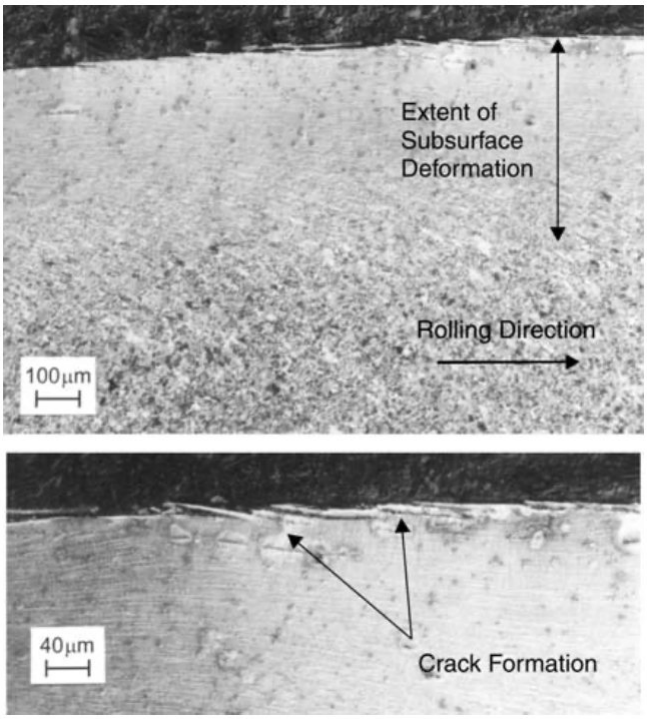

Figure 3.23: Subsurface plastically deformed layer and crack formation (1.5GPa slip = 3%) [44]

Wear is highly dependant on the level of slip at the interface which is a product of the difference between the wheels rotation speed and how fast the wheel moves along the rail (see Section 3.3.3). Past studies into railway wheels and rails were able to identify three wear regimes: mild, severe and catastrophic [45, 46]. The three wear regimes are explained in Figure 3.24 by the three different wear rate gradients. Wear rates increase steadily initially (slip $= 0 - 2\%$). During this mild wear regime, wear is dominated by surface oxidation. Wear rates then level off (slip $= 2 - 20\%$), before increasing rapidly (slip $> 20\%$) as the severity of the contact conditions are increased. During these severe and catastrophic wear regimes, wear is dominated by surface cracking and mass loss due to delamination.

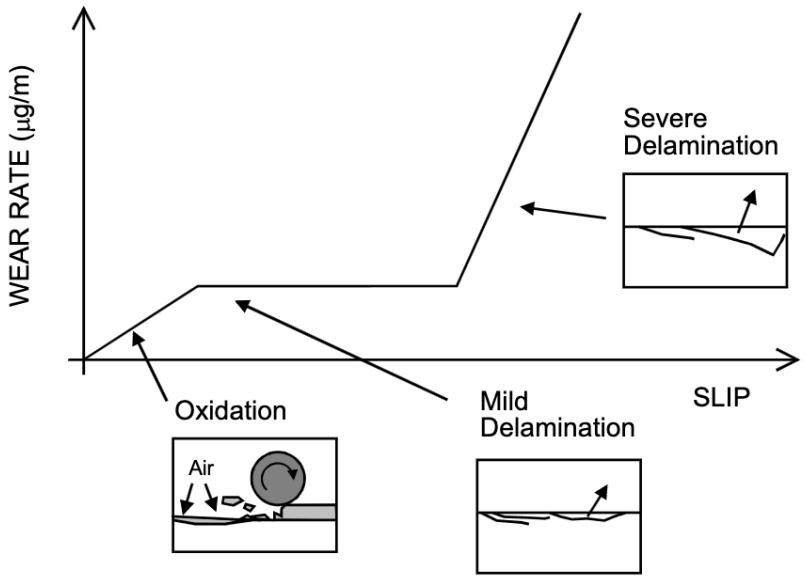

Figure 3.24: Wear regimes of wheels and rails [44]

Lewis and Dwyer-Joyce used twin-disc testing to demonstrate that wear rates show good agreement with a typical elastic creep-curve (the Carter creep-curve [47]) and measured adhesion/traction coefficients (see Figure 3.25). This indicates that wear and friction are intrinsically linked at least for smooth dry contacts. The transition from partial slip to pure slip occurs around slip = 2%. Beyond this, wear is independent of sliding velocity, suggesting that the wear is controlled solely by the contact stress and friction coefficient. At higher rates of slip, temperature effects act to lower the yield strength and other material properties of the two contacting surfaces, thereby allowing wear rates to increase once more (note the logarithmic wear rate scale) [44].

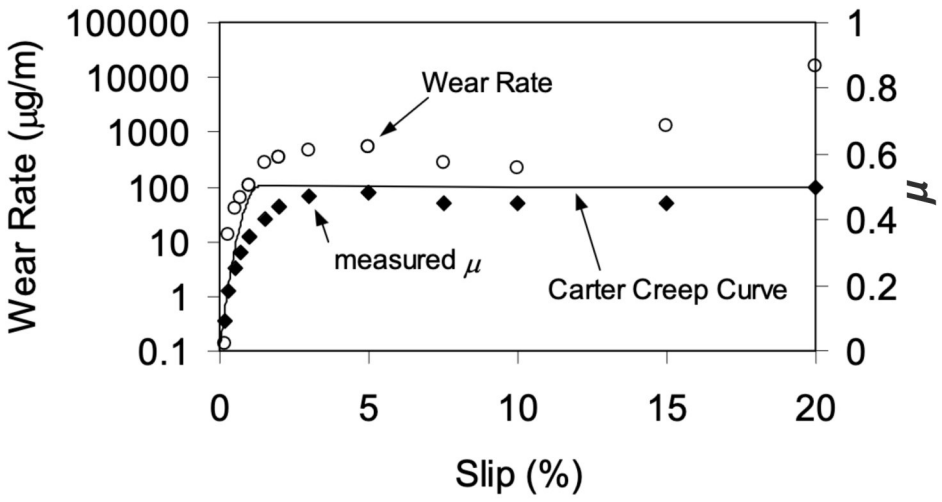

Figure 3.25: Wear rate and it's relationship with slip and friction [44]

Whilst this thesis focuses predominantly on roughness and the effect this has on traction/adhesion, it is now known that elevated roughness leads to more frequent crack initiation and pitting. Since this alters the surface topography and roughness, an understanding of this process is required. In addition, wear regimes have been shown to be closely linked to friction and slip at the interface [44]. Therefore to understand roughness and adhesion, one must first be aware of the wear processes roughness and adhesion induce.

3.4 Friction Management

The wheel-rail interface operates within certain margins of allowable force, contact stress and traction. A number of interfacial compounds that modify these parameters can occur naturally or be applied. In the world of tribology, these are known as third-body layers (3BLs). Natural 3BLs include leaves, water and oxides. Unnatural 3BLs also known as friction modifiers include grease, sand and other top of rail products of which there are many. Sand is commonly used to increase the traction coefficient, whereas grease is used to lower the traction coefficient. These friction modifiers are applied to return the wheel-rail system to within its operational limits, either to improve sections of track exhibiting low adhesion or else to improve rail efficiency and reduce cornering forces [48]. Friction modifiers are additionally applied the curves to reduce levels of squeal. This high pitched loud noise often occurs on metros and underground networks where corner radii need to be more severe to

navigate space scarce cities.

3.4.1 Natural Contaminants at the Wheel-Rail Interface

The majority of natural 3BLs are detrimental to performance at the wheel-rail interface as they contribute to undesirable levels of traction. Many contaminants occur due to environmental conditions such as humidity and temperature, and some are seasonal. Leaves are one such seasonal contaminant in that they are far more prominent in the autumn. Leaves themselves are not entirely problematic, however when they form a leaf layer on the railhead, extremely low and dangerous traction coefficients have been measured and observed [49–51]. Leaf layers are formed when multiple leaves lying on the railhead are subjected to repeated compressive stresses. These compressive stresses are achieved during the interaction of the wheel and rail. Bearing in mind that a single train consists of many wheelsets, a great number of cycles can occur in just a few train passes. Leaf layers can therefore form very quickly. Furthermore, they have an ability to spread over large portions of track from their original position. In the work of Lanigan et al., from a 3 metre long leaf application zone, leaf layers were measured to have spread to 10 metres away after just a few train passes. The result is what is known as a 'black layer'. This black layer is difficult to remove from the railhead, has an ultra-low friction coefficient and is electrically insulating [52].

In addition to leaves, water is also known to lower traction (see Figure 3.26). These processes however do not typically occur in isolation. In many cases where other contaminants are present, water is also present. Small amounts of water such as dew or when it has just started to rain make for very low friction coefficients [53]. These friction coefficients can be an order of magnitude lower than those of the wet surface condition shown in Figure 3.26.

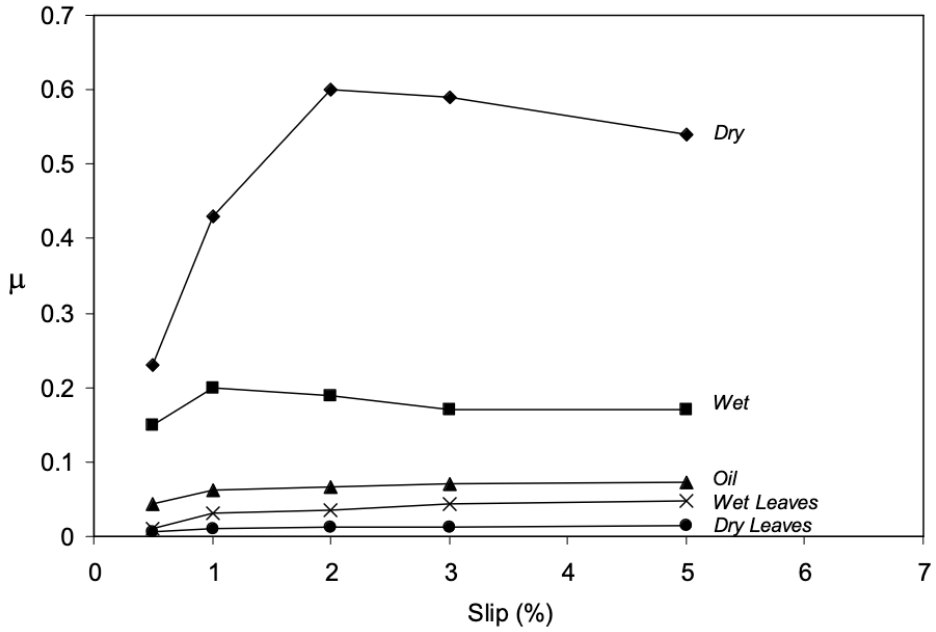

Figure 3.26: Creep curve showing various rail surface conditions and their affect on the traction coefficient [7]

3.4.2 Friction Modifiers

Friction modifiers are products that are purposely applied to the wheel-rail interface to alter the level of traction. These can be greases applied to the gauge face to lower friction, thereby reducing cornering forces, noise and rates of wear. Top of rail (TOR) friction modifiers are entrained with additives to tailor friction on the railhead. Both of these friction modifiers can be applied by trackside applicators and more recently have been distributed from vehicle mounted applicators. Solid lubricants are now used more frequently to lower flange friction and reduce the risk of derailment.

3.5 Scaling Down the Wheel-Rail Interface

Small scale test rigs offer a way to produce data quickly without the cost and red tape of testing at larger or full scale levels. Tribology has a well established research path from initial theory through a series of small scale and full scale test rigs. Pre-computational modelling the outputs from these small scale test rigs were scaled up using scaling factors that would be applied to the forces, geometries and pressures

involved. For example if the contact patch area is increased due to the increased scale, the applied forces must be higher to achieve similar pressures to approximate what would happen in real life. More recently the small scale data produced can be used to parameterise models that predict the full scale outcome. These models use various theoretical equations to predict the outcomes. Modelling results are only as good as the data you input and should always be accompanied by experimental results, therefore the model outcomes should ultimately be validated with full-scale testing. In the following sections some common tribological test rigs as well as some wheel-rail specific rigs are reviewed.

3.5.1 Pin-on-Disc

The pin-on-disc testing apparatus is perhaps the most common tribological test. The test comprises of a loaded pin that is pressed onto a rotating disc as seen in Figure 3.27. The load, rotation speed and pin geometry can be adjusted. This type of test is used extensively in wear testing as the material removed is easily calculable and wear scars are visible. Analytical solutions are also possible when the interacting geometries are simplified, and as such numerical models can be validated against both analytical and experimental results. By having industry standard tribological tests with well trodden experimental process routes, results obtained at numerous different tribological research institutions can be compared on equal terms.

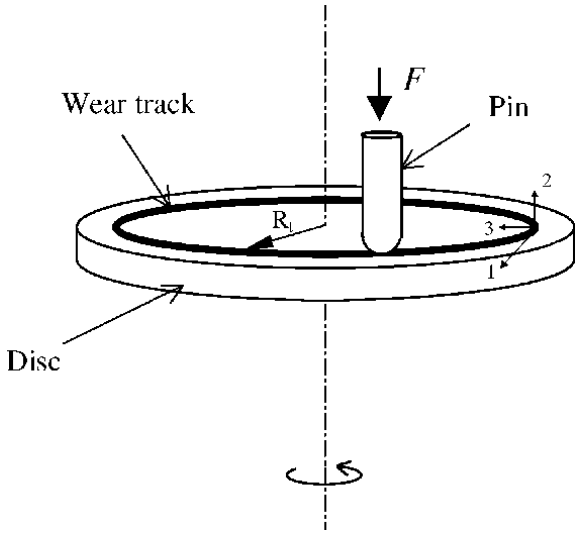

Figure 3.27: Pin-on-disc test rig schematic [54]

3.5.2 Twin Disc

Like the pin-on-disc test, the twin disc test is also widely used by industry. Twin disc test rigs comprise of two powered rotating discs positioned on top of one another, thereby producing a line contact patch. The test is used extensively to study the wheel-rail interface as slip can be generated by altering the relative motion of the two discs. 3BLs can be introduced relatively easily often whilst the test is running [55]. Figure 3.28 shows a schematic of the SUROS twin disc test rig developed at the University of Sheffield.

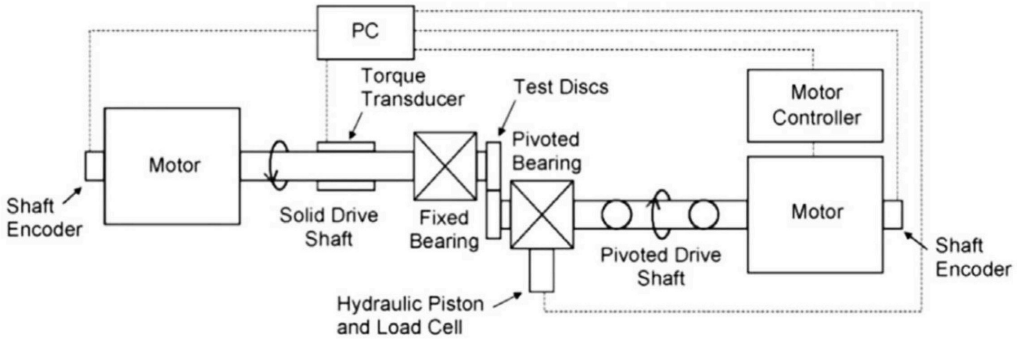

Figure 3.28: SUROS twin disc test rig schematic [55]

3.5.3 High Pressure Torsion

The High Pressure Torsion (HPT) Rig is a more specific test that consists of two flat specimens that twist through a predefined angle and compression. A tension-compression-torsion load cell measures the normal and tangential forces whilst a rotary variable differential transformer (RDVT) measures the rotational speed [56]. Originally this test machine was used to generate specific microstructures, however it is more recently being used to imitate the wheel-rail interface. The information required to generate creep-curves can be generated in less than one rotation. 3BLs can be introduced and due to the flat contacts, initial roughness can be applied to the specimens with relative ease [57]. All this makes the HPT a highly versatile and fast way of understanding the wheel-rail interface.

Figure 3.29: The HPT rig at the University of Sheffield

3.5.4 Full-Scale

The penultimate level of testing before testing on the actual machine or equipment, is a full-scale test rig. Depending on the interface you are studying this test rig uses the real components loaded either statically or dynamically in a lab. For the wheel-rail interface a full-scale wheel-rail rig (FSR) is used. This one-to-one scale wheel-rail rig mimics most closely the loading conditions experienced on track. Not only are the size and forces the same as those experienced in real life, but also the geometry of the contact is the same as wheels and rails can be directly obtained from the rail sector and be implemented onto the rig. An example of such rig can be seen in Figure 3.30.

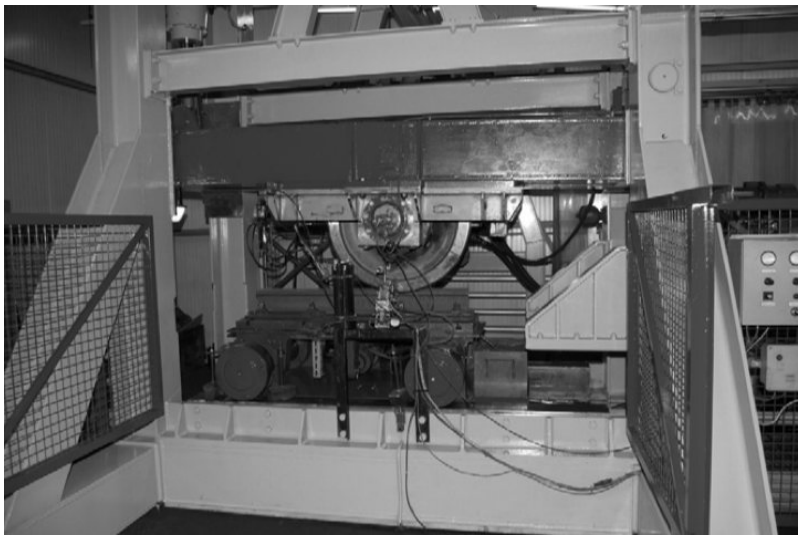

Figure 3.30: Full scale rig at Voestalpine Schienen GmbH [58]

3.6 Creep-Force Models

Modelling the wheel-rail interface is essential as real data can be difficult to obtain due to the nature of the rail industry and the time pressures already placed on rail networks. Small-scale testing is relatively easy to perform but is not particularly representative of the the full-scale wheel-rail interface. By using small-scale test outputs to parameterise models, we can then predict full-scale outcomes.

Creep-force models are used throughout the industry to predict a system's frictional response. Creep was covered in Section 3.3.3 and in a railway context relates to the difference between the wheel's rotation and the wheel's movement along a section of rail. A system's frictional response is contained within a creep curve. These creep curves are generated by inputting small-scale experimental data into a creep-force model. Typical experimental parameters that need to be measured are tangential and normal pressure. These can be obtained from any of the testing apparatus outlined in Section 3.5. A great number of these creep-force models exist, a few of which have been summarised below.

The CONTACT model is a half space friction model that uses Kalker's exact theory to solve time-dependent normal and tangential contact problems [59]. Each material may have its own individual properties, but are assumed to be elastic, isotropic and homogenous in nature. CONTACT is computationally expensive to solve.

The FASTSim model decreases the computational complexity by modelling the half space as a series of springs and by reducing the number input parameters, for example assuming both bodies consist of the same material [60]. The spring's tangential surface displacement is therefore proportional to the traction in the contact. The stiffness of the springs is such that tangential forces calculated with FASTSim equal that of half space theory. By adjusting the stiffness of these springs, third-body layers can be taken into account. The solution no longer varies with time and the model can only solve for elliptical contacts. Whilst this may seem very limiting, it is ideal for the wheel-rail contact in which the rail and wheel are made out of the same material and the contact area is elliptical.

The Polach model builds on the FASTSim model by describing changes in the initial slope of the traction curve as well as accounting for large slips by decreasing the traction.

The Tomberger model incorporates a roughness parameter and also temperature effects into the FASTSim model to give a better representation of the wheel-rail interface. Whilst this model includes a roughness input, this is simply a measured R_a value that does not vary temporally.

The extended creep-force (ECF) model is perhaps the most advanced model currently in use and considers an elastic rail and wheel separated by an elasto-plastic 3BL with normal stress and temperature dependant material properties. In addition to this, the ECF model incorporates time dependency for the inclusion of transient effects [61].

3.7 An Overview of Ultrasound and the Wheel-Rail Interface

Nearly always, interfaces are concealed and inaccessible during operation. The interfacial surfaces can of course be assessed when not in operation either by disassembling the machine or separating the surfaces. This kind of assessment is time consuming and no information can be gained of the loaded system. Operational stresses would be inferred from how worn or deformed the surfaces were when assessed. Naturally we require ways in which to monitor interfaces as they move relative to one another in real-time. Early attempts to accomplish this involved using optical sensors and transparent materials, however most engineering materials

including those used in the wheel-rail interface are not transparent. By studying the interface between components in real-time, we can potentially measure how roughness evolves and determine how varying roughness effects friction at the interface.

Ultrasonic reflectometry is one such way we can analyse these concealed interfaces and is covered in detail in Chapter 4. Ultrasound has been used for decades to non-destructively test components for cracks. The growth of these cracks can be monitored by rescanning the component at various intervals to predict its lifetime. The same theory can be applied to the wheel-rail interface as the gap between the wheel and rail reflects ultrasound in the same way. Ultrasound has already been used to calculate interfacial properties such as the contact pressure and interfacial stiffness of a contact.

3.7.1 Ultrasonic Measurements of Static Contacts

Early attempts to measure the wheel-rail interface using ultrasonic methods were performed on static contacts [10], [62] [63]. Properties such as the interfacial stiffness, contact area and the reflection coefficient at the interface were obtained from these early attempts and are in agreement with available theory and finite element methods. A schematic of the typical equipment used can be seen in Figure 3.31.

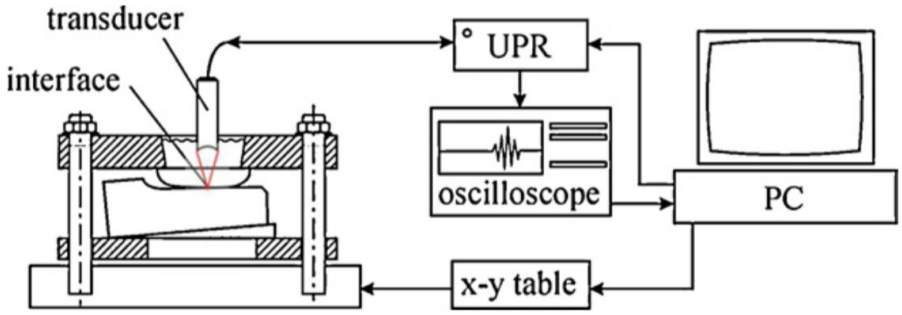

Figure 3.31: Early wheel-rail ultrasonic measurement equipment schematic [31]

The ultrasonic transducer can be moved over a surface to create a 2D map of the the contact pressure at various loads which can be seen in Figure 3.32. Further attempts produced more detailed pictures of contact areas [64–66].

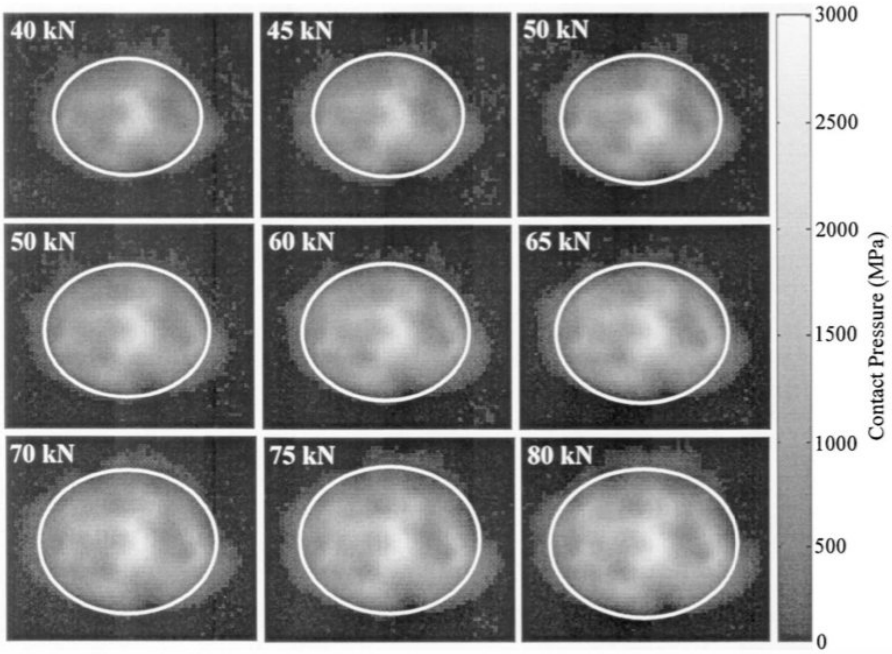

Figure 3.32: Static contact pressure scans made with an ultrasonic sensor [11]

3.7.2 Ultrasonic Measurements of Dynamic Contacts

Early dynamic ultrasonic measurements were first tested by Dwyer-Joyce et al. [12]. Ultrasonic arrays were used to measure a wheel-rail contact quickly without having to move the ultrasonic sensors; these measurements were in agreement with pressure sensitive film measurements and single probe scans. Figure 3.33 shows one of the first dynamic wheel-rail contact patch scans with an applied rolling speed of 1mm/s. Whilst this is still far slower than a train's typical operational speed, it demonstrated that the method worked. Depending on the number of sensors and the size of the contact, the measurable train speeds could be increased by many orders of magnitude.

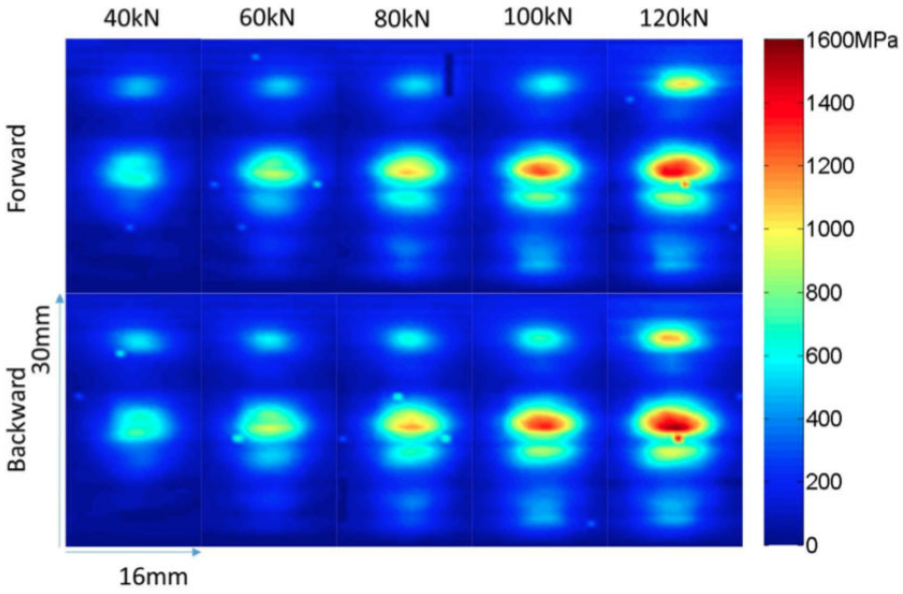

Figure 3.33: Dynamic contact pressure scans made with ultrasonic sensors [67]

3.7.3 Future Ultrasonic Reflectometry Methods

As mentioned in Section 3.1, the interaction of microscopic asperities determines the tribological conditions, wear processes and wear rates of interfaces. Future ultrasonic reflectometry methods are likely to monitor the interaction of individual asperities so as to gain more understanding of what is happening at the interface. Early attempts to do so are outlined in a paper by Reda et al. [68]. The method used was able to measure the surface roughness of a bonded interface of silicon and silica on a nanoscopic scale. The use of ultrasonic matrices is set to provide an even more detailed picture of interfacial conditions [69, 70].

3.8 Summary

In this section literature pertaining to roughness, the wheel-rail interface, tribological testing and modelling were reviewed, as well as how one might use ultrasound to measure interfacial contact conditions at the wheel-rail interface. Ways of quantifying roughness were found, as well as ways in which to measure them. The wheel-rail interface was studied in detail; geometry, creep and wear were discussed. Methods of mimicking conditions on track were reviewed. HPT and FSR testing were found to be the most suitable small-scale and full-scale testing apparatus for this work.

Ways of predicting full-scale frictional behaviour at the wheel-rail were reviewed in Section 3.6. The ECF model was identified as the most suitable model for this work. This was due to the model's ability to take account of roughness and as it can be parameterised by the outputs of HPT tests. Ultrasonic measurement approaches were discussed and found to be an effective way of monitoring wheel-rail interfacial conditions in-situ. Section 4 reviews ultrasonic theory in more detail, and what measurements and relationships might be obtained through using ultrasonics in this work.

4 Ultrasonic Theory and Practice

Ultrasound is sound too high in frequency for the human ear to detect. Whilst this varies from person to person, $20kHz$ is generally agreed to be the lower end of the ultrasonic scale. Ultrasonic reflectometry is the process whereby ultrasonic waves are purposely emitted through a material and are then partially reflected when the wave interacts with a change in material properties. This change can take the form of cracks, inclusions or material interfaces such as the wheel-rail interface. Whilst $20kHz$ is still technically ultrasonic, the frequencies used in ultrasonic reflectometry are usually far higher (in the order of MHz) in order to interact with microscopic interfaces. Figure 4.1 shows a schematic of this process.

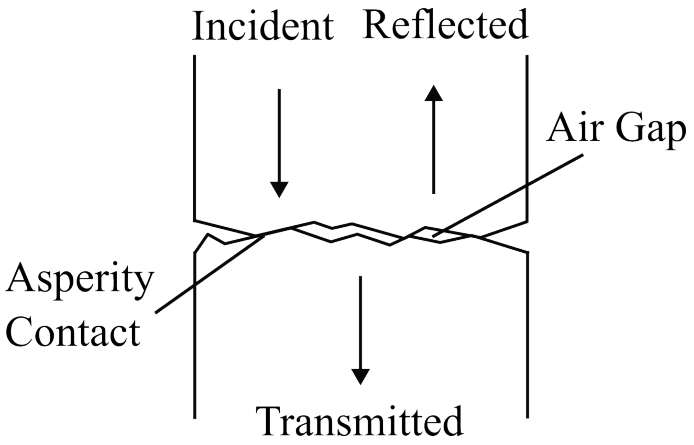

Figure 4.1: Ultrasonic reflectometry schematic

4.1 Acoustic Theory

Like audible sound, ultrasound is governed by the same acoustic laws which are discussed in the following sections.

4.1.1 Wave Propagation

The process by which acoustic (and therefore ultrasonic) waves propagate is through the compression and rarefaction of molecules held together by elastic forces within the medium the sound is propagating through. These molecules oscillate around a stationary point, thereby creating variations in density which are then passed

through the medium transporting acoustic energy [71]. This is perhaps best visualised by Figures 4.2 and 4.3 which describe the two types of wave that can occur.

4.1.2 Longitudnal Waves

When the oscillation of the molecules is in the same plane as the direction of propagation, the wave is known as a longitudinal wave as seen in Figure 4.2. This wave and the one seen in Section 4.1.3 occur most prominently in solids where particles are tightly packed in layers, however they can also be seen in liquids and compressed gases. λ represents the wavelength of the sound.

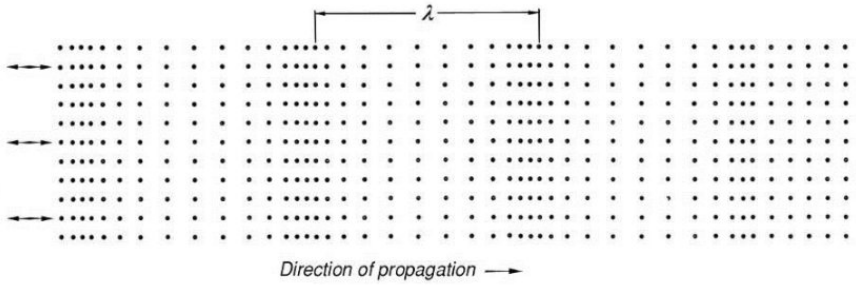

Figure 4.2: Longitudinal wave [71]

4.1.3 Transverse (Shear) Waves

When the oscillation of the molecules is perpendicular to the direction of propagation, the wave is known as a transverse or shear wave as seen in Figure 4.3. In solids, shear force can be transmitted to particles in adjacent planes, causing particles to move sinusoidally up and down in phase [71]. Both these waves can be purposely created with the use of ultrasonic transducers.

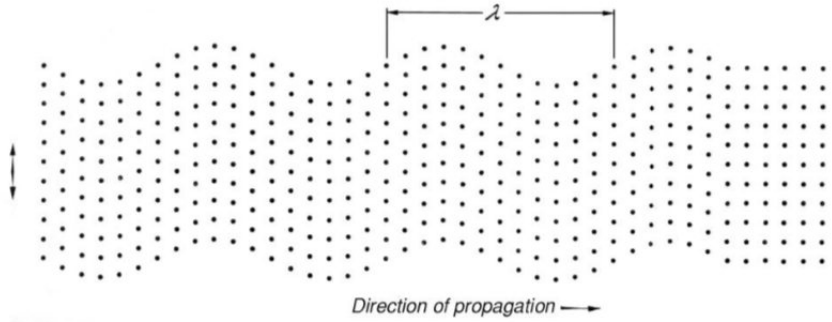

Figure 4.3: Transverse wave [71]

4.1.4 Wave Velocity

Wave velocity (c), more commonly referred to as the speed of sound, is the rate at which a wave propagates through a medium. The speed of sound through air is $343m/s$, however it can differ enormously depending on the medium through which the sound is propagating. The exact value of c is determined by both material density (ρ) and the elastic modulus (E) as seen in Equation 4.1:

$$c = \sqrt{\frac{E}{\rho}} \tag{4.1}$$

The speed of sound is also proportional to the product of the wave frequency (f) and the acoustic wavelength (λ) as outlined in Equation 4.2:

$$c = f\lambda \tag{4.2}$$

The wave velocities for various materials can be found in reference tables [72] from which you can measure the thickness of a material using the velocity, time and distance relation (see Section 4.3.5).

4.1.5 Acoustic Impedance

Acoustic impedance (z) is a material's opposition to acoustic flow and is defined as the product of the material's density and wave velocity as described by Equation 4.3:

$$z = \rho c \tag{4.3}$$

Therefore, sound struggles to travel through materials with high acoustic impedance. This highlights a potential limitation of ultrasonic reflectometry in that it is difficult to study a system if materials in that system have a high acoustic impedance. Some common engineering materials and their impedances can be seen in Table 4.1.

Material	**Velocity** (km/s)	**Density** (g/m^3)	**Impedance** $(MRayls)$
Aluminium	6.42	2.77	17.33
Brass	4.70	8.64	40.60
Concrete	3.10	2.60	8.00
Copper	5.01	8.93	44.60
Epoxy	2.70	1.21	3.25
Glass	5.64	2.24	13.10
Iron	5.9	7.69	46.40
Lead	2.20	11.20	24.60
Steel	5.90	7.90	46.00
Tin	3.30	7.30	24.20
Titanium	6.10	4.48	27.30

Table 4.1: Common engineering materials and their associated longitudinal wave velocities and impedances

As a sound wave travels from one material to another, there will be a change in acoustic impedance. The ratio of reflected sound intensity to incident sound intensity is known as the reflection coefficient. The reflection coefficient (R) is defined by Equation 4.4:

$$R = \frac{z_1 - z_2}{z_1 + z_2} \tag{4.4}$$

where z_1 and z_2 are the acoustic impedances of materials 1 and 2 respectively. The reflection coefficient for air is 0.0004286. Using Equation 4.4 and Table 4.1, it can be seen that for a a sound wave travelling through steel and encountering a steel-air interface, almost all the sound will be reflected. It is the discrepancy between the impedances of these two mediums that allows for the detection of cracks and non destructive testing (NDT).

4.1.6 Acoustic Attenuation

As a wave is emitted from a source through a material, it begins to break down due to the imperfect transmission of energy. The organised vibrating particles that make up this wave turn into rand vibrations which manifest as heat. Therefore, the

magnitude of the wave reduces exponentially with the distance from the source (see Figure 4.4).

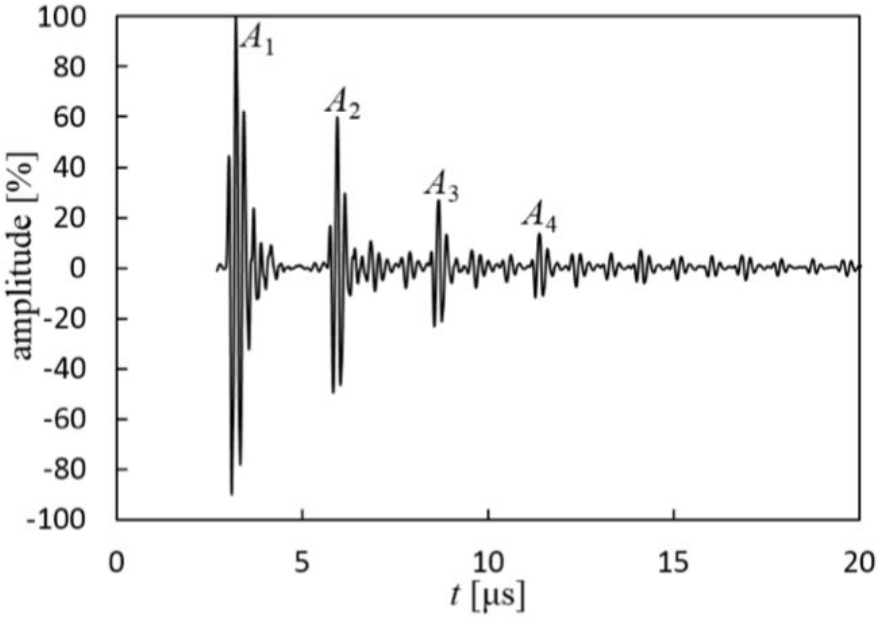

Figure 4.4: Wave attenuation

The rate at which a wave attenuates depends on the material. Scatter occurs due to the boundaries within a material and is caused by various inhomogeneities such as inclusions, pores and grains. The varying impedances that these inhomogeneities present transmit and reflect waves in various directions, thereby decreasing the wave energy in the direction of original propagation. The size of these grains relative to the wavelength determine the extent to which these reflections occur. Therefore the higher the frequency of the wave, the greater the attenuation [73].

4.2 Ultrasound Uses in Industry

The two primary methods of evaluating ultrasound are through A-scans and B-Scans. An A-scan is a one dimensional amplitude measurement and records a reflected wave's amplitude, hence A-scan. A B-scan is a two dimensional cross sectional measurement and records the 'brightness' of many reflected waves, hence B-scan. This work focuses on A-scans and the information we can obtain from them. By analysing the sent and received signal on an A-Scan it is possible to determine the pressure and interfacial stiffness at an interface as well as the distance from the reflector to the interface. Ultrasonic waves attenuate faster than low frequency waves,

meaning the use of ultrasonic sensors for measuring distances longer than 1 metre is not ideal [74].

The resultant applications from these measurements often lean towards imaging of opaque materials through relatively short distances. This includes pregnancy scans, crack detection and NDT. These all use time-of-flight measurements (see Section 4.3.5). More recently ultrasonics are being used to look at the interfacial conditions to assess the condition of components in real-time. These require wave amplitude measurements (see Section 4.3.4).

4.3 Ultrasonic Sensor Design

Ultrasonic sensors rely on the piezoelectric effect to work. Piezoelectric materials such as quartz or Lead zirconate titanate (PZT) compress and expand cyclically when exposed to an AC electric field (see Section 4.3.1). When such a material is attached to a rigid body, it forms a pressure differential that manifests as a sound wave. Each ultrasonic sensor has its own resonant frequency (the frequency at which the ultrasonic sensor vibrates most readily) which is generally between 1 and 10MHz, however a wide range of resonant frequencies are possible. The material composition and geometry of the ultrasonic sensor determine the resonant frequency. Generally the thicker the sensor the lower its resonant frequency [75]. Commercial ultrasonic sensors consist of a piezo-ceramic material sandwiched between two electrodes; these are often housed in a metal casing (see Figure 4.5). This type of sensor can be attached and removed from the component of interest. A couplant is used to fill the air gaps between the wear plate and the piezo sensor.

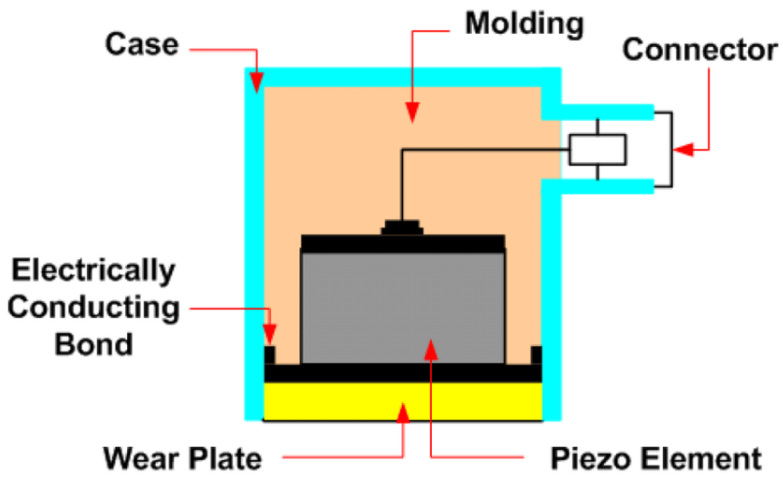

Figure 4.5: Commercial sensor schematic [76]

Sensors can also be bonded to components: this is known 'permanently embedded ultrasonics'. One electrode is bonded to the electrically conductive material you want to pulse through. The circuit is then completed by connecting a positive wire to the exposed electrode and the negative wire to the conductive workpiece. Wraparound electrodes can also be used if the material you want to pulse through is non conductive. With wraparound electrodes, both the anode and cathode are on the upper surface of the piezo-ceramic separated by an etched non conductive strip.

4.3.1 Piezoelectric Effect

The piezoelectric effect is the generation of electrical charges from certain materials when subjected to pressure. This effect can also happen in reverse whereby electrical fields cause these materials to deform. When this field is driven at the resonant frequency of the piezo element, it will deform cyclicly producing pressure waves at specific frequencies. Since pressure waves are sound waves, ultrasonic sound generation can be achieved with these piezo elements, which when pulsed through materials, can tell us certain properties about a mechanical system. Figure 4.6 shows this effect whereby applied electrical energy expands the crystalline unit cell.

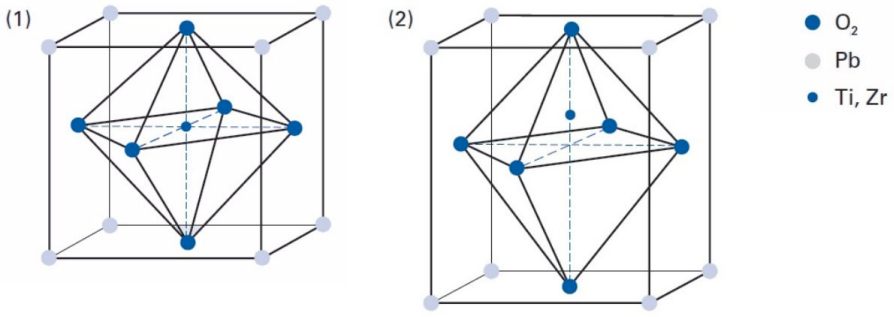

Figure 4.6: Piezoelectric effect on crystalline unit cell [77]

Both monocrystalline materials and polycrystalline ferroelectric ceramics exhibit piezoelectric behaviour. For this to be useful, it requires the material to be polarised (separation of the positive and negative charge concentrations). This occurs instantaneously within ceramics and causes instantaneous extension in the axis of polarisation whereby spontaneous strain occurs. Monocrystalline materials such as quartz exhibit relatively little piezoelectric behaviour. Polycrystalline ferroelectric ceramics exhibit far more piezo electric behaviour; these include barium titanate (BaTiO3) and lead zirconate titanate (PZT). PZT piezo ceramic materials are the most popular piezo materials and are available in many varieties [77].

4.3.2 Sound Field

The sound field produced from a transducer can bit split into two regions: the near field and the far field. Both of these regions have their own characteristics as seen in Figure 4.7. The near field includes a series of echo peaks before entering the far field whereby these signals attenuate gradually as outlined in Section 4.1.6. This makes studying the effects in the far field much more predictable.

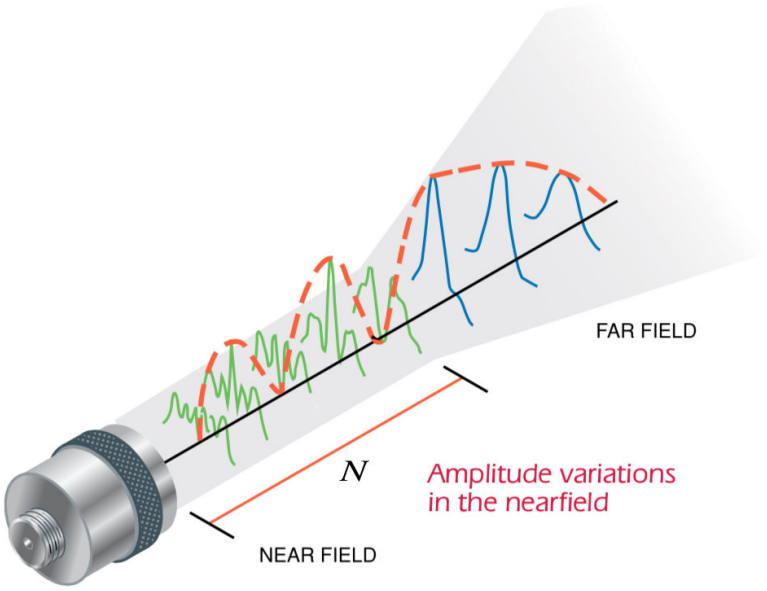

Figure 4.7: Near and far field [73]

Equation 4.5 outlines how to calculate N, (the distance at which the near field ends and the far field starts).

$$N = \frac{D^2 f}{4c} = \frac{D^2}{4\lambda} \tag{4.5}$$

where D is the diameter of the transducer. The smaller the beam diameter (BD) of the transducer the greater the intensity of ultrasonic sound wave produced. This beam diameter depends on the diameter of the transducer, the wavelength λ and the focal length (F) as seen in Equation 4.6:

$$BD(-6dB) = 1.02\frac{F\lambda}{D} \tag{4.6}$$

Figure 4.8 shows how the near field relates to the beam spread.

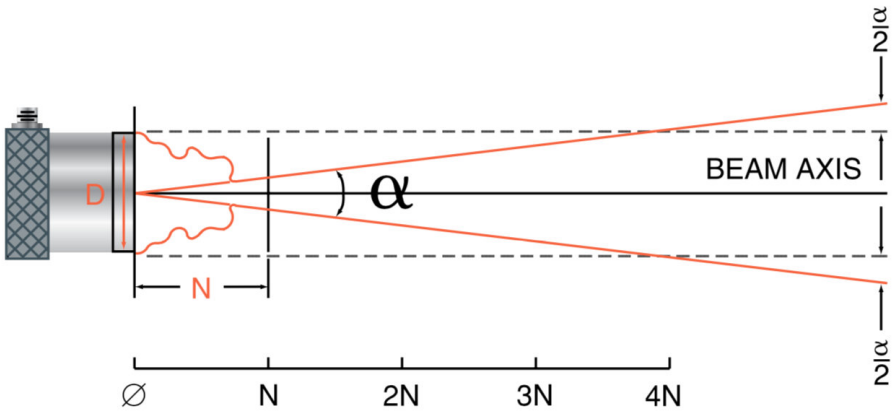

Figure 4.8: Beam spread [73]

The beam spread angle (α) outlined in Figure 4.8 can be calculated (see Equation 4.7). Using Equation 4.2, beam spread can be reduced by increasing frequency or decreasing the transducer diameter. Due to the high frequencies present in ultrasonic reflectometry, beam spread can often be considered negligible whereby the reflecting area is the same as that of the transducer area.

$$Sin(\alpha/2) = 0.514\frac{\lambda}{D} \tag{4.7}$$

4.3.3 Huygens Principle

For a theoretical point source of acoustic energy, energy is emitted equally in all directions with a spherical wavefront [78]. This principle can be used to model the wavefronts of ultrasonic transducers. Figure 4.9 shows that when discretised into multiple point sources, the wavefront emitted from an acoustic transducer approximates to a flat wavefront. If this flat wavefront interacts with a parallel surface, it will be reflected back towards the transducer.

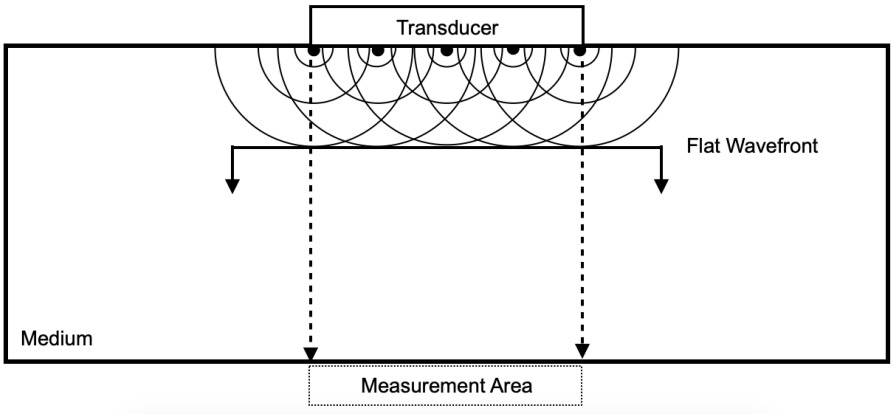

Figure 4.9: Formation of a flat wavefront from a discretised transducer

Parts of the wave either side of the emitting body are not reflected back towards the sensor, therefore the measurement area is approximately the same size as the sensor.

4.3.4 Wave Amplitude Measurement Technique

The wave amplitude measurement technique uses the ratio of the amplitudes of the loaded and unloaded wave amplitude (H and H_0 respectively) to assess the reflectivity or reflection coefficient R of an interface (see Equation 4.8).

$$R = \frac{H}{H_0} \tag{4.8}$$

The less air gaps there are between the surfaces, the more of the wave will be transmitted and therefore the lower R will be. This can occur through the surface's natural conformity or else through high loads that press the two surfaces together. As such this measurement can be used to assess surface roughness and also interfacial stiffness (see Section 4.4).

4.3.5 Time-of-Flight Measurement Technique

Time-of-flight (ToF) is simply the time it takes for a pulsed wave to travel to the point of reflection and back again. It is therefore calculated using the speed equation (see Equation 4.9).

$$d = \frac{tc}{2} \tag{4.9}$$

where d is the distance, t is time and c is the speed of sound within that specific medium. In this way the subsurface location of various changes in media can be calculated. In the rail industry this is predominantly used for the detection of cracks.

4.4 Measuring Interfacial stiffness

All materials have micro asperities no matter how apparently smooth, as outlined in Section 3.2. This means that when two materials are in contact with one another, the apparent contact area is far larger than the real contact area. Many interacting asperities make up the true contact area which deform plastically with increased load. The more these interfaces are pressed into one another, the more the asperities deform and conform to one another. If we assume that this deformation is elastic, two contacting materials can be modelled as two masses separated by a series of springs; this is known as the spring model (see Figure 4.10) [79].

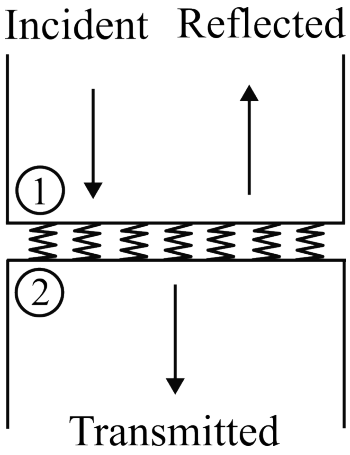

Figure 4.10: The spring model

Each spring has stiffness (K) and is defined by Equation 4.10 where $d\sigma$ is the change in stress between the two bodies and $d\delta$ is the change in asperity displacement [80].

$$K = \frac{Change\ in\ stress\ on\ the\ adjacent\ surfaces}{Change\ in\ asperity\ displacement} = \frac{d\sigma}{d\delta} \tag{4.10}$$

This spring stiffness is often referred to as the interfacial stiffness. $d\sigma$ and $d\delta$ can of course be in the normal or tangential directions. Figure 4.11 shows this schematically.

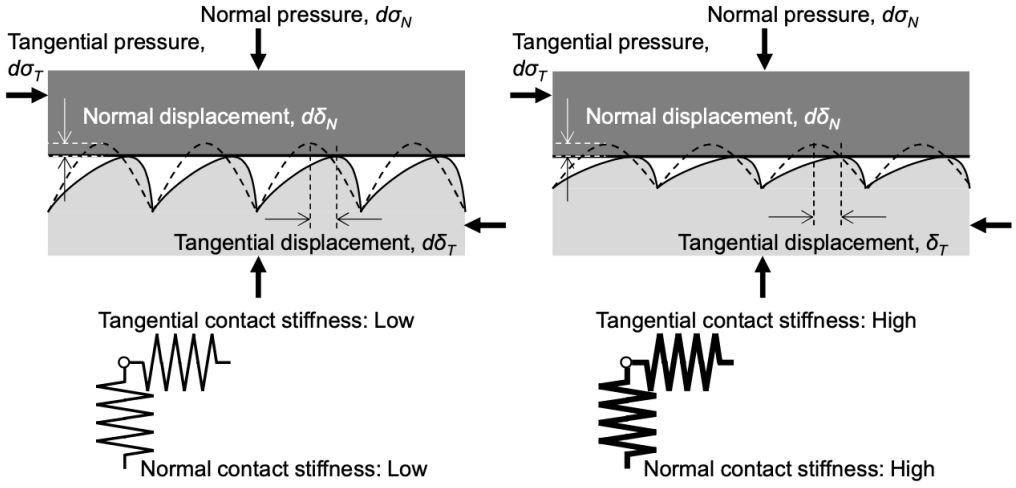

Figure 4.11: Schematic of an imperfect interface with ideal asperities undergoing normal and tangential loads [81]

This means that interfacial stiffness can be further subcategorised into two types: normal interfacial stiffness (K_N) and tangential interfacial stiffness (K_T). These are defined by Equations 4.11 and 4.12 and can be measured using longitudinal or shear wave ultrasonic transducers respectively. Because of this, K_N is often referred to as the longitudinal interfacial stiffness K_L. Similarly, K_T is often referred to as the as the shear interfacial stiffness (K_S). If the coordinate systems are more complex (i.e three dimensional cartesian or cylindrical coordinates), then tangential interfacial stiffness can be defined in two directions.

$$K_N = \frac{d\sigma_N}{d\delta_N} \tag{4.11}$$

$$K_T = \frac{d\sigma_T}{d\delta_T} \tag{4.12}$$

When an acoustic wave hits an interface, part of the wave is transmitted and part is reflected. The reflection coefficient at the interface R_{12} is defined by Equation 4.13, where ω is the angular frequency of the wave ($\omega = 2\pi f$). z_1 and z_2 are the acoustic impedances of the two materials as mentioned in Section 4.1.5.

$$R_{12} = \frac{z_1 - z_2 + i\omega(z_1 z_2/K)}{z_1 + z_2 + i\omega(z_1 z_2/K)} \tag{4.13}$$

If materials 1 and 2 are known to be the same or similar and Equation 4.13 is solved explicitly, this simplifies to Equation 4.14:

$$|R| = \frac{1}{\sqrt{1 + (2K/\omega z)^2}} \tag{4.14}$$

This can then be rearranged to obtain the interfacial stiffness as seen in Equation 4.15. The reflection coefficient (R) is obtained experimentally through the ratio of the wave intensities which is covered in Section 4.3.4.

$$K = \frac{\omega z}{2}\sqrt{\frac{1}{R^2} - 1} \tag{4.15}$$

Whilst interfacial stiffness is an interesting thing to know, it is only really useful due to it being remotely measurable. For it to be practical it must be related to either the interfacial stress in order to assess if materials are in danger of failing, or else related to some other factor such as the surface roughness or the traction coefficient. It is these factors that directly affect how a railway is run, what maintenance is required and ultimately whether customers can rely on rail as a mode of transport. As such, this work focuses not on one-off interfacial stiffness measurements, but on how interfacial stiffness changes with varying surface roughness and traction.

4.4.1 Interfacial Stiffness and the Breakdown of Frequency Independence

Interfacial stiffness is often quoted as being independent of frequency. Figure 4.12 shows the relationship between frequency and interfacial stiffness obtained in the work of Drinkwater et al. [10].

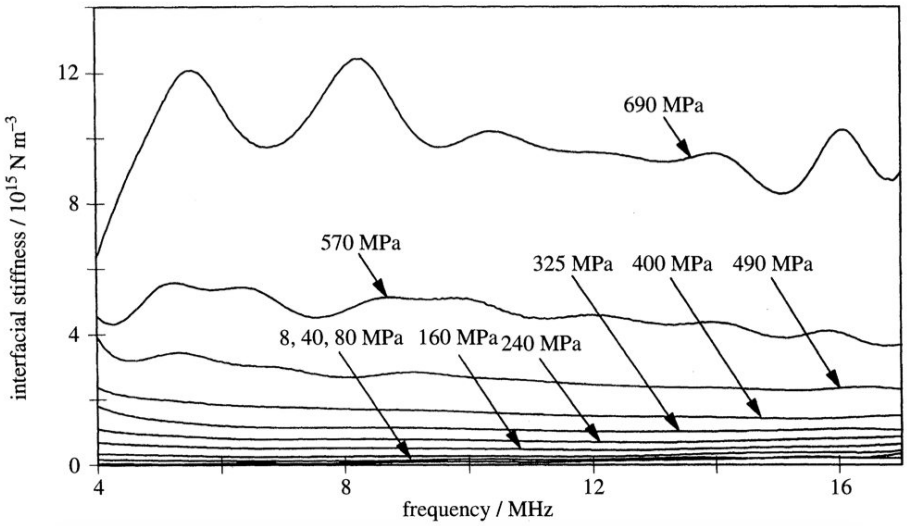

Figure 4.12: Variation of interfacial stiffness with frequency for various contact pressures (aluminium-aluminium interface) [10]

Interfacial stiffness is independent of frequency for lower pressures (see Figure 4.12). At higher contact pressures however, the calculation of K becomes unstable. Equation 4.15 shows how to calculate K. As $R \to 0$, $K \to \infty$, therefore small errors in R lead to large errors in calculated K [10]. The same is true for very low contact pressures, where $R \to 1$, $K \to 0$. Limits to the reflection coefficients used in Equation 4.15 should be enforced to mitigate these errors (R_{MAX} and R_{MIN}).

By increasing the measurement frequency, higher interfacial stiffnesses are measurable. The interface represented in Figure 4.12 is an aluminium-aluminium interface. As the acoustic impedance z of steel is roughly 3x higher than that of aluminium, interfacial stiffness remains stable across frequencies up to $1.5GPa$. This is the upper limit of pressures experienced at the wheel-rail interface.

4.5 Summary

Acoustic theory and how ultrasonics might be used to make in-situ measurements were reviewed in this chapter. This included the basic properties of a sound wave and how one might use ultrasonic transducers to measure interfacial stiffness. It is known that roughness and interfacial stiffness are linked, so by pairing ultrasonic measurements with HPT testing outputs and roughness data, a relationship between interfacial stiffness, friction and roughness may be found.

Figure 4.13 shows this process schematically. As the surfaces slide against one another, the roughness evolves. As interfacial stiffness varies with this roughness evolution, it follows that the roughness could be inferred from ultrasonic measurements. There is currently no way to determine these changes in real-time, however ultrasound may be able to provide answers.

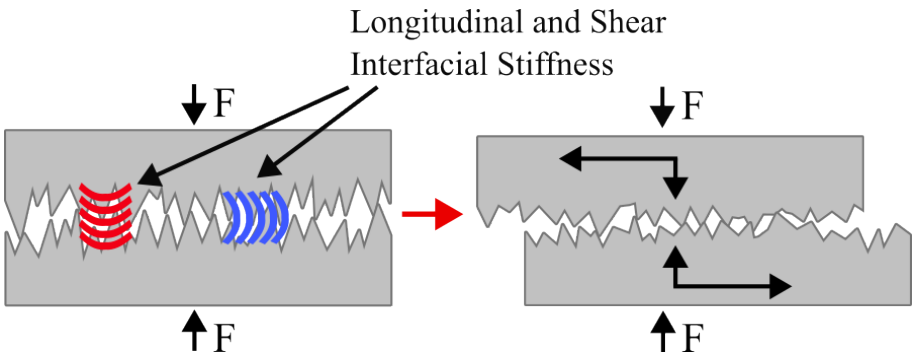

Figure 4.13: Schematic showing rough surface contact and proposed ultrasonic measurements

5 Testing Methodology

Two test approaches were used to study roughness at the wheel-rail interface: the small-scale High Pressure Torsion (HPT) test and the full-scale wheel-rail rig (FSR) test. The methodologies of these two tests are discussed in the following chapter. The way in which ultrasonic data was captured during the HPT tests is also discussed. In addition, how the roughness, traction and ultrasonic data from each of these two tests was processed is explained.

5.1 HPT Testing Methodology

Of the small-scale testing approaches considered in Section 3.5, the High Pressure Torsion (HPT) Rig was found to be the best suited for the required outcomes. The HPT rig is a relatively new tribological test and has advantages over twin-disc and pin-on-disc testing, as 3BLs can be applied and initial roughnesses implemented onto the specimens with relative ease. Additionally only one cycle is required to produce shear stress data. This data is useful on its own, however it can also be used to parameterise analytical prediction tools such as the extended creep-force (ECF) model. The ECF model and other creep-force models can produce creep-force curves from this HPT data (see Chapter 7). These can then be validated against field or full-scale rig data to develop full-scale predictive capability [82].

5.1.1 HPT Rig Layout

The HPT test approach is not new, but has historically been used to generate specific deformed rail steel microstructures; however it is now being used to imitate tribological conditions at the wheel-rail interface [57]. This involves the use of two flat specimens: an upper wheel specimen and a lower rail specimen (1 and 2 respectively in Figure 5.1), that are pressed together with a certain force and then twisted through a predefined rotation angle. These specimens are attached to the rig with specimen holders (3). Specimens are kept separate initially and then brought together during testing. Normal pressure is applied with an axial hydraulic actuator (4) and the rotation is applied using a rotational hydraulic actuator (5). These actuators are pressurised using a hydraulic ring main (10) to around 250 bar. Servo valves control the flow of hydraulic fluid to these actuators which are controlled with

an electrical control unit (8). A Linear Variable Differential Transformer (LVDT) and load cell (7) send axial displacement and load information to the control unit. Similarly a Rotary Variable Differential Transformer (RVDT) and load cell (6) send rotational displacement and load information to the control unit. The control unit is equipped with two channels (axial and rotational), thereby permitting the control of test specimens in both these directions. A hydraulic cross-head (9) allows specimens up to 2 metres in length to be tested.

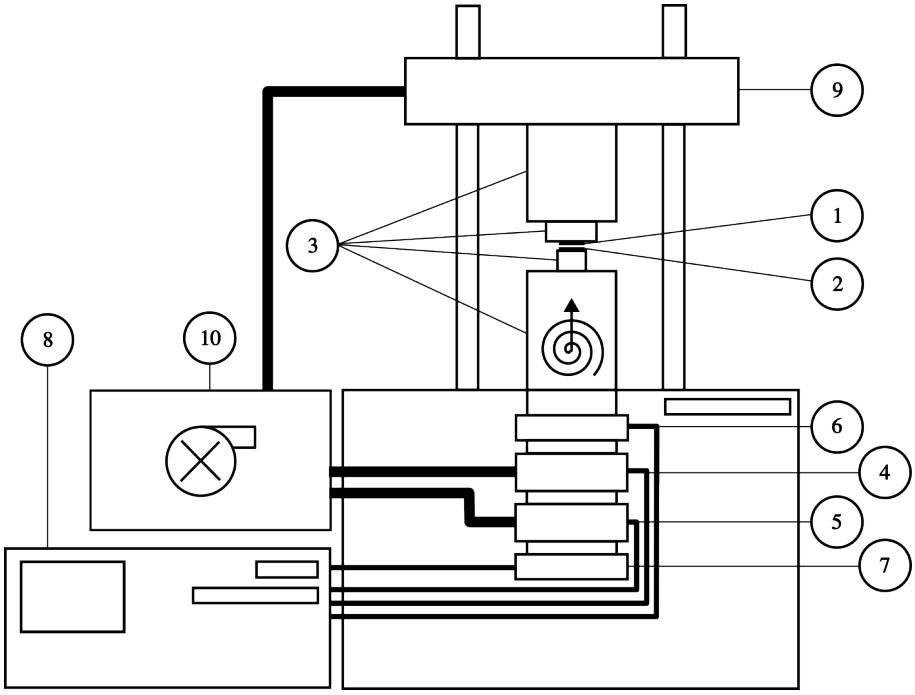

Figure 5.1: HPT rig schematic

The HPT rig can be seen in Figure 5.2 as well as the specimen assembly. Specimens can be separated and removed between test cycles either to apply 3BLs or take surface replicas. The operational limits of the HPT machine are shown in Table 5.1.

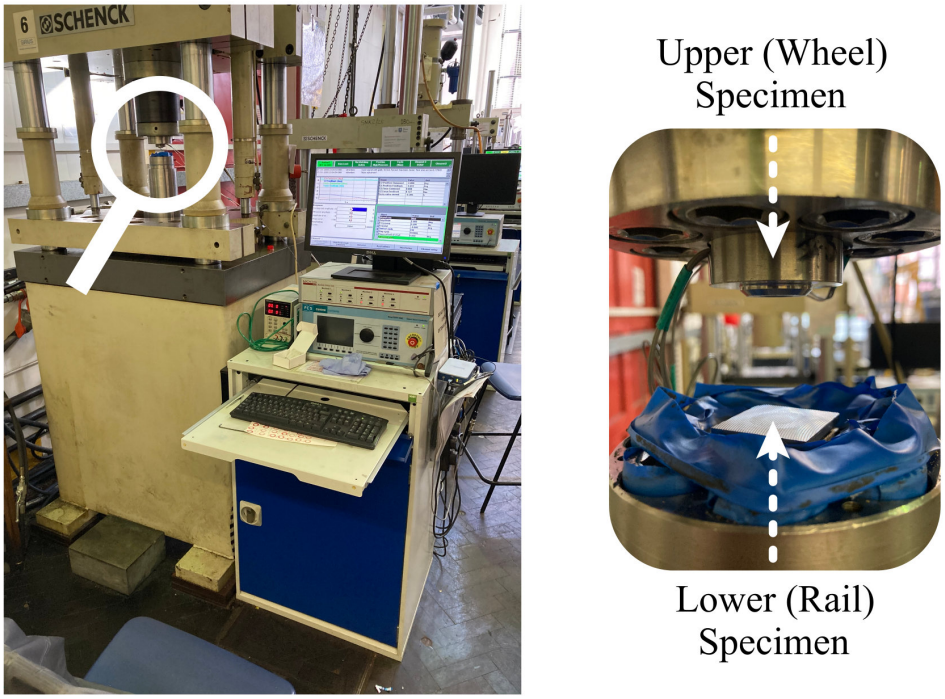

Figure 5.2: HPT rig at the University of Sheffield

Operation	**Operation Limit**
Axial Load (Tension and Compression)	+/- 400 kN
Axial Displacement Range	+/- 25 mm
Torque	+/- 1000 Nm
Torsional Displacement Range	+/- 40 degrees

Table 5.1: HPT Operational Limits

5.1.2 HPT Specimen Geometry

The upper and lower specimen geometries can be seen in Figures 5.3 and 5.4 respectively. The HPT requires two specimens: the upper (wheel) specimen which is fixed and presents an annular surface and the lower (rail) specimen which is a flat rotated tile. The specimen design is one used frequently on the HPT rig and is designed as such that it is able to be attached onto the rig with a single bolt. The chamfers on the interacting annulus stop large body deformation of the specimen

due to the applied torsion. The only adaptation to the upper specimens was to deepen the milled channel from 6mm to 9mm so as to make space for ultrasonic transducers on the top surface.

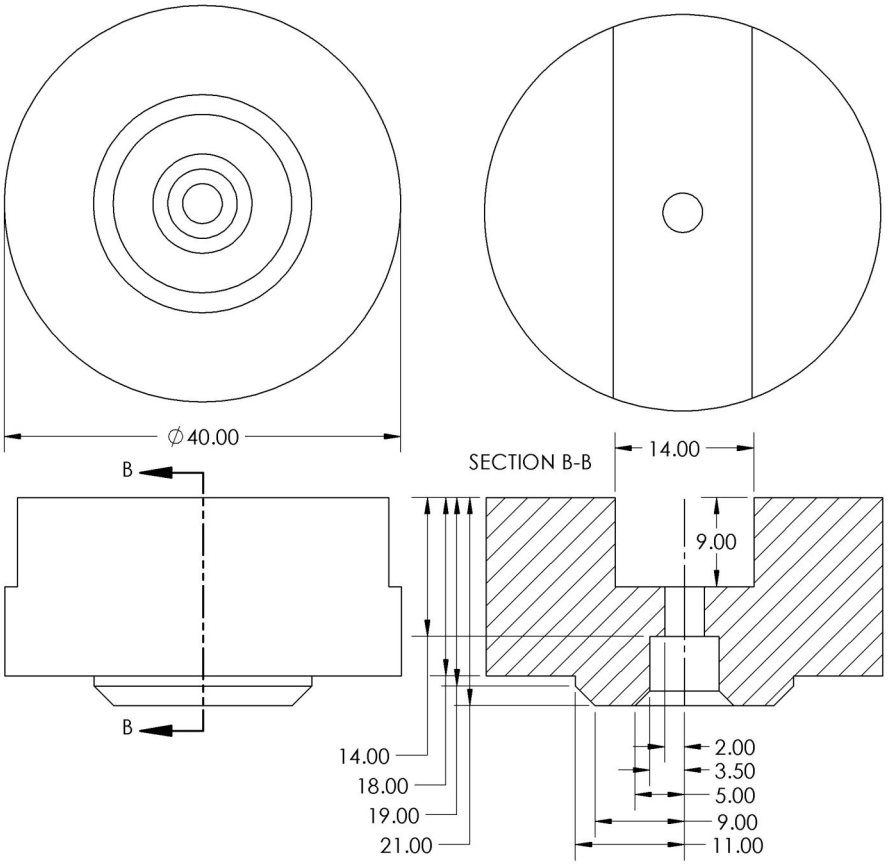

Figure 5.3: Upper HPT specimen geometry

No adaptations were made to the geometry of the lower specimens. Both upper and lower specimens were reground after they were tested which removes material from their interacting faces. There is a milled wear indicator on two sides of the lower specimen. After multiple tests, the top surface will be worn back to this indicator, thereby showing users when to replace specimens.

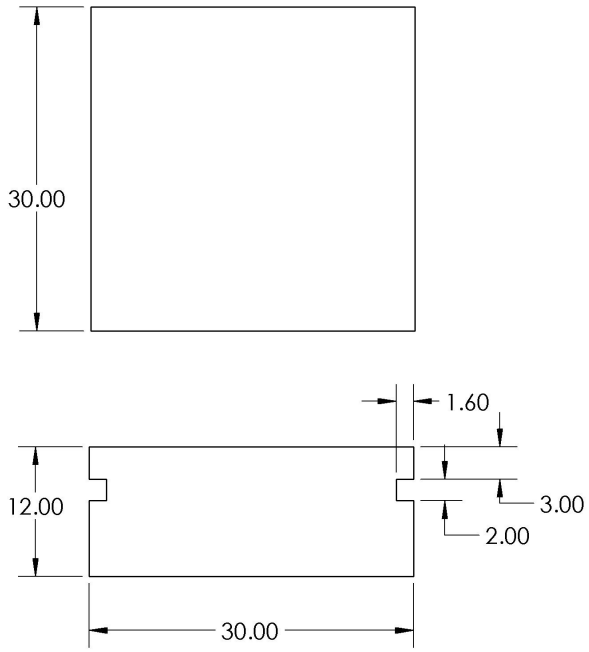

Figure 5.4: Lower HPT specimen geometry

The upper specimen was bolted to the HPT rig while the lower specimen sits in a square pocket. Figure 5.5 shows the upper and lower specimens interacting. The upper specimen was pressed into the lower specimen whilst the lower specimen was rotated. The interface is shown in red.

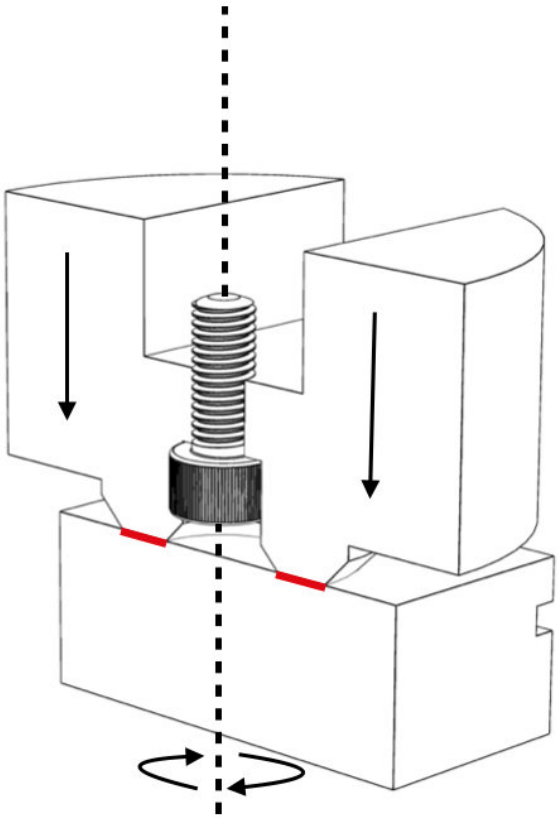

Figure 5.5: Sectioned view of the upper and lower specimens interacting when attached to the HPT rig (interface is shown in red)

5.1.3 HPT Specimen Materials

Rail R260 steel was used for the bottom specimen and wheel ER8 steel was used for the upper specimens to best mimic the conditions at the wheel-rail interface. Figure 5.6 shows the rail R260 sample from which the specimens were made. This sample was determined to be R260 using a Rockwell hardness test. The wheel specimens were made from ER8 block samples machined from a decommissioned wheel.

Figure 5.6: R260 rail sample

The samples were then machined from their respective samples into the geometries described in Figures 5.3 and 5.4. These can be seen in Figure 5.7.

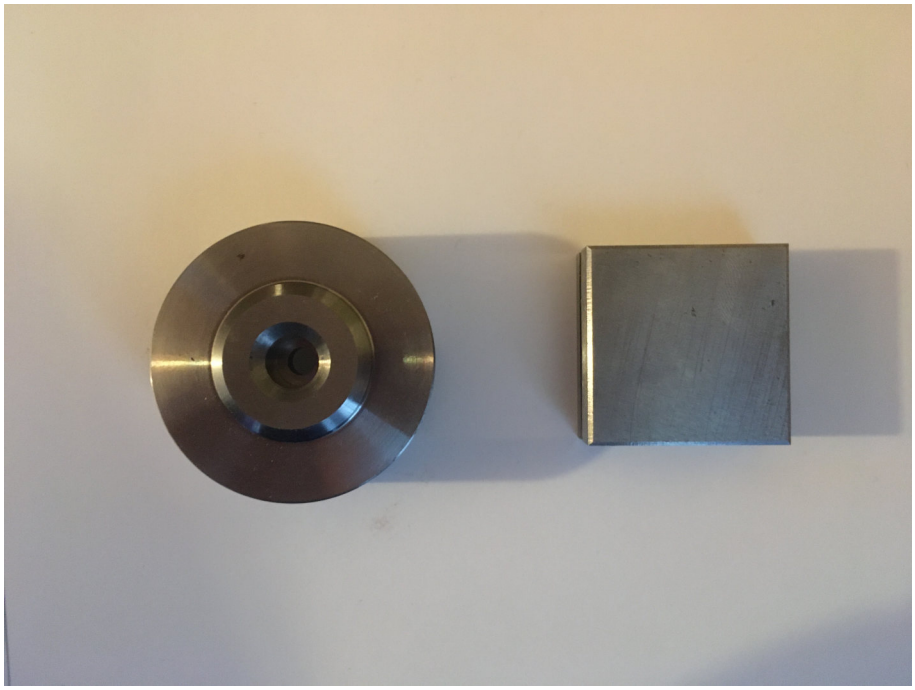

Figure 5.7: ER8 and R260 machined HPT samples (left: Upper (ER8), right: Lower (R260))

5.1.4 HPT Specimen Relevant Roughness

In order to apply roughness to specimens, one must first know how rough the specimens need to be. As FSR testing campaign was planned (see Section 5.3), and as applying a roughness to a full-scale wheel would be difficult and costly it was decided that roughness should be applied to the lower rail specimens only. Rail grinding is a process performed on the railhead to correct the rail profile when a rail is worn or to reduce crack growth. To conduct this process in the short time available, material is removed quickly which results in a high resultant roughness. During the rail grinding process, the hardened plastically deformed layer on the railhead is removed to make way for a softer and rougher machined surface. The railhead is then run-in by traffic whereby the surface asperities created by the grinding process are plastically deformed resulting in a surface that has been hardened and is lower in roughness. Field measurements show roughness starts around 6-10μm post grinding and reduces to around 1-2μm when run-in (see Figure 3.15). A cyclical HPT test approach was used to simulate the passing of wheels whilst allowing the intermittent measurement of roughness. Ground and run-in rail was scanned using an Alicona microscope to create 3D maps of the two surfaces to ensure these were consistent with the field data; these are shown in Figure 5.8.

(a) Ground rail

(b) Run-in rail

Figure 5.8: Rail scans of ground and run-in rail

By using the parameters outlined in Section 3.2.1, a roughness can be assigned to these two rail states (see Table 5.2). These measurements are in agreement with those of Lundmark et al. as shown in Section 3.2.4 [9].

Rail State	Sa (μm)	Sq (μm)	Ssk	Sku
Ground	6.092	9.132	-1.007	9.726
Run-in	1.578	2.199	4.199	133.492

Table 5.2: Measured roughness for ground and run-in rail

5.1.5 Applying Roughness to HPT Specimens

The real ground roughness values outlined in Table 5.2 were measured from sections of real track, and their roughness profiles were made using a grinding train. Since this machining method could not be applied to the small-scale HPT specimens, alternative machining processes were tested that achieved similar roughness values. Figure 5.9 shows two such machining processes that were performed to mimic the rail states in Table 5.2. Shot blasting produces a very even surface finish, whereas flycutting produces clearly visible ridges that intersect one another in a crosshatch.

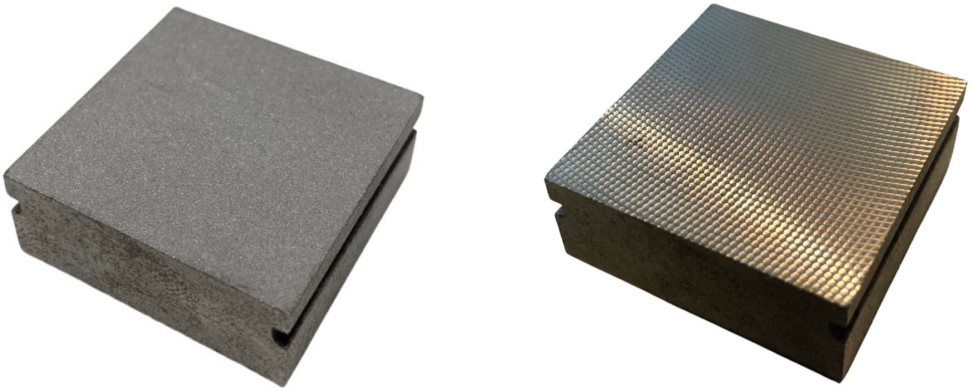

(a) Shot blasted *(b) Flycut*

Figure 5.9: Visual difference between two machining processes performed on R260 steel specimens

Scans of these surfaces and two more machining processes can be seen in Figure 5.10.

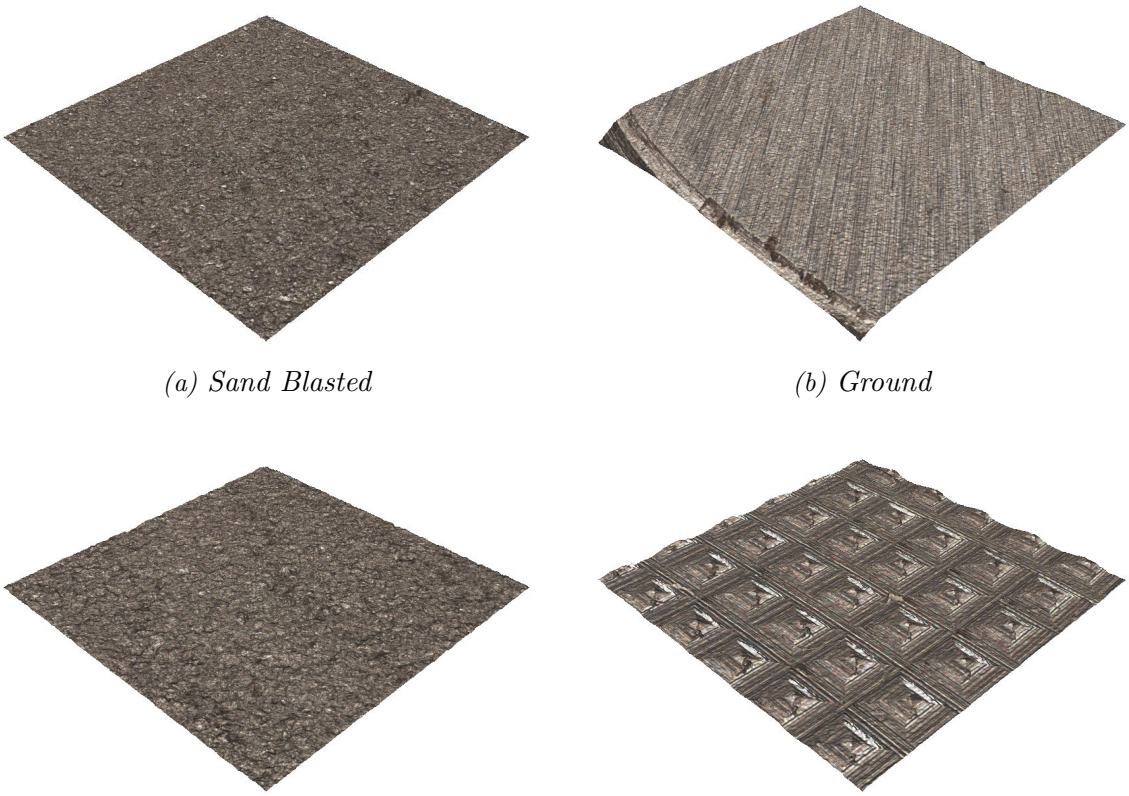

(a) Sand Blasted

(b) Ground

(c) Shot Blasted

(d) Flycut (0.75mm spacing)

Figure 5.10: Alicona scans of various machining processes (scan size: 3X3mm)

The scans shown in Figure 5.10 are just $3X3mm$, ($1/20th$ of the size of the full specimen), however they represent the full width of the contact patch created on the HPT.

Machining Process	**Sa** (μm)	**Sq** (μm)	**Ssk**	**Sku**
Sand Blasting	1.603	2.208	-0.551	8.357
Grinding	1.850	2.368	0.045	3.700
Shot Blasting	3.292	4.234	-0.329	3.677
Fly Cutting	7.579	9.573	1.012	3.628

Table 5.3: Recreating ground and run-in rail roughness using various machining processes

As can be seen from Table 5.3, only flycutting produced roughnesses anywhere near those found post grinding, so this machining process was used to recreate this

roughness.

5.1.6 HPT Test Data Process Route

The path through which data is gathered from the HPT rig is shown in Figure 5.11. A Film Measurement System (FMS) was used to pulse the ultrasonic transducers. This computer is capable of achieving extremely high pulse rates. These same transducers receive the reflected signal and transfer it back to the FMS; this measurement technique is known as pulse-echo. An electronic control unit (ECU) operates the HPT rig by giving axial and rotational commands that are measured using the LVDT, RVDT and associated load cells. This can be done manually, but is more commonly achieved through the use of a script. This analogue data (axial position, axial load, rotational position and torsional load) is then outputted to the FMS through a data acquisitions device (DAQ). This digitises the analogue signal so that it can be understood by the FMS and synced with the ultrasonic data. Ultrasonic data is routed directly from the ultrasonic transducers into the FMS using subminiature version B (SMB) connectors and coaxial cable whilst the analogue HPT data routes through the ECU, then the DAQ and into the FMS.

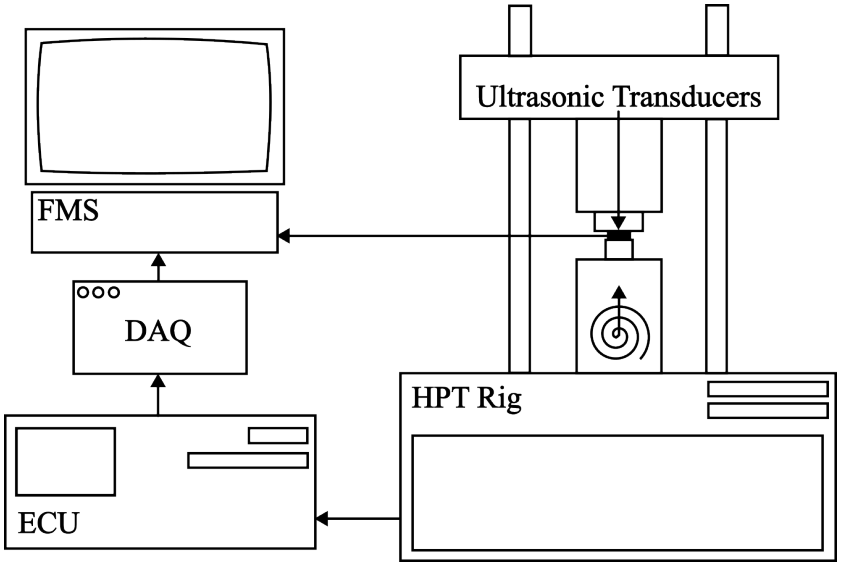

Figure 5.11: HPT testing process route for data acquisition

The gain, delay, range etc of each signal can all be changed on the FMS, meaning signals can be compared at similar amplitudes. High sample rates require large

memory banks, so reducing the range of a recorded signal so that you are only capturing the reflected signal is a good way of minimising memory usage whilst retaining all the useful data (see Section 5.2.2).

5.1.7 HPT Contact Area and Alignment Check

The tension-compression-torsion load cell on the HPT is able to measure the force being applied through the HPT. In order to convert this force into pressure, the contact area between the two specimens must be calculated. This was achieved with pressure sensitive film that creates a measurable annulus, as seen in Figure 5.12. This stage was also conducted to check the alignment of the two specimens to ensure an even load distribution over the entire annulus. Large tonal variations in the pressure sensitive film indicated misalignment. The alignment check was performed at 150MPa at the $-40°$, $0°$ and $40°$ locations.

(a) Specimen attachment

(b) Ready for alignment check

(c) Alignment check

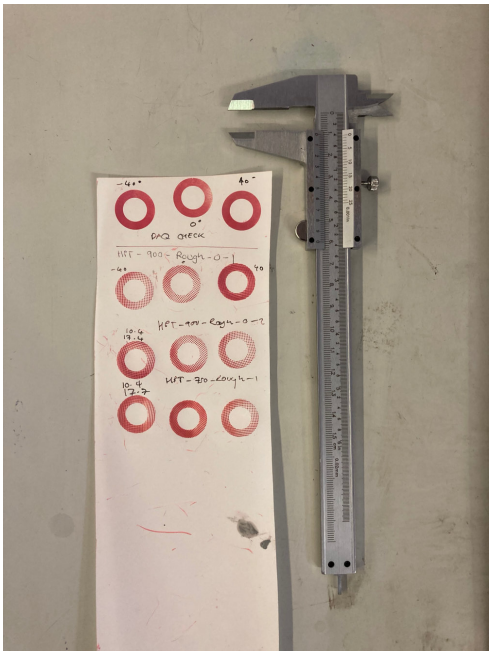

(d) Contact area measurement

Figure 5.12: HPT rig alignment check and contact area measurement

Whilst creep stresses are assumed to be uniform across the annular contact patch, at higher radii these same creep stresses have a greater contribution to the torque. This means the midpoint between the inner and outer radius cannot be used to calculate the creep stress from the measured torque. Therefore in addition to the

area calculation, the effective radius of friction (ERF) must be calculated to define a point through which torque acts. Figure 5.13 and Equation 5.1 show the effective radius of friction and how it is calculated, where r is the inner radius and R is the outer radius.

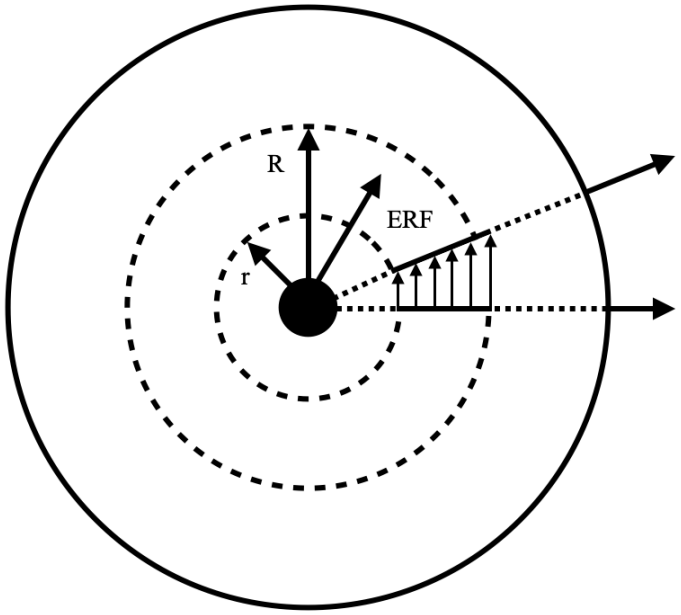

Figure 5.13: Effective radius of friction

$$ERF = \frac{2}{3}\left(\frac{R^3 - r^3}{R^2 - r^2}\right) \tag{5.1}$$

Inner and outer radii are measured using callipers, as seen in Figure 5.12d. The ERF must be measured for each test as specimen geometry varies due to manufacturing processes. Additionally specimens were reused which required them to be reground to achieve the desired initial roughness. When this occurred, the annular area increased due to the chamfered nature of the geometry and so the ERF was recalculated and the HPT test parameters were updated.

5.1.8 HPT Script Design

As with most tribological tests, the testing process was automated using a script. Test parameters were inputted into this script which then ran using these parameters. A PID controller used these parameters to command the servo valves to move

the HPT rig in both axial and rotational directions at the desired speed and force. A list of test parameters is shown below:

- Number of cycles
- Pressure
- Contact Area
- ERF
- Sweep Length
- Sweep Rate
- Step Rotation

Temperature and humidity were measured, but were not able to be controlled. Some parameters were defined by the specimen, such as the contact area and ERF and some were inputted by the operator. These included the contact pressure, number of cycles, sweep rate and sweep length. In addition to these, there were certain aspects of the testing process that could be specified in order to tailor the tests to the operator's needs. Figure 5.14 shows the test sweeps of test cycles one and two. By overlapping tests many repeats could be performed within the HPT rotational limits outlined in Table 5.1. However once the majority of the contact reached a limiting creep stress, this method often caused the specimens to slip; releasing some of the elastic energy that had been built up. This release of elastic energy decreases the creep stress required to stop the slippage and the process repeats itself as a feedback loop [82]. In order to perform 20 cycles and avoid this behaviour, ten separated cycles were performed, then the specimens were rotated back to the start and the process was repeated. This process mitigated undesirable slipping events whilst allowing 20 cycles to be performed.

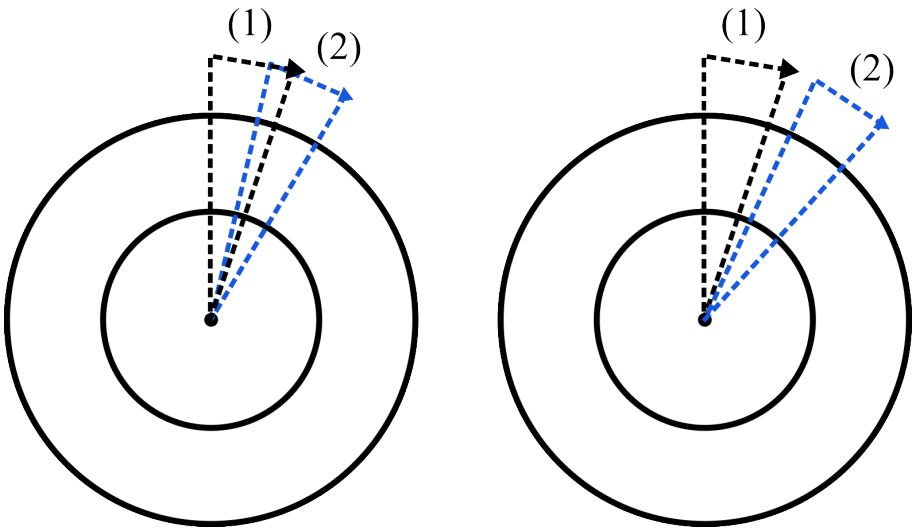

Figure 5.14: Schematic showing overlapped (left) and separated (right) test sweeps

The sweep distance acts at the ERF which for the HPT specimens was around 7.3mm. The sweep length must be large enough to ensure all the frictional behaviour is obtained for use in model parameterisation. Evans et al. concluded that a sweep length of 0.4mm ensured the whole interface had entered the sliding regime [82]. This translates to a sweep angle of around 3 degrees. To ensure that the cycles do not overlap, a step rotation of around 2 degrees is added between each cycle. Table 5.4 shows the rotation start and end points for the first ten cycles. The second ten cycles use the same start and end points as the rotation range of $-40°$ to $40°$ is not sufficient to host 20 cycles without potentially exceeding the rigs rotational limits. Note the two degree discrepancy between rotation end points and start points. This is the step rotation shown in Figure 5.14 to mitigate undesirable slip. Between cycles the HPT specimens are separated to allow for specimen cleaning, roughness measurements and to apply 3BLs.

Cycle	Rotation Start (°)	Rotation End (°)
1	-30	-27
2	-25	-22
3	-20	-17
4	-15	-12
5	-10	-7
6	-5	-2
7	0	3
8	5	8
9	10	13
10	15	18

Table 5.4: HPT cycle rotation index

The final parameter is the sweep rate. Slower sweep rates ($\approx$ 0.02 deg/s) result in very repeatable results, but extend the test time. Higher sweep rates ($\approx$ 1 deg/s) result in fast tests, but introduce frictional heat that manifests as a rising creep stress as sliding progresses [82]. A middle ground was needed as long test durations were undesirable due to the amount of ultrasonic data that was being obtained. A sweep rate of 0.1 deg/s was used for all HPT tests. The full list of HPT test parameters can be seen in Table 5.5.

Parameter	Value	Units
Number of Cycles	20	
Pressures	600, 750, 900	MPa
Contact Area	Measured	mm^2
ERF	Measured	mm
Sweep Length	≈ 3	deg
Sweep Rate	0.1	deg/s
Step Rotation	≈ 2	deg
Temperature	Measured	$^\circ C$
Humidity	Measured	%

Table 5.5: HPT test parameters

5.1.9 HPT Roughness Measurement Method

Overall, the parameters that can be used to define surface topography number over 50 which makes studying roughness challenging. A single combined roughness parameter σ outlined in Section 3.2.1 was used to study the evolution of interfacial surface roughness. The measurement of roughness evolution was achieved using surface replicas. The replicating compound used was MICROSET 101RF. The technical information of this compound is shown in Table 5.6.

Microset Grade	Resolution (Microns)	Shrinkage (%)	Operating Temperature ($^{\circ}C$)	Setting Time (Mins)
101RF	0.1	<0.1	-10 - 180	5

Table 5.6: Microset replication compound technical information

Three pressures were tested at (600, 750 and 900MPa) and two initial roughness. Rough tests started at $9-10\mu m$ and smooth tests started at $1-2\mu m$. Specimens were loaded axially and then twisted at the specified axial pressure. Each test was cycled 20 times. Replication compound was applied to the upper and lower specimens at various intervals during testing to study roughness evolution as shown in Figure 5.15.

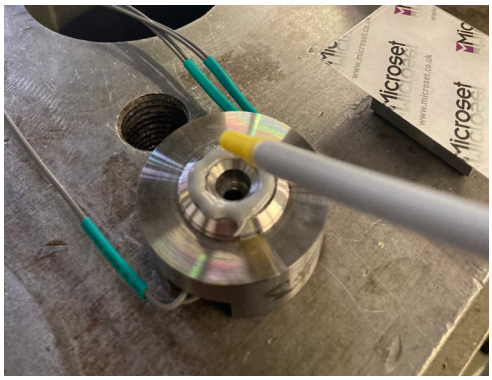

(a) Replication compound application to upper specimen

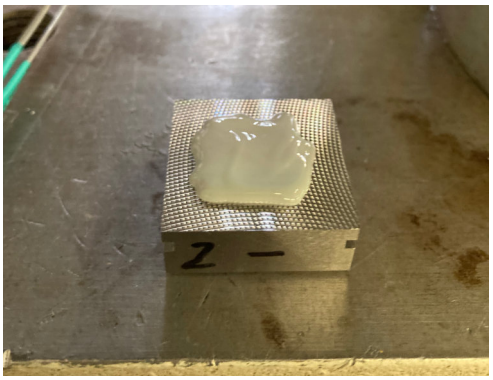

(b) Applied replication compound to lower specimen

(c) Curing under backing slides (5 mins)

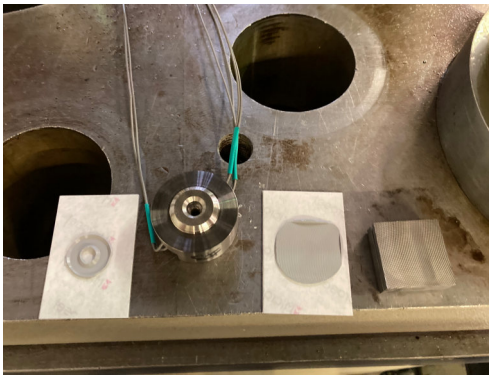

(d) Remove slides to reveal replicas

Figure 5.15: HPT specimen replication procedure

The frequency of replication depended on the test. Where surfaces were dry or the 3BL could easily be removed, replication occurred often, and when the 3BL was difficult to remove replication occurred less often (see Table 5.7). The specimens were cleaned with acetone after replication had occurred. These replicas were then observed through an Alicona microscope to measure surface roughness.

Test	**Replication Occurred After Cycles...**
Dry	0,1,2,3,4,6,8,10,15,20
Water	0,1,2,3,4,6,8,10,15,20
Grease	0,5,10,15,20
Leaves	0,20

Table 5.7: Replication frequency

5.1.10 Application and Removal of Third-Body Layers

In addition to dry tests, 'wet' tests were also conducted, whereby 3BL material was introduced to the HPT interface as well as different surface roughnesses. The three 3BLs chosen are shown below.

- Distilled Water
- Grease
- Sycamore Leaves

Water, grease and leaves are typical 3BLs found on the UK rail network. In order to apply these 3BLs consistently, tailored application procedures were devised for each 3BL. These application procedures were similar to those used by Skipper [83]. This work was conducted on the HPT rig primarily studying the effects of sand at the wheel-rail interface, however some work was conducted to study the effects of water and leaf layers. With this in mind, the application procedures, amounts of material and type of material were kept the same to enable the potential for result comparison in the future. To take replicas of the specimen surfaces, 3BLs must first be removed, therefore the removal of 3BLs is also discussed.

5.1.10.1 Water

Water occurs naturally on the railhead. Low amounts of water such as when it has just started to rain or early in the morning in the form of dew cause low adhesion [84]. $20\mu L$ of distilled water was applied to the lower specimen contact area with a pipette before testing and after each cycle. Specimens were cleaned with acetone before testing and after each cycle.

5.1.10.2 Grease

Grease and other friction modifier products are applied to the rail gauge corner and the top of the rail to modify the interfacial friction conditions, reduce wear and reduce lateral forces. The grease used was a common off-the-shelf multipurpose grease to enable these tests to be repeated without the need to source highly specialised greases/friction modifiers. 0.012g was applied to the lower specimen contact area

before the test and after cycles 5, 10 and 15. The specimens were cleaned with acetone after these cycles to measure the roughness.

5.1.10.3 Leaves

Leaf layers are formed by repeatably subjecting leaf material to compressive stresses between two contacting surfaces. They form over a number of cycles with the HPT test approach, but may form during a single train pass on track. To best simulate the conditions found on track, sycamore leaves were dried and crushed into a powder. This powder could then be applied consistently over the contact patch (see Figure 5.16a). At the start of the test $0.025g$ of leaf material was applied to the contact patch along with $20\mu L$ of distilled water (see Figure 5.16b).

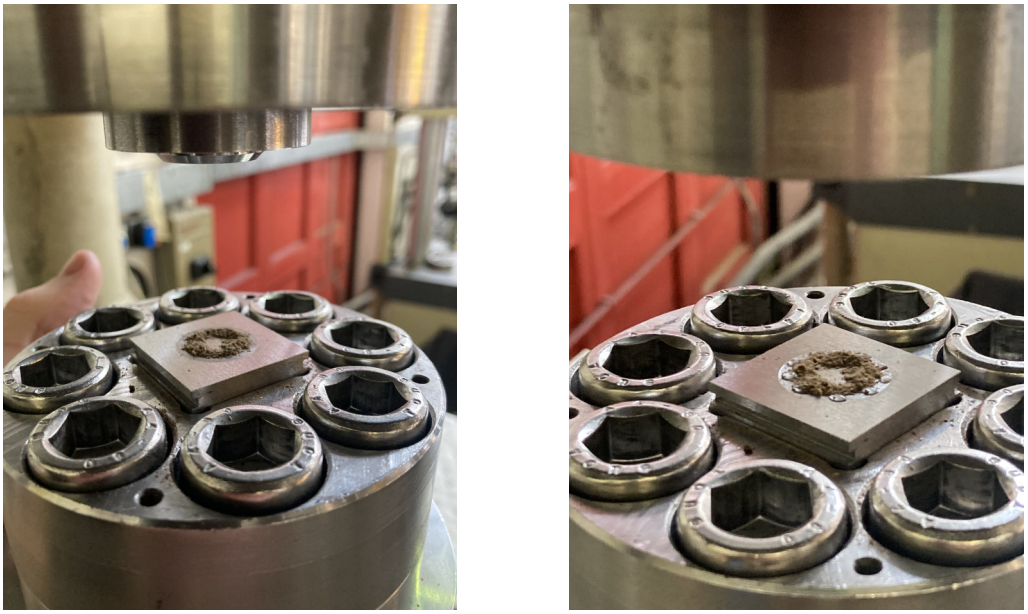

(a) Leaf material application *(b) Water application*

Figure 5.16: Creating leaf layers on the HPT rig

Hydration is an important factor in the creation of leaf layers and low adhesion scenarios. This occurs naturally on track whereby the leaf material is not fully dehydrated or else water is introduced through environmental processes. The applied leaf material dries out over the course of the HPT test so rehydration is necessary at various points during the test. Rehydration occurred before the test and after the 1st, 4th, 7th, 10th, 13th and 17th cycles. The interface was rehydrated each time with $20\mu L$ as seen in Figure 5.16b.

5.1.11 HPT Test Procedure

The overall test procedure is presented below. It includes the alignment check and test parameters covered in Sections 5.1.7 and 5.1.8.

1. Attach specimens to the HPT.
2. Insert some pressure sensitive paper between the specimens.
3. Perform alignment check at 150 MPa at $-40°$, $0°$ and $40°$ locations.
4. Check the tone of the paper to ensure the load is uniformly distributed at the contact surface.
5. Measure inner and outer radii from the annulus on the pressure sensitive film.
6. Use these measurements to calculate the contact area and ERF.
7. Enter these values into the script along with the test temperature, humidity and other test parameters.
8. Take replica of surfaces (this is the initial roughness).
9. Clean specimens with acetone.
10. Apply 3BLs if necessary.
11. Pressurise servo valves.
12. Run the script.
    (a) Bring together specimens.
    (b) Apply compression to specified pressure.
    (c) Apply torque.
    (d) Rotate through specified sweep length at specified sweep rate.
    (e) Release torque.
    (f) Release compression.
    (g) Separate specimens.
    (h) Rotate to next sweep point.
13. Depressurise servo valves.

14. Remove the specimens and take a replica if necessary.

15. Clean specimens with acetone if necessary.

16. Repeat up to 20 cycles taking replicas after the cycles specified in Table 5.7.

From the above test procedure, part 12 is subcategorised into 8 stages; these stages make up an individual test cycle. A typical 600MPa cycle can be seen graphically in Figure 5.17.

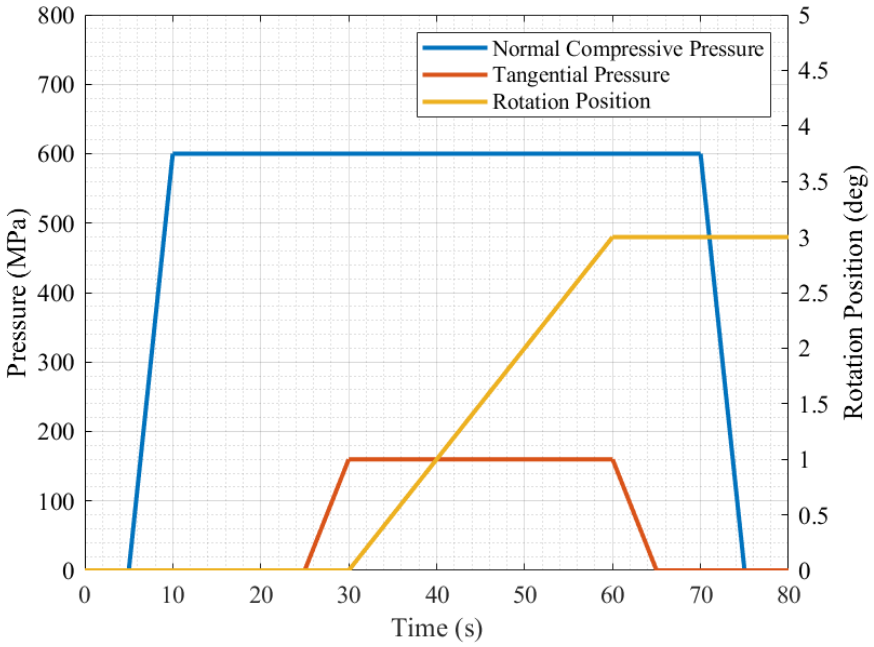

Figure 5.17: Theoretical HPT test cycle procedure (Test: Dry 600MPa Rough)

Whilst the control systems on the HPT try to achieve the precise changes seen in Figure 5.17, the reality is that only an approximation can be achieved due to slip. Figure 5.18 shows a real 600MPa HPT test. It can be seen that the applied axial pressure is relatively stable whereas the torsional elements such as tangential pressure and rotation position are less so.

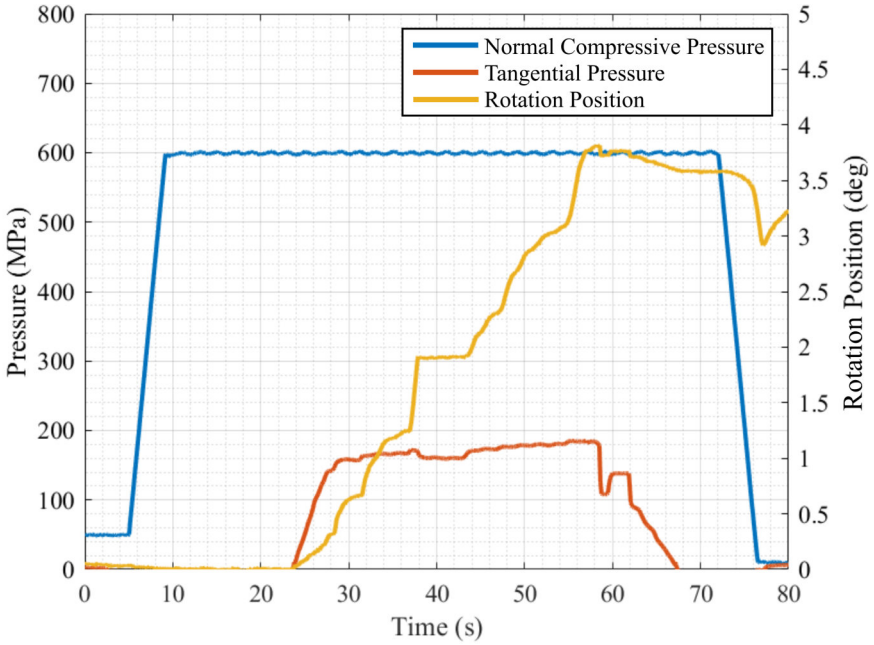

Figure 5.18: Real HPT test cycle procedure (Test: Dry 600MPa Rough)

5.1.12 HPT Test Outputs

The normal pressure (σ_N) can be calculated using Equation 5.2. This uses the normal load (N) over the nominal interfacial area (A) which is that of an annulus. This annulus can be calculated as the difference of two circles with external radius (R) and internal radius (r).

$$\sigma_N = \frac{N}{\pi(R^2 - r^2)} \tag{5.2}$$

The relationship between tangential load (T) and torque (T_q) can be calculated using Equation 5.3. The denominator of this equation is known as the effective radius of friction (ERF) which is outlined in Section 5.1.7.

$$T = \frac{T_q}{\frac{2}{3}\left(\frac{R^3 - r^3}{R^2 - r^2}\right)} \tag{5.3}$$

This can then be converted into tangential pressure (σ_T) using Equation 5.4:

$$\sigma_T = \frac{T}{\pi(R^2 - r^2)} \tag{5.4}$$

Both σ_N and σ_T are calculated directly from the HPT rig given a certain contact area which is measured using callipers during the pressure sensitive film calibration phase (see Section 5.1.7). Normal pressure is a predefined input which alongside the rotation rate achieves a torque which is recorded. The ratio of T to N provides the dimensionless traction coefficient as seen in Equation 5.5:

$$Traction\ Coefficient = \frac{T}{N} \tag{5.5}$$

5.2 Ultrasonic Testing Methodology

Ultrasonic reflectometry was used during the HPT tests to measure the interfacial stiffness. Initially this was attempted for all pressures, however there were issues when testing for higher pressures (750MPa and 900MPa). During these higher pressure tests damage was incurred to the ultrasonic transducers. This was possibly due to small amounts of bending on the face the sensors were bonded to. The transducers on specimens 1, 3, 4 and 6 all incurred damage. Without redesigning the HPT rig and specimens, this was unavoidable. Since this was out of the scope of this work, ultrasonic reflectometry was only used for the 600MPa tests. Specimens 2 and 5 were used to gather ultrasonic data for the tests including the 3BL tests at this pressure. Similar issues were observed in the work of Fukagaia et al., however lower pressure interfacial stiffness measurements were obtained in this work [81]. The design of these specimens requires further consideration if higher pressures are to be tested in future work.

5.2.1 Ultrasonic Transducer Selection and Instrumentation

In order to study interfacial stiffness, the HPT rig specimens must be instrumented with ultrasonic sensors. Whilst commercially available ultrasonic transducers do exist, they are often large and unsuitable for many applications; these are removable reusable sensors that require an intermediary couplant to transmit through a surface. As mentioned in Section 4.3.1, PZT piezo-ceramic materials are the most popular piezo materials and can be cut down to extremely small dimensions ($< 1mm^2$).

These are available in a wide range of frequencies, but 1-10MHz frequency piezo elements are most commonly used and can emit either longitudinal or shear waves depending on their polarisation direction.

5.2.1.1 Longitudinal and Shear Transducers

Two types of ultrasonic transducer were used: longitudinal and shear transducers. Both longitudinal and shear transducers are able to measure distances. Longitudinal transducers are used to measure the longitudinal interfacial stiffness K_L and shear transducers are used the measure the shear interfacial stiffness K_S.

5.2.1.2 Frequency Selection

Selecting the frequency of an ultrasonic sensor depends on a number of factors. These factors include the material and distance through which the ultrasound must travel and what property is intended to be measured. Higher frequencies attenuate faster than lower ones, however they give you more detailed information as to what is happening at the interface and are able to measure interfaces under higher contact pressures (see Section 4.4.1). The longitudinal sensors used were 10MHz whilst the shear sensors used were 5MHz. Lower frequency sensors are thicker than higher frequency sensors (see Section 4.3.1), however the structure of piezo ceramic sensors means that longitudinal sensors are twice the thickness of shear sensors for the same frequency. Selecting longitudinal sensors with double the frequency rating of the shear sensors meant similar sensor thicknesses for both the longitudinal and shear sensors; this aided the bonding process (see Section 5.2.1.4).

5.2.1.3 Sensor Size and Layout

Signal strength is a function of the sensor size, however there are limitations to how large the sensors could be for this application. The annular contact patch leaves only a $3.75mm$ window for sensors to be bonded. It is convenient to cut shear sensors as a square for they can be cut from the same sensor plate and orientated differently to study shear stiffnesses in various directions. The piezo-ceramics were cut by hand using a scalpel or razor blade so naturally have some variation in their size. The transducer geometry can be seen in Figure 5.19.

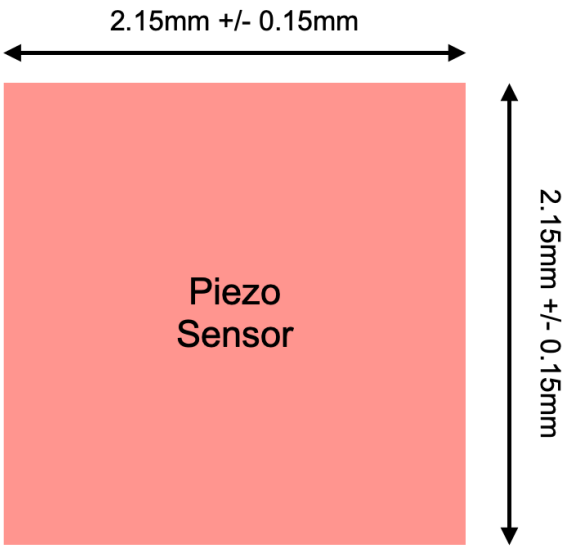

Figure 5.19: Transducer geometry

For consistency, the longitudinal transducers were cut to the same size as the shear transducers: this was $2.15mm +/- 0.15mm$ which gave an area range of $4mm^2 - 5.29mm^2$. Signal strength variations based on the transducer size could be adjusted using the individual gains on the film measurement system (FMS) (see Section 5.2.2). Transducers were positioned on the specimen by hand, therefore there was some variation in their orientation and radial location. Using the nearfield equations in Section 4.3.2, nearfield effects ceased at 0.6mm from the shear transducers and 1.6mm from the longitudinal transducers. With reference to the specimen geometry in Section 5.1.2, it can be seen that the distance to the annular surface was 6mm meaning nearfield effects are negligible at these transducer sizes.

Transducers were positioned in an arc to measure the annular contact patch (see Figure 5.20). The upper array (transducers 1, 2, 3 and 4) consisted of shear transducers: two with a radial orientation (transducers 1 and 2) and two with a circumferential orientation (transducers 3 and 4). The lower array consisted of two longitudinal transducers (transducers 5 and 6). Having two of each transducer type enabled ultrasonic data to be validated and allowed specimens to be used even if one transducer was damaged. Figure 5.20 shows the layout of these transducers on the upper wheel specimen.

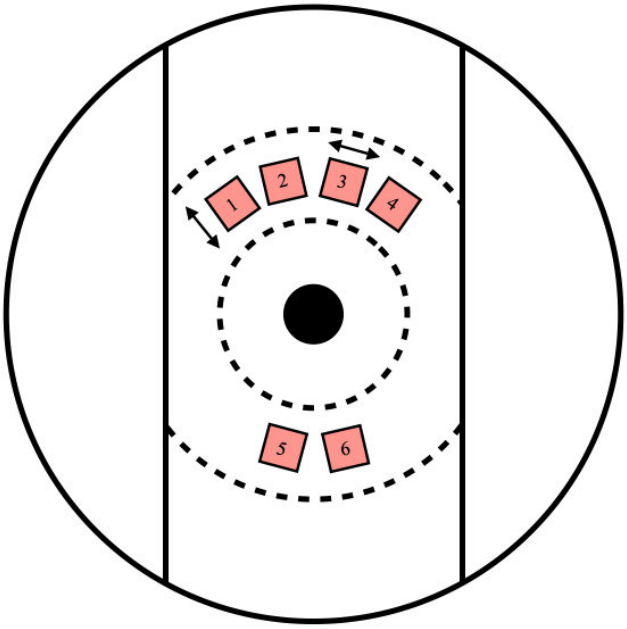

Figure 5.20: Transducer layout on wheel specimen (viewed from above)

Tables 5.8, 5.9 and 5.10 show the measured dimensions of each individual transducer of the six specimens that were made (h = radial dimension, w = circumferential dimension, A = area).

One				**Two**			
Transducer No.	**h (mm)**	**w (mm)**	**A (mm^2)**	**Transducer No.**	**h (mm)**	**w (mm)**	**A (mm^2)**
1	2.16	2.04	4.41	1	2.19	2	4.38
2	2.04	2.04	4.16	2	2.3	2.02	4.65
3	2.15	2.17	4.67	3	2.05	2.14	4.39
4	2.01	2.29	4.60	4	2.2	2.3	5.06
5	2.23	2.08	4.64	5	2.06	2.16	4.45
6	2.2	2.11	4.64	6	2.25	2.05	4.61

Table 5.8: Specimen transducer dimensions (one and two)

Three				Four			
Transducer No.	**h (mm)**	**w (mm)**	**A (mm^2)**	**Transducer No.**	**h (mm)**	**w (mm)**	**A (mm^2)**
1	2.23	2.11	4.71	1	2.23	2.11	4.71
2	2.15	2.11	4.54	2	2.15	2.11	4.54
3	2.19	2.07	4.53	3	2.19	2.07	4.53
4	2.18	2.14	4.67	4	2.18	2.14	4.67
5	2.2	2.21	4.86	5	2.2	2.21	4.86
6	2.13	2.07	4.41	6	2.13	2.07	4.41

Table 5.9: Specimen transducer dimensions (three and four)

Five				Six			
Transducer No.	**h (mm)**	**w (mm)**	**A (mm^2)**	**Transducer No.**	**h (mm)**	**w (mm)**	**A (mm^2)**
1	2.11	2.08	4.39	1	2	2	4.00
2	2.27	2.28	5.18	2	2.19	2.12	4.64
3	2.19	2.07	4.53	3	2.17	2.09	4.54
4	2.18	2.01	4.38	4	2.04	2.24	4.57
5	2.16	2.27	4.90	5	2.29	2.16	4.95
6	2.23	2.25	5.02	6	2	2.16	4.32

Table 5.10: Specimen transducer dimensions (five and six)

The circumferential orientation was such that the transducers were positioned in the middle of the milled channel to aid bonding (see Section 5.2.1.4). Gaps between transducers were approximately 2mm centre to centre. The real sensor layout can be seen in Figure 5.21.

Figure 5.21: Real sensor layout

5.2.1.4 Bonding

Bonding ultrasonic transducers presents one of the greatest challenges within the instrumentation phase. The transducers and bonding surfaces must be cleaned well as any layer between them will result in substandard signal responses. M-Bond 610 adhesive was used to bond the sensors to the specimen (see Figure 5.22). This requires careful application, a curing period and then a heating cycle up to $160°C$ to set. Clamps, silicon pads, metal shims and tough crosshatch fabric were used to apply a consistent pressure to the sensors during the heating phase. Digital measuring callipers were used at each end of the clamp to ensure the bolts were providing equal loads. Matching the sensor thickness by using 10MHz longitudinal sensors and 5MHz shear sensors aided this even pressure distribution. Without these

measures, sensors can crack under too much load or give poor signal responses post bonding.

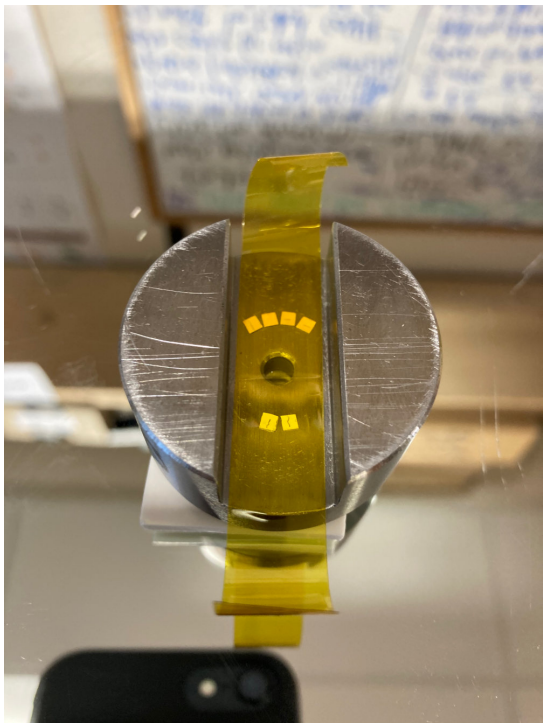

(a) Fix the sensor layout with Kapton tape

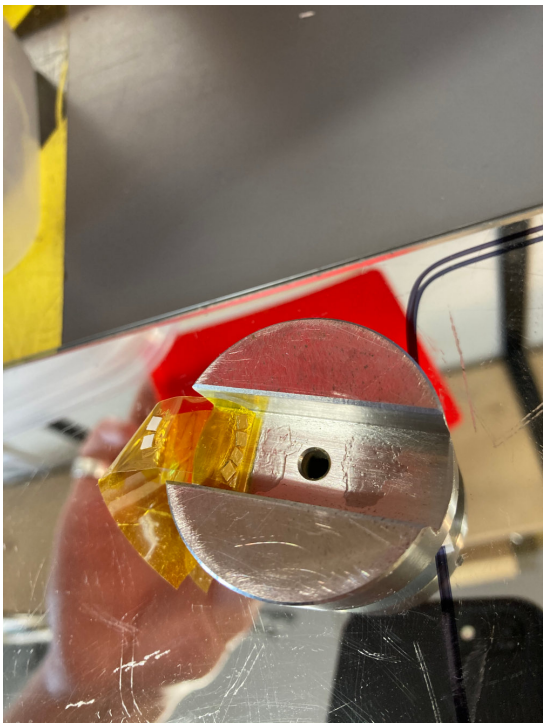

(b) Peel back the tape to apply the M-Bond

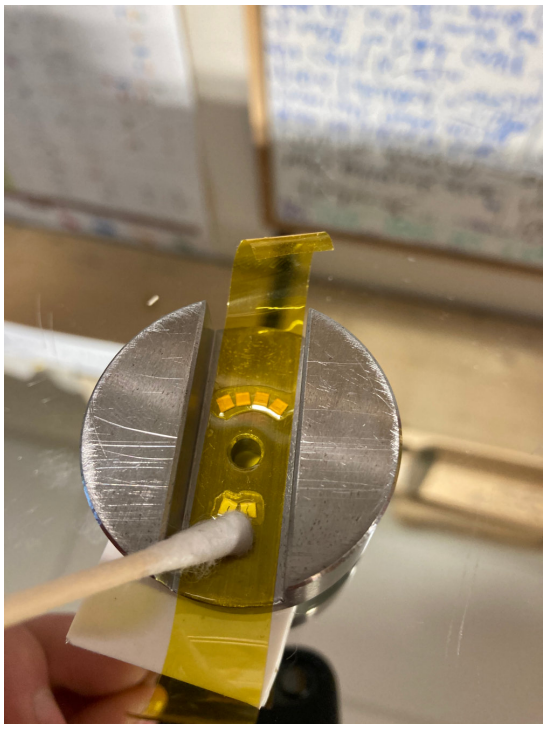

(c) Reattach tape and use a cotton bud to ensure a good bond

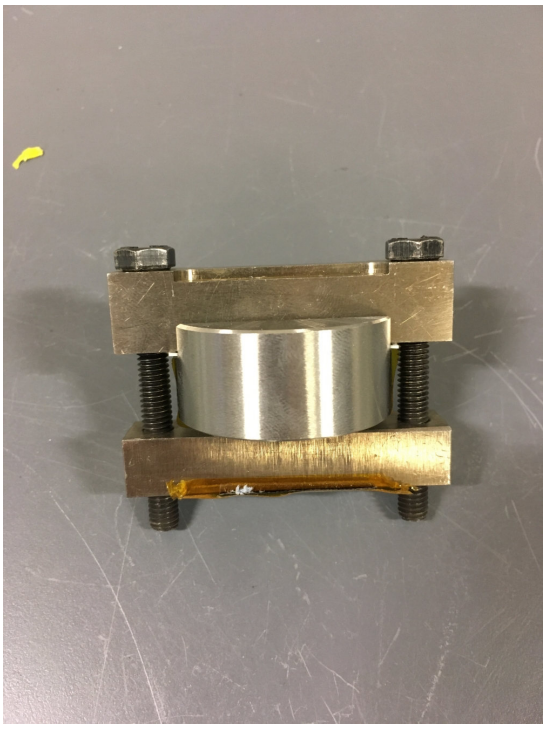

(d) Apply downward force through sensors with a clamp

Figure 5.22: Bonding ultrasonic sensors

5.2.1.5 Wiring

Post bonding, sensors must be connected to a pulser which in turn is connected to a data gathering system. The visible electrode of the sensor is the positive whilst the surface to which the sensor is bonded is the negative. The two are isolated from one another by the ceramic material between them. Coaxial cable is used to connect these sensors which consists of a positive conductor surrounded by a dielectric, a negative shield and an outer jacket (see Figure 5.23).

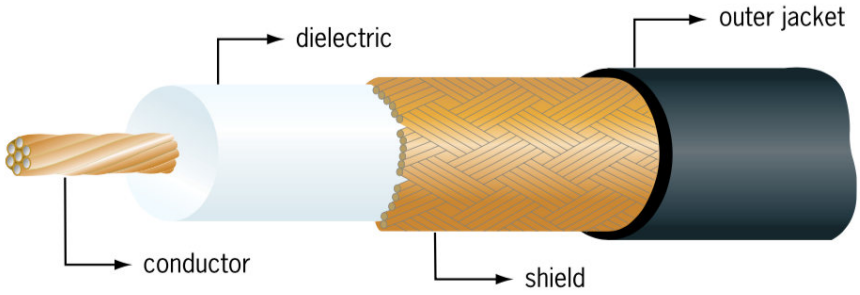

Figure 5.23: Coaxial cable schematic [77]

The coaxial cable is then connected to the negative and positive terminals using silver epoxy (a conductive two part epoxy). This sets in 20 minutes at $80 - 100°C$). This method is preferred to soldering when using small sensors as the heat from a soldering iron can damage the sensor surface. The resulting silver epoxy bond is fragile so an additional potting phase is required to secure the connected wires in place (see Section 5.2.1.6). Continuity checks ensure that the cables are connected correctly at this stage as this cannot be rectified once the potting phase has taken place.

5.2.1.6 Potting

Once the wires were connected and the continuity checks completed, the cables were secured in place using a Robnor potting compound. Robnor is electrically insulating and can withstand high temperatures. Robnor is a two part compound that sets in 24 hours. The set potting compound can be seen in Figure 5.24. Subminiature version B (SMB) connectors were soldered to the wires to enable them to be connected to either the FMS or a Picoscope.

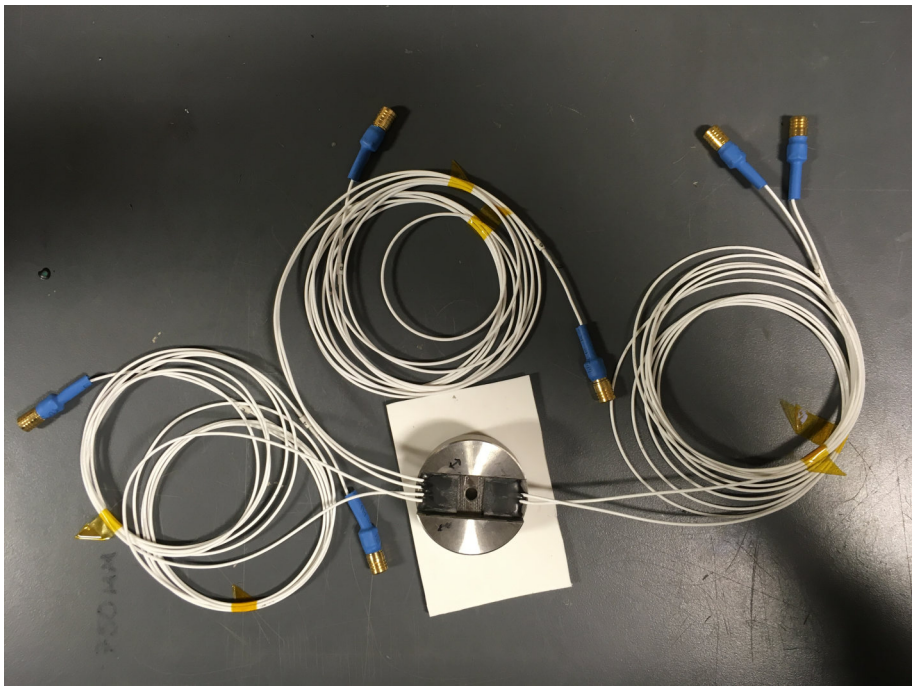

Figure 5.24: Upper specimen complete with SMB connectors and black Robnor potting compound

5.2.2 Ultrasonic Data Acquisition

Ultrasonic data was captured through the data process route discussed in Section 5.1.6. This raw data was then subsequently processed which is covered in Section 5.4.3. This section details the set up of the film measurement system (FMS) for data capture. Ultrasonic transducers are connected to the FMS through coaxial cable and SMB connectors. The graphical programming environment Labview was used to control and save the ultrasonic transducer outputs and inputs. The FMS is capable of controlling up to 8 transducers simultaneously and these transducers can be pulsed with various different signal shapes such as sine waves, square waves and saw waves.

There are a number of advantages for using an FMS over a Picoscope or other pulsing hardware, including the higher pulse rates and voltage outputs achievable when using an FMS. High pulse rates enable high resolution real-time data acquisition. High pulse voltages allow reflection detection through large volumes. Signals can also have their own dedicated gain, range, delay, pulse width and filters applied to them as well as a global pulse rate and output voltage. Figure 5.25 shows the Labview user interface indicating the primary settings tabs and the recording win-

dow. These settings adjust what is included in the recording window to ensure only the necessary data is being collected whilst maximising signal strength and clarity.

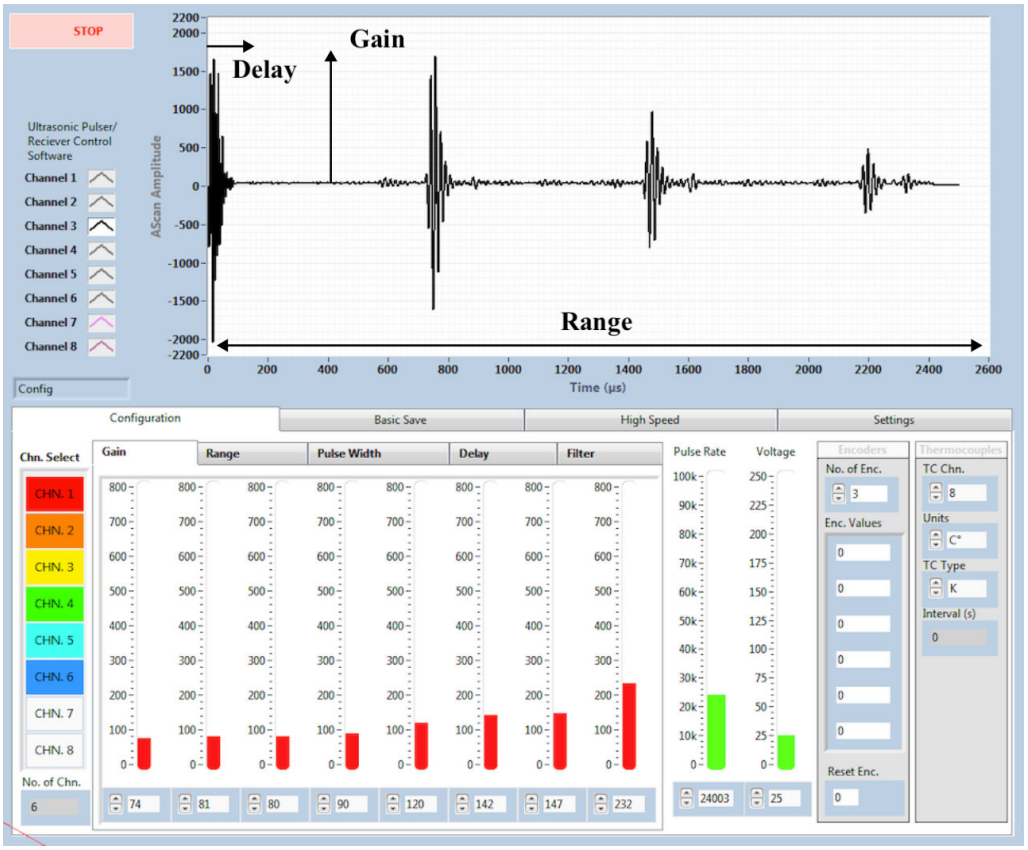

Figure 5.25: FMS settings and Labview user interface

The settings shown in Figure 5.25 are explained in the list below:

- **Gain**: Individual channel voltage amplification (Gain can be adjusted for individual channels allowing the signal strengths to be matched)
- **Range**: Individual channel signal capture range (Range can be shortened to include just a single reflection)
- **Pulse Width**: Elapsed time between leading and trailing edges of a pulse for each channel (Pulse width is usually adjusted to maximise the signal amplitude)
- **Delay**: Individual channel signal shift (Delay can be altered to change the start of the recording window)

- **Filter**: Individual channel signal filter (Filter amount can be changed to reduce signal noise)
- **Pulse Rate**: Global pulses per second (Pulse rate is divided up by the number of channels used)
- **Voltage**: Global input voltage amplitude

Figure 5.26 shows an A-scan for a single longitudinal transducer. This A-scan occupies the recording window. It can be seen that this A-scan includes the original sinusoidal pulse and the first six reflections. For most applications this in not necessary and will take up a lot of data should this be saved. Only the first reflection is useful for interfacial stiffness measurements so this signal needs to be cropped using the settings to include only the first reflection, as seen in Figure 5.27.

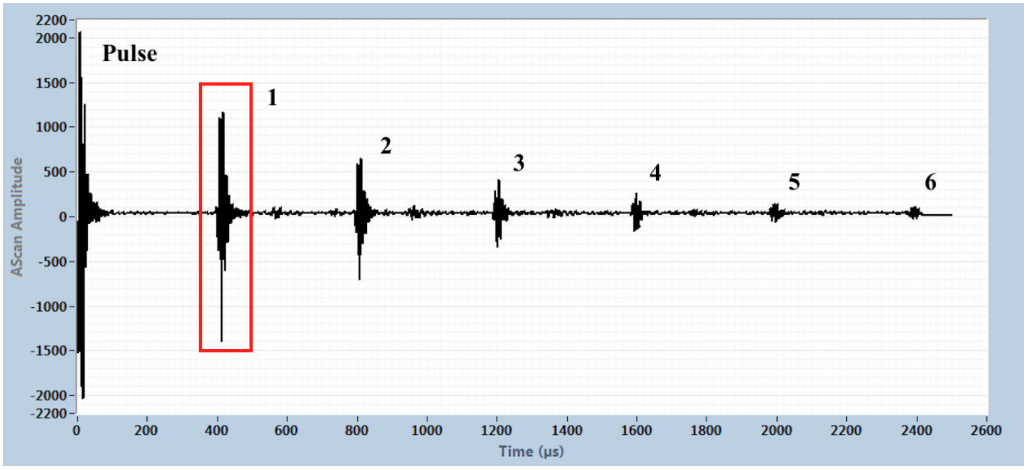

Figure 5.26: A-scan showing reflected signals and attenuation

In Figure 5.27 the signal has been cropped to include just the first reflection. An additional transducer signal has been included to demonstrate that each of the signals can be individually adjusted so that they all appear lined up in the recording window. This dramatically reduces the amount of data that needs to be saved, meaning higher pulse rates can be used.

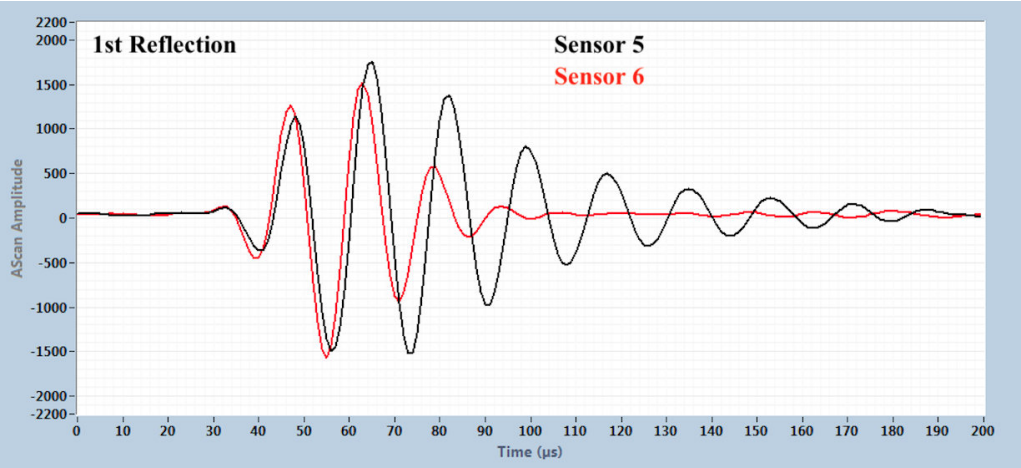

Figure 5.27: Windowed signal A-scan

Table 5.11 shows the FMS settings that were used to capture ultrasonic data. Gains are selected on a test by test basis to ensure transducer signals are at a similar amplitude for each test. Global pulse rate was set to 6000 which was split between the six channels. The pulse width and the filter were chosen to maximise signal amplitude and quality. Shear and longitudinal transducers have different sound speeds so they require different delays to line up the first reflection in the recording window.

FMS Setting	**Transducer Number**					
	1	**2**	**3**	**4**	**5**	**6**
Gain	Test	Test	Test	Test	Test	Test
Range (μs)	95	95	95	95	95	95
Pulse Width (μs)	10	10	10	10	9	9
Delay (μs)	700	700	700	700	425	425
Filter	4	4	4	4	4	4
Individual Pulse Rate	1000	1000	1000	1000	1000	1000
Voltage (V)	25	25	25	25	25	25

Table 5.11: FMS settings (gains are selected on a test by test basis)

Using these settings, the raw ultrasonic amplitude data was captured for the 600MPa tests. This raw data was then processed (see Section 5.4.3).

5.2.3 HPT Testing Methodology Summary

A bespoke HPT test approach has been devised that outputs frictional data. This can then be used to parameterise a creep-force model that can in theory predict full scale tests. A way of monitoring the roughness has been devised whereby replicas of the interacting surfaces can be taken between test cycles. These replicas can then be scanned using an Alicona to provide the surface roughness. Ultrasonic data can be obtained in-situ, which through the use of a DAQ and an FMS can be synced with the frictional outputs from the HPT. Figure 5.28 gives an overview of the test stages for the HPT testing and when the three primary measurements (roughness, interfacial stiffness and traction coefficient) were taken.

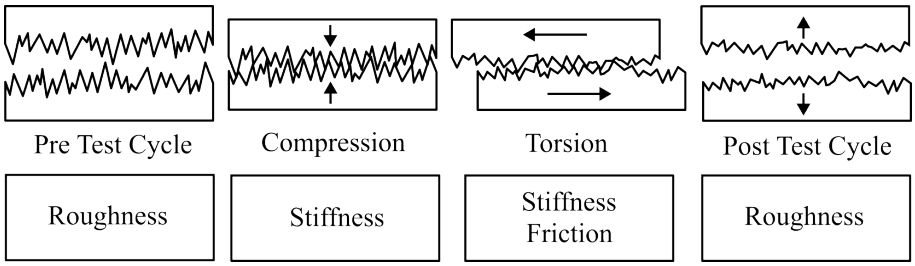

Figure 5.28: HPT test stages and associated measurements

5.3 FSR Testing Methodology

Upon completion of the small-scale testing on the HPT and the subsequent ECF modelling (see Chapter 7), full-scale testing was used to validate the outputs of the ECF model. This required a full sized wheel to be rolled over a full sized rail with the correct interfacial geometry and roughness to those found on track. Two roughnesses were applied just like those on the HPT specimens; these were done with grinding and fly cutting procedures for the low and high initial roughnesses respectively.

5.3.1 FSR Layout

Full-scale testing was achieved using the full-scale wheel-rail rig (FSR) at the University of Sheffield. An FSR test involves the use of two full-scale specimens: the rail specimen and the wheel specimen (7 and 11 respectively) that are pressed together

with a certain axial load by the wheel actuator (1). The wheel is free to rotate about the wheel axle (10) and the assembly has around 100mm of vertical travel due to the FSR frame pivot point point (12). The chain (6) is bolted to the chain mount weight (9) through the chain mount (8). This in turn is bolted to the wheel; a counterweight (2) keeps the wheel balanced. Preload and horizontal load is applied to the chain with the chain actuator (4): this allows various levels of slip to be achieved between the wheel and the rail. The rail is clamped to the rail trolley (5). The rail trolley is pulled from under the wheel using the rail trolley actuator (3) causing the wheel to roll over the rail. Maximum rolling speed is 100mm/s, maximum axial load is $110kN$ and maximum horizontal load depends on the interfacial conditions. The ratio of the vertical to horizontal load is the traction coefficient which will vary depending on the applied slip and the interfacial conditions.

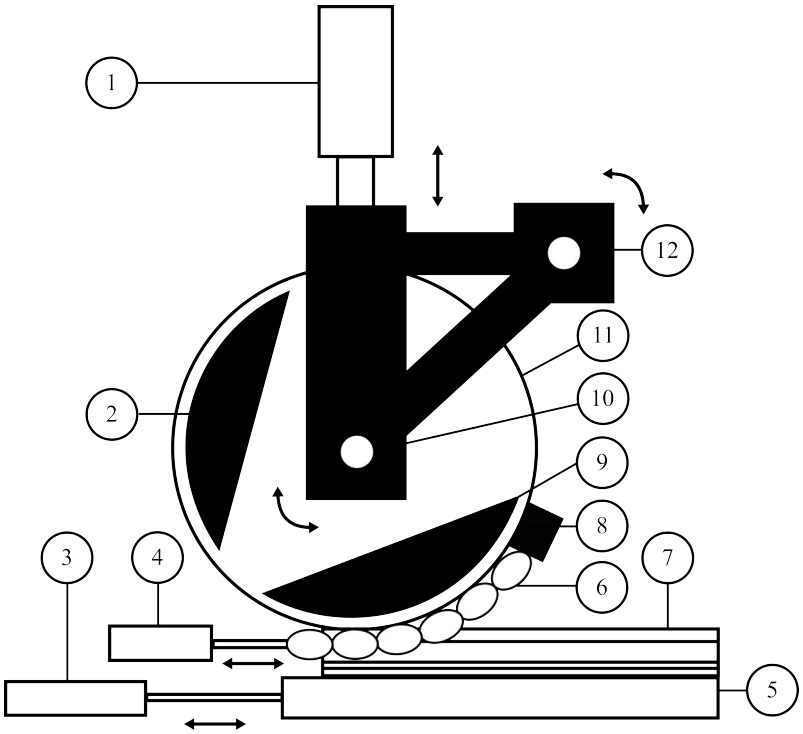

Figure 5.29: FSR schematic

Operation	Operation Limit
Axial Load (Compression)	+/- 110 kN
Chain Load (Tension)	+ 50 kN
Longitudinal Displacement	350 mm
Creep	0-10%

Table 5.12: FSR operational limits

5.3.2 FSR Specimen Geometry

The FSR specimens were cut from an R260 UIC60 section of rail. A custom test rail was used that has a pocket milled out of the railhead for the specimen to sit in (see Figure 5.30).

Figure 5.30: FSR specimen in-situ

Specimens could be bolted into the pocket to secure them in place. The FSR specimen dimensions are shown in Figure 5.31.

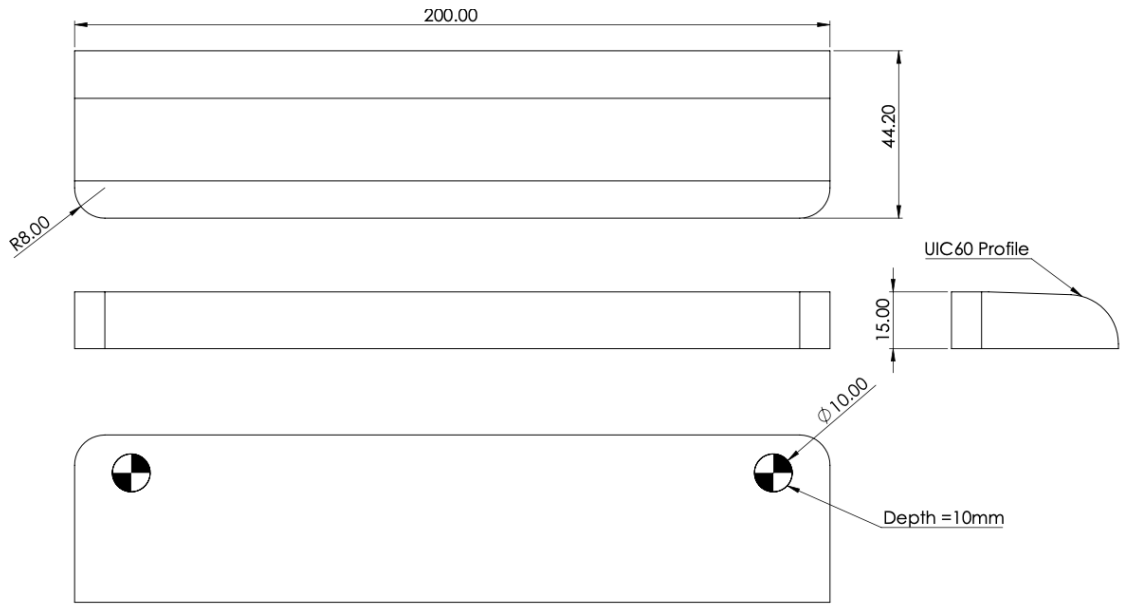

Figure 5.31: FSR specimen dimensions

5.3.3 The FSR Contact Patch and Adapting 3BL Application Amounts

In addition to dry tests, 'wet' tests were also conducted, whereby 3BL material was introduced to the FSR interface. The three 3BLs chosen were the same as those for the HPT tests and are shown below.

- Distilled Water
- Grease
- Sycamore Leaves

The contact patch for the HPT rig tests is relatively small (around $200mm^2$) and theoretically the entire specimen interfaces are in contact with one another for the duration of the test. For the FSR tests, the wheel rolls over the rail specimen on a running band which has a width (around 10mm) and is the length of the rail specimen (200mm) (see Figure 5.32). This results in a running band area of around $2000mm^2$: roughly 10x that of the HPT tests. This means the 3BL amounts applied to the FSR rail specimens need to be increased to mimic the small-scale HPT tests.

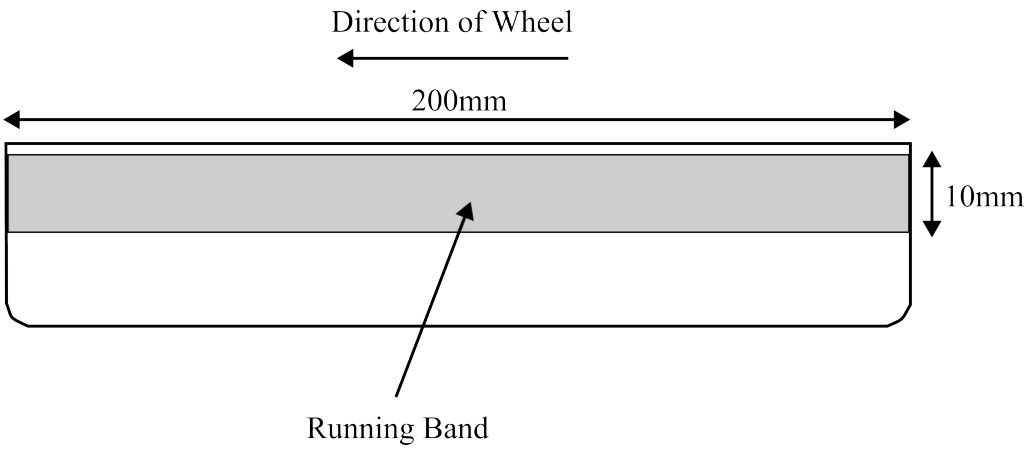

Figure 5.32: FSR rail specimen running band

5.3.4 Application and Removal of third-body Layers

The application of 3BLs to the FSR specimens is discussed in the following sections. 3BL material was increased by ten to account for the larger contact area. For the first 20 cycles 3BLs were applied at the same intervals as for the HPT tests. 3BL application for the remaining 80 cycles varied depending on how frequently replicas were taken.

5.3.4.1 Water

Due to the large contact area, the application of distilled water was done with a small spray bottle as apposed to a pipet. The amount of water produced by a single spray was weighed and it was concluded that two sprays produced roughly $200\mu L$. This was applied to the specimens; care was taken to make the coverage as even possible over the running band (see Figure 5.33). Water was applied before each cycle for the first 20 cycles and then every 10 cycles. Specimens were cleaned with acetone after replication.

Figure 5.33: FSR water application

5.3.4.2 Grease

0.12g of grease was applied to the running band with the tip of a pipet before the test and after cycles 5, 10, 15, 20, and 60 (see Figure 5.34). Specimens were cleaned with acetone after replication.

Figure 5.34: FSR grease application

5.3.4.3 Leaves

At the start of the test, $0.25g$ of sycamore leaf material was applied to the contact patch along with $200\mu L$ of distilled water (see Figure 5.35). For the first 20 cycles, rehydration occurred at the same intervals as for the HPT tests. For the remaining 80 cycles, rehydration occurred every 10 cycles. The interface was rehydrated each time with $200\mu L$. After the test, the leaf layer needed to be removed from the specimen to take a replica. An ultrasonic bath was used to clean the lower specimen and the wheel was cleaned with acetone.

Figure 5.35: FSR leaf application

5.3.5 FSR Test Data Process Route

Unlike the HPT tests, no ultrasonic data was captured during the FSR tests so no additional computer or DAQ was needed to process this data. An ECU was used to give vertical, horizonatal and chain commands to the respective actuators. This was done in both displacement and force modes depending on the stage of a test. The results were analysed in Matlab.

5.3.6 Applying Roughness to the FSR Specimens

Unlike the HPT specimens, the wheel remains in place and is reused during the FSR tests, meaning only the rail specimen had a roughness applied to it. It was hoped that the specimens could be cut from freshly ground rail that so that the surface was as representative of ground rail as possible, however this was not possible. Rail

grinding is a process that must be done on track by a grinding train and the process is only done to rails still in service. Instead the roughness was done with a flycutting procedure on a CNC machine for the rough specimens. Multiple reference points were used to account for the curved profile. A grinding procedure was used for the smooth specimens. Specimens were tilted incrementally using shims to account for the curved profile. The result was a rough and smooth portion of the specimens which could be used as the running band.

5.3.7 FSR Roughness Measurement Method

Like the HPT tests, roughness was measured with the use of replicas. Due to the curved geometry of both the wheel and the rail, the contact patch is usually ovular in shape and will vary in pressure from one part to another, the highest pressures can be found in the centre and the lowest towards the edge. Consequently the roughness will be affected differently across the running band as the surface is exposed to varying pressures. Roughness was measured at three locations across the running band as seen in Figure 5.36.

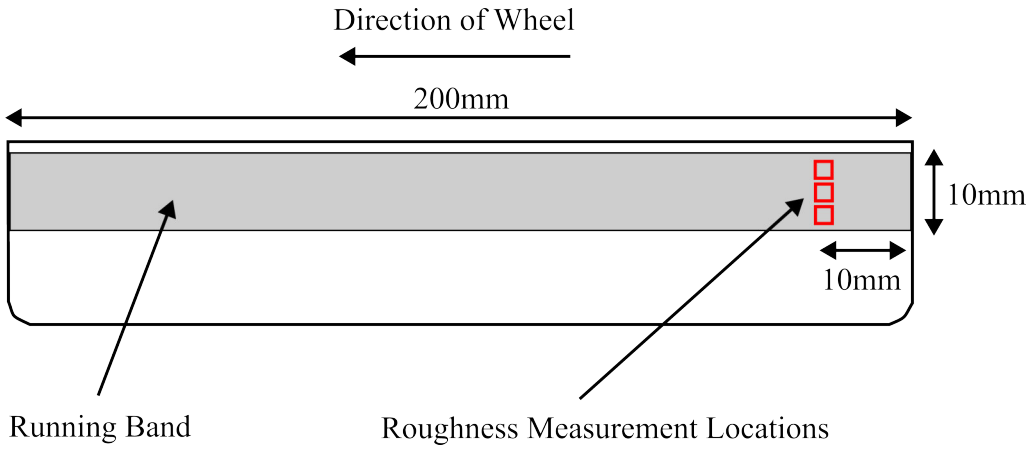

Figure 5.36: FSR rail specimen roughness measurement locations

Replicas of the two surfaces were taken at the intervals shown in Table 5.13.

Test	Replication Occurred After Cycles...
Dry	0,1,2,3,4,6,8,10,15,20,60,100
Water	0,1,2,3,4,6,8,10,15,20,60,100
Grease	0,5,10,15,20,60,100
Leaves	0,100

Table 5.13: Replication frequency

5.3.8 FSR Test Procedure

The overall FSR test procedure is outlined below.

1. Attach rail specimen to the FSR.
2. Clean specimens with acetone.
3. Take replica of the wheel and rail surfaces (this is the initial roughness).
4. Clean specimens with acetone.
5. Apply 3BLs if necessary.
6. Pressurise servo valves.
7. Run the script.
   (a) Lift the wheel off the rail.
   (b) Move the rail to the start location.
   (c) Apply compression to specified force.
   (d) Apply chain tension to specified tension.
   (e) Pull the rail causing the wheel to rotate with specified slip.
   (f) Stop the rail.
   (g) Release the chain torsion.
   (h) Release the wheel compression.
   (i) Separate specimens.
8. Depressurise servo valves if necessary.

9. Clean specimens with acetone if necessary.
10. Take a surface replica if necessary.
11. Clean specimens with acetone if necessary.
12. Apply 3BL if necessary.
13. Repeat.

5.3.9 FSR Testing Methodology Summary

A bespoke FSR test approach has been devised that outputs frictional data. This data can be used to validate the output from the ECF model. In addition to this, replicas of the interacting surfaces can be taken between test cycles. These replicas can then be scanned using an Alicona to provide roughness data. To understand how the rail inserts change globally over the course of a test, laser scans of the FSR rail inserts were taken prior to and after testing. Figure 5.37 gives an overview of the test stages for the FSR testing and when the two primary measurements (roughness and traction coefficient) were taken.

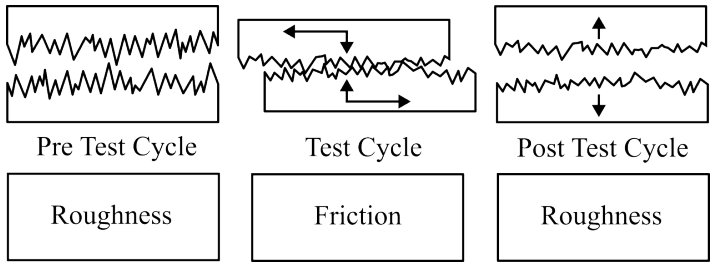

Figure 5.37: FSR test stages and associated measurements

5.4 Data Processing

As roughness, interfacial stiffness and traction coefficient data is acquired through different methods and systems, various ways of processing this data were required. The following section covers the processing methodology for the roughness, interfacial stiffness and traction coefficient data.

5.4.1 Roughness Data Processing

Once replication was completed using the method described in Section 5.1.9. The replicas were observed through an Alicona 3D microscope. This enabled quick areal surface roughness scans to be captured. Three scans of each surface replica were captured in order to take and average, and to enable error analysis to be undertaken. Table 5.14 shows the Alicona Microscope settings used. 5X magnification should generally not be used for roughness measurements, but may be used when considering high roughnesses. A comparison between 5X and 10X showed that 5X magnification roughness measurements were similar to those obtained using a 10X magnification lens when $S_q > 1.5\mu m$. By using 5X magnification, a larger lateral measurement area could be viewed in a single scan that better represented the interface.

Alicona Setting	**Value**
Magnification	$5X$
Working Distance	$34mm$
Vertical Resolution	$460nm$
Horizontal Resolution	$4\mu m$
Lateral Measurement Area	$3.61mm^2$

Table 5.14: Alicona settings

Figure 5.38 show the three scan locations as they would be on the real specimens (these locations are mirrored when scanning the replicas). Scanning at these locations produced three $3.61mm^2$ scans for every replica. These were then processed using the inbuilt Alicona Measurement Suite image processing program.

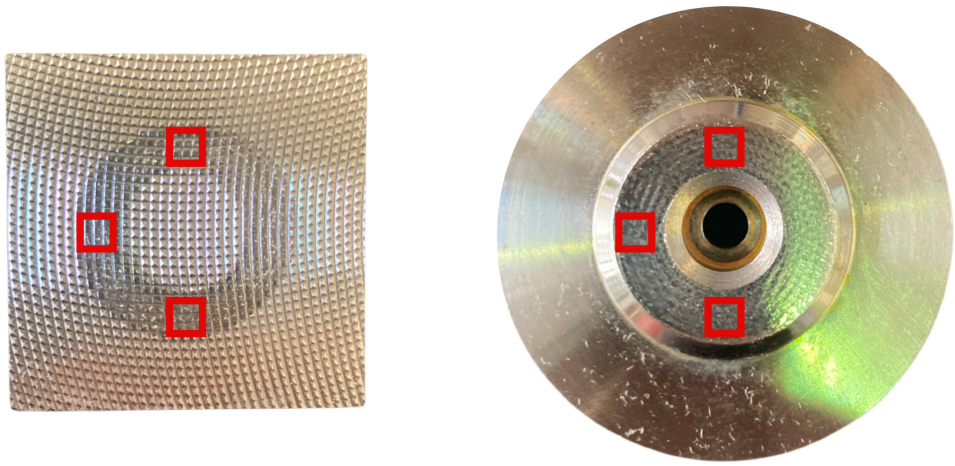

(a) Lower Specimen *(b) Upper Specimen*

Figure 5.38: HPT specimen scanning locations

Surfaces exhibit two kinds of topography: small-scale variations (Roughness) and large-scale variations (Waviness) (see Section 3.2.2). These two characteristics are often studied separately. In order to do this, high and low pass filters are applied to separate small-scale and large-scale surface elements. By applying a cut-off wavelength (λ_c) to surface roughness measurements, low frequency waviness can be filtered out as seen in Figure 5.39. The filter removes large variations in surface height, creating a flat plain from which surface texture protrudes and recesses. This enables uneven replica height, machining periodicity and other imposed large scale height variations to be eliminated from the surface roughness measurement.

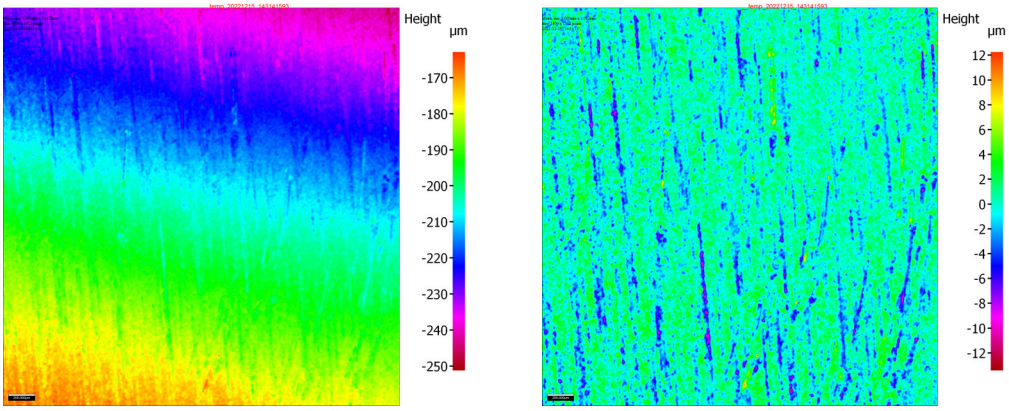

(a) Filter off *(b) Filter on*

Figure 5.39: Separating waviness and roughness with Gaussian filters

ISO standards 4287 and 4288 outline how to correctly measure roughness by applying an appropriate λ_c to the roughness profile. The rougher the surface, the longer the evaluation length (L_n) must be to generate a reliable roughness measurement (see Table 5.15). Note that by increasing L_n, we must also increase λ_c.

Profile	**Cut-off**	**Evaluation Length**
$\boldsymbol{R_a(\mu m)}$	$\boldsymbol{\lambda_c(mm)}$	$\boldsymbol{L_n(mm)}$
up to 0.02	0.08	0.4
0.02 - 1	0.25	1.25
1 - 2	0.8	4
2 - 10	2.5	12.5
10 - 80	8	40

Table 5.15: Cut-off wavelength selection for various surface roughnesses

To study roughness, values for λ_c are initially set to 1/5 of the evaluation length (see table 5.15), provided you can achieve the required L_n value from your sample. This is in accordance with ISO 4288. The process for measuring roughness using an Alicona microscope and ISO 4288 is as follows:

- Scan the specimen.
- Draw a straight line across your specimen of length L_n (choose the maximum value you can obtain from your specimen that is listed in table 5.15).
- This will automatically set λ_c to $L_n/5$.
- If the roughness measurement obtained is in the correct row (e.g $L_n = 4mm$ $\lambda_c = 0.8mm$ and measured $R_a = 1.5\mu m$), this is your roughness value in accordance with ISO 4288.
- If however the roughness value calculated is greater than $2\mu m$, you must increase L_n and λ_c until the roughness value returned is in the same row.
- Increasing L_n can be achieved by taking multiple scans and stitching them together (e.g using three scans stitched together $L_n = 12.5mm$ $\lambda_c = 2.5mm$ and measured $R_a = 8\mu m$), this is your roughness value in accordance with ISO 4288.

- This process should be done in both the x and y directions.
- Once you have found the λ_c value that provides a roughness in the correct roughness range, this λ_c can then be applied to a 3D surface to calculate areal surface roughness S_a and S_q.

It becomes clear, however, that when studying high roughness on small samples, L_n can no longer be achieved. For the roughness ranges seen after reprofiling events of $2 - 10\mu m$, an evaluation length of $12.5mm$ would be required which was simply not possible to achieve on the HPT specimens due to their size and annular shape. For roughness to be measured, it required a deviation from ISO 4288 and a more topographical approach. By looking at the machining processes the specimens underwent, it became clear that to eliminate large scale variations λ_c should be set to the pitch of the rough fly-cut specimens, therefore $\lambda_c = 800\mu m$. This cut-off was also applied to the smooth ground specimens where $S_q \approx 2\mu m$. When using λ_c values that deviate from ISO 4288, they should be quoted on any scans or alongside declared roughness values.

Scan size was cropped from $3.61mm^2$ to $3mm^2$ which was the largest area size that could be reasonably and consistently measured from the contacting annulus. Therefore $L_n = 3mm$ and $\lambda_c = 800\mu m$. It can be seen from Figure 5.39 that this cut-off wavelength produced a good representation of roughness, reducing waviness whilst not destroying surface texture. This measurement area and cut-off wavelength were then applied to every other roughness measurement to ensure a consistent measurement approach was being applied. Upon completion of the surface scans, the roughness values were exported to Matlab and plotted.

5.4.2 Traction Data Processing

Section 5.1.12 outlined the outputs generated from the HPT rig. These include the traction coefficient which encompasses both the normal and tangential pressure into a single dimensionless quantity that represents the interfacial friction. Figure 5.40 shows the formation of the traction coefficient during a HPT test. Axial load is applied through the interface resulting in an axial pressure. The specimens are then rotated relative to one another and the resistance to that rotation manifests as tangential pressure. By using Equation 5.5 in Section 5.1.12, the traction coefficient can be calculated.

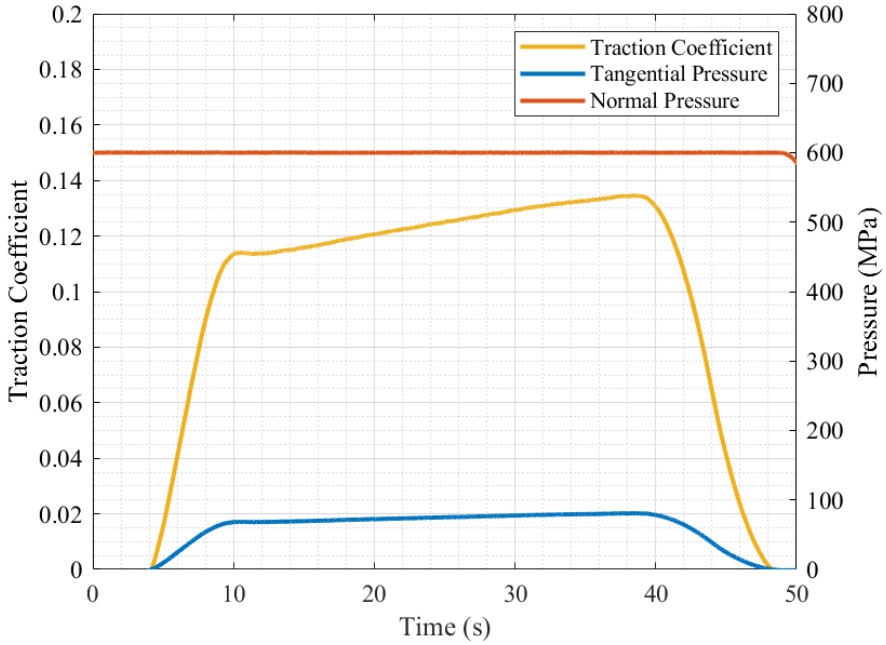

Figure 5.40: Traction coefficient formation

Whilst using the traction coefficient has gone some way to simplifying the many outputs from the HPT, the result is time dependant data for each individual cycle. Figure 5.41 shows this data for multiple cycles.

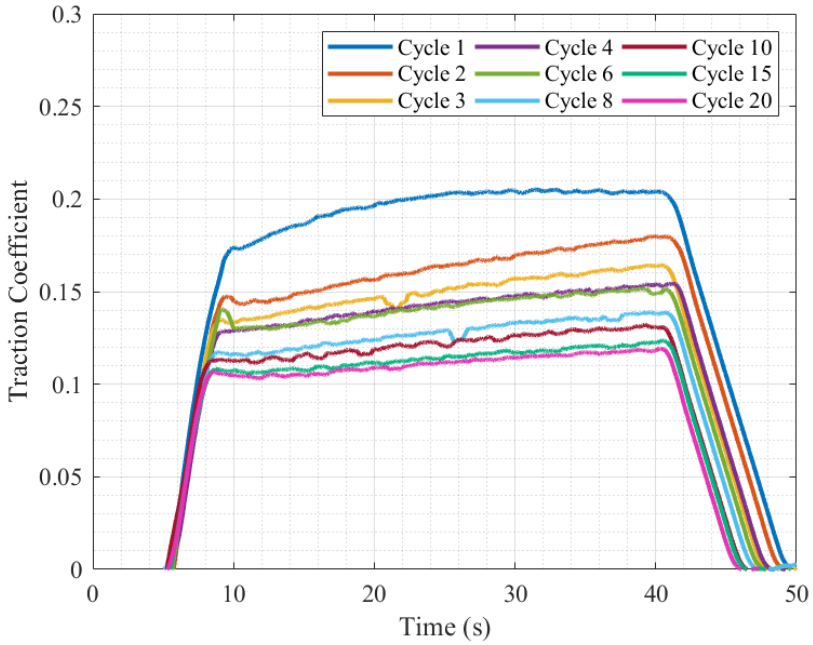

Figure 5.41: Typical traction coefficient data for multiple cycles

It can be difficult to ascertain whether friction is increasing or decreasing per cycle when the data is in this form. In addition, the roughness data is not time dependant but is instead measured on a cycle by cycle basis. In order for the traction coefficient to be compared to roughness, it must be averaged resulting in a single traction coefficient value for each cycle. Averages were taken during the rotation phase of the test cycle whereby the tangential pressure has reached a 'steady state'. Figure 5.42 shows this process whereby an average cyclical traction coefficient is calculated.

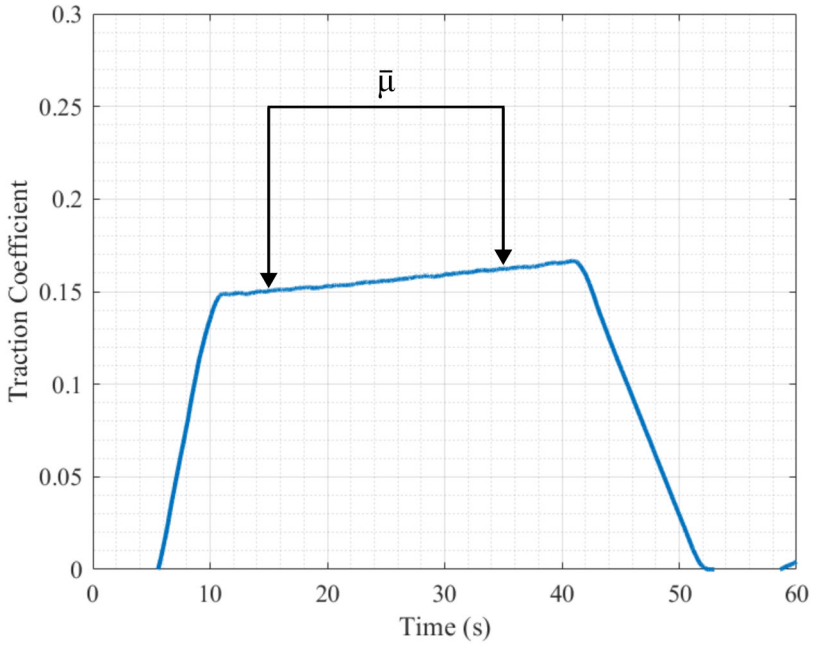

Figure 5.42: Converting time dependant traction coefficient data to cyclical traction coefficient data

Equation 5.6 shows how the average traction coefficient $\bar{\mu}$ was calculated. $\bar{\mu}$ was averaged over a 20 second window. When the specimens slipped, tangential pressure was released resulting in a drop in the traction coefficient. This was most likely to occur as torque was applied and released at the start and end of the rotation phase. A 5 second offset was included either side of this average window whereby the specimens were still rotating relative to one another. This was to mitigate the chances of these slips being included in the average calculations.

$$\bar{\mu} = \sum_{15}^{35} \overline{\mu(t)} \tag{5.6}$$

Figure 5.43 shows the average traction coefficient over a 20 cycle test. In this form, the traction coefficient data can be compared to the roughness data

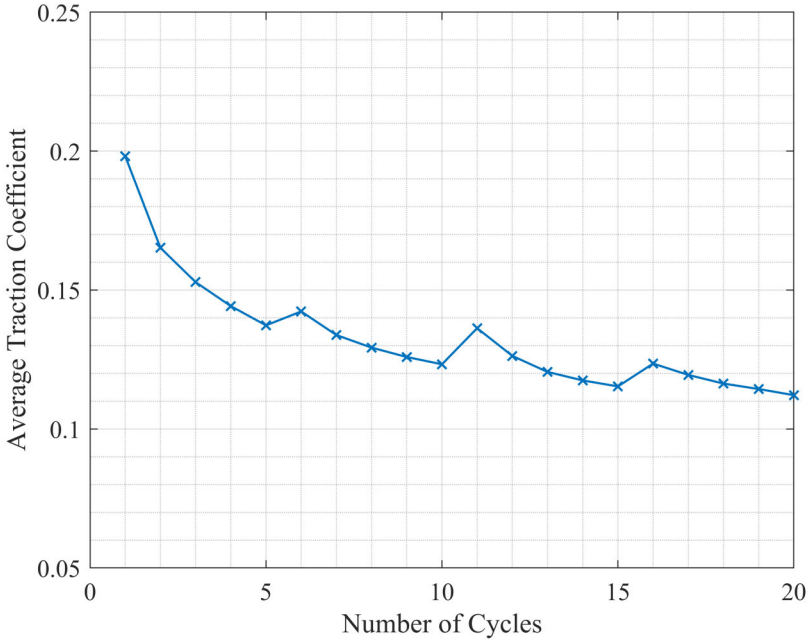

Figure 5.43: Average traction coefficient for cyclical data

5.4.3 Ultrasonic Data Processing

Processing the raw ultrasonic data captured from the ultrasonic sensors required a number of steps. The tdms file produced from the FMS contained high pulse rate voltage amplitude data, meaning the resultant file size was large. This data required processing in order to convert it into interfacial stiffness data. Labview was used to convert the tdms files into csv files. Figure 5.44 shows two A-scans: one without loading (reference A-scan) and the other with loading (Test A-scan). The amplitude difference between the two A-scans indicates how stiff the interface is as less signal is reflected back to the sensor when the materials are under load. The range seen in Figure 5.44 must be the same as the range chosen on the FMS in Section 5.2.2.

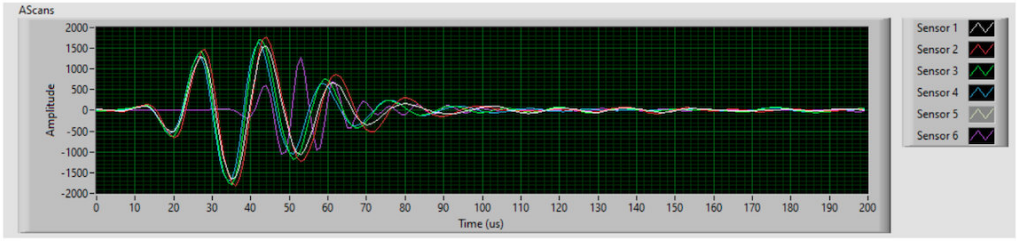

(a) Without loading (reference)

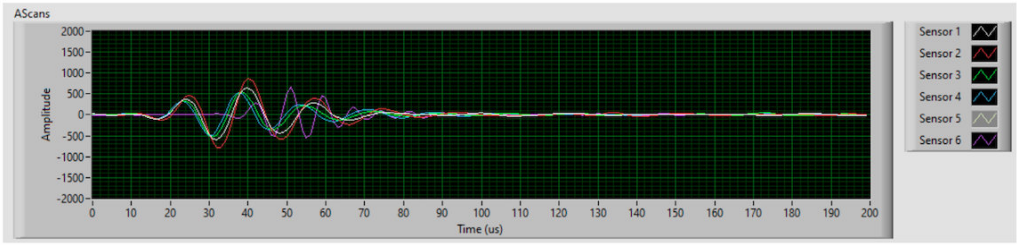

(b) With loading (test)

Figure 5.44: A-scans from HPT testing with and without loading

An evaluation window from the A-scans shown in Figure 5.44 could then be applied (see Figure 5.45). A-scan length determines the length of the evaluation window and A-scan index shifts signals to allow them to be lined up (useful when longitudinal and shear sound speed is different).

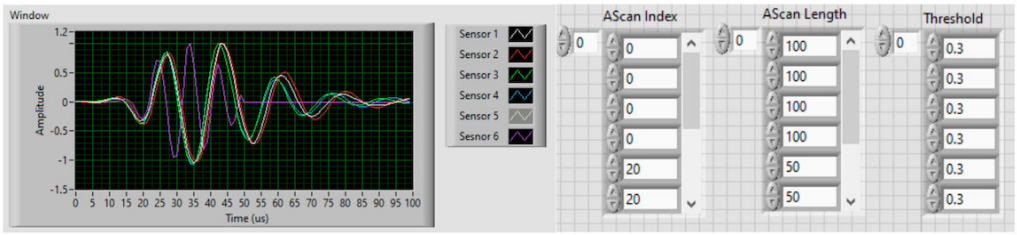

Figure 5.45: Windowed A-scan signals

By applying a Fast Fourier Transform (FFT) to the windowed signal, the reflected pulses can be seen in the frequency domain (see Figure 5.46).

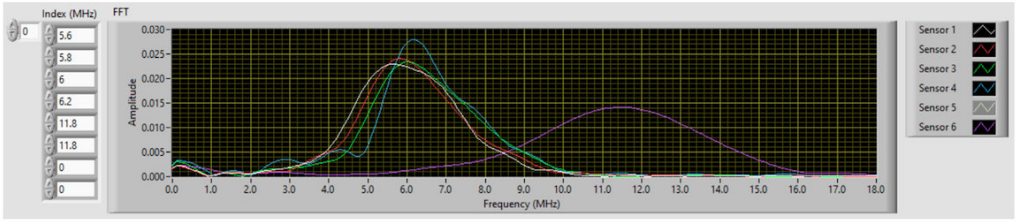

Figure 5.46: Signal amplitude vs frequency for each sensor

Piezo transducers pulse over a bandwidth of frequencies, the peak of which is called the index frequency (f_i). The signals received have their own independent index frequency at which amplitude measurements are taken. The quoted resonant shear and longitudinal sensor frequencies used were 5MHz and 10MHz respectively. The FFT showed that these were reasonably accurate with shear and longitudinal sensors acting most effectively at around 6MHz and 12MHz respectively. By bonding the sensors to a mass, you alter the frequency response. The individual signal index frequencies are quoted in Table 5.16 and are used in the interfacial stiffness calculations (see Equation 5.12).

Sensor (n)	$\boldsymbol{f_i}$ **(MHz)**
1	5.60
2	5.80
3	6.00
4	6.20
5	11.8
6	11.8

Table 5.16: Index frequencies

As the surfaces are loaded against one another, the amplitude of these peaks decreases. This produces an amplitude plot as seen in Figure 5.47. Time was measured in ms meaning this particular cycle took 80 seconds to complete.

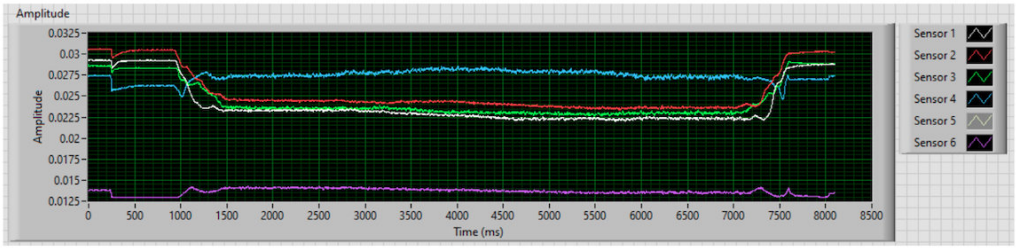

Figure 5.47: Signal amplitude vs time for each sensor

This amplitude data was then exported as a csv file which could then be imported onto Matlab and converted into interfacial stiffness. The amplitude data is a matrix defined as **H**. It has m rows and and n columns. Any data point within this matrix can be defined as $H(m,n)$. Since there are six sensors, $n = 6$ so **H** is a $(mx6)$ matrix (see Equation 5.7). m is the number of data points per sensor and varies from test to test. As each sensor pulses 1000 times per second and a test ranged from around 60 to 100 seconds, m can be as high as 1×10^5.

$$\mathbf{H} = \begin{bmatrix} h_{11} & h_{12} & ... & h_{16} \\ h_{21} & h_{22} & ... & h_{26} \\ ... & ... & ... & ... \\ h_{m1} & h_{m2} & ... & h_{m6} \end{bmatrix} \tag{5.7}$$

A reference amplitude measurement was taken for each sensor at the start of each test and these were compared to check for any drift. This was the average amplitude value over the first 100 measurements when the surfaces were unloaded. This produced a (1x6) reference amplitude vector and is defined as $\mathbf{H_0}$. Any data point within this vector is defined as $H_0(n)$.

$$\mathbf{H_0} = \begin{bmatrix} \bar{h}_1 & \bar{h}_2 & ... & \bar{h}_6 \end{bmatrix} \tag{5.8}$$

Equation 5.9 shows how the test amplitude matrix **H** was normalised by the reference amplitude data $\mathbf{H_0}$. This is based on Equation 4.8 in Section 4.4.

$$R(m,n) = \begin{cases} \frac{H(m,n)}{H_0(n)}, & \text{if } \frac{H(m,n)}{H_0(n)} < R_{MAX} \\ R_{MAX}, & \text{otherwise} \end{cases} \tag{5.9}$$

This gives the reflection coefficient data matrix **R** (see Equation 5.10).

$$\mathbf{R} = \begin{bmatrix} r_{11} & r_{12} & ... & r_{16} \\ r_{21} & r_{22} & ... & r_{26} \\ ... & ... & ... & ... \\ r_{m1} & r_{m2} & ... & r_{m6} \end{bmatrix} \tag{5.10}$$

Any data point within this matrix is defined as $R(m, n)$ and is outlined by Equation 5.9 where R_{MAX} is the highest reflection coefficient that can used to obtain reliable interfacial stiffness values (see Section 4.4.1). If the value of the normalised reflection coefficient exceeded 0.95, the reflection coefficient was said to be 0.95 and the stiffness was deemed to be unreliable. Upon calculation of the reflection coefficient matrix $\mathbf{R}$, the interfacial stiffness matrix $\mathbf{K}$ could be obtained and is defined in Equation 5.11:

$$\mathbf{K} = \begin{bmatrix} k_{11} & k_{12} & ... & k_{16} \\ k_{21} & k_{22} & ... & k_{26} \\ ... & ... & ... & ... \\ k_{m1} & k_{m2} & ... & k_{m6} \end{bmatrix} \tag{5.11}$$

Any data point within the matrix $\mathbf{K}$ is defined as $K(m, n)$ and is outlined by Equation 5.12. This is Equation 4.15 in Section 4.4 which has been adapted to convert large data matrices.

$$K(m, n) = z(w)\pi f_i(n)\sqrt{\frac{1}{R(m, n)^2} - 1} \tag{5.12}$$

Here $f_i(n)$ is the index frequency for each sensor shown in Table 5.16 and $z(w)$ is the acoustic impedance of steel. w relates to the wave type (see Table 5.17).

Wave Type (w)	**Acoustic Impedance z (MRayl)**
Longitudinal	46
Shear	24.8

Table 5.17: Longitudinal and shear acoustic impedance in steel

Interfacial stiffness can be either longitudinal or shear interfacial stiffness. K_L has a direction that is normal to the interface. K_S can be measured in any direction across the interface. When using a cylindrical coordinate system, K_S is made up of the circumferential interfacial stiffness (K_C) and the radial interfacial stiffness (K_R). Figure 5.48 shows the direction each interfacial stiffness component acts in. Whilst interfacial stiffness is directional due to the type of transducer used and its orientation, it is always quoted as a positive value. This is due to the oscillating nature of both longitudinal and shear waves. Interfacial stiffness acts both in the directions shown in Figure 5.48 and the reverse.

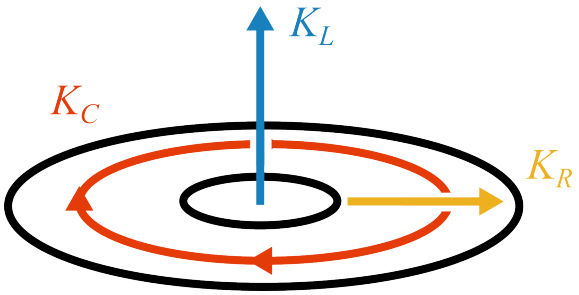

Figure 5.48: Interfacial stiffness components

These three interfacial stiffness components were measured using ultrasonic transducers throughout each test cycle (see Figure 5.49). Transducers were pulsed 1000 times per second to achieve high resolution interfacial stiffness measurements.

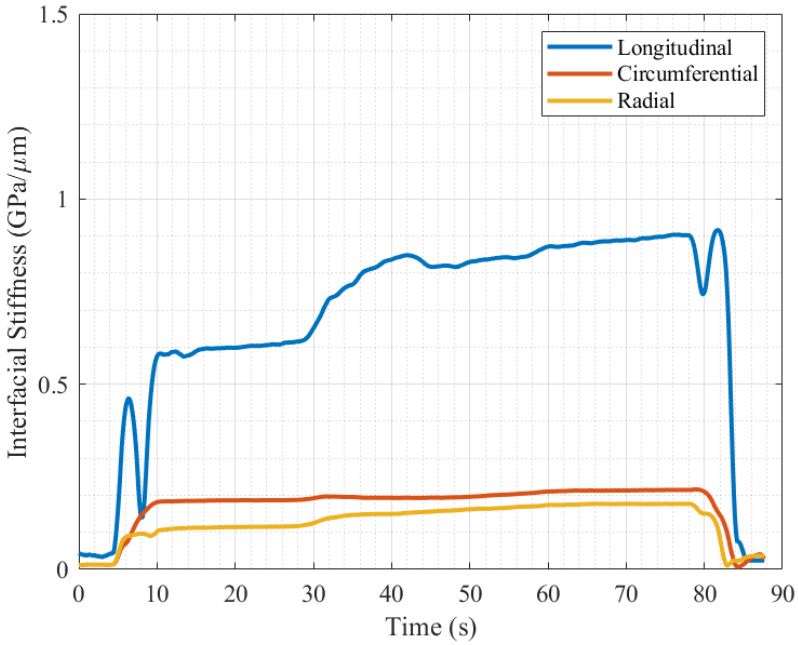

Figure 5.49: Longitudinal, circumferential and radial interfacial stiffnesses vs time

Figure 5.50 shows K_L for various cycles. Whilst interfacial stiffness is evaluated in the time domain, it can be difficult to visualise how interfacial stiffness changes cyclically when the data is in this form.

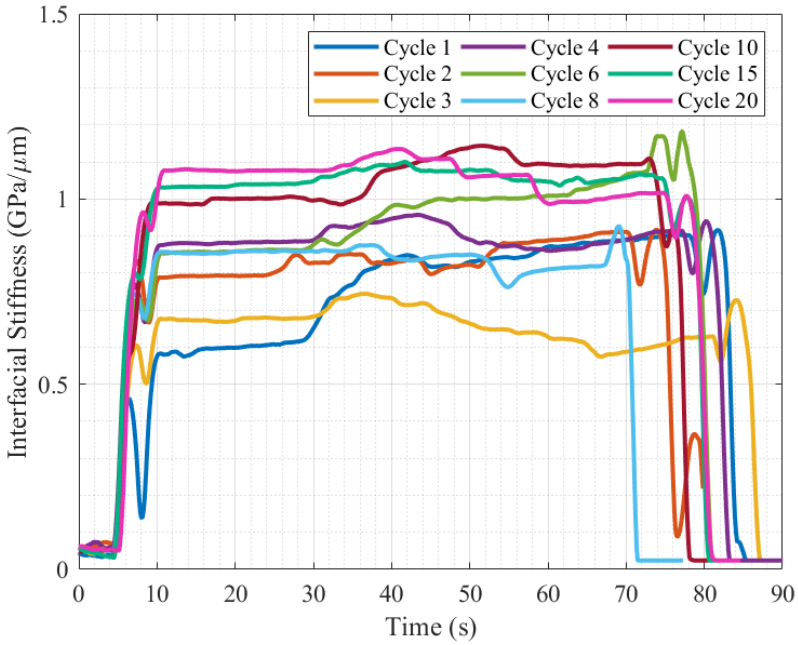

Figure 5.50: Typical temporal longitudinal interfacial stiffness data for numerous cycles

To compare this temporal data to the roughness data, an average must be taken for each cycle. Figure 5.51 shows this process conducted for longitudinal interfacial stiffness for a typical cycle.

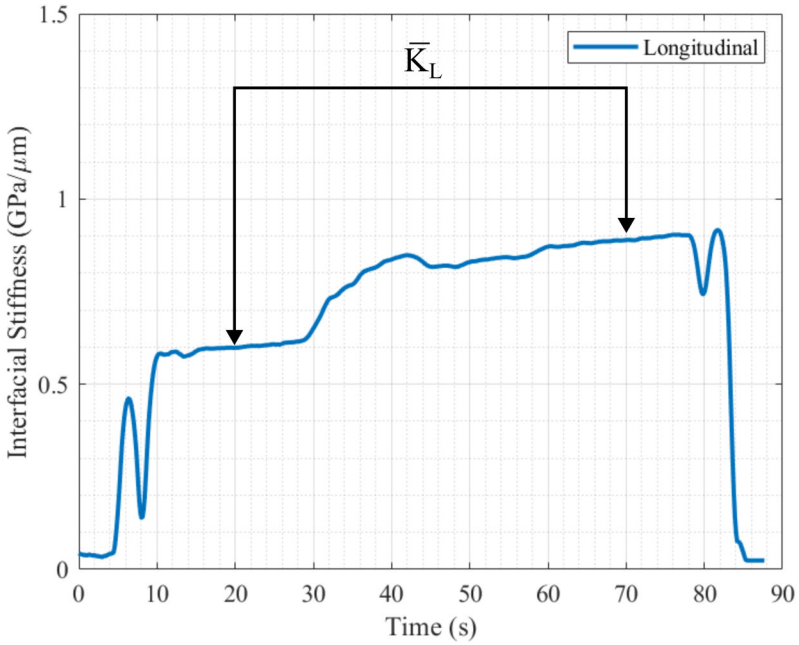

Figure 5.51: Obtaining average interfacial stiffness values from temporal interfacial stiffness data

The average interfacial stiffness ($\bar{K}$) is calculated for all three interfacial stiffnesses: $\bar{K_L}$, $\bar{K_C}$ and $\bar{K_R}$ are defined as the average longitudinal, circumferential and radial interfacial stiffness respectively. These values are described by Equations 5.13 to 5.15:

$$\bar{K_L} = \sum_{20}^{70} \overline{K_L(t)} \quad (5.13) \qquad \bar{K_C} = \sum_{20}^{70} \overline{K_C(t)} \quad (5.14) \qquad \bar{K_R} = \sum_{20}^{70} \overline{K_R(t)} \quad (5.15)$$

Upon calculation of these averages they can be presented cyclically. Figure 5.52 shows the average longitudinal interfacial stiffness $\bar{K_L}$ over a 20 cycle test. In this form ultrasonic data can be compared to both roughness and traction coefficient data.

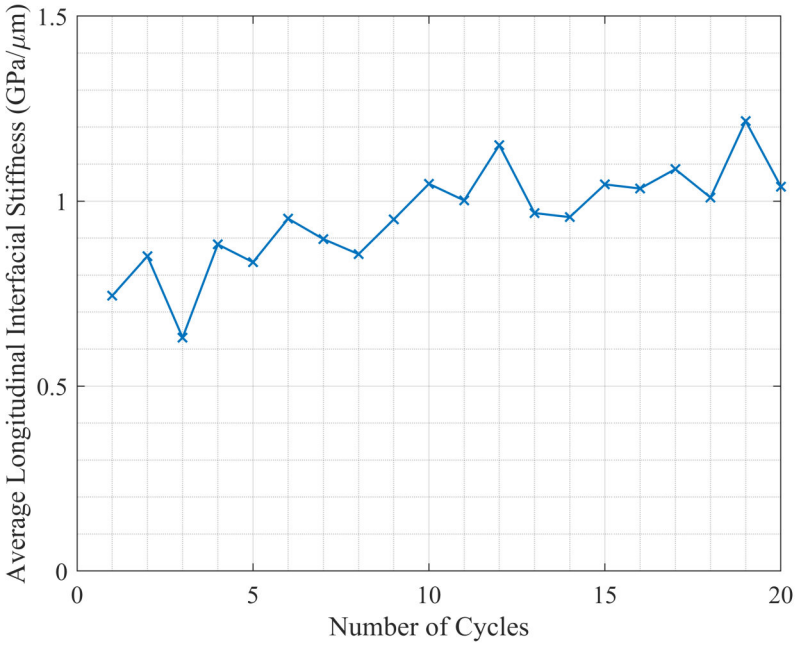

Figure 5.52: Average interfacial stiffness for cyclical data

5.5 Summary

In this chapter, both the HPT and FSR test methodologies have been discussed. The instrumentation of HPT specimens with ultrasonic sensors was also covered. Six instrumented specimens were manufactured, each with six ultrasonic sensors: 2X longitudinal, 2X circumferential shear and 2X radial shear. The sensor frequency was selected to be 10MHz for the longitudinal sensors and 5MHz for the shear sensors: this was to aid the bonding process. The sensor size was selected to be around $2mm^2$ so as to only measure the contact and to reduce near-field effects. Sensors were bonded with M-Bond 610, connected with coaxial cable and potted to ensure they were robust enough to be used multiple times without breaking. The test procedures have been explained, as has the way in which the roughness, traction and ultrasonic data was captured. Following this the data processing methodology was discussed so as to allow these different parameters to be compared cyclically.

6 Results and Discussion

The following chapter covers the results for both the HPT and FSR testing. Throughout testing, the primary factors of concern were roughness, traction coefficient and interfacial stiffness. The aim of these tests was to improve our understanding of how these measured properties influence one another over repeated cycles. This was initially done with the HPT rig for dry and wet contacts and was then scaled up and carried out on the FSR.

6.1 HPT Results

Small-scale testing offers a relatively low cost way of conducting an extensive test campaign and evaluating how a system might behave before you construct or use a full-scale system. The benefits of using the HPT rig were geometrical simplifications, ease of specimen manufacture and cost reductions. Whilst small-scale testing has many benefits, it is not the full-scale system and so requires an additional step to predict what will happen on the full-scale system. This can be a simple scaling factor that is applied to the results, or if the small-scale system is very different from the full-scale system, the small-scale outputs can be used to parameterise a model (see Section 7.2). The model then needs to be validated by comparing the model results to those found from the full-scale testing. Small-scale testing does not replace full-scale testing, but instead acts as a stepping stone to help focus efforts when testing on the full-scale system. For the HPT rig testing, three outputs were considered: surface roughness, traction coefficient and interfacial stiffness. These results are presented and discussed in the following sections.

The hardness of the HPT specimens was measured with a Rockwell hardness tester and then converted to Brinell hardness. The hardness for both the upper and lower specimens for the dry 600MPa test can be seen in Figure 6.1. This was measured at the start and end of the HPT test.

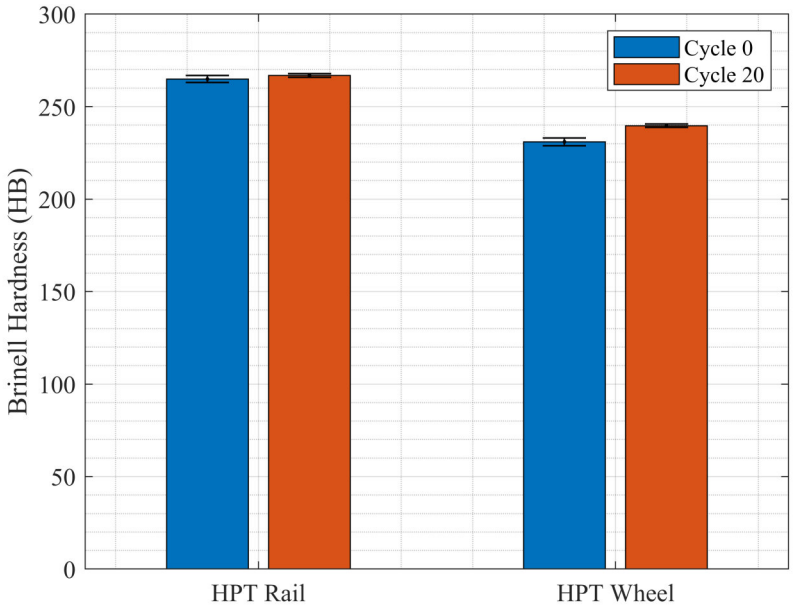

Figure 6.1: Brinell hardness preogresson over the course of a HPT test (Test: Dry 600MPa LIR)

Whilst these increases both to the upper wheel and lower rail specimen were only minor, only 20 cycles were performed. With the addition of further cycles, it is expected that the hardness would increase [37]. The hardness of a specimen increases wear rates which is linked to the traction coefficient (see Section 3.3.6). In addition, elevated hardness of two contacting surfaces causes surfaces to interact differently and ultimately affects the way roughness evolves. Hardness is referred to often in the following results section. No hardness data was obtained for the FSR tests as the wheel was too large and the rail specimens were curved so it was difficult to get a consistent measurement. It was impossible to measure the hardness of the rough specimens due to their topography.

6.1.1 Roughness

Two initial roughnesses were studied: high initial roughness (HIR) and low initial roughness (LIR) which relate to the relative roughness' of the lower specimens. Three pressures were tested: 600, 750 and 900MPa. The 600MPa and 900MPa tests are shown in the following sections and the 750MPa results can be found in the appendices. Figure 6.2 shows the separate roughness evolutions for lower (rough)

and upper (smooth) HPT specimens for the dry HIR tests.

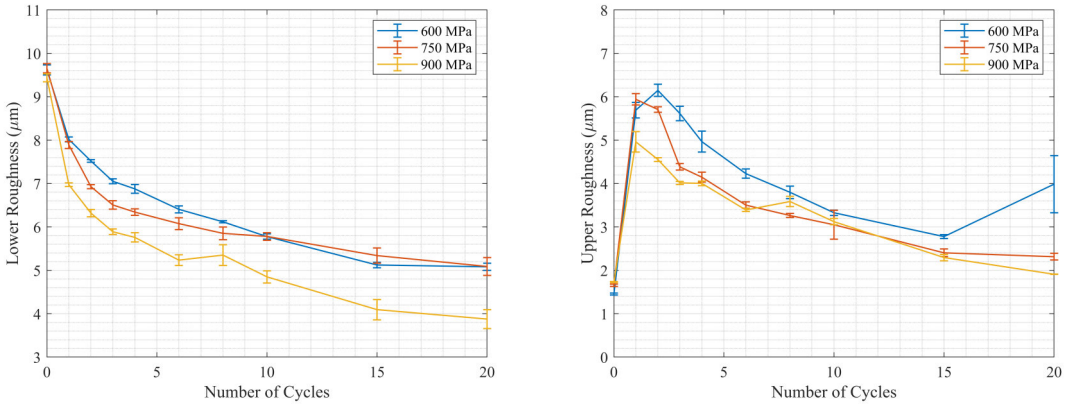

(a) Lower areal roughness (S_{q1}) *(b) (Upper areal roughness (S_{q2})*

Figure 6.2: Upper and lower specimen roughness evolution (Test: HIR - Dry)

The two separate roughness' were combined using Equation 3.7 to produce the combined roughness ($S_{q\sigma}$) shown in Figure 6.3. Initial roughness' were applied using fly cutting (rough) and grinding (smooth) procedures. Aside from the small amounts of work hardening that these processes induce, no prior run-in was performed on the specimens as this would alter the initial roughness.

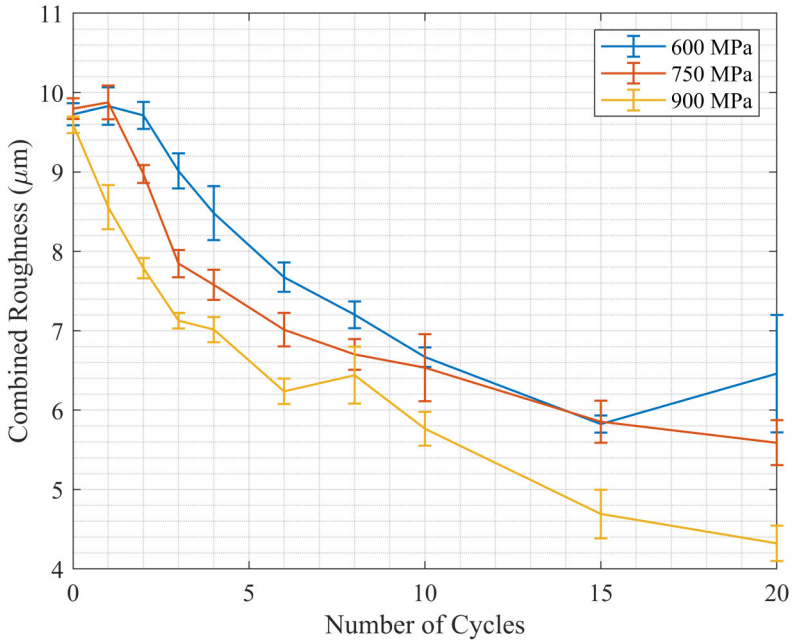

Figure 6.3: Combined roughness ($S_{q\sigma}$) evolution (Test: HIR - Dry)

The upper smoother ground surface was penetrated by the lower rougher fly cut surface which resulted in roughness transfer from the lower to the upper specimens which collectively decreased with increased cycles. This process is shown schematically in Figure 6.4.

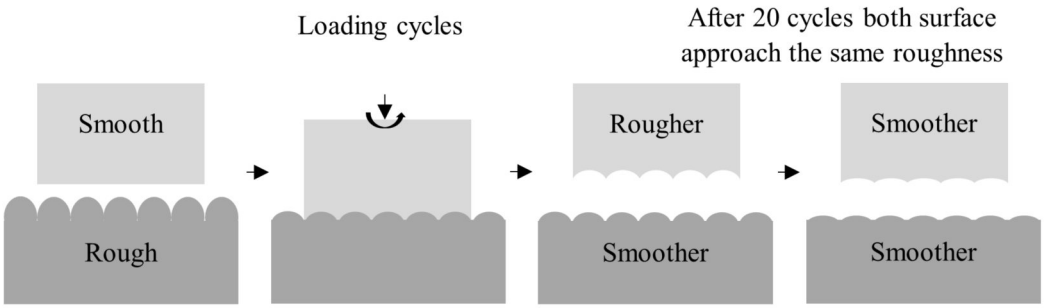

Figure 6.4: Upper and lower specimen roughness evolution schematic (Test: HIR - Dry)

The rate at which the roughness changes is altered due to the work hardening and conformation of the two materials as they are pressed together and rotated against one another. Whilst only 20 cycles were performed in these tests, similar work by Lewis et al. using a twin disc machine has shown roughness progressions of around $9-10\mu m$ to $1-2\mu m$, although this was performed for many more cycles [85]. The field measurements produced by Lundmark et al. also show this level of roughness evolution following reprofiling events in the real world [9]. Given a sufficient number of cycles, the roughness of the two opposing surfaces in Figure 6.2 are expected to reach a common roughness similar to those found in these two studies.

HIR tests began at a combined roughness of around $9-10\mu m$. The combined roughness decreases for dry, water, grease, and leaf tests as shown in Figure 6.5. Greater pressures result in larger roughness reductions. This is in agreement with previous HPT HIR tests carried out without 3BLs present [86].

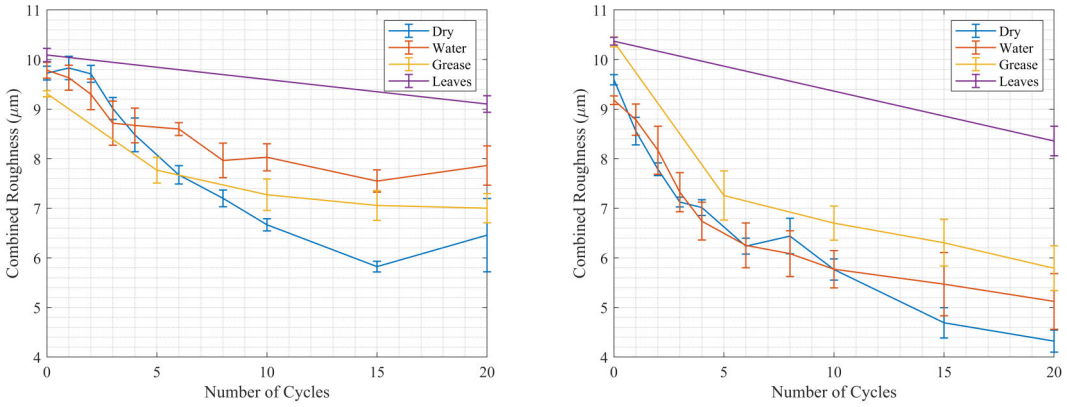

(a) 600MPa *(b) 900MPa*

Figure 6.5: Combined roughness ($S_{q\sigma}$) evolution (Tests: HIR)

Both grease and leaves provided a protective barrier that resulted in lower roughness reductions during the HIR tests; this process is shown schematically in Figure 6.6. Leaves were particularly effective at this as demonstrated by the higher resultant roughnesses in Figure 6.5.

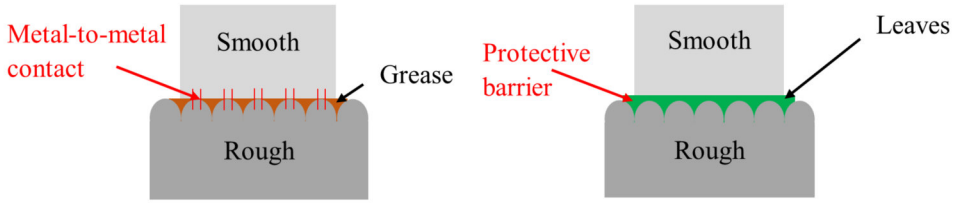

Figure 6.6: 3BL protective layer schematic (Tests: HIR)

The specimens were reused by grinding back the worn surfaces and applying a new surface roughness before each new test. No manufacturing process is perfect and slight variations in surface texture were introduced due to the manufacturing uncertainties. The operator, feed rate, depth of cut and the sharpness of the tool all alter the finished surface. Pairing this with variation in the measurement process meant that the initial roughness varied from specimen to specimen by up to $1\mu m$.

Figure 6.7 shows the lower HIR specimens after 20 cycles. The presence of leaves protected the surface from wear damage resulting in only small roughness reductions. As the roughness was only measured at the start and end of the test, the roughness progression for leaves looks linear, however this is unlikely to be the case. Dry, water and grease specimens were visually similar after 20 cycles with small amounts

of wear being incurred on the dry specimen. However, the water and grease did provide some protection as indicated in their lower roughness reduction. It is perhaps surprising that the grease did not offer more protection; it is possible that the roughness may have provided a space for grease to accumulate so not all of it is in the interface, allowing some metal-to-metal contact as shown in the mechanism schematic in Figure 6.6.

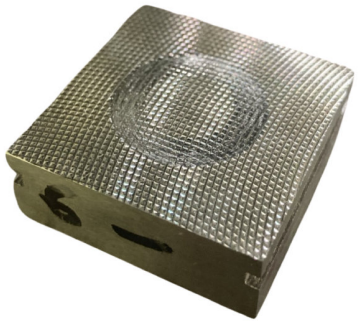

(a) Dry - HIR - 900MPa - 20 cycles

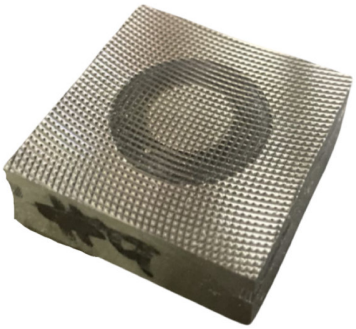

(b) Water - HIR - 900MPa - 20 cycles

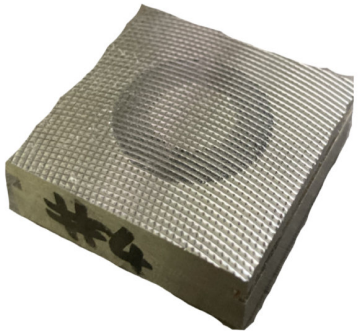

(c) Grease - HIR - 900MPa - 20 cycles

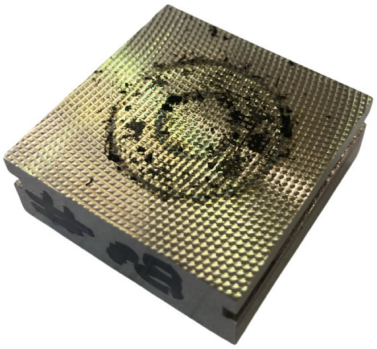

(d) Leaves - HIR - 900MPa - 20 cycles

Figure 6.7: Lower specimen surfaces after undergoing 20 test cycles at 900MPa

Low initial roughness tests began at a combined roughness of around $2 - 3\mu m$ (see Figure 6.8). During dry tests, adhesive wear occurred which led to the increased combined roughness seen. Wear debris was created which potentially acted as a solid lubricant increasing the likelihood of larger slip events. The production of this debris promoted third-body abrasive wear which further increases surface wear (see Figure 6.9). Debris was removed during intercycle cleaning and replication, thereby reducing this effect. Water tests were susceptible to large slip events as the amounts of water were not sufficient to fully lubricate the surfaces, but were sufficient to permit oxide build up (see Figure 6.10). Small amounts of water alongside iron oxides are known to form a paste that lowers adhesion [87]. Surfaces are initially

protected by the oxides, but are then cleared during slip and intercycle cleaning. When the interfacial shear stress exceeds the shear strength of these oxides, slip occurs as the oxides break away. The nature of this stress build up and subsequent release may have increased the likelihood of these larger more damaging slip events [56]. Grease and leaves effectively lubricated the interface resulting in very little roughness change over the entirety of the tests. The presence of grease resulted in a mild, controlled wear process that reduced system roughness slightly by polishing the surfaces. Roughness for most tests was assumed to be constant around the annular contact. However, for tests that incurred such large amounts of random localised wear, this assumption was no longer reasonable.

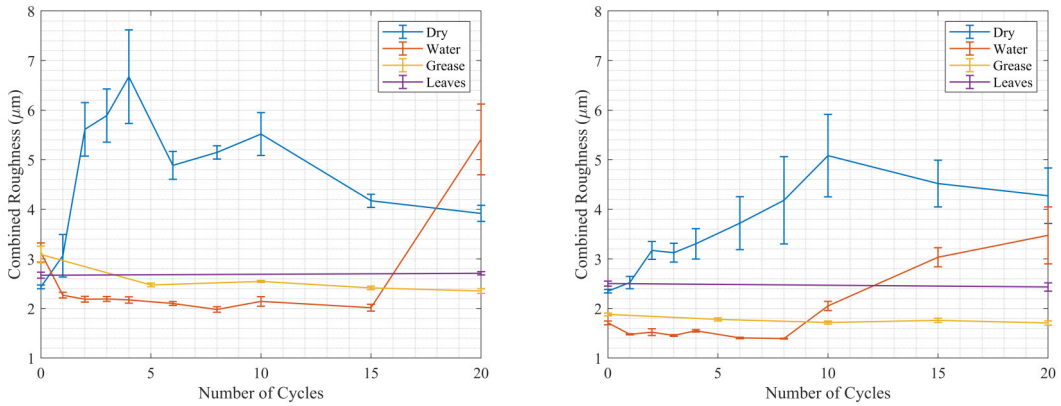

(a) 600MPa *(b) 900MPa*

Figure 6.8: Combined roughness ($S_{q\sigma}$) evolution (Tests: LIR)

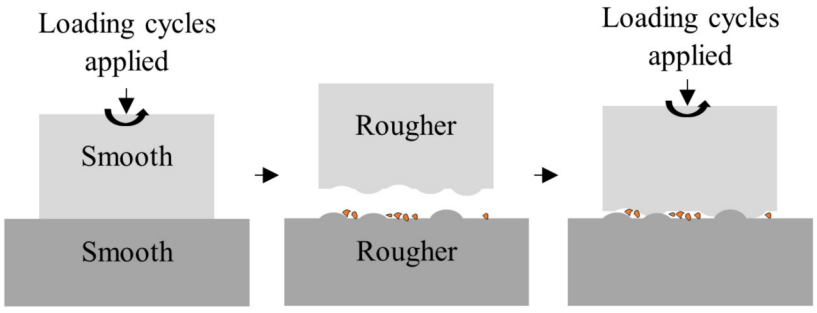

Figure 6.9: Wear debris production acts to increase roughness (Tests: LIR)

Figure 6.10 shows an Alicona scan of a replica indicating the presence of oxides as well as evidence of adhesive and abrasive wear. These oxides and debris were detached from the metal surface when the replica was removed. The formation of an

oxide paste may have lowered adhesion and caused portions of the interface to break free. This debris was then introduced into the interface, causing additional third-body wear. During cleaning between cycles, these particles were mostly removed. This was essential to measure the surface roughness, but it is expected that the wear would have been greater if these debris particles were left in place.

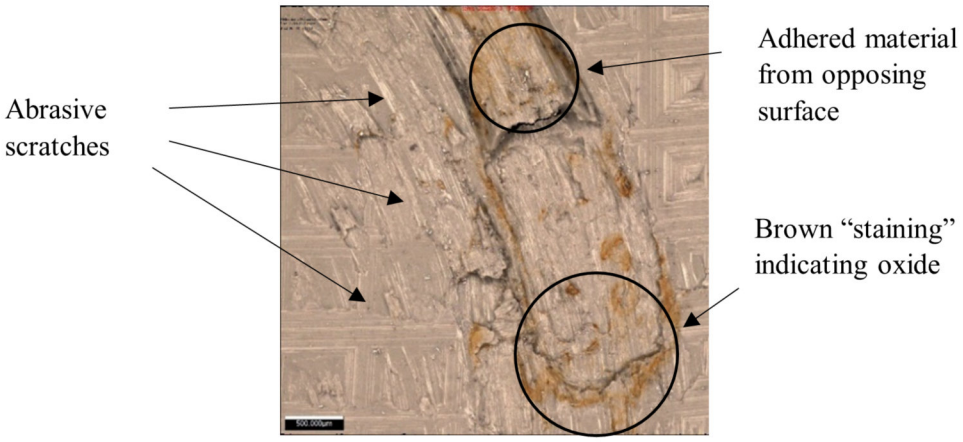

Figure 6.10: Wear induced by oxide layers on water tests

6.1.2 Friction

Friction is quantified by the traction coefficient: the ratio of tangential to normal load (see Equation 5.5). During running-in, the surface topography changes which in turn changes the way the two surfaces interact. This indicates that during the run-in phase, a system's friction is dependent on the surface roughness [88]. To compare the traction coefficients of different tests, an average of the traction coefficient was used. This average was taken during the middle 20 seconds of the rotation phase of the test cycle.

Figure 6.11 shows the traction coefficient evolution for the HIR tests. Contact pressure had negligible effect on traction coefficients, although surface roughness reduced faster when the surfaces were under higher contact pressures as shown in Figure 6.3. The greater the contact pressure, the faster the surfaces were run-in. Friction force is made up of two components: the adhesion force and the ploughing force. The adhesion force depends on the real area of the contact made by the interacting asperities, whereas the ploughing force depends on the hardness of the two interacting materials: specifically the force required to force the harder materials asperities into the softer material. For run-in surfaces, friction is dominated by

the adhesion component. However, during running-in, the ploughing component is relevant which depends on the surface roughness.

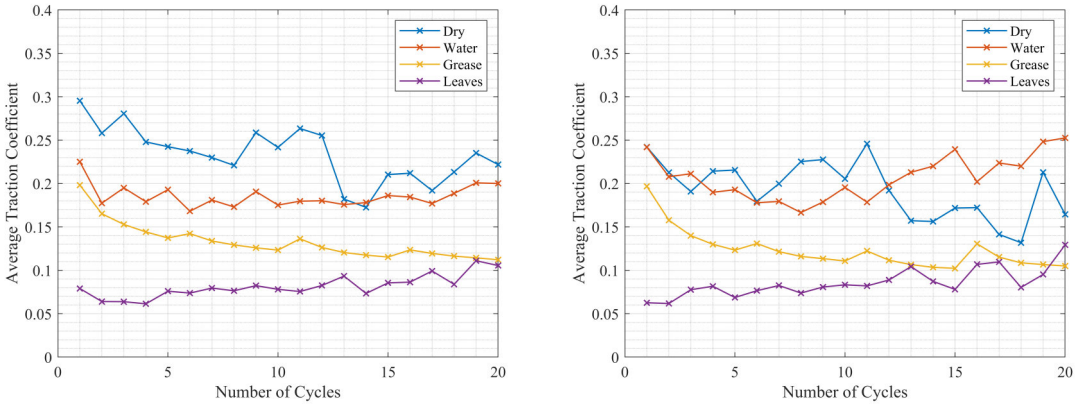

(a) 600MPa *(b) 900MPa*

Figure 6.11: Traction coefficient evolution (Tests: HIR)

As shown in Figure 6.11, leaves produced extremely low traction coefficients ($\mu < 0.1$) This is in line with previous HPT tests with leaves and leaf layers [82]. Friction rose with increased cycles as the leaf layer was degraded and more metal-to-metal contact occurred. The presence of water lubricated the interface, thereby slightly lowering the traction coefficient from dry conditions. The amount of lubricant, its viscosity and the load all alter the lubrication regime at the interface. Lower viscosity fluids such as water are more easily squeezed out than higher viscosity fluids such as oil or semi-solids such as grease [85].

Small amounts of water present on a high roughness surface results in a boundary lubrication regime whereby asperities still interact with one another due to the insufficient lubricant film layer. Higher loads may act to reduce the amount of lubricant further by physically squeezing the water from the interface. Higher loads may have also increased the levels of wear at the interface and this could have caused the friction increase at higher cycles (see Figure 6.11). Grease lubricated the interface well, thereby lowering the traction coefficient considerably and provided a smooth run-in for rough surfaces. As the surfaces became smoother during grease tests, the likelihood of full separation increased contributing to the friction reduction (see Figure 6.12). These results are in agreement with the twin-disc tests conducted by Lewis et al. whereby grease was less effective at higher roughnesses [89]. Small amounts of wear were incurred on both the dry and water tests.

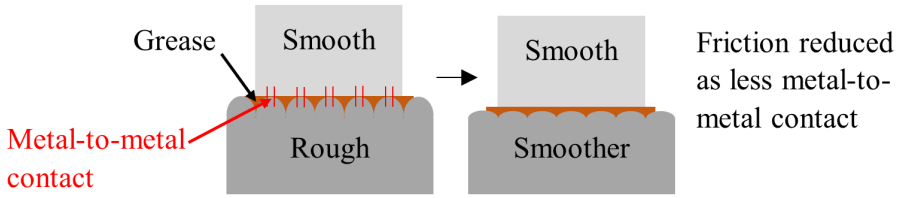

Figure 6.12: A schematic showing the effects of grease on running-in (Test: HIR - Grease)

Leaves also lubricated the interface well, thereby lowering the traction coefficient considerably. The leaves protected the rough surface as shown by the higher resultant roughnesses in Figure 6.5, meaning the surface roughness remained relatively constant during the 20 cycles. Over this time leaves were removed from the interfaces exposing some of the metal which may have contributed to the increase in friction shown in Figure 6.11. This is demonstrated schematically in Figure 6.13.

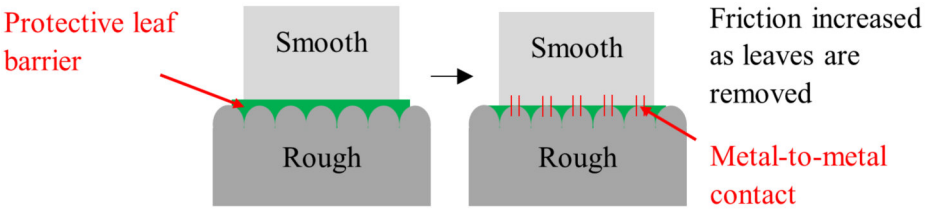

Figure 6.13: A schematic showing the effects of leaves on running-in (Test: HIR - Leaves)

Figure 6.14 shows the traction coefficient evolution for the LIR tests. The traction coefficients for the LIR tests are generally lower than for the HIR tests, however this is not always the case. It is expected that for these tests the ploughing force was lower than during the HIR tests. However, despite these tests having a LIR they are not run-in. They have instead undergone a grinding process to achieve a specific initial roughness that is repeatable. Their initial roughness does, however, represent close to run-in roughness for wheels and rails. As the cycles increase and the surfaces hardness increases, friction resorts to being adhesion force led and stabilises at the interface's natural tractive state. This can then be altered by the introduction of additional 3BLs or due to drastic topographical changes such as when surfaces incur wear. Wear was incurred on both the dry and water tests, however visually the

water tests incurred more, which may have resulted in the higher traction coefficients measured at later cycles. Grease and leaves lubricated the interface well throughout the test which reduced metal-to-metal contact, thereby reducing wear. Resultant friction values were similar to the high initial roughness resultant friction values.

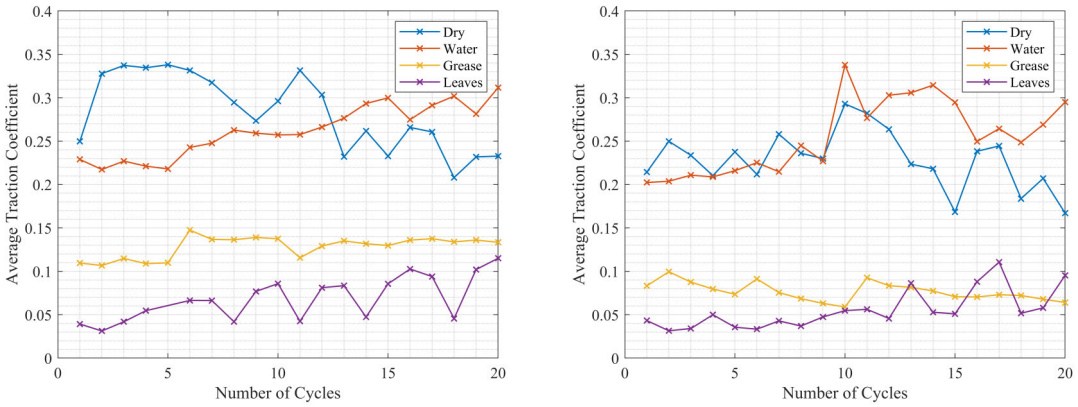

(a) 600MPa *(b) 900MPa*

Figure 6.14: Traction coefficient evolution (Tests: LIR)

6.1.3 Friction vs Roughness

To study the influence surface roughness has on the traction coefficient, replica surface roughnesses measurements were taken and compared to the average traction coefficients at various cycles. This has been performed for both HIR and LIR tests and for all 3BLs.

6.1.3.1 Dry

The traction coefficient appears to be proportional to the combined roughness during run-in for HIR dry contacts (see Figure 6.15). As there was no lubrication, some wear was observed during tests due to metal-to-metal contact which may have contributed to the erratic traction coefficient progression most notably at higher pressures.

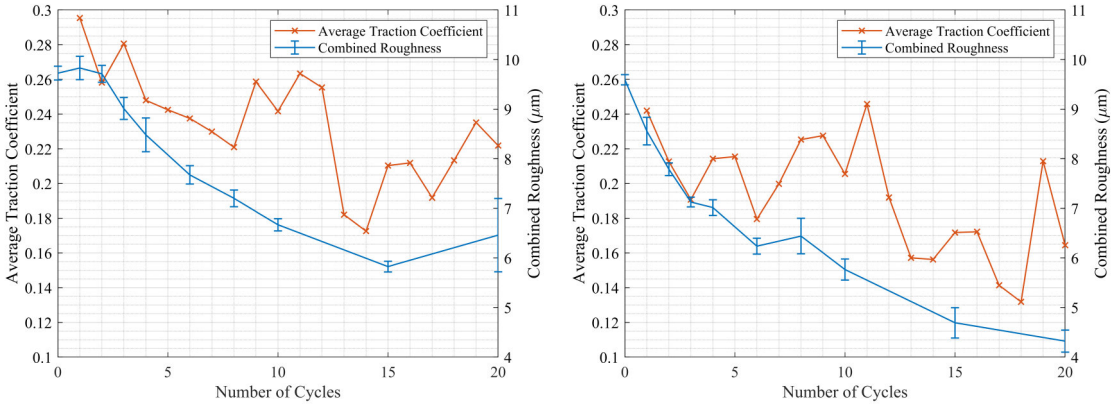

(a) 600MPa *(b) 900MPa*

Figure 6.15: Average traction coefficient vs combined roughness (Tests: HIR - Dry)

At first glance the relationship between surface roughness and traction coefficient for the dry LIR tests appears to be good (see Figure 6.16), however large errors in the roughness measurements due to highly localised wear mean that these results are not particularly reliable. Further statistical analysis show that these two parameters are not well correlated across all contact pressures (see Figure 6.47).

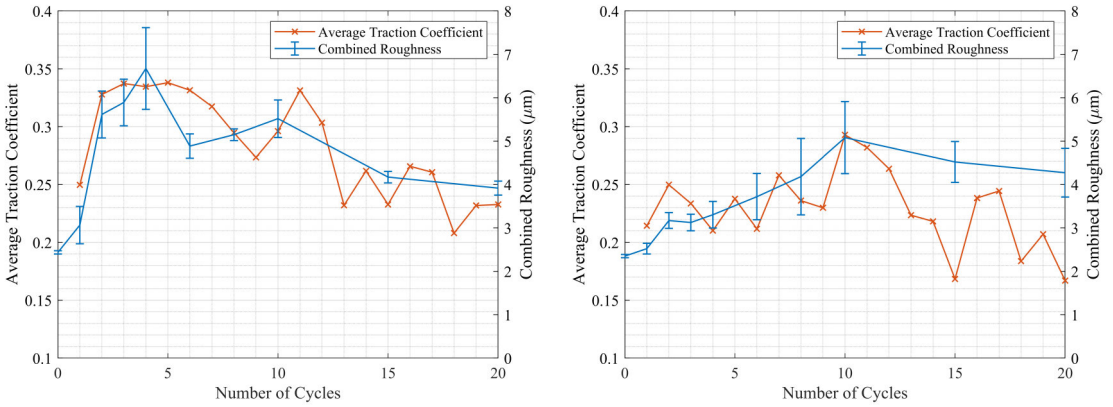

(a) 600MPa *(b) 900MPa*

Figure 6.16: Average traction coefficient vs combined roughness (Tests: LIR - Dry)

6.1.3.2 Water

The traction coefficient may be proportional to the combined roughness during run-in for HIR water contacts. However, due to wear, the roughness measurements were not representative of the full contact (see Figure 6.17). Measured roughness continues to drop for the 900MPa test, yet the traction coefficient increases. This could

be due to the global roughness increasing due to the wear that was incurred that is not represented in the measured roughness (see Figure 6.18). Wear mechanisms have been shown to be closely linked to friction and slip [44]. As the roughness reduced, the real contact area may have increased as asperities were 'wiped away' or plastically deformed. This could have resulted in a more adhesion focused wear mechanism. Additionally, as wear occurs, the production of wear debris increases the rate of wear which could act to raise the traction coefficient.

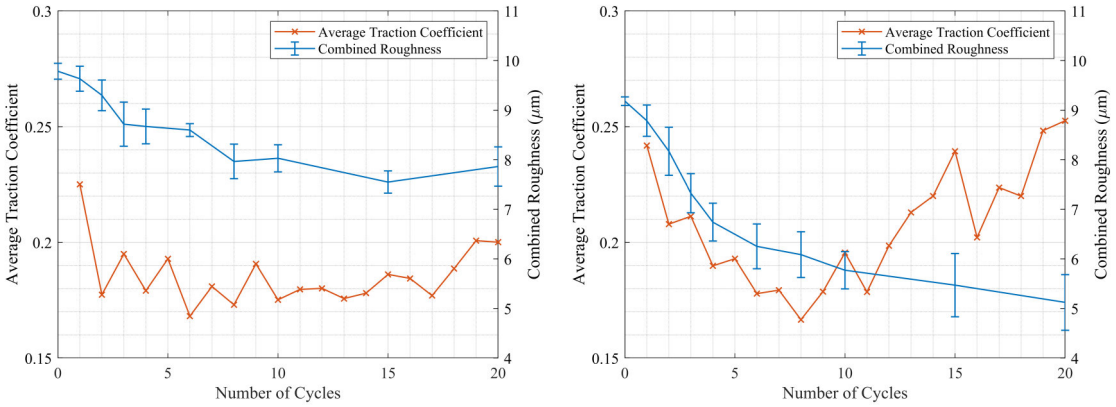

(a) 600MPa *(b) 900MPa*

Figure 6.17: Average traction coefficient vs combined roughness (Tests: HIR - Water)

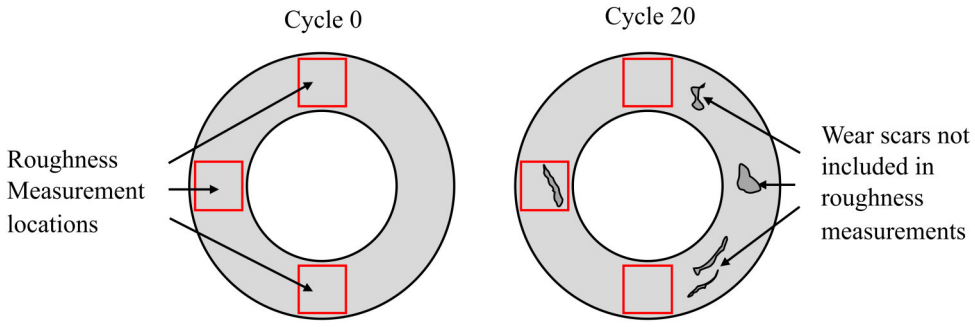

Figure 6.18: Effects of localised roughness contributions on global roughness measurements during HPT tests

The LIR water tests show similar results across contact pressures. Surface roughness remains low up to a point when enough wear occurs to dramatically change the surface roughness. When the surface roughness did increase, so did the traction coefficient (see Figure 6.19).

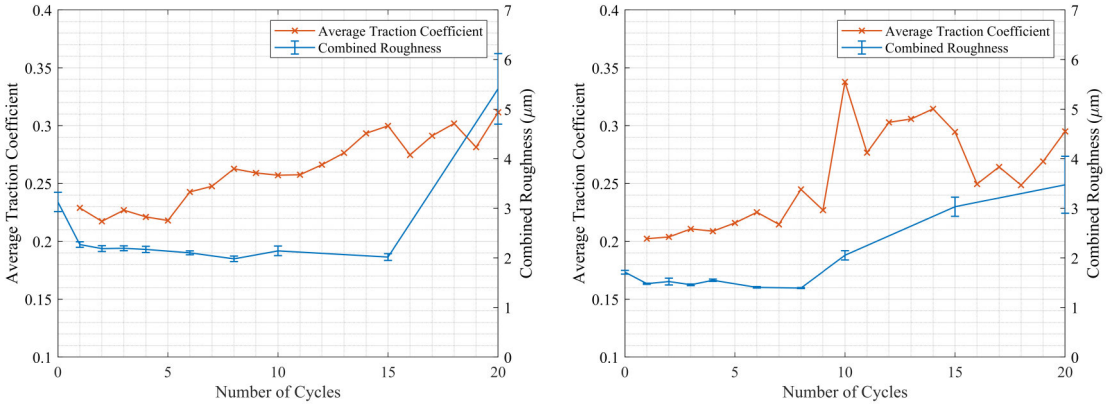

(a) 600MPa *(b) 900MPa*

Figure 6.19: Average traction coefficient vs combined roughness (Tests: LIR Water)

6.1.3.3 Grease

The traction coefficient decrease was similar for both pressures during the grease tests, however higher pressures caused both a quicker reduction in roughness and traction coefficient for HIR grease tests (see Figure 6.20). As expected, grease lubricated the interface well which resulted in little to no wear being incurred on either specimen. This meant that the measured roughness was representative of the global roughness. Higher pressures produced larger roughness reductions which may have contributed to the larger traction coefficient reductions during running in. Grease was applied at various intervals during a test; the relative motion of the two specimens caused this grease to form an established lubricant layer over time. Hill et al. have shown that the disruption of established lubricant layers acts to increase the traction coefficient [90]. Reapplication of the grease was necessary after replication, but this caused sharp increases in the traction coefficient as seen in Figure 6.20. Despite this, these peaks are still well below the traction values seen during dry tests.

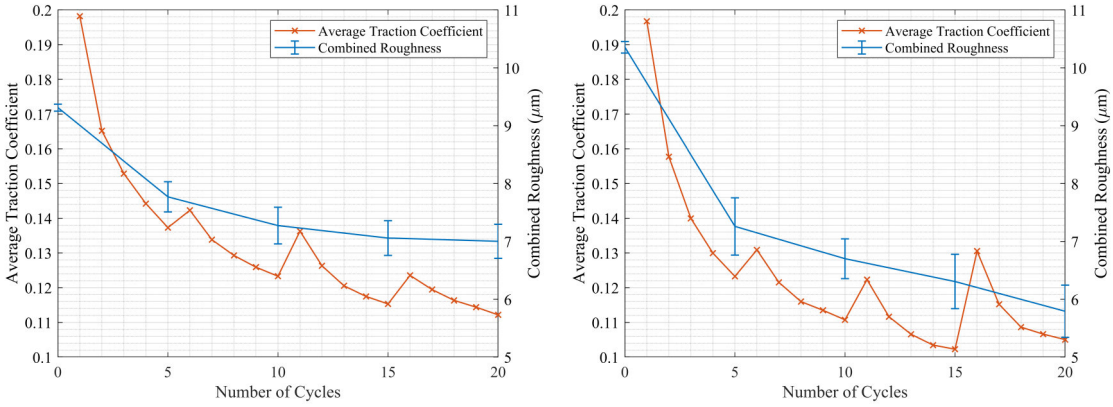

(a) 600MPa *(b) 900MPa*

Figure 6.20: Average traction coefficient vs combined roughness (Tests: HIR - Grease)

Although much of the grease was expelled from the interface under loading after application, the cleaning and reapplication of grease will have altered the amount of lubricant in the interface and where it is located. This grease must be spread over the surface to form a good lubricant layer which may take numerous cycles. Lubricant film thickness also affects the shear stress between surfaces, and for most fluids, viscosity is influenced by the applied pressure and the lubricant temperature. Larger amounts of grease could have acted as a heat sink which could have lowered the interfacial temperature, thereby increasing fluid viscosity contributing to the higher tangential forces required to move the surfaces relative to one another. As lubricant temperature was not measured this is only speculation, however the reapplication of grease temporarily increased the measured traction coefficient until the amount/nature of the grease had stabilised.

The combined roughness for the LIR grease tests remained constant and the roughness was similar across the interface. As a result the traction coefficient remained relatively constant throughout the tests and across contact pressures (see Figure 6.21).

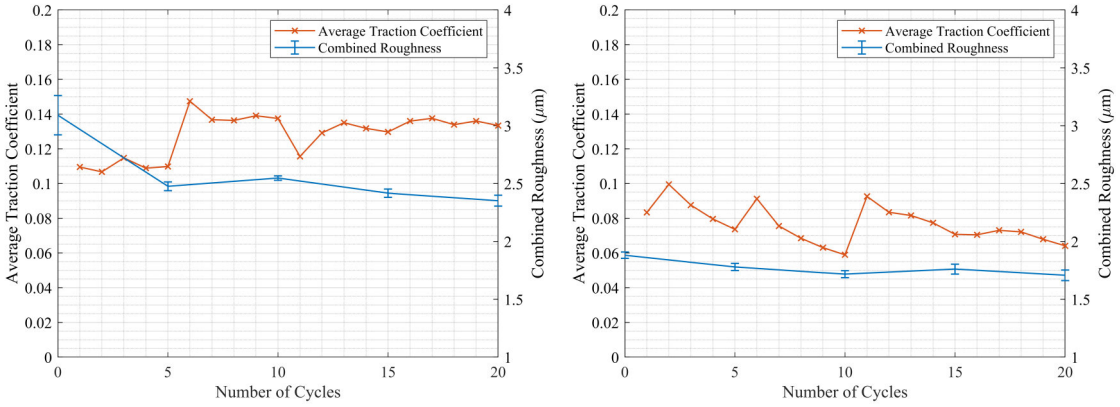

(a) 600MPa *(b) 900MPa*

Figure 6.21: Average traction coefficient vs combined roughness (Tests: LIR - Grease)

6.1.3.4 Leaves

The traction coefficient is not proportional to the combined roughness during run-in for HIR leaf contacts (see Figure 6.22). Unlike for other 3BLs, the traction coefficient increases with increased cycles. The traction coefficient is altered considerably by the presence of leaf layers meaning roughness may no longer be a primary factor.

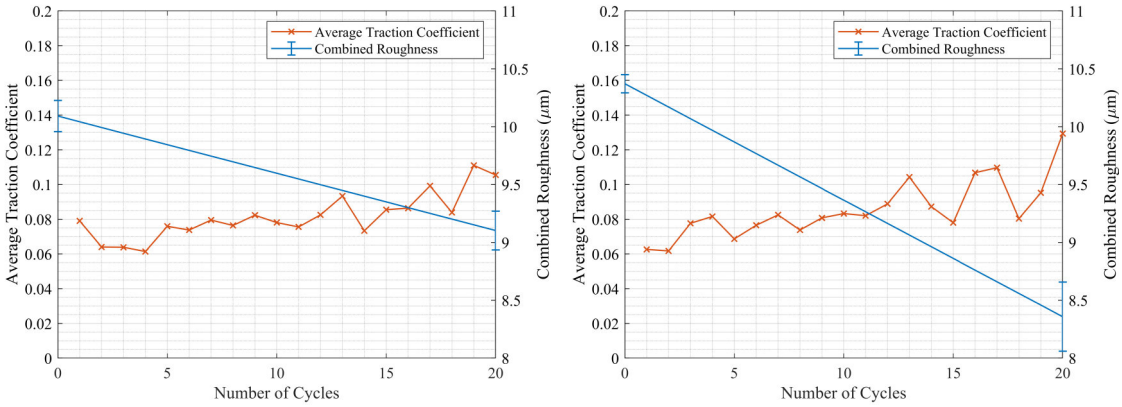

(a) 600MPa *(b) 900MPa*

Figure 6.22: Average traction coefficient vs combined roughness (Tests: HIR Leaf)

Higher roughness disrupts the build-up of leaf layers whilst simultaneously slowing the running in process. Whilst it appears that roughness is no longer a primary factor affecting the traction coefficient directly, by disrupting leaf layers that produce ultra-low adhesion conditions ($\mu < 0.1$) higher traction coefficients were observed

for the leaf tests when the contacts were rougher. At lower roughnesses the leaf layer lubricates and protects the surfaces extremely well. Almost no roughness change was measured over the 20 cycles across contact pressures (see Figure 6.23). Changes to the traction coefficient therefore seem to have arisen solely through the quality and distribution of the leaf layers.

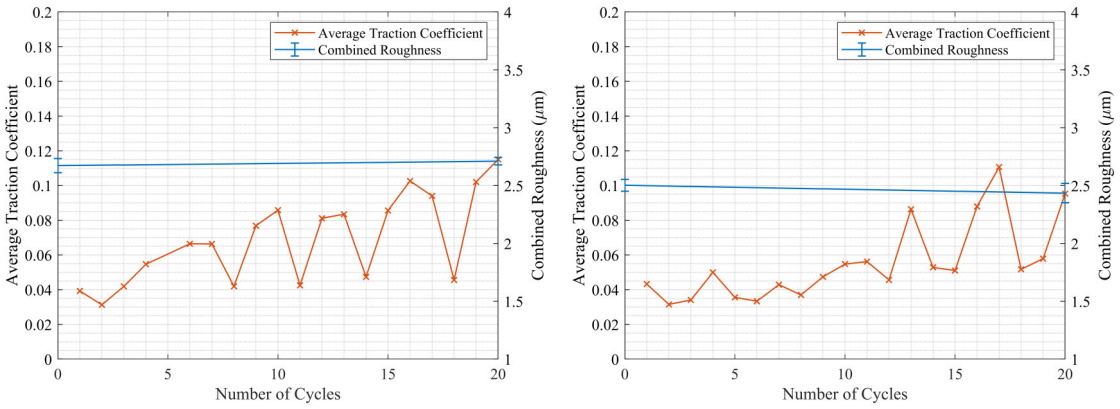

(a) 600MPa *(b) 900MPa*

Figure 6.23: Average traction coefficient vs combined roughness (Tests: LIR Leaf)

6.1.4 Interfacial Stiffness

In the following section, interfacial stiffness (K) is assessed both over the course of individual test cycles and on a cycle to cycle basis. This was achieved by averaging the interfacial stiffness during a cycle. Interfacial stiffness was ony measured for the 600MPa tests. At higher pressures damage occurred to the sensors which rendered the results unusable. As an ultrasonic wave hits an interface, part of the wave reflects and part of the wave transmits through the interface. The interfacial stiffness is a function of the size of the reflected wave, the smaller the reflected wave the higher the interfacial stiffness.

It is worth noting that the interfacial stiffness measured is just that of the section of interface covered by the ultrasonic sensor (3x3mm). Therefore, the measured interfacial stiffness can be highly localised and is not necessarily indicative of the entire interface. The interfacial stiffness was measured in three directions: the normal direction using longitudinal sensors and the circumferential and radial directions using shear sensors (see Figure 5.48). In order to understand how interfacial stiffness changes with surface roughness, the surface roughness for cycles 1 and 20 have been tabulated in Tables 6.1 and 6.2 for all interfacial conditions. These can be used as

a reference to better understand the following figures.

Test Case	$S_{q\sigma}$ Cycle 1 (μm)	$S_{q\sigma}$ Cycle 20 (μm)
Dry	9.73	6.46
Water	9.78	7.86
Grease	9.31	7.00
Leaves	10.1	9.10

Table 6.1: Combined roughness values for test cycles 1 and 20 (Tests: HIR)

Test Case	$S_{q\sigma}$ Cycle 1 (μm)	$S_{q\sigma}$ Cycle 20 (μm)
Dry	2.47	3.92
Water	3.13	5.41
Grease	3.09	2.35
Leaves	2.67	2.71

Table 6.2: Combined roughness values for test cycles 1 and 20 (Tests: LIR)

The cyclical interfacial stiffness for the three directions is shown in Figures 6.24, 6.25 and 6.26 for both the HIR and the LIR tests.

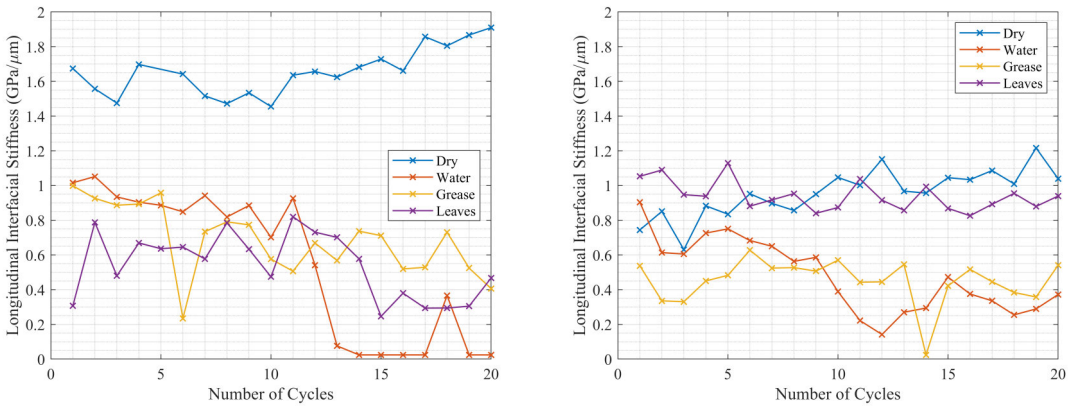

(a) LIR *(b) HIR*

Figure 6.24: Longitudinal interfacial stiffness evolution

Longitudinal Interfacial stiffness (K_L) was consistently higher for the LIR dry tests than the HIR tests as predicted. Smoother more conformal interfaces have a higher real contact area and are therefore stiffer than an interface containing large asperities. When using ultrasound, more of the wave is reflected back due to the air

pockets these large asperities create which indicates a lower Interfacial stiffness. The presence of 3BLs lowered K_L significantly for the LIR tests. The overall Interfacial stiffness is a combination of the asperity contact (metal-to-metal) stiffness and that of the 3BL (REF). The 3BL usually has a lower stiffness than the metal, meaning that a more established 3BL/lubricant film results in a lower Interfacial stiffness. This 3BL can take time to develop. As it does, we can see that K_L tends to decrease. In the case of grease and leaves when roughness remains constant, K_L still decreases, meaning it is possible that these lubricant films became more developed over the course of the test. The LIR water tests incurred large amounts of wear in the later cycles; it is possible that large amounts of material were removed forming a large air gap that acted as an ultrasound reflector. K_L for the LIR water tests was nearly always measured to be 0 from cycle 14 to cycle 20. The fact that the other sensors during these tests produced positive circumferential interfacial stiffness K_C and radial interfacial stiffness K_R measurements indicates that the problem was localised above the longitudinal sensor.

The HIR tests showed generally lower K_L values except for the leaf test which was very similar to the dry test. It is proposed that the asperities disturbed the formation of the leaf layers, meaning acoustically the fragmented leaf matter altered the interface very little. The smoother the surfaces got, the higher K_L was for the dry test. The inverse was true for the 3BL tests, whereby as the surfaces got smoother, a more defined lubricant layer was formed, thereby lowering K_L. K_C and K_R remained relatively constant for all tests (see Figures 6.25 and 6.26). As two surfaces are brought together under various loads, the interfacial contact changes. This causes both the surface roughness and the traction coefficient to change. If little change in K_C and K_R is seen from cycle to cycle, it may be that surface roughness does not influence these measurements.

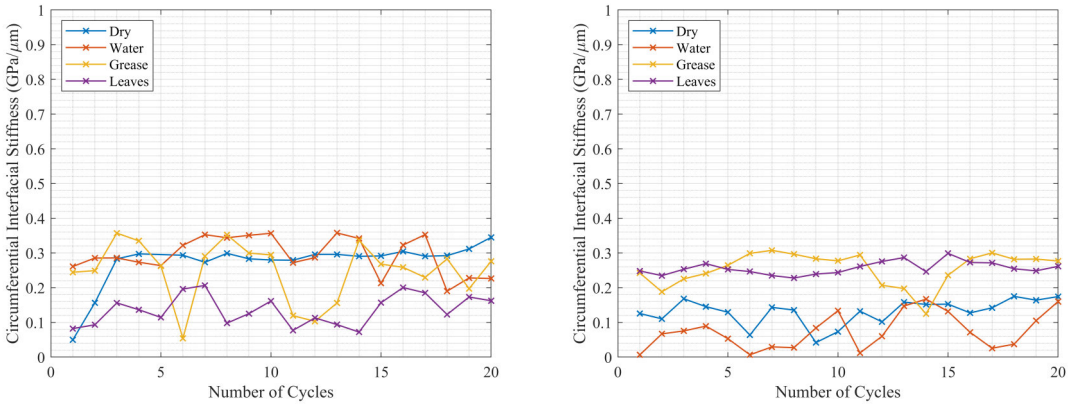

(a) LIR *(b) HIR*

Figure 6.25: Circumferential interfacial stiffness evolution

The spikes seen in Figure 6.26 were most likely caused by discrepancies in the surface conditions during the ultrasonic reference and test measurements. This is explained in Section 6.1.4.3.

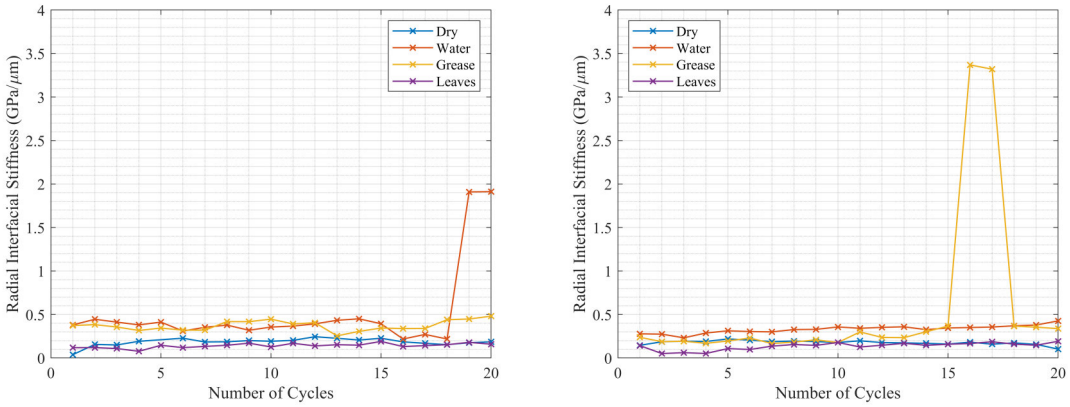

(a) LIR *(b) HIR*

Figure 6.26: Radial interfacial stiffness evolution

It is worth noting that K_L, K_C and K_R are meaningless unless related to a quantity that is generally understood by industry such as load, stress, displacement or traction coefficient, or else they are able to characterise an interface by determining what 3BLs are present. Their value is that they are remotely and non destructively measurable with an ultrasonic sensor. From the above data some general outcomes are observed:

- K_L is higher for dry smooth surfaces than dry rough surfaces.

- The presence of 3BLs lowers K_L for smooth surfaces.
- K_C and K_R do not depend on surface roughness.

6.1.4.1 Dry HIR

The individual test cycle ultrasonic data was evaluated for all cycles, but for conciseness only the 1st and 20th cycles for all three interfacial stiffnesses are presented here. Figure 6.27 shows the interfacial stiffness during cycle 1 and 20 for the HIR tests. K_L is much higher than K_C and K_R. This was expected as much larger normal loads are applied than circumferential or radial loads attained. The normal and tangential loads are not individually shown in any of these figures as they are collectively represented by the traction coefficient. For the entirety of these tests, 600MPa normal pressure was applied through the interface. The normal force varied slightly from test to test due to the slight differences in interfacial area. At lower cycles when the surfaces are rougher and less hard, the specimens are rotated against one another at a consistent rotation rate (see Figure 6.27a). It is possible that the lower hardness at these early cycles may have influenced the way in which the surfaces interacted, causing one surface to plough through the other. At higher cycles, this relationship breaks down as the surfaces are smoother and harder. The test is made up of large slip events which are characterised by sudden increases in rotation position (see Figure 6.27b).

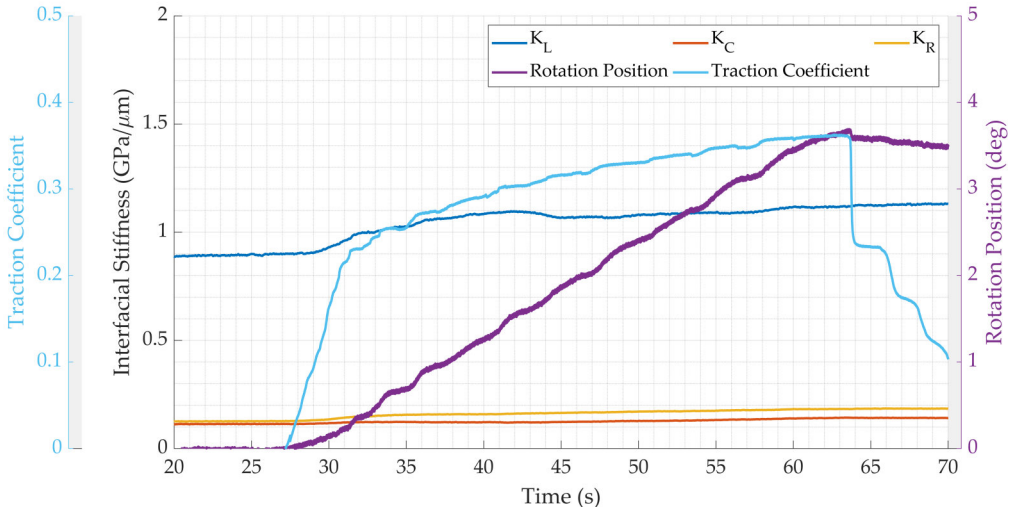

(a) Cycle 1

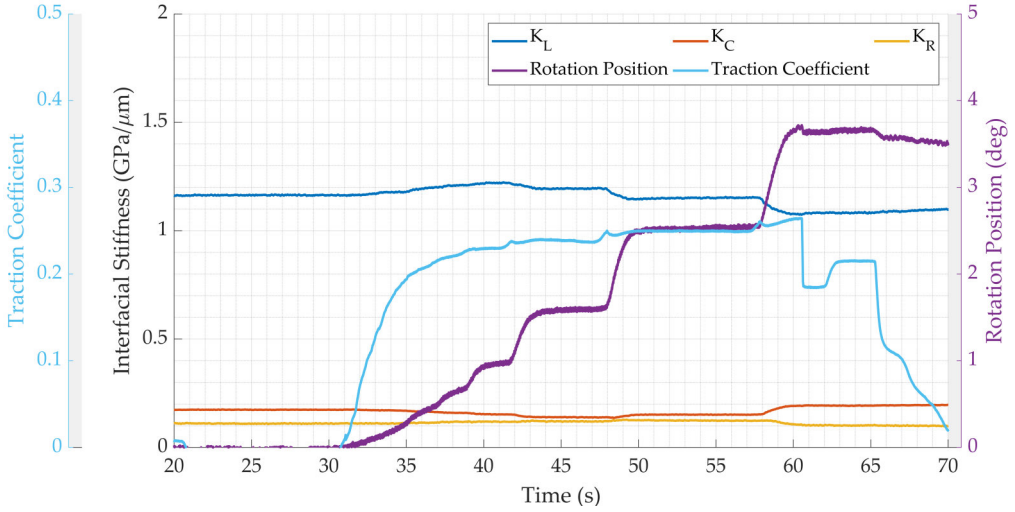

(b) Cycle 20

Figure 6.27: Longitudinal interfacial stiffness vs traction coefficient (Tests: HIR Dry)

As the interfacial stiffnesses are very different and the test cycles are long, it can be difficult to understand how interfacial stiffness changes when slip occurs as this often happens quickly. To better understand this, each interfacial stiffness was evaluated over a 10 second window and the figure scale was customised. When this is done it can be seen that all three interfacial stiffnesses at lower cycles increase with increased rotation and traction coefficient (see Figures 6.28a, 6.30a and 6.31a).

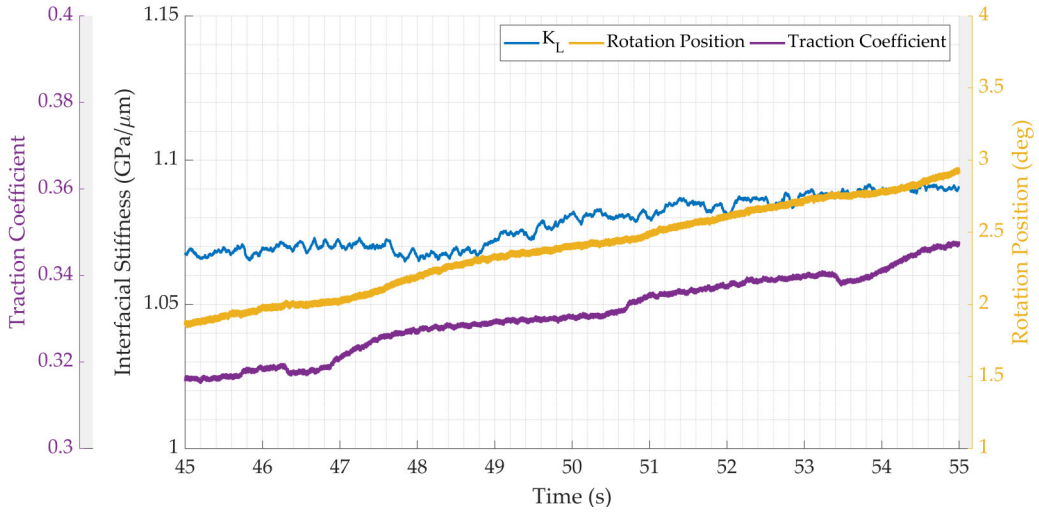

(a) Cycle 1

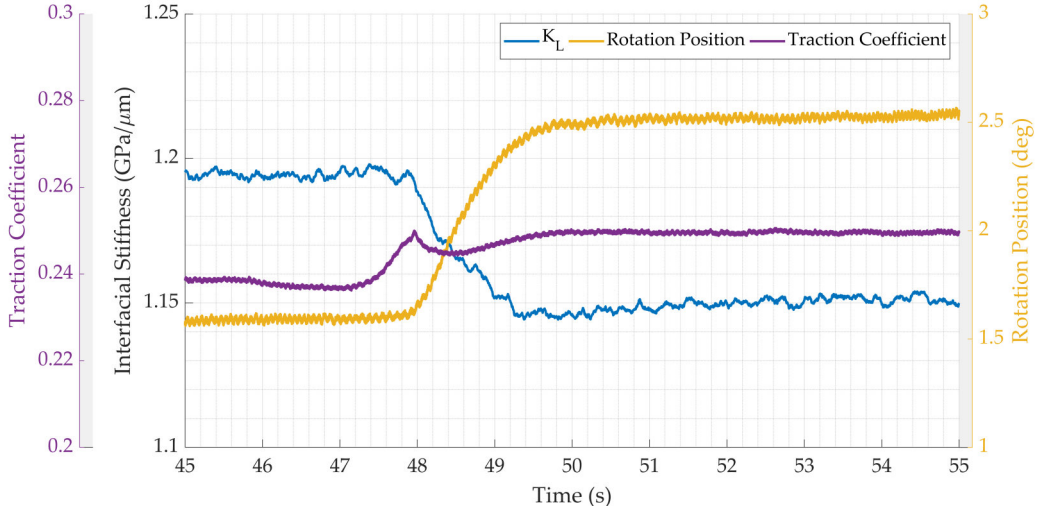

(b) Cycle 20

Figure 6.28: Longitudinal interfacial stiffness vs traction coefficient(Tests: HIR Dry)

At higher cycles, we often see a drop in longitudinal interfacial stiffness during a slip event (see Figure 6.28b). During a test cycle, a certain amount of angle is rotated through; this can occur in one continuous movement or in jerky steps. The controller was set to rotate the specimens at 0.1deg/s. When these large slips occur, the surfaces over-rotate, meaning the surfaces must stop rotating in order to rejoin with the command from the controller. Ahead of these slips, the traction coefficient rises slightly as the controller increases the tangential pressure to allow the surfaces to rotate. The pressure is then released and the surfaces slip once more. It is proposed that as the surfaces slip, delamination occurs. The resulting air gaps that this process produces may explain the drops in K_L (see Figure 6.29).

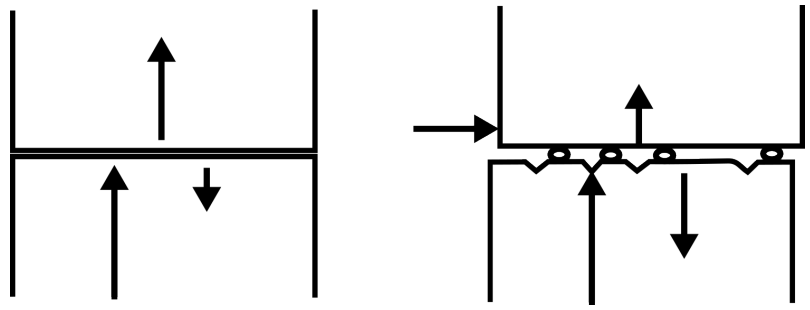

Figure 6.29: Schematic showing why longitudinal interfacial stiffness drops during slip

At higher cycles, K_C tended to increase during a slip (see Figure 6.30). K_C appeared to respond to the rotation not traction coefficient, however once the rotation was complete, both K_C and the traction coefficient had increased during this 10 second window.

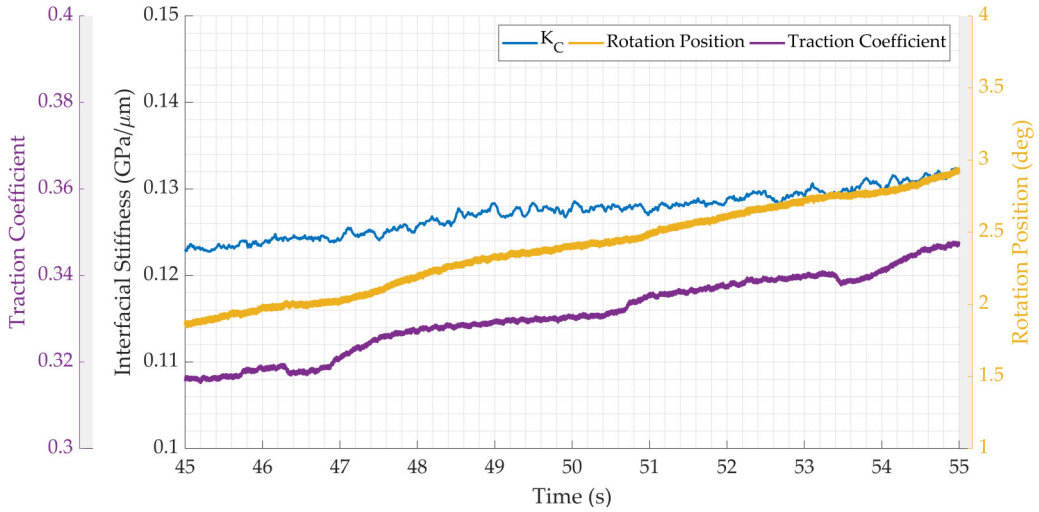

(a) Cycle 1

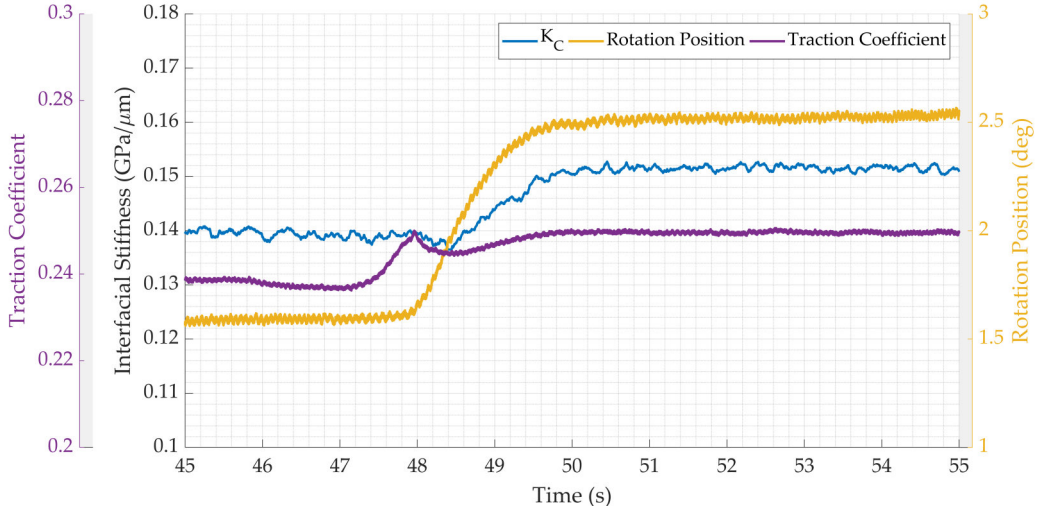

(b) Cycle 20

Figure 6.30: Circumferential interfacial stiffness vs traction coefficient (Tests: HIR Dry)

At higher cycles, K_R tended to increase during a slip (see Figure 6.31). K_R appeared to respond to the rotation not traction coefficient, however once the rotation was complete both K_R and the traction coefficient had increased marginally during this 10 second window.

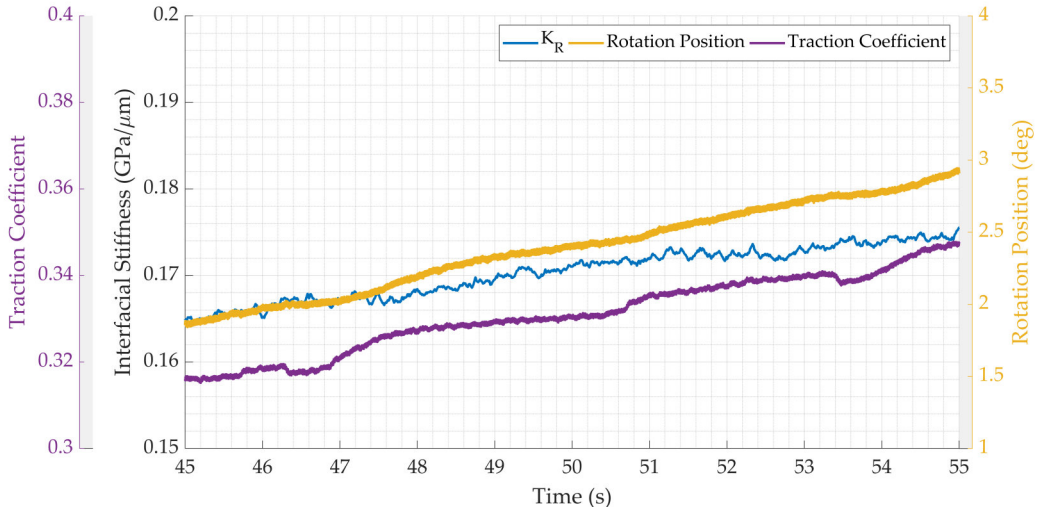

(a) Cycle 1

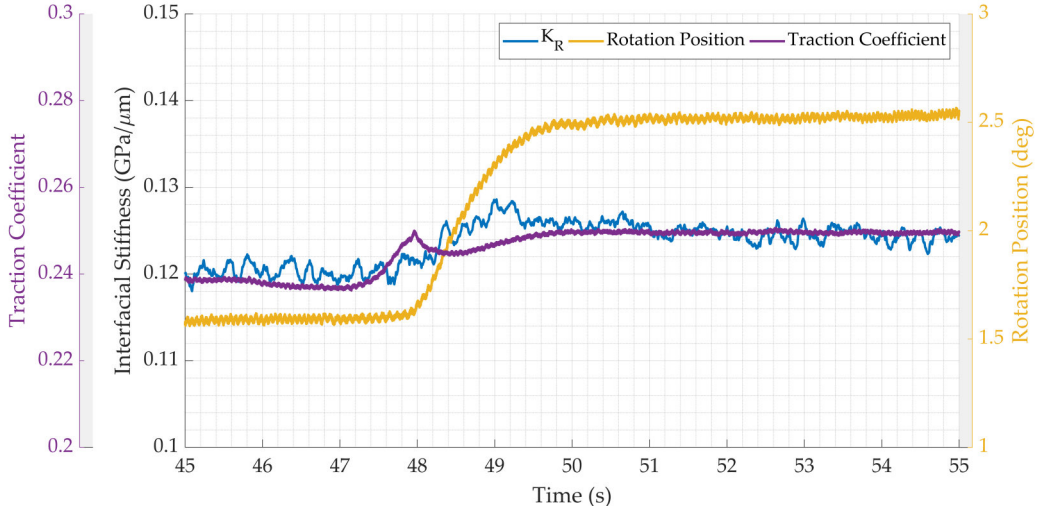

(b) Cycle 20

Figure 6.31: Radial interfacial stiffness vs traction coefficient (Tests: HIR Dry)

It is worth noting that although the interfacial stiffness behaved in this way for these 10 second intervals, this was not the case for all tests and all slip events. These represent a general theme to the data, but as the interface is so complex and the variables so many ,it is likely that much is happening at the interface that is still not understood. Some general outcomes observed were:

- At lower cycles, rotation was steady. K_L, K_C and K_R all increased with both rotation position and traction coefficient.
- At higher cycles, rotation was unsteady. K_L often reduced during slip events

and K_C and K_R often both increased with both rotation position and traction coefficient.

6.1.4.2 Dry LIR

Figure 6.32 shows the interfacial stiffness during cycle 1 and 20 for the dry LIR tests. Like the HIR tests, K_L is much higher than K_C and K_R. At lower cycles, the combined roughness is low ($S_{q\sigma} = 2.47\mu m$) and the surfaces are soft; rotation occurs fairly consistently (see Figure 6.32a). Since this surface is smooth unlike for the HIR tests, it is expected that this phenomena relies on the extent to which a surface is run-in. At higher cycles the roughness was actually measured to increase ($S_{q\sigma} = 3.92\mu m$). This increase was due primarily to abrasive wear which is characterised by wear scars that act to increase roughness measurements. Despite this roughness increase, the slip behaviour seen in the higher cycle HIR tests was also seen in the higher cycle LIR tests, indicating that this behaviour was independent of surface roughness (see Figure 6.32b). It instead depends on the cycle number, more specifically the higher hardnesses associated with higher cycles and more run-in surfaces.

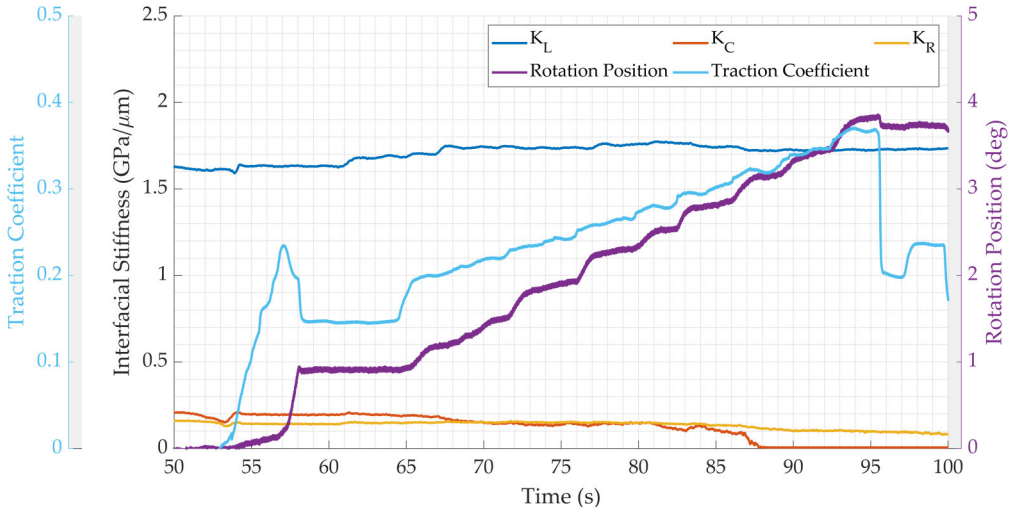

(a) Cycle 1

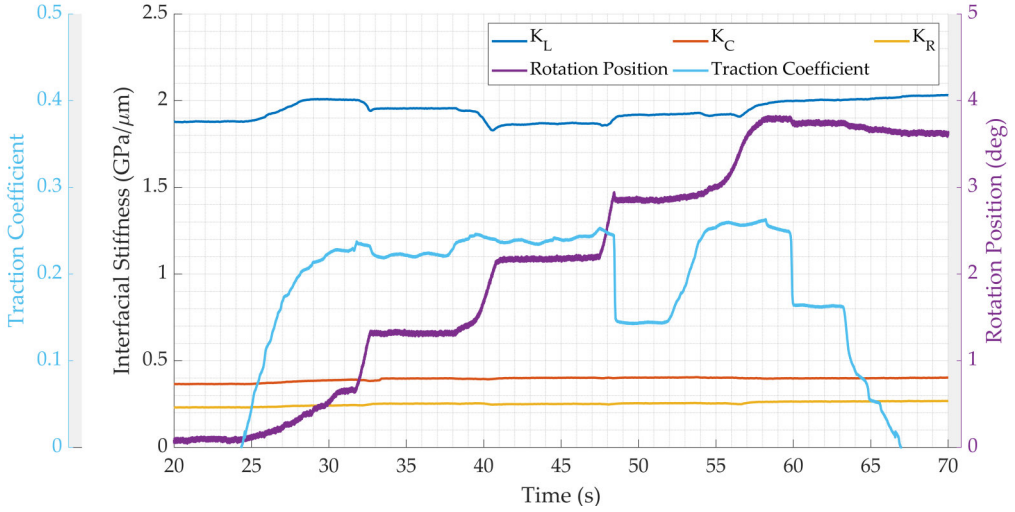

(b) Cycle 20

Figure 6.32: Longitudinal interfacial stiffness vs traction coefficient (Tests: LIR Dry)

When these cycles are looked at in more detail, it can be seen that unlike the HIR tests, K_L, K_C and K_R do not necessarily increase with increasing traction coefficient and rotation position (see Figures 6.33a, 6.34a and 6.35a). As Interfacial stiffness is known to depend on the surface roughness, this is to be expected for the LIR tests. Interfacial stiffness is more erratic at lower cycles, this is perhaps due to the wearing process whereby very small bits of material are removed and then driven back into the soft material. At higher cycles interfacial stiffness is more stable as the surfaces are more run-in; K_L is seen to drop like in the HIR tests. It is assumed that the same process occurs whereby material is removed during these slip events.

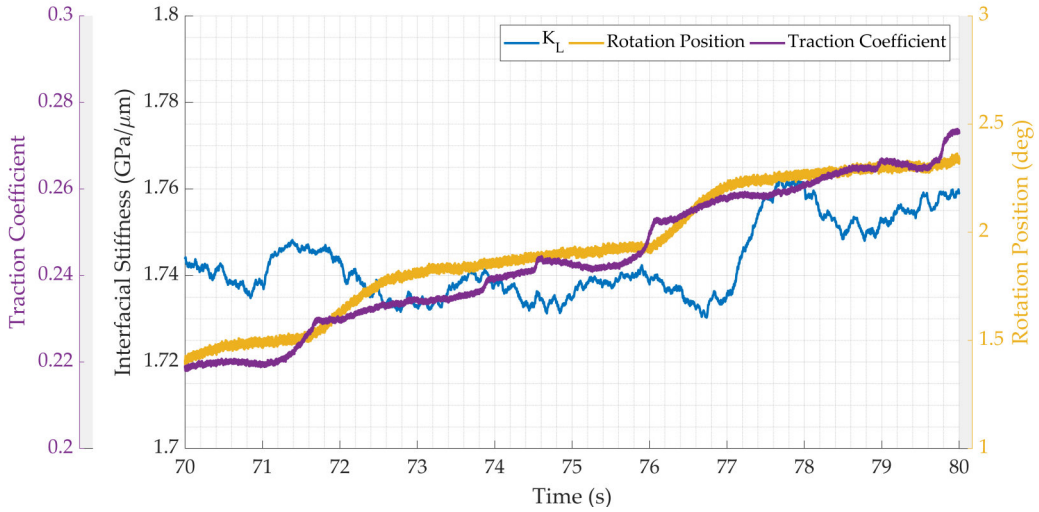

(a) Cycle 1

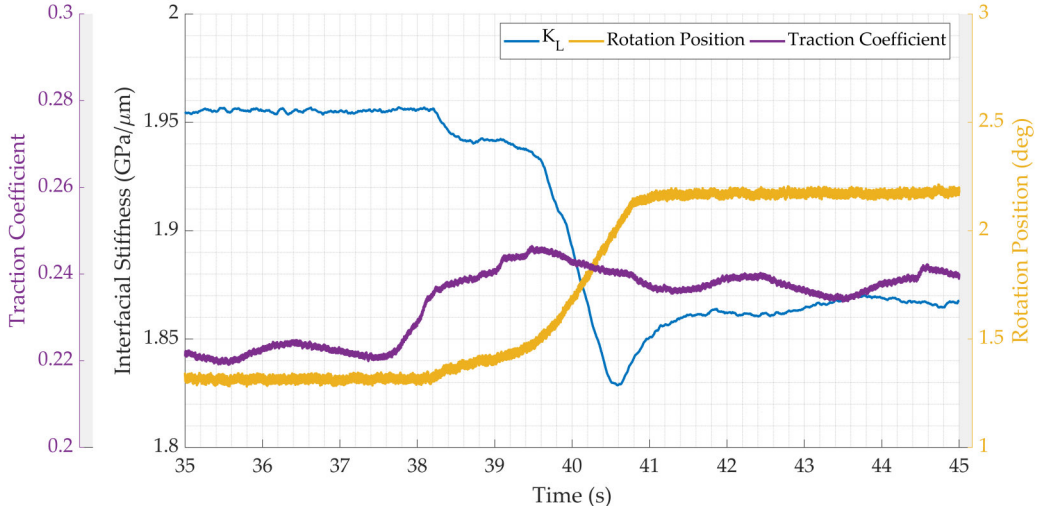

(b) Cycle 20

Figure 6.33: Longitudinal interfacial stiffness vs traction coefficient (Tests: LIR Dry)

Unlike for the HIR tests, very little change was measured in K_C or K_R at higher cycles (see Figure 6.34b and 6.35b). The traction coefficient changed considerably during this slip event, and whilst K_C or K_R did change marginally, it would be a stretch to be able to link these measurements to the traction coefficient.

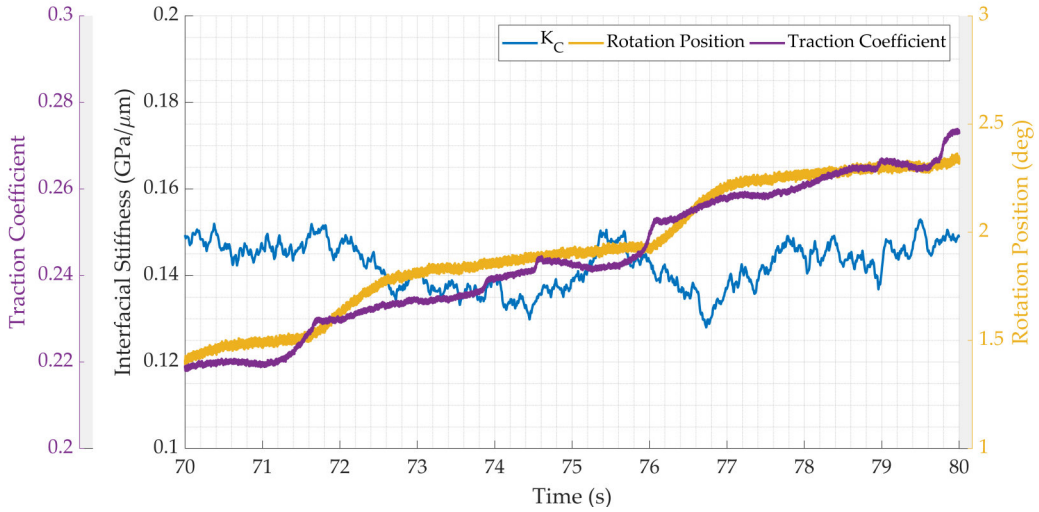

(a) Cycle 1

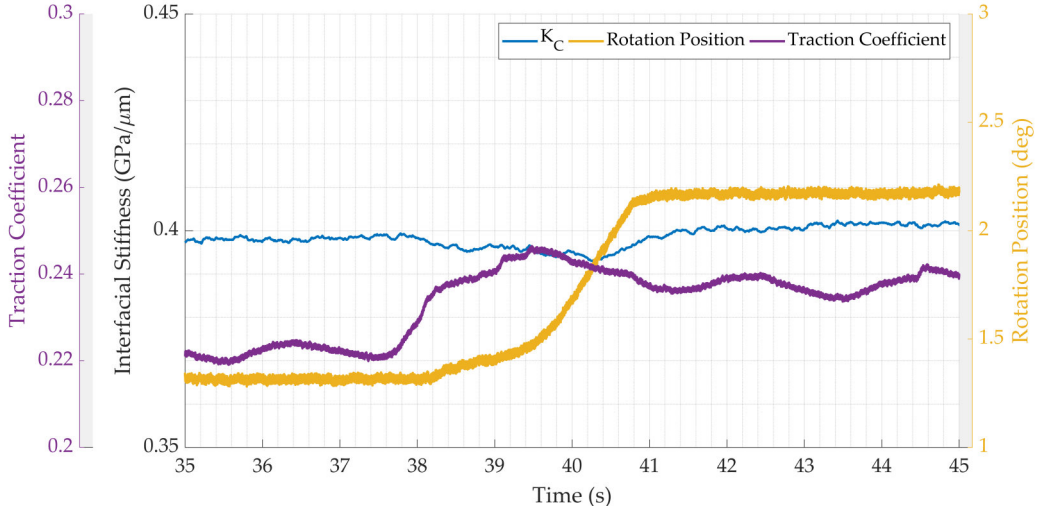

(b) Cycle 20

Figure 6.34: Circumferential interfacial stiffness vs traction coefficient (Tests: LIR Dry)

(a) Cycle 1

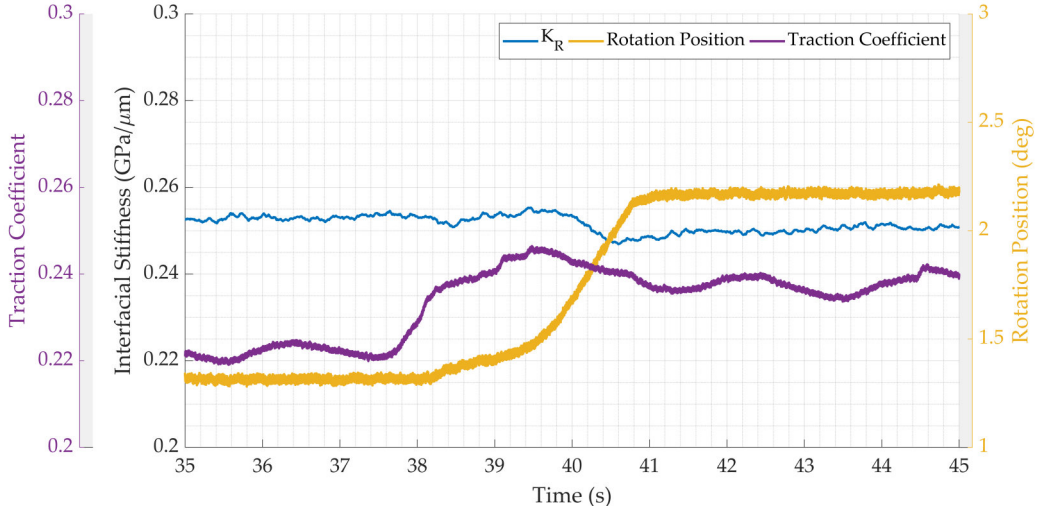

(b) Cycle 20

Figure 6.35: Radial interfacial stiffness vs traction coefficient (Tests: LIR Dry)

Again this ten second window represents a general theme to the LIR data and there is much more to understand when it comes ultrasonic measurements. Further testing and repeats could go a long way to aid this understanding, as well as provide better statistical analysis to inform computational models. Nevertheless some general outcomes observed were:

- At lower cycles, rotation was steadier than at higher cycles. Whilst K_L, K_C and K_R did change with rotation position and traction coefficient, no pattern was observed.

- At higher cycles, rotation was unsteady. K_L often reduced during slip events.

6.1.4.3 Issues Arising from Interfacial Stiffness Measurements when 3BLs are Present

Ultrasonic reflectometry requires both an unloaded reference measurement and a loaded test measurement to calculate the reflection coefficient and ultimately the interfacial stiffness. When there is no 3BL present on the surface, the interface off which the ultrasonic wave reflects is that of steel-air. As air has an extremely low acoustic impedance ($z_{air} \approx 0$), the majority of the ultrasonic wave is reflected. If a 3BL is present on the surface then the interface off which the ultrasonic wave reflects is that of steel-3BL. 3BLs have a range of acoustic impedances which are greater than zero, which means some of the ultrasonic wave is transmitted through the interface into the 3BL. This reduces the amount of reflected signal.

Unfortunately 3BLs do not stay in one place, but shift around the interface when it is loaded. This means that the unloaded reference measurement can be taken with or without a 3BL present and the loaded test measurement can also be taken with or without a 3BL present. In addition, a test measurement may be taken on a portion of surface with large amounts of wear. The large air gaps this wear creates can cause the interfacial stiffness value to be zero locally even when loaded. The interface as a whole however will have an interfacial stiffness if they are touching. Any discrepancy between the conditions at the interface when the reference and test measurements are taken will cause the interfacial stiffness measurement to be different to the true interfacial stiffness. This is an issue when trying to link local interfacial stiffness measurements to a global tribological values such as the traction coefficient. Figure 6.36 shows the potential reference and test conditions.

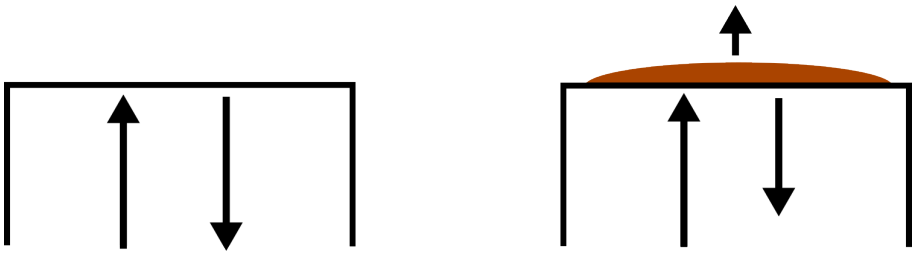

(a) Reference: Left: Clean, Right: 3BL

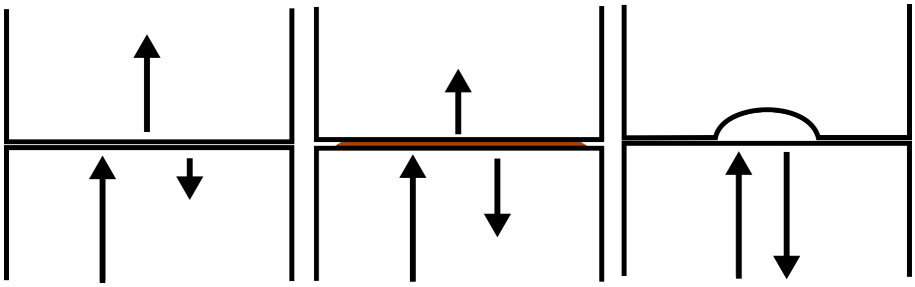

(b) Test: Left: Clean, Middle: 3BL, Right: Wear

Figure 6.36: Effect of 3BLs a wear on an ultrasonic wave for both reference and test measurements

Table 6.3 uses the reflection coefficient and interfacial stiffness equations to estimate what effect 3BLs and wear have on the final interfacial stiffness measurement. If the reference and the test are taken under the same conditions, then the local interfacial stiffness measurement is correct. If, however, there is a discrepancy between the reference and test conditions, this will cause either an under or overestimation of the interfacial stiffness or else it is measured to be zero.

Case	**Reference (Unloaded)**	**Test (Loaded)**	**R**	**K (GPa/μm)**
1	Clean	Clean	Normal	Normal
2	Clean	3BL	Incorrect	Smaller K
3	Clean	Wear	1	0
4	3BL	Clean	Incorrect	Larger K
5	3BL	3BL	Normal	Normal
6	3BL	Wear	1	0

Table 6.3: Effects of 3BLs and wear on interfacial stiffness measurements

The application of water was done with a pipette onto the lower specimen. The water tension causes the water to form droplets on the lower surface (see Figure

6.37). As the ultrasonic wave passed through the upper specimen, it is highly unlikely that the ultrasonic reference measurements were taken with water present. During the test, water will be present in the interface, meaning water tests are most represented by case number 2 in Table 6.3. Dry tests are of course represented best by case number 1 or case 3 if the wear is particularly severe.

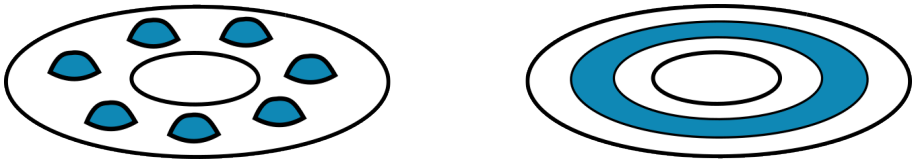

Figure 6.37: Water presence when applied (left) vs presence during a test (right)

Grease was applied with the tip of a pipet to both the lower and upper surfaces. The grease covered the entire surface with portions of the surface more generously covered than others (see Figure 6.38). Due to its high viscosity, the grease was able to cling to the upper surface. It was therefore highly likely that the ultrasonic reference measurement was taken with grease present. During the test, grease will be present in the interface meaning that grease tests are best represented by case 5 in Table 6.3.

Figure 6.38: Grease presence when applied (left) vs presence during a test (right)

Leaf powder was poured and distributed over the lower surface and then hydrated with water (see Figure 6.39). This turns into an ultra low friction well bonded black layer at later cycles. However, for early cycles, no leaf material would be on the upper surface so the ultrasonic reference measurement at these early cycles was almost certainly made without a 3BL present. The leaf layers were patchy throughout the tests, so it is not possible to say with any certainty whether the loaded test measurement was made with 3BLs present. Interfacial stiffness measurements for the leaf tests are therefore extremely difficult to accomplish with any accuracy. At later cycles, large amounts of the leaf material are transferred to the upper surface, meaning the ultrasonic reference measurements are more likely to be made with a

3BL present. Leaf tests therefore are best represented by cases 2 and 4 in Table 6.3.

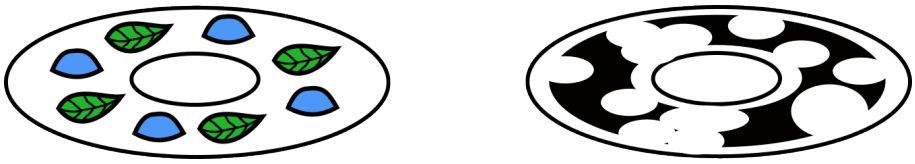

Figure 6.39: Leaf presence when applied (left) vs presence during a test (right)

Wear of course can occur whether a 3BL is present or not and can cause extremely low interfacial stiffness measurements. It should be noted that this analysis is simplified, but it should at least impart the idea that interfacial stiffness measurements with the presence of 3BLs are extremely difficult to get right. It should also go some way to explaining why sometimes the interfacial stiffness measurements appear to be zero even when two surfaces are in contact, and also why interfacial stiffness can be measured to be much higher or lower than expected.

6.1.4.4 Water

For the HIR water tests, higher roughness at lower cycles provided space for the 3BL to escape into. The result is a higher stiffness as the contact is closer to a metal-metal contact (see Figure 6.40a). As the roughness reduces, these gaps are less prevalent and more water is directly between the two metal surfaces. This causes the interfacial stiffness to drop (see Figure 6.40b). The effects of the 3BL can be seen as K_C is not measured at cycle 1 and is at cycle 20 when a new reference measurement is taken. This is a theme seen with many ultrasonic measurements when 3BLs are present.

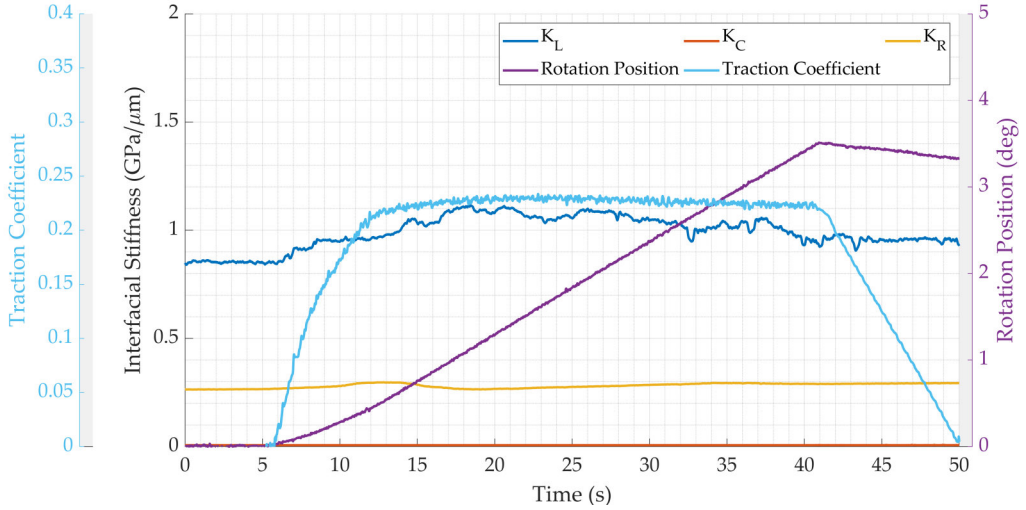

(a) Cycle 1

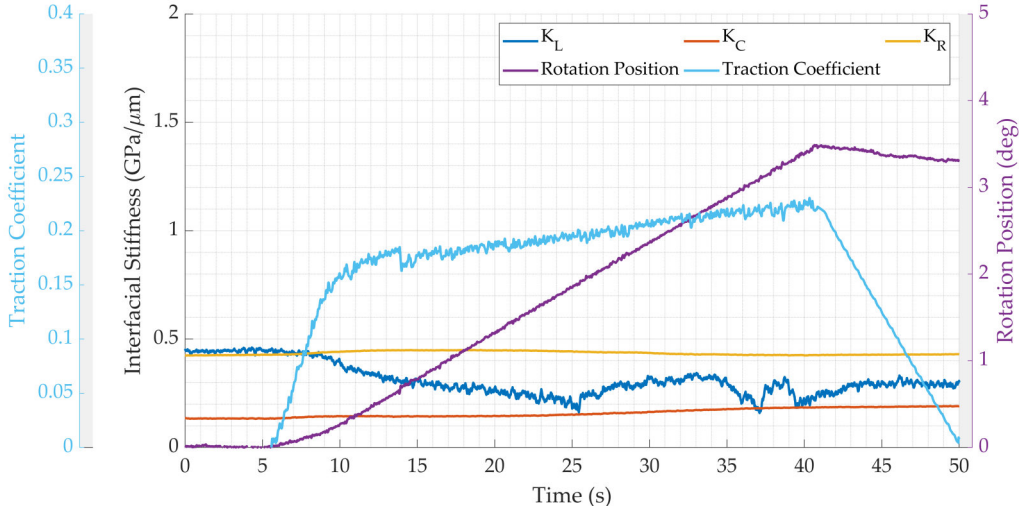

(b) Cycle 20

Figure 6.40: Interfacial stiffness vs traction coefficient (Tests: HIR Water)

For the LIR water tests, K_L was measured for cycle 1, although it was measured to be much lower than for the dry tests. When contacts are smooth, there is more metal-to-metal contact. The presence of 3BLs therefore separates these surfaces well and acts to lower the interfacial stiffness which is represented in Figure 6.41a. For cycle 20, K_L was not measured, most probably due to discrepancies between the reference and test measurements. Issues were seen with the K_R signal which caused extremely high interfacial stiffnesses to be measured (see Figure 6.41b). This sensor was used again and had similar issues (see Figure 6.42a), however it is also possible that this was due to 3BLs.

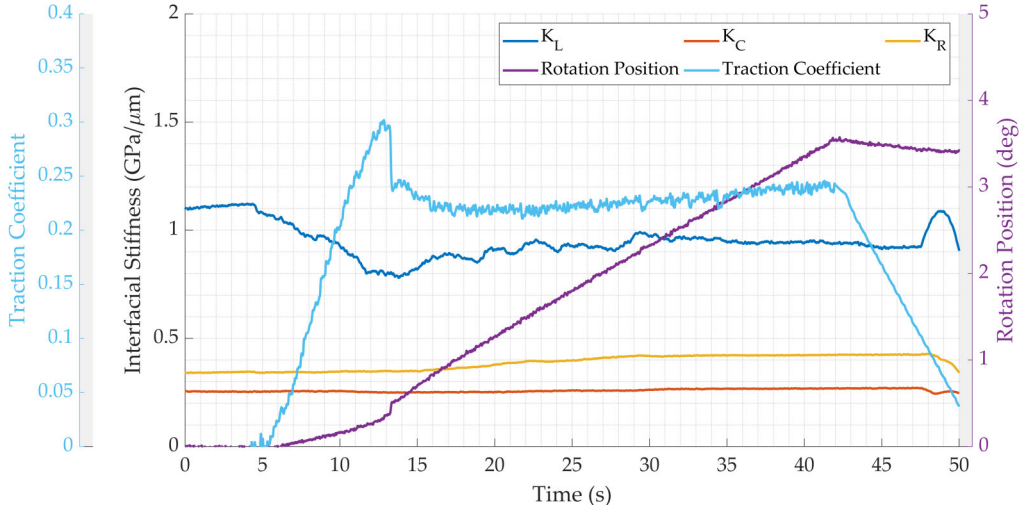

(a) Cycle 1

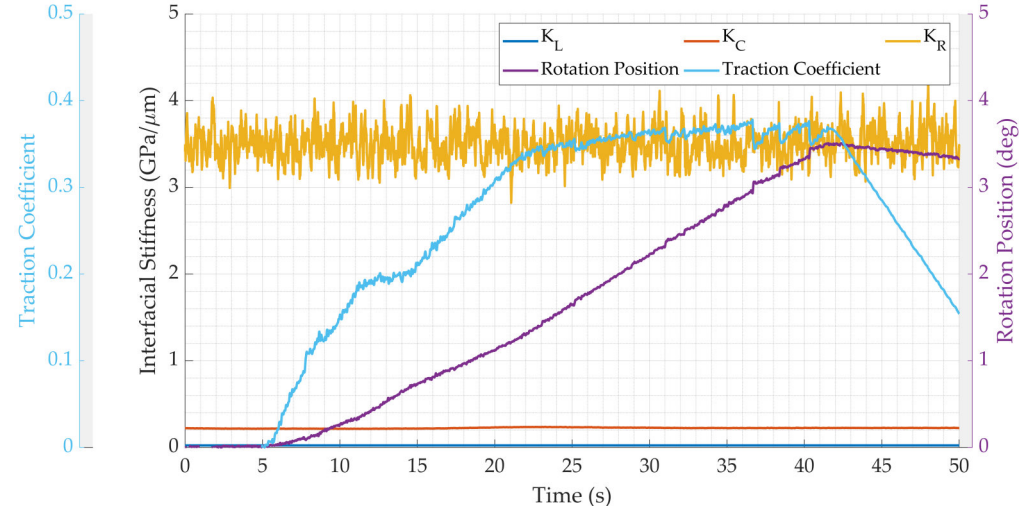

(b) Cycle 20

Figure 6.41: Interfacial stiffness vs traction coefficient (Tests: LIR Water)

6.1.4.5 Grease

For the HIR grease tests, interfacial stiffness was similar from cycle 1 to cycle 20 (see Figure 6.42). The K_R sensor suffered the same interfacial stiffness jump as it did during the LIR water tests; it is unlikely that this was caused by a global surface change as the other sensors would have changed as well. It seems this was most likely caused by an issue with the sensor or else by a sudden localised change in interfacial conditions where the sensor was measuring.

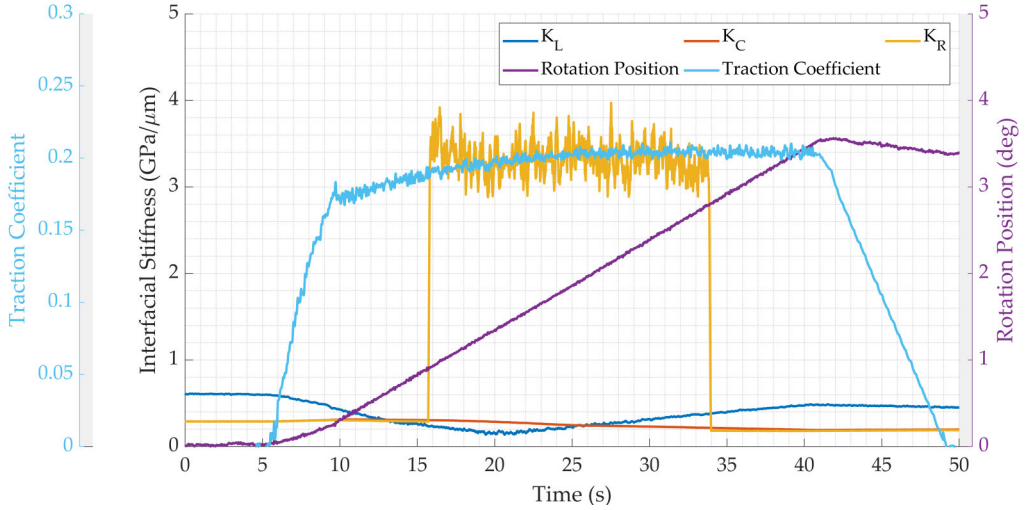

(a) Cycle 1

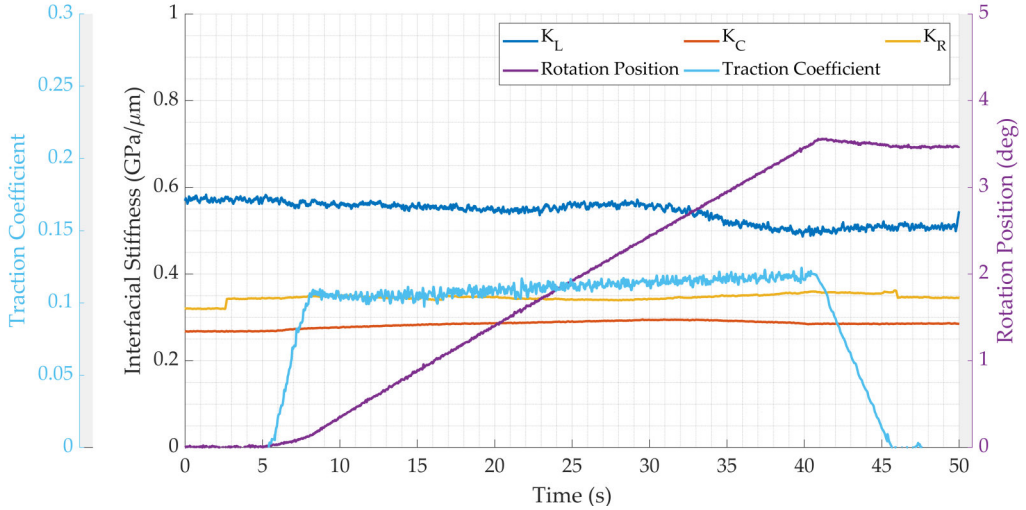

(b) Cycle 20

Figure 6.42: Interfacial stiffness vs traction coefficient (Tests: HIR Grease)

K_L was higher for the lower cycle LIR grease tests than the higher cycle tests (see Figure 6.43). Grease is viscous and may take some cycles to coat the interfaces evenly. As a result more metal-metal contact is present at lower cycles. As the surfaces conform and the 3BL is dispersed, K_L drops. The signal is less stable at cycle 20. This was probably due to the amount of 3BL changing as the surfaces rotated against one another. This is a theme of the LIR tests where greater amounts of 3BL are able to separate the two interacting surfaces. K_C and K_R were relatively similar for both cycle 1 and cycle 20.

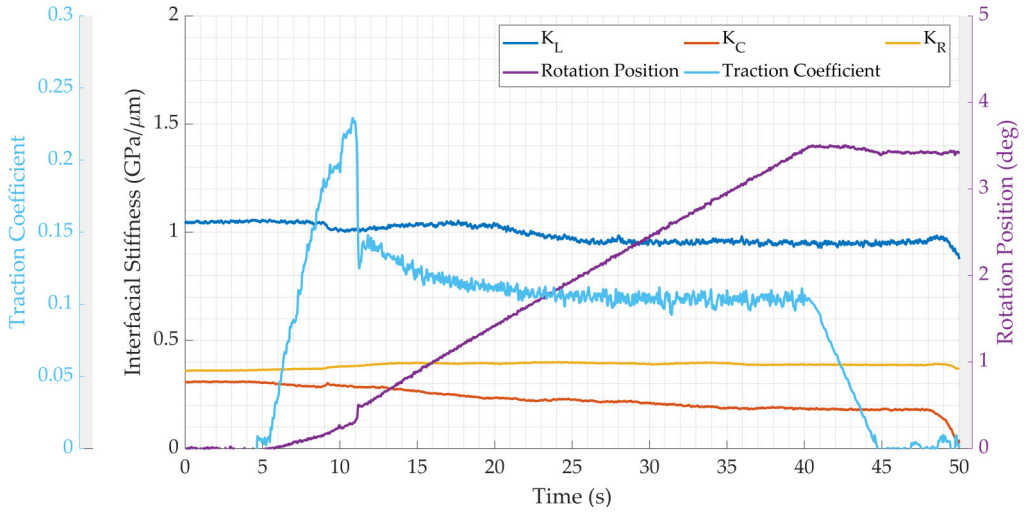

(a) Cycle 1

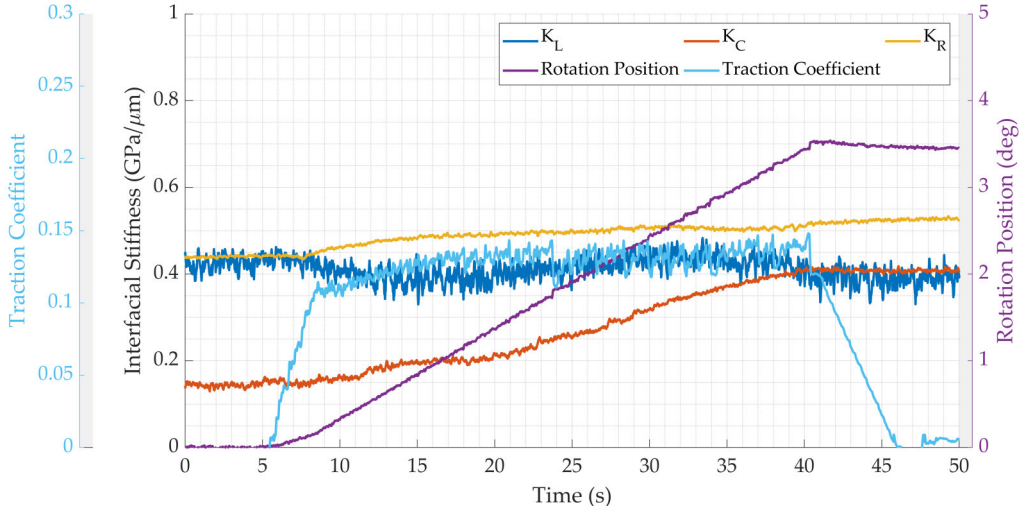

(b) Cycle 20

Figure 6.43: Interfacial stiffness vs traction coefficient (Tests: LIR Grease)

6.1.4.6 Leaf

Interfacial stiffness level for the HIR leaf tests was remarkably similar to the dry tests at low cycles (see Figure 6.44a). It is expected that the high roughnesses imposed disrupted the formation of leaf layers at these early cycles. As roughness reduced, K_L reduced as more 3BL was present in at the interface. K_C remained relatively constant across cycles whilst K_R could be seen to drop to almost zero at times (see Figure 6.44b). This highly localised interfacial stiffness response was typical for 3BL ultrasonic measurements.

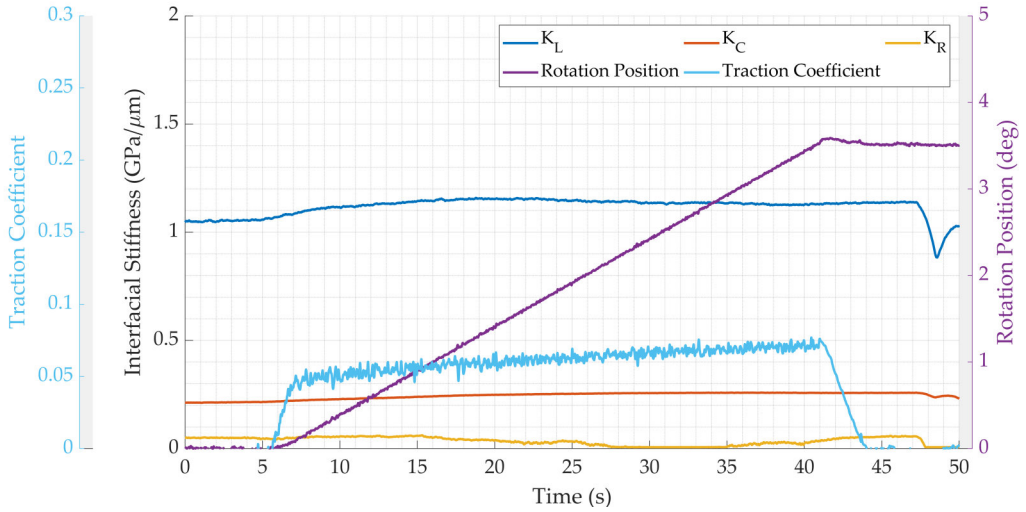

(a) Cycle 1

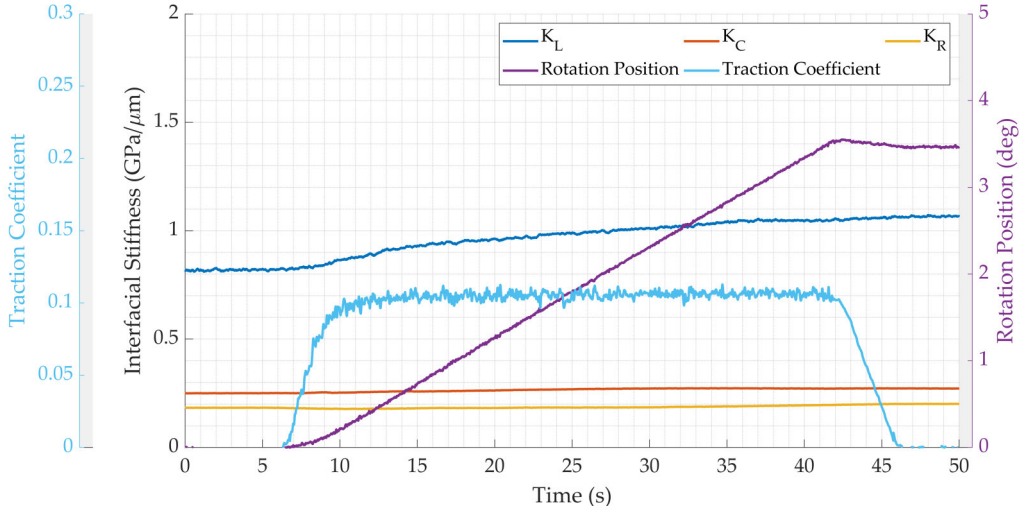

(b) Cycle 20

Figure 6.44: Interfacial stiffness vs traction coefficient (Tests: HIR Leaf)

K_L for the LIR leaf tests was much lower; leaf material was able to form a black layer on these smoother surfaces (see Figure 6.45). Leaf material was applied to the lower specimen and the ultrasonic measurements were taken through the upper specimen. Leaf material transfer was observed on these tests, meaning references and tests were often made with leaf material. The results are quite stable and representative of a leaf layer. If these tests are compared to the equivalent dry tests, then it seems that longitudinal interfacial stiffness may be a good indication of 3BL presence on the railhead (see Figure 6.24a). This could have wide implications for future track monitoring. At higher cycles, K_L increases again, No additional leaf material was applied to the interface over the tests so as the material was gradually squeezed out

of the interface, more metal-metal contact was present.

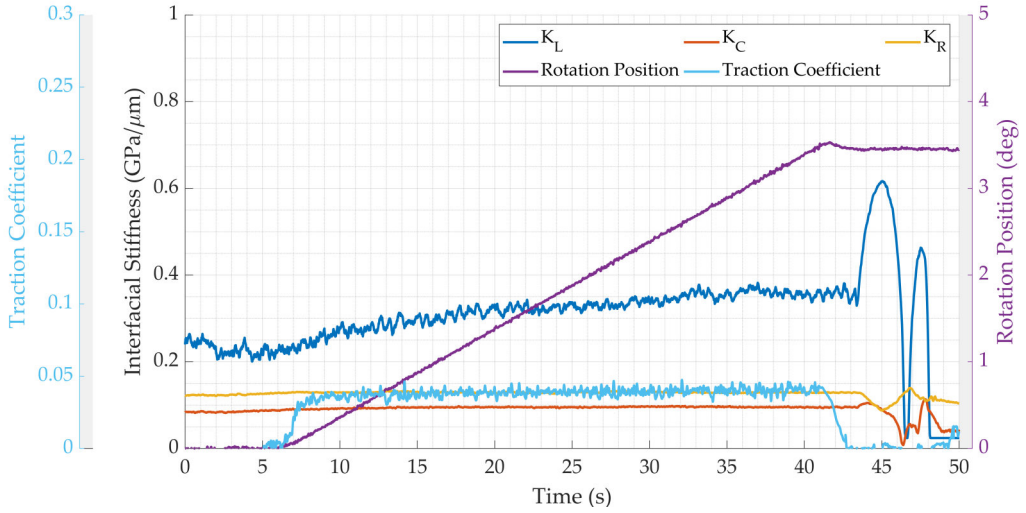

(a) Cycle 1

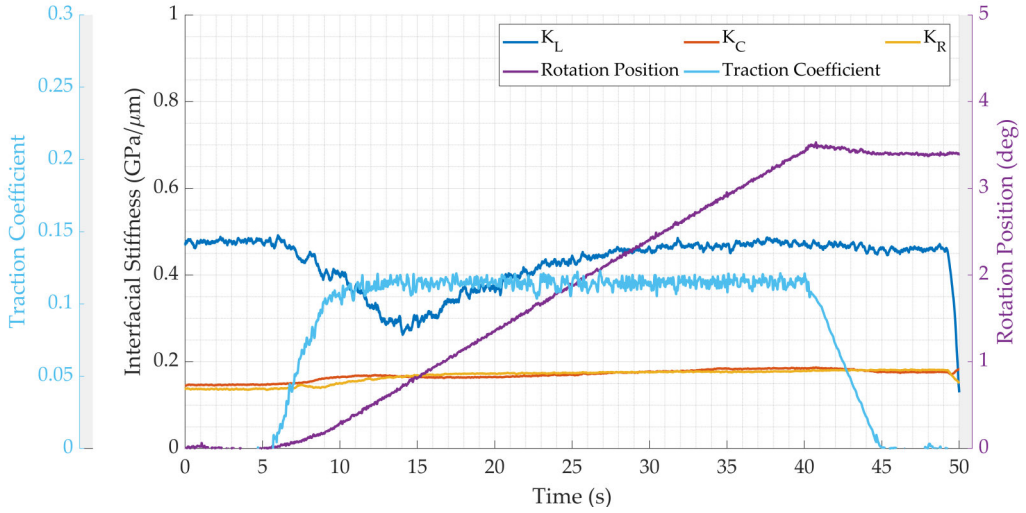

(b) Cycle 20

Figure 6.45: Interfacial stiffness vs traction coefficient (Tests: LIR Leaf)

6.1.4.7 3BL Summary

The simplified equations used to calculate interfacial stiffness require metal-metal contact. The introduction of 3BLs to the interface changes this. The calculation of Interfacial stiffness requires a reference measurement and a test measurement which depend on the surface conditions and the presence of 3BLs. The way 3BLs move in the interface is complex and depends on the viscosity of the 3BL, the pressure at the interface and the surface roughness. 3BLs are either retained or ejected or

else present or absent from the interface. When surfaces are rough, a 3BL may be retained, but not present at the interface due to the asperity gaps. When surfaces are smooth, 3BLs are predominantly present, but can be ejected easily as there is no place for them to sit between two conformal surfaces. An observation during testing was that lower viscosity 3BLs such as water are quickly ejected after perhaps just one cycle, whereas higher viscosity 3BLs such as grease and leaves may be retained for many cycles even for the LIR tests.

Ultrasonic pulses were passed down through the top specimen which meant that for lower viscosity 3BLs, references were taken without water present as the 3BL could not cling to the upper surface. This was shown in the results which were often erratic and sometimes the measurements obtained were incorrect or zero. Improvements to the reliability of these measurements could be made be increasing the number of ultrasonic sensors and thereby the amount of surface that is measured. By comparing multiple measurements from many sensors, it would become clearer which of these were providing realistic interfacial stiffness measurements. Higher viscosity 3BLs were able to cling to the top surface, meaning references were most likely taken with the 3BL in place. The measurements obtained were more stable and representative. Whilst the 3BL ultrasonic results were extremely complex, some general outcomes were observed:

- The presence of 3BLs lowered the measured interfacial stiffness.
- 3BL detection may be achieved through ultrasonic measurements.
- 3BL characterisation may require additional work.
- The presence of 3BLs resulted in highly localised interfacial stiffness.
- Higher roughnesses reduced the impact of 3BLs on interfacial stiffness measurements.
- No consistent relationship was found between K_L, K_C and K_R and the traction coefficient for any 3BL.

6.2 HPT Statistical Analysis

Statistical analysis was performed to determine if any significant relationships existed between roughness, friction, interfacial stiffness. As Interfacial stiffness is

remotely measurable using ultrasonic sensors, relationships between this and other parameters are of particular interest. A number of statistical studies were conducted: these included Pearson correlations and linear regression models. Many parameters were cross referenced in order to assess their statistical significance.The parameters analysed are listed below:

- Combined Roughness $S_{q\sigma}$
- Average Traction Coefficient
- Average Skewness S_{sk}
- Average Kurtosis S_{ku}
- Longitudinal Interfacial Stiffness K_L
- Circumferential Interfacial Stiffness K_C
- Radial Interfacial Stiffness K_R

Where relationships have been found to be statistically significant, comments have been made on how certain we can be that they are in fact linked. This is done by quantifying the co-occurrence of the two variables by assessing the correlation coefficient (r) and the p-value (p) of a dataset. The correlation coefficient ranges from -1 to 1 whereby -1 is a perfectly negative correlation and 1 is a perfectly positive correlation. The p-value is the probability of obtaining the observed results if the null hypothesis is true (i.e it is a measure of statistical significance). This depends on a significance value or α-value which is set by the statistician, however a common α-value is 0.05 which is used here. Therefore, for the following analysis, $p<0.05$ is significant and $p>0.05$ is not significant. This α-value is arbitrary and it is merely a convention to set it at 0.05, so it should be noted that whilst p-values are useful, their misuse is frequent and they are by no means definitive.

The p-values were determined using a Pearson correlation. Where a p-value was obtained that was lower than 0.05, a linear regression model was also applied to that dataset to see how much one variable depended on another. The beta coefficient (B) describes how the dependent variable will change given a unit increase of the independent variable, e.g. given a unit increase in the measured roughness or interfacial stiffness (independent variables), how much did the traction coefficient (dependent variable) change. The standard error (SE) is the error associated with the beta

coefficient value. The R^2 value is a measure of how well the linear model fits the data. Where $R^2 > 0.7$, the fit is said to be good and the independent variables have a strong effect on the dependent variables. In addition to the significant relationships found, some relationships that show no significance are also included. Ideally statistical analysis should be performed on large datasets and with multiple repeat tests which due to the scope of this work were not completed, so this analysis should act only to direct researchers in the direction of possible significant relationships.

6.2.1 Friction vs Roughness

How roughness affects friction is of interest to the railway industry as various maintenance procedures such as rail grinding and wheel turning produce interfacial surfaces whose roughnesses are elevated. Friction is quantified by the traction coefficient which is compared to the combined roughness in the following section. This is subcategorised into the four interfacial conditions: dry, water, grease and leaves.

6.2.1.1 Dry

One of the few relationships that was shown to be significant was the combined surface roughness and the traction coefficient for HIR tests (see Figure 6.46). All three pressures showed a positive correlation indicating that at elevated roughnesses, elevated traction coefficients were also observed.

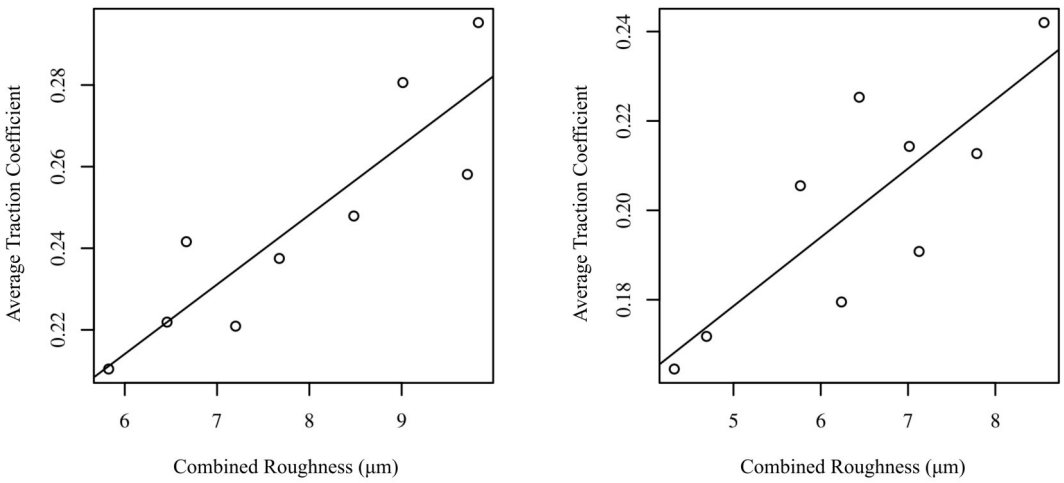

(a) 600MPa *(b) 900MPa*

Figure 6.46: Average traction coefficient vs combined roughness (Tests: HIR Dry)

Pressure (MPa)	***r***	***p***	***R²***	***B***	***SE***
600	0.88	0.002	0.78	0.02	0.003
750	0.72	0.027	0.53	0.009	0.003
900	0.82	0.007	0.67	0.02	0.004

Table 6.4: Average traction coefficient vs combined roughness (Tests: HIR Dry)

At lower roughnesses, this relationship was not seen across the pressures tested (see Figure 6.47). This could be due to the wear that was incurred during these LIR tests or because the surface roughness was too low to make a difference to the traction coefficient. Whichever it was, it seems that roughness only plays a major role in affecting the traction coefficient when running in from high roughnesses for dry contacts.

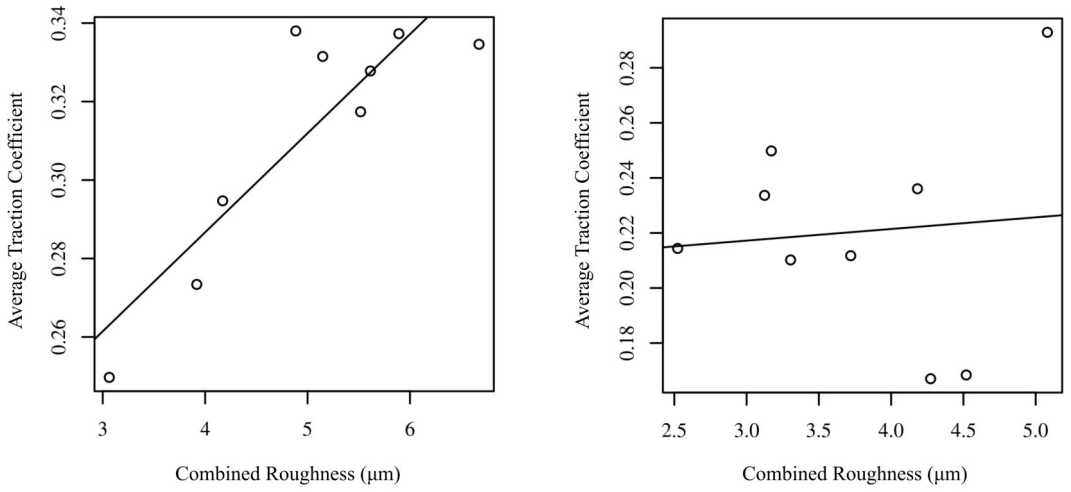

(a) 600MPa *(b) 900MPa*

Figure 6.47: Average traction coefficient vs combined roughness (Tests: LIR Dry)

Pressure (MPa)	r	p	R^2	B	SE
600	0.88	0.002	0.70	0.03	0.008
750	0.40	0.327	N/A	N/A	N/A
900	0.09	0.823	N/A	N/A	N/A

Table 6.5: Average traction coefficient vs combined roughness (Tests: LIR Dry)

6.2.1.2 Water

When a third-body layer is present, the interfacial conditions change, altering the level of traction. Whilst roughness does impact the traction coefficient for dry contacts (see Figure 6.46), the presence of 3BLs have an altogether greater impact on the tribology of a system as a whole. When we compare the roughness and the traction coefficient for the water tests, the clear relationship shown in Figure 6.46 disappears (see Figure 6.48).

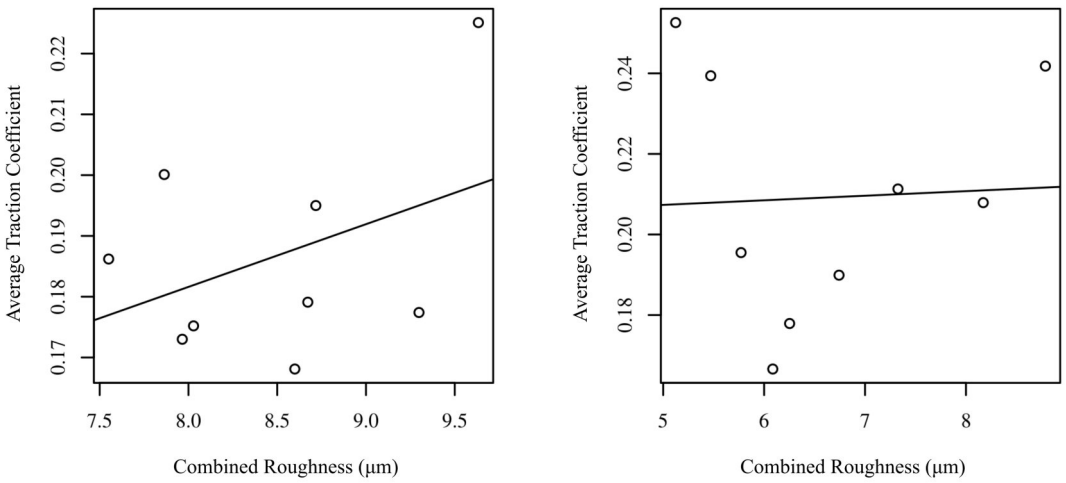

(a) 600MPa *(b) 900MPa*

Figure 6.48: Average traction coefficient vs combined roughness (Tests: HIR Water)

Pressure (MPa)	***r***	***p***	R^2	***B***	***SE***
600	0.40	0.285	N/A	N/A	N/A
750	0.37	0.324	N/A	N/A	N/A
900	0.05	0.905	N/A	N/A	N/A

Table 6.6: Average traction coefficient vs combined roughness (Tests: HIR Water)

Likewise for the LIR water tests, no correlation was seen between roughness and traction coefficient (see Figure 6.49).

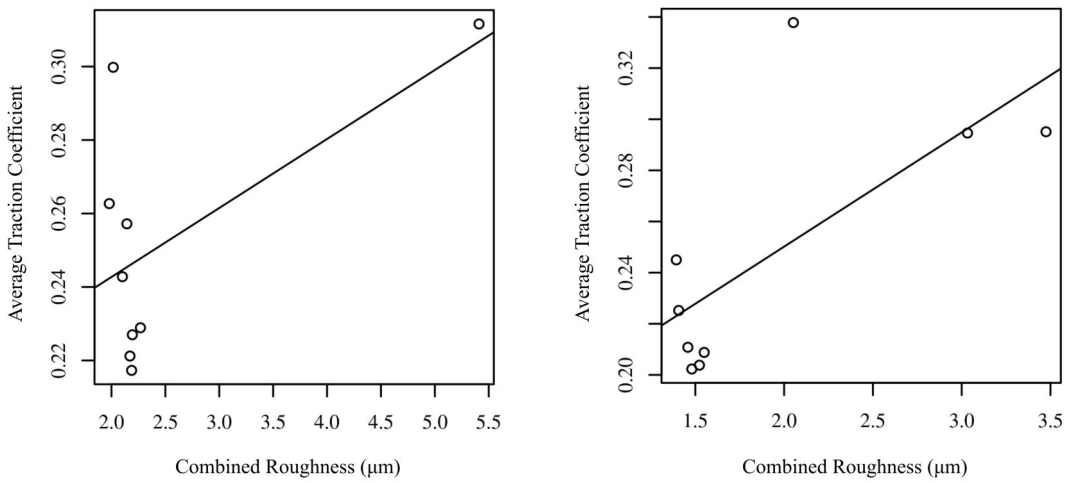

(a) 600MPa *(b) 900MPa*

Figure 6.49: Average traction coefficient vs combined roughness (Tests: LIR Water)

Pressure (MPa)	***r***	***p***	R^2	***B***	***SE***
600	0.60	0.087	N/A	N/A	N/A
750	0.39	0.333	N/A	N/A	N/A
900	0.70	0.035	N/A	N/A	N/A

Table 6.7: Average traction coefficient vs combined roughness (Tests: LIR Water)

6.2.1.3 Grease

There was some correlation between the traction coefficient and combined roughness for the the grease tests. Lower pressure HIR tests showed some of the most statistically significant results in this work. This could indicate that roughness plays a role in the effectiveness of semi-solid lubricants at lower pressures. At higher pressures, this relationship is not seen statistically, however from Figure 6.20 it shows that the traction coefficient responds in a similar way to the change in roughness. It may be that at these higher pressures roughness is reduced quickly, thereby eliminating potential troughs for lubricant to be inactive and the metal-to-metal contact this potentially causes. Linear regressions assume linearity which may not be the most suitable fit in this case.

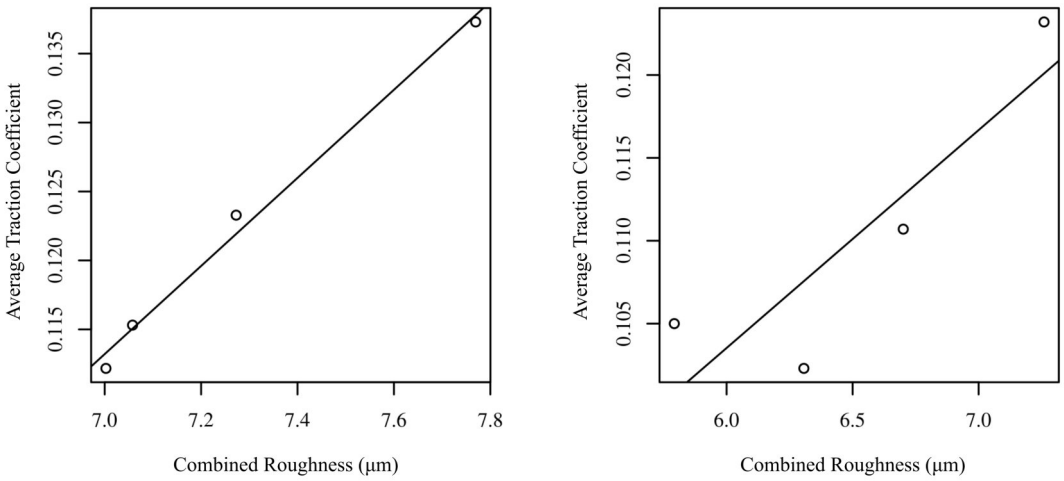

(a) 600MPa *(b) 900MPa*

Figure 6.50: Average traction coefficient vs combined roughness (Tests: HIR Grease)

Pressure (MPa)	r	p	R^2	B	SE
600	1.00	0.005	0.99	0.03	0.002
750	0.97	0.029	0.94	0.03	0.005
900	0.80	0.200	N/A	N/A	N/A

Table 6.8: Average traction coefficient vs combined roughness (Tests: HIR Grease)

The LIR tests show a stranger response whereby there is no significance at 750MPa and 900MPa and the correlation at 600MPa is reversed. LIR grease tests showed very little change in roughness as they were so well lubricated and so incurred no wear.

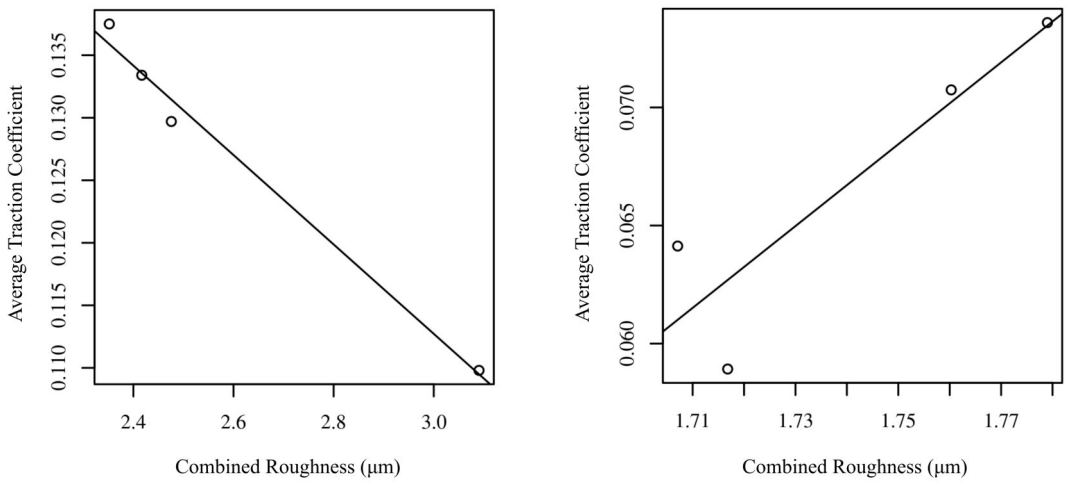

(a) 600MPa *(b) 900MPa*

Figure 6.51: Average traction coefficient vs combined roughness (Tests: LIR Grease)

Pressure (MPa)	***r***	***p***	R^2	***B***	***SE***
600	-0.99	0.006	0.99	-0.04	0.003
750	0.50	0.499	N/A	N/A	N/A
900	0.90	0.097	N/A	N/A	N/A

Table 6.9: Average traction coefficient vs combined roughness (Tests: LIR Grease)

6.2.1.4 Leaves

No statistical analysis was conducted due to lack of roughness data points.

6.2.2 Interfacial Stiffness vs Roughness

Interfacial stiffness is compared to the combined roughness in the following section. This is subcategorised into the four interfacial conditions: dry, water, grease and leaves.

6.2.2.1 Dry

It was expected that roughness would be able to be deduced using ultrasonic reflectometry. Gaps created by the asperities present on every surface produce air gaps when surfaces come into contact. This acts as a barrier to ultrasound which translates to an increased reflection size. This was detectable for the HIR tests whereby a strong negative correlation was found between longitudinal interfacial stiffness, K_L and combined roughness (see Figure 6.52). This relationship makes sense: as the roughness is reduced the air gaps are reduced and the interfacial stiffness increases. This relationship is not seen for the LIR tests, however this may be due to outliers caused by wear effects.

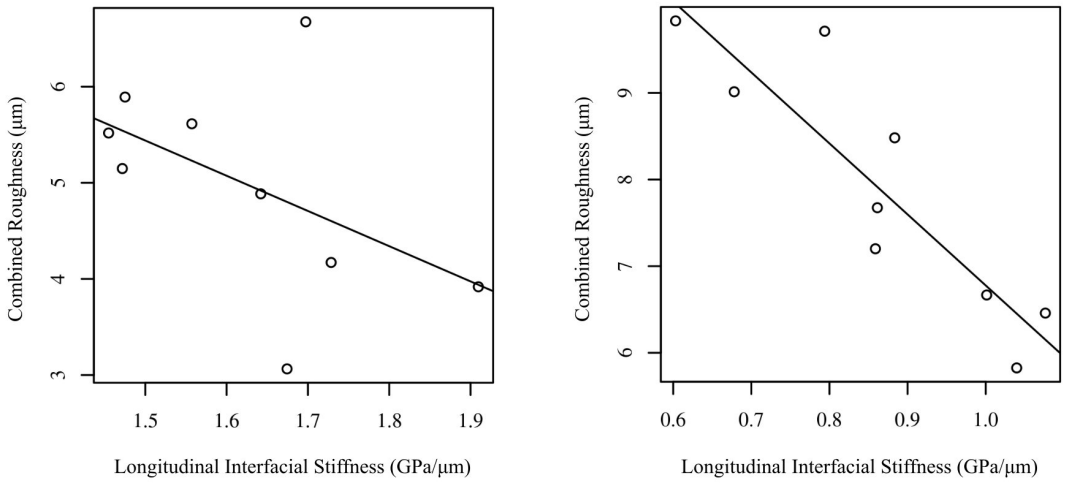

(a) LIR *(b) HIR*

Figure 6.52: Longitudinal interfacial stiffness vs combined roughness (Tests: 600MPa Dry)

Initial Roughness	***r***	***p***	$\boldsymbol{R^2}$	***B***	***SE***
LIR	-0.49	0.177	N/A	N/A	N/A
HIR	-0.89	0.001	0.80	-8.20	1.55

Table 6.10: Longitudinal interfacial stiffness vs combined roughness (Tests: 600MPa Dry)

The same analysis was performed for both the circumferential interfacial stiffness (K_C) and the radial interfacial stiffness (K_R) (see Figures 6.53 and 6.54). A similar

negative correlation was seen for K_C for the HIR tests and no correlation was seen for the LIR tests. No relationship between combined roughness and K_R was found for the dry tests.

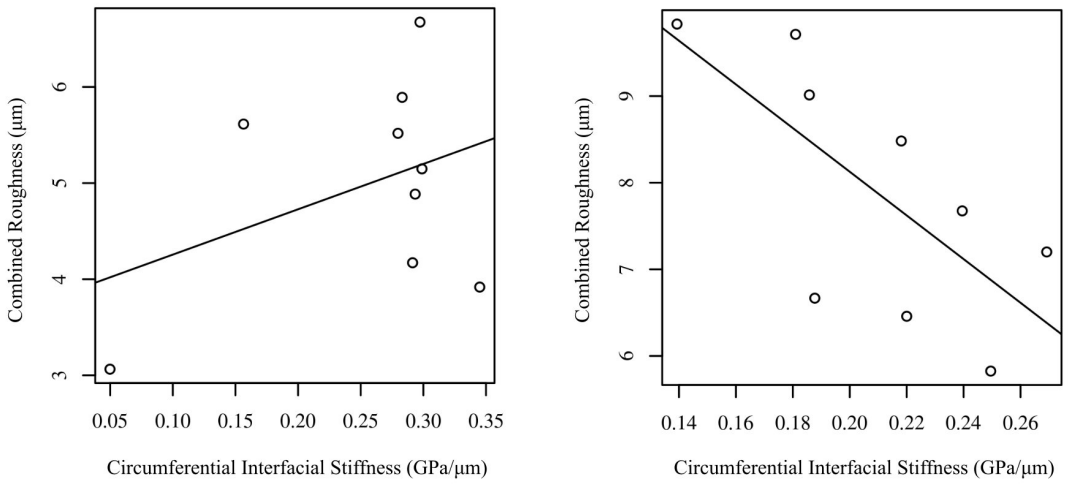

(a) LIR *(b) HIR*

Figure 6.53: Circumferential interfacial stiffness vs combined roughness (Tests: 600MPa Dry)

Initial Roughness	***r***	***p***	$\boldsymbol{R^2}$	***B***	***SE***
LIR	0.39	0.298	N/A	N/A	N/A
HIR	-0.70	0.037	0.49	-25.21	9.79

Table 6.11: Circumferential interfacial stiffness vs combined roughness (Tests: 600MPa Dry)

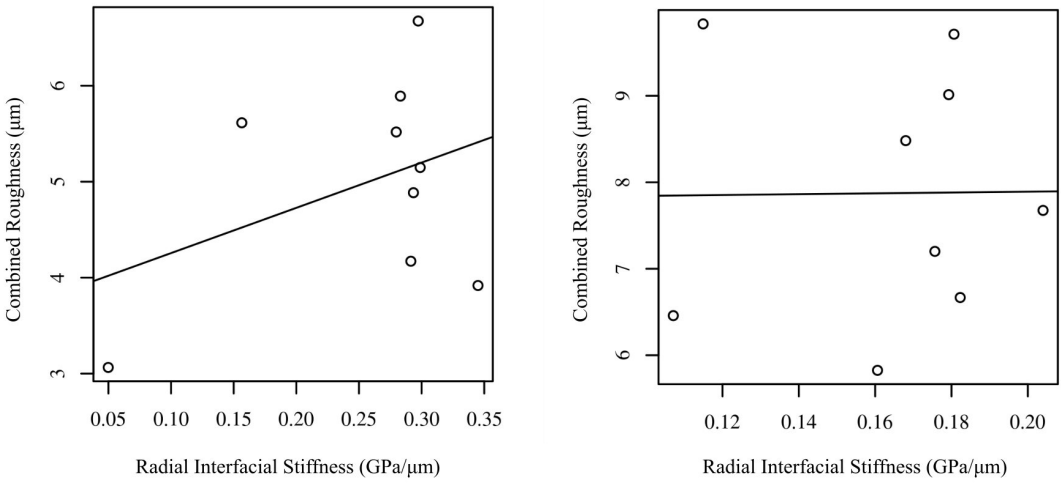

(a) LIR *(b) HIR*

Figure 6.54: Radial interfacial stiffness vs combined roughness (Tests: 600MPa Dry)

Initial Roughness	r	p	R^2	B	SE
LIR	0.41	0.269	N/A	N/A	N/A
HIR	0.01	0.978	N/A	N/A	N/A

Table 6.12: Radial interfacial stiffness vs combined roughness(Tests: 600MPa Dry)

6.2.2.2 Water

With the addition of water, K_L increases with increasing roughness for the HIR tests (see Figure 6.58). Whilst this may seem strange at first, it makes sense that as the roughness decreases, more water is present at the interface. Lower interfacial stiffnesses are expected if a 3BL is present: a rougher surface more closely mimics a dry surface as there is less contacting surface area for the 3BL to influence. No relationship was found between combined roughness and K_L for the LIR tests.

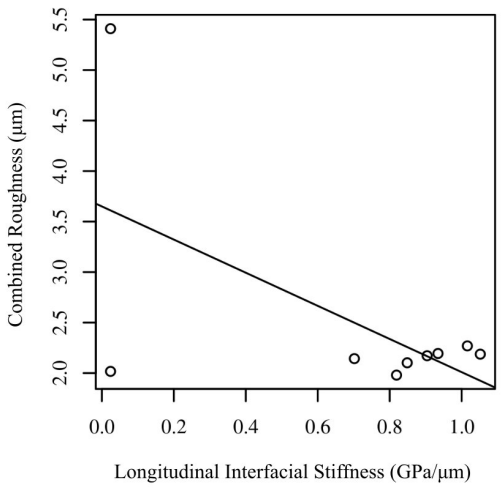

(a) LIR

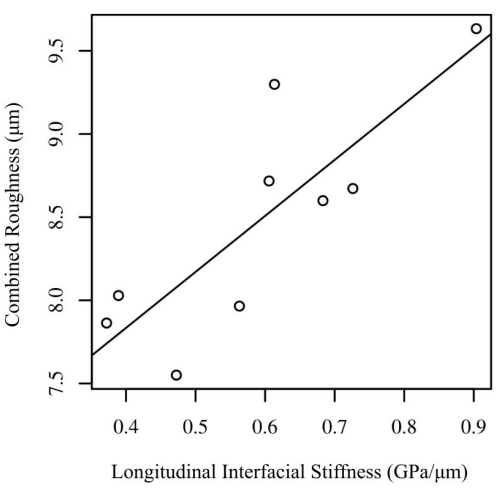

(b) HIR

Figure 6.55: Longitudinal interfacial stiffness vs combined roughness (Tests: 600MPa Water)

Initial Roughness	***r***	***p***	R^2	***B***	***SE***
LIR	-0.60	0.090	N/A	N/A	N/A
HIR	0.82	0.006	0.68	3.37	0.88

Table 6.13: Longitudinal interfacial stiffness vs combined roughness (Tests: 600MPa Water)

No correlation between K_C and combined roughness was found for either the HIR or LIR tests.

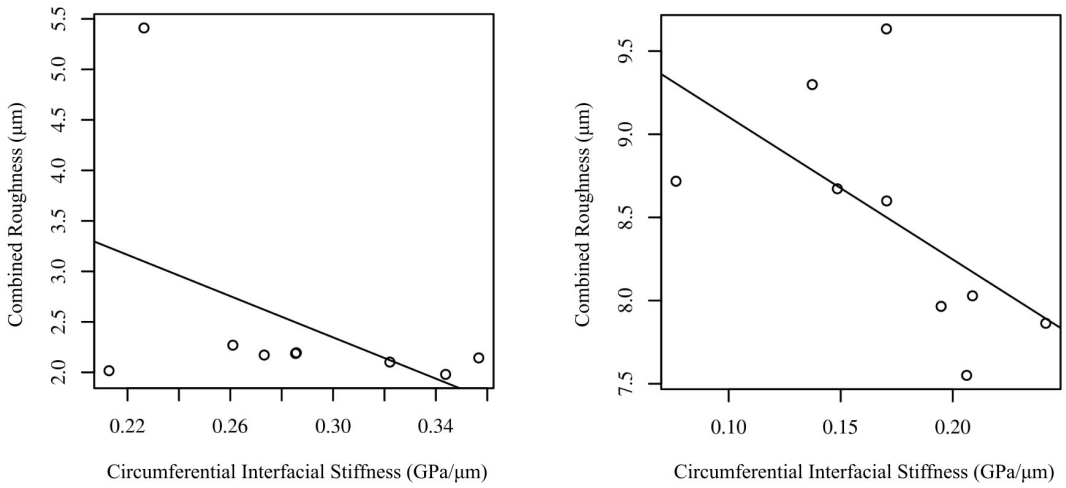

(a) LIR *(b) HIR*

Figure 6.56: Circumferential interfacial stiffness vs combined roughness (Tests: 600MPa Water)

Initial Roughness	***r***	***p***	R^2	***B***	***SE***
LIR	-0.46	0.215	N/A	N/A	N/A
HIR	-0.60	0.088	N/A	N/A	N/A

Table 6.14: Circumferential interfacial stiffness vs combined roughness (Tests: 600MPa Water)

A correlation was found between K_R and combined roughness for the HIR water tests however it is difficult to say if this would occur for every test (see Figure 6.57). The nature of 3BLs mean that interfacial stiffness measurements can be made with or without the 3BL present. This means that one sensor could be measuring very different interfacial conditions to its neighbouring sensor.

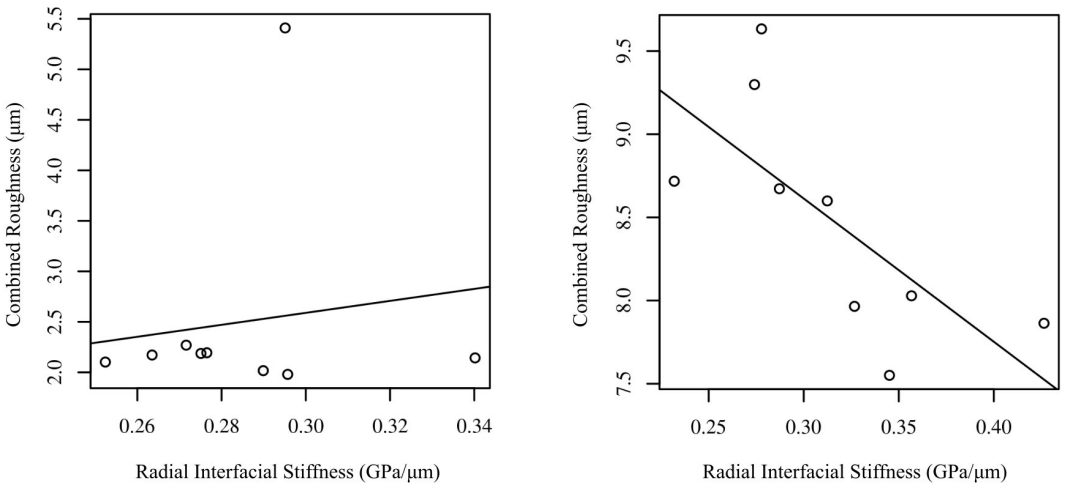

(a) LIR *(b) HIR*

Figure 6.57: Radial interfacial stiffness vs combined roughness (Tests: 600MPa Water)

Initial Roughness	***r***	***p***	R^2	***B***	***SE***
LIR	0.14	0.725	N/A	N/A	N/A
HIR	-0.71	0.032	0.51	-8.61	3.22

Table 6.15: Radial interfacial stiffness vs combined roughness (Tests: 600MPa Water)

6.2.2.3 Grease

No significant correlations were found between the combined roughness and interfacial stiffness for grease tests. This is most probably due to the grease disturbing the interfacial measurements which rely on a metal-metal contact to work best. The Interfacial stiffness results could have been evaluated further by separating the interface into metal and 3BL component parts, but this was beyond the scope for this work. 3BLs with high viscosities such as grease and leaves act as a matching layer between the two bodies which are not expelled when the surfaces are brought together under load. Full separation was not always achieved, especially when the surfaces were rough which meant measurements were taken with varying amounts of grease in the interface. Ultrasonic measurements rely on a reference measurement which is taken when the surfaces are unloaded. This reference is also taken with varying amounts of grease on the surface before each cycle. It is therefore difficult to determine whether changes in the interfacial stiffness are correct.

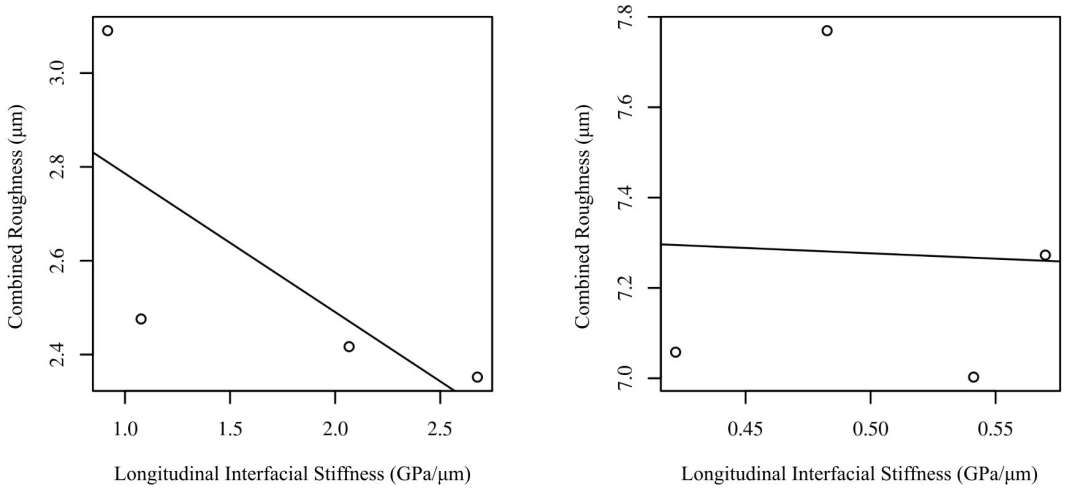

(a) LIR *(b) HIR*

Figure 6.58: Longitudinal interfacial stiffness vs combined roughness (Tests: 600MPa Grease)

Initial Roughness	r	p	R^2	B	SE
LIR	-0.72	0.279	N/A	N/A	N/A
HIR	-0.04	0.956	N/A	N/A	N/A

Table 6.16: Longitudinal interfacial stiffness vs combined roughness (Tests: 600MPa Grease)

6.2.2.4 Leaves

No statistical analysis was conducted due to lack of roughness data points.

6.2.3 Average Traction Coefficient vs Interfacial Stiffness

One of the desirable outcomes from this work was a correlation between interfacial stiffness and the traction coefficient. Traction coefficients are a primary factor in how effectively and safely a railway is run. The interfacial stiffness is remotely and non-destructively measurable using ultrasonics, meaning if a correlation between the two can be found, inference of the traction coefficient through ultrasonic measurement is possible. Longitudinal, circumferential and radial interfacial stiffness were all

compared with the traction coefficient. Since the interfacial stiffness data was only captured at 600MPa, they have only been compared at this pressure.

6.2.3.1 Dry

Both the LIR and HIR tests showed a negative correlation with the traction coefficient, however for low roughnesses this correlation was more pronounced (see Figure 6.59).

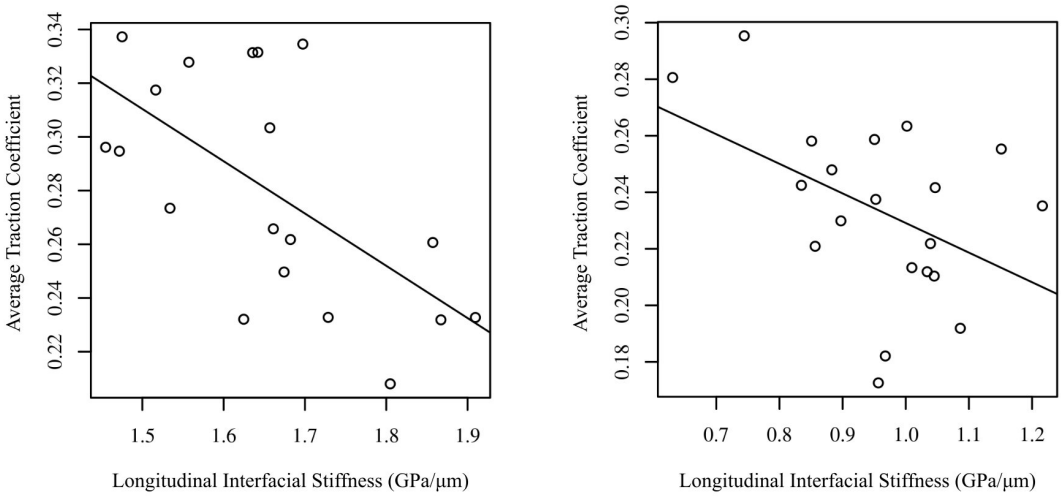

(a) LIR *(b) HIR*

Figure 6.59: Average traction coefficient vs longitudinal interfacial stiffness (Tests: 600MPa Dry)

Initial Roughness	***r***	***p***	R^2	***B***	***SE***
LIR	-0.62	0.004	N/A	N/A	N/A
HIR	-0.45	0.045	0.21	-0.10	0.05

Table 6.17: Average traction coefficient vs longitudinal interfacial stiffness (Tests: 600MPa Dry)

Overall very little correlation was found between shear interfacial stiffness and the traction coefficient. They have been included for the dry tests (see Figures 6.60 and 6.61), but after this they are omitted. It was expected that the shear stiffness would be impacted by tractive forces at the interface, however this was found not to be the case.

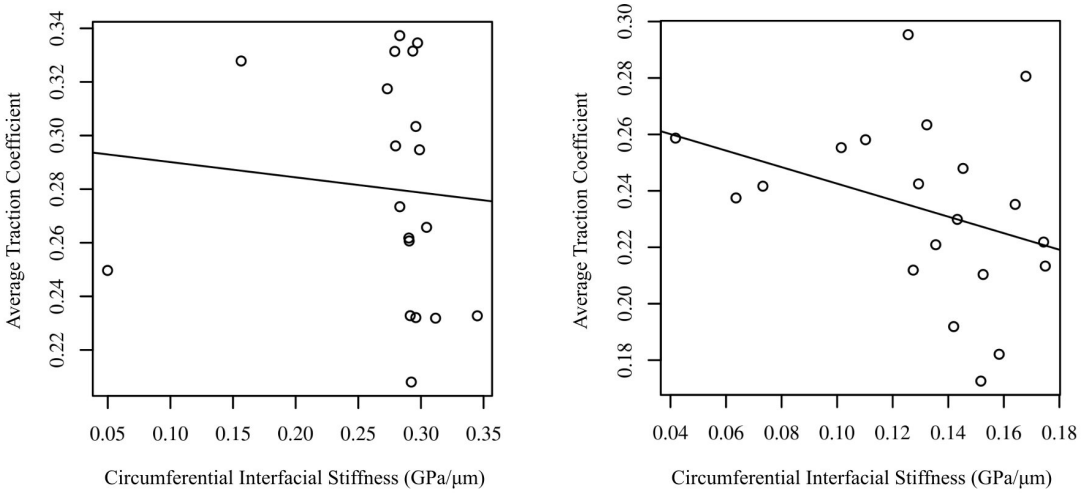

(a) LIR *(b) HIR*

Figure 6.60: Average traction coefficient vs circumferential interfacial stiffness (Tests: 600MPa Dry)

Initial Roughness	r	p	R^2	B	SE
LIR	-0.09	0.723	N/A	N/A	N/A
HIR	-0.34	0.141	N/A	N/A	N/A

Table 6.18: Average traction coefficient vs circumferential interfacial stiffness (Tests: 600MPa Dry)

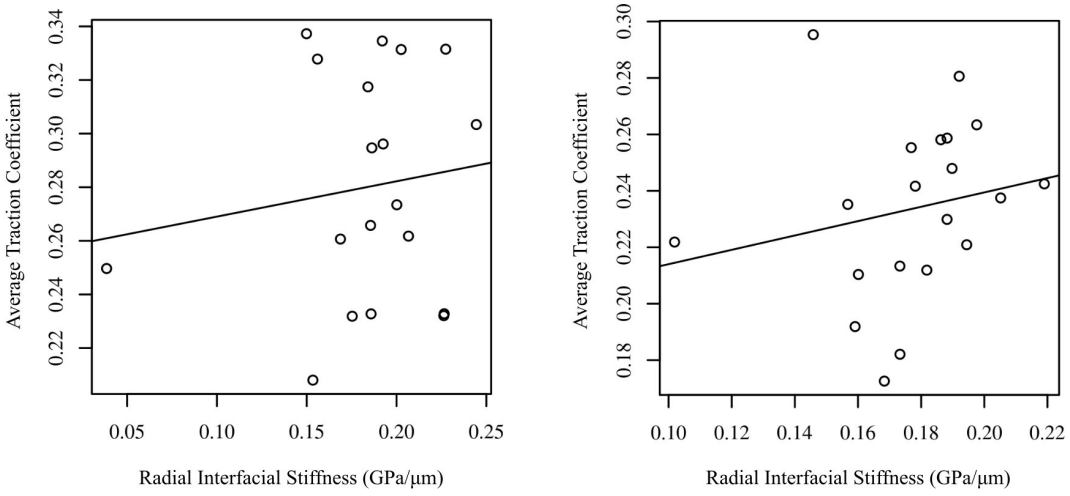

(a) LIR *(b) HIR*

Figure 6.61: Average traction coefficient vs radial interfacial stiffness (Tests: 600MPa Dry)

Initial Roughness	r	p	R^2	B	SE
LIR	0.14	0.577	N/A	N/A	N/A
HIR	0.20	0.395	N/A	N/A	N/A

Table 6.19: Average traction coefficient vs radial interfacial stiffness (Tests: 600MPa Dry)

6.2.3.2 Water

Figure 6.62 shows the correlation between the traction coefficient and the longitudinal interfacial stiffness for water tests. No correlation was found for the HIR tests, but a strong negative correlation was found for the LIR tests.

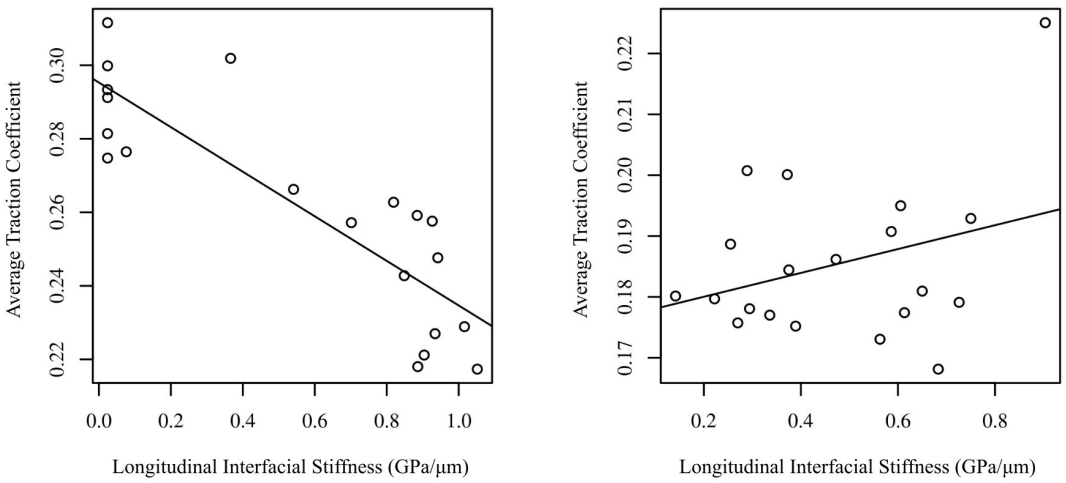

(a) LIR *(b) HIR*

Figure 6.62: Average traction coefficient vs longitudinal interfacial stiffness (Tests: 600MPa Water)

Initial Roughness	***r***	***p***	R^2	***B***	***SE***
LIR	-0.86	0.001	0.74	-0.06	0.008
HIR	0.32	0.172	N/A	N/A	N/A

Table 6.20: Average traction coefficient vs longitudinal interfacial stiffness(Tests: 600MPa Water)

6.2.3.3 Grease

Figure 6.63 shows the correlation between the traction coefficient and the longitudinal interfacial stiffness for grease tests. No correlation was found for the HIR tests, but a strong negative correlation was found for the LIR tests.

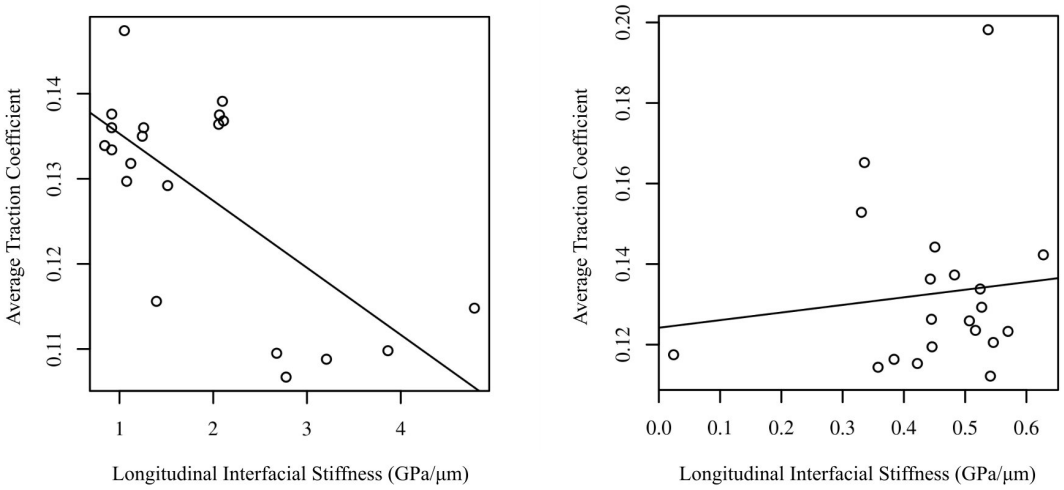

(a) LIR *(b) HIR*

Figure 6.63: Average traction coefficient vs longitudinal interfacial stiffness (Tests: 600MPa Grease)

Initial Roughness	r	p	R^2	B	SE
LIR	-0.70	0.001	0.48	-0.008	0.002
HIR	0.12	0.623	N/A	N/A	N/A

Table 6.21: Average traction coefficient vs longitudinal interfacial stiffness (Tests: 600MPa Grease)

6.2.3.4 Leaves

Figure 6.64 shows the correlation between the traction coefficient and the longitudinal interfacial stiffness for leaf tests. No correlation was found for the HIR or LIR tests. This was unlike the dry, water and grease tests. Leaf layers are often patchy with portions of the interface covered and others left exposed. The interfacial stiffness is measured over a small portion of the interface which may be covered at times and not at others, making linking it to the traction coefficient difficult.

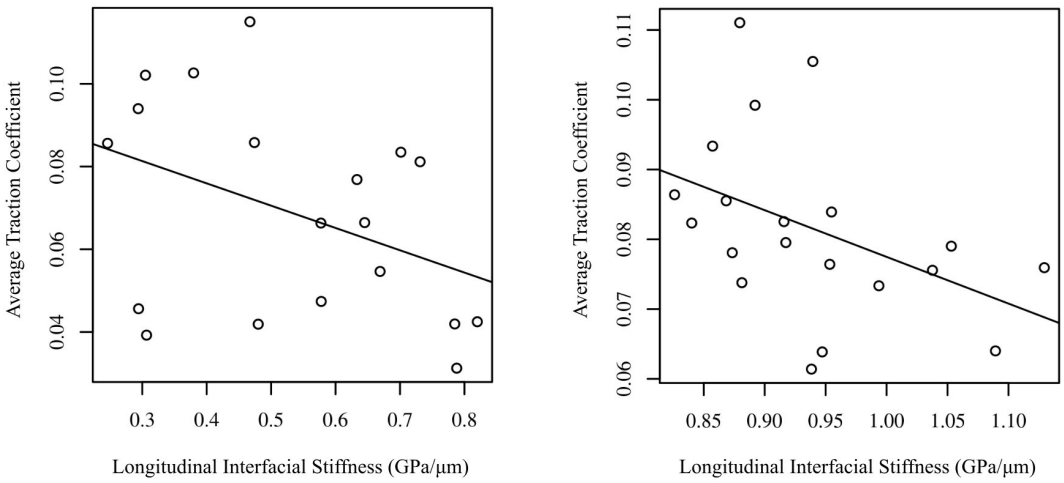

(a) LIR *(b) HIR*

Figure 6.64: Average traction coefficient vs longitudinal interfacial stiffness (Tests: 600MPa Leaves)

Initial Roughness	***r***	***p***	R^2	***B***	***SE***
LIR	-0.40	0.085	N/A	N/A	N/A
HIR	-0.43	0.057	N/A	N/A	N/A

Table 6.22: Average traction coefficient vs longitudinal interfacial stiffness (Tests: 600MPa Leaves)

6.2.4 Summary

Statistical analysis was performed to ascertain whether there were any statistically significant relationships between friction, roughness and interfacial stiffness. To study how roughness impacts these parameters the HIR tests were of greater interest, as these changed in roughness as they were run-in. Some conclusions are outlined below:

- Traction coefficient and combined roughness are linked and showed a strong positive correlation for dry HIR tests across all pressures.
- Traction coefficient and combined roughness are linked and showed a strong positive correlation for grease HIR tests at lower pressures.

- Traction coefficient and combined roughness are not linked and showed no correlation for water tests.
- Longitudinal interfacial stiffness and combined roughness are linked and showed a strong negative correlation for dry 600MPa HIR tests.
- No consistent correlations were found between interfacial stiffness and combined roughness for any other tests.
- No consistent correlation was found between Interfacial stiffness and the traction coefficient.

6.3 FSR Results

Full-scale testing was conducted with the use of rail inserts that had specific surface textures applied to them. These processes were fly cutting to produce the high initial roughness (HIR) surfaces and grinding to produce the low initial roughness (LIR) surfaces. These surfaces had 3BLs applied to them to mimic conditions on track. The purpose of the full-scale testing was to validate the outputs of the ECF model as well as to provide a more realistic idea of roughness progression that included true geometrical effects. During the FSR tests, 100kN normal load was applied with 2% slip. When the contact patch size was assessed, this equated to around 900MPa of contact pressure. As slip was set to 2%, the outputted traction coefficients should be representative of a close to full-slip regime.

6.3.1 Roughness

Roughness was measured regularly up to 20 cycles as with the HPT tests. The resultant combined roughness evolutions are shown in Figure 6.65. These show similar roughness evolutions to the HPT tests, however much of the combined roughness is reduced in just the first cycle. It is possible that the hardness of the wheel contributed to this, having already been run-in and work hardened. Wheel roughness was similar to the wheel specimen used in the HPT tests, however due to the higher hardness, the rail insert roughness decreased more quickly without suffering any of the roughness transfer seen in the HPT tests where specimen hardness was closely matched.

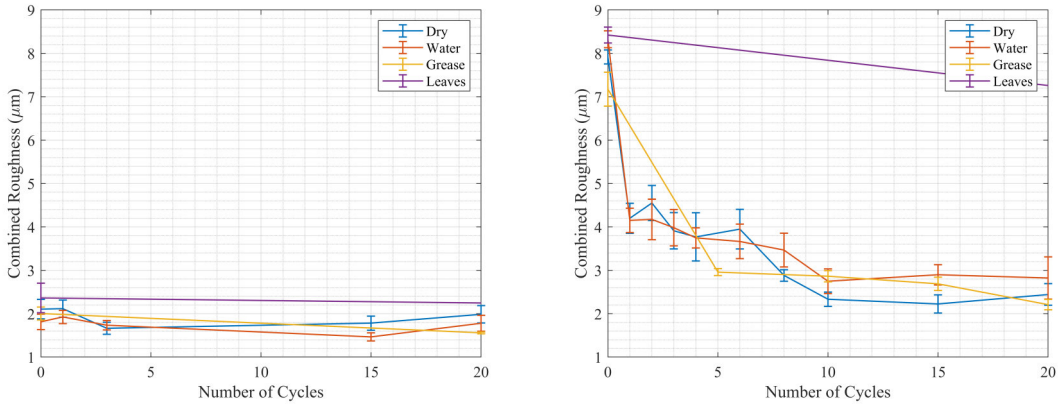

(a) LIR *(b) HIR*

Figure 6.65: FSR combined roughness ($S_{q\sigma}$) evolution (20 cycles)

One of the advantages of the FSR is the capacity to run many cycles with relative ease. Figure 6.66 shows the same roughness progression for up to 100 cycles. Roughness was measured again at 60 cycles and again at 100 cycles for all but the leaf tests. It can be seen, however, that the surfaces have been predominantly run-in by cycle 20 for the HIR tests. By cycle 100 the measured roughness values were very similar to those of the LIR tests. Most trains in the UK do not exceed 10-12 carriages: this is due to due to the length of many platforms in the UK. Each carriage has two bogies and each bogie has two wheels on each rail. This means that rough track is smooth after just two passenger train passes and perhaps only a single freight train pass. This represents a step forward in our understanding of railway roughness evolution whereby previously run-in roughness was measured in days not individual trains [9].

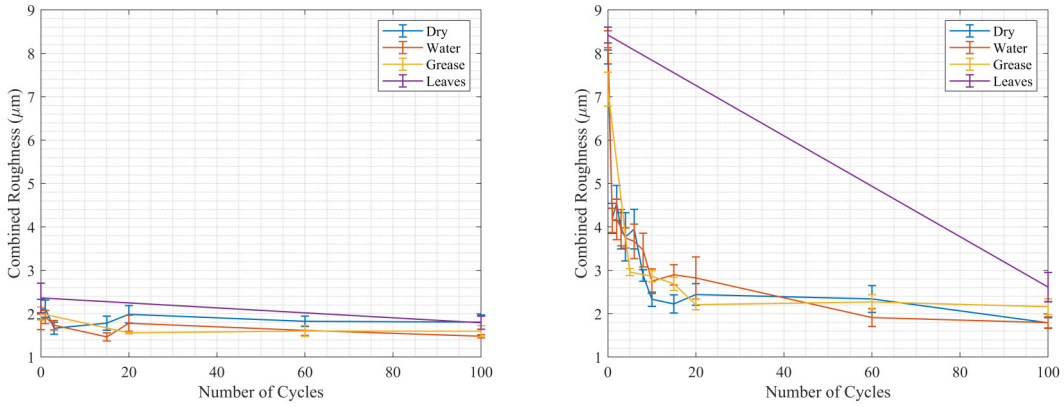

(a) LIR *(b) HIR*

Figure 6.66: FSR combined roughness ($S_{q\sigma}$) evolution (100 cycles)

It is worth noting that this roughness reduction occurred only on a single running band by presenting the same section of wheel to the same section of rail 100 times. Rail grinding is a procedure whereby the entire railhead is reprofiled, resulting in elevated roughness across the railhead. Every wheel is different and has its own interaction with the rail, resulting in a variety of running bands. This roughness evolution may take marginally longer on track. In addition, the roughness of certain sections of the railhead may remain elevated for long periods such as on the sides of the rail head. These sections are rarely used except on curves or where the VTI conditions are incorrect. When the wheel is in contact with these regions, the rail is not subject to as high loads, which from the results of the HPT tests, means longer run-in periods. High roughnesses may remain in these regions, which when paired with a specific wheel or VTI conditions, could produce conditions favourable to wheel climb.

6.3.2 Friction

The traction coefficient was measured throughout the FSR tests. Figures 6.67 to 6.70 show the responses based on the horizontal location of the rail. The average traction coefficient was evaluated over a 100mm window which was approximately the first 100mm of the rail insert. The same 3BLs were applied to these rail inserts as used in the HPT tests. The amounts of these 3BLs were increased by about 10x to account for the larger contact area (see Section 5.3.3). Whilst the inserts and the wheel were cleaned with acetone, it is clear that these tests were contaminated despite this. Extremely low traction coefficients were present when the wheel was not on the insert, despite these sections being cleaned as well. At lower cycles when roughness was measured frequently, the traction coefficients remained low (see Figure 6.67).

The process of measuring roughness and cleaning the surface influences the traction coefficient greatly. When left alone, the traction coefficients increased to levels you would expect to see for dry conditions, however it would be wrong to suggest that these interfaces are completely free from contaminants. Unnatural contaminants such as the replication compound are replaced by natural oxides over time. The majority of railways have a multitude of contaminants present. Traction coefficients on these stretches are typically between 0.25 and 0.3 [91]. It is clear, however, that the traction coefficients did not reach a steady state with the potential exception of the grease tests. This was believed to be caused by the continued contamination of

the test rig and incorrect chain settings. The wheel was rotated to present a new unworn surface to the rail and in doing so, this effected the wheel balancing. It is possible that this altered the amount of initial load on the chain.

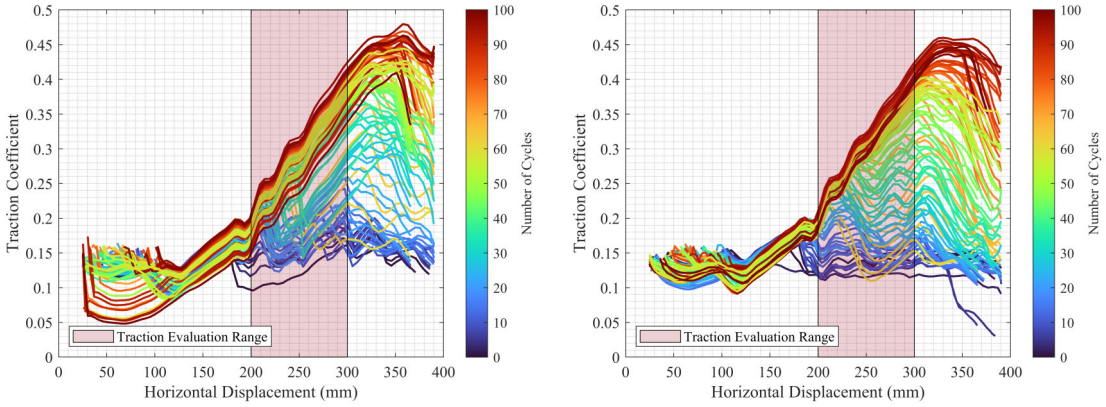

(a) LIR *(b) HIR*

Figure 6.67: Dry FSR test traction coefficient progression

The amount of water in the interface affects the traction coefficient, however due to its low viscosity and the heat generated during a test, it is either expelled from the interface or evaporates. A means of adding water continuously during tests was not set up, so intermittent hydration occurred at various intervals (see Section 5.3.4). In addition, tests were stopped to measure the roughness, this meant water had to be removed and reapplied during these intermissions. At lower cycles where hydration occurred frequently, traction coefficients remained low, similar to those of twin disc tests [7]. This was also the case for the dry tests, therefore it seems reasonable that although it is known that small amounts of water reduce traction, the contamination as a whole and the poor wheel balancing were greater influences. It is suspected that the low traction coefficients were caused by contamination and the climbing traction response was caused by the incorrectly balanced wheel and a rising chain load during the test. It seems that the slip was not kept constant during these tests. Expense and limited time meant they could not be repeated.

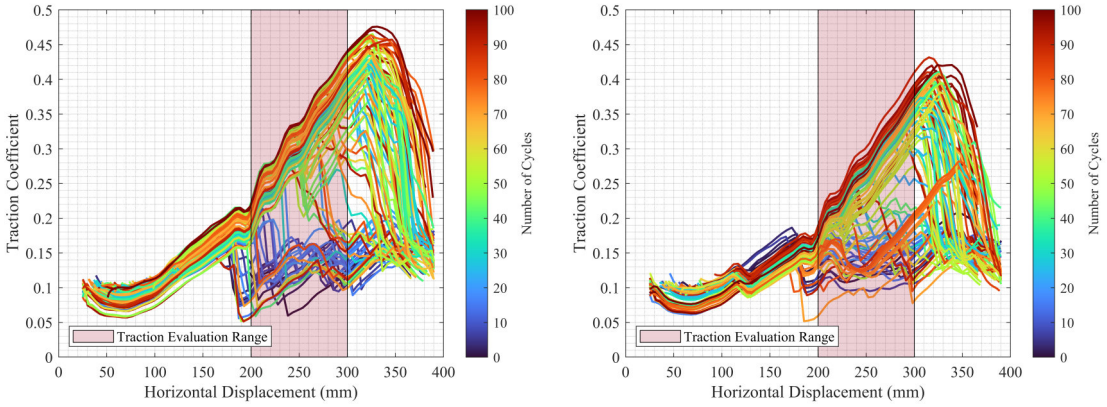

(a) LIR *(b) HIR*

Figure 6.68: FSR water traction coefficient evolution

It is clear that disturbing the interface by removing and reapplying 3BLs and taking replicas contaminates the interface, thereby lowering the traction coefficient. During the grease tests, where the interface is intentionally contaminated, the tractive response is most consistent (see Figure 6.69). What is more, when roughness is high, elevated traction coefficients are observed like the HPT tests. This only occurs in the first 10 cycles when roughness levels are higher.

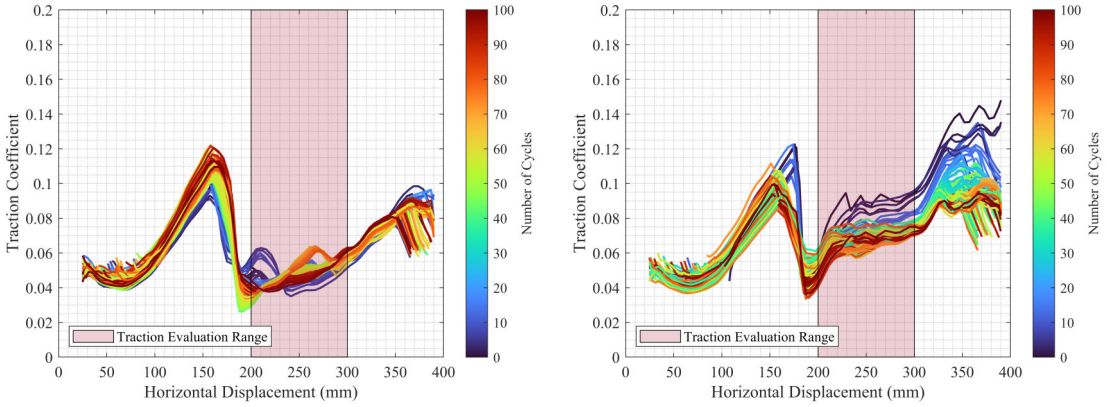

(a) LIR *(b) HIR*

Figure 6.69: FSR grease traction coefficient evolution

Leaf tests showed the most erratic and localised response (see Figure 6.70). Leaf layers were produced whilst roughness evolved and full coverage was not achieved. The leaf material was applied to the rail, however most of the leaf material was transferred to the wheel. This meant patches of the running band were covered

and patches were left clear. When the entire contact amounts to just $10mm^2$, the interfacial conditions the wheel and rail experience change quickly. Traction coefficients react correspondingly to these rapid changes in surface conditions.

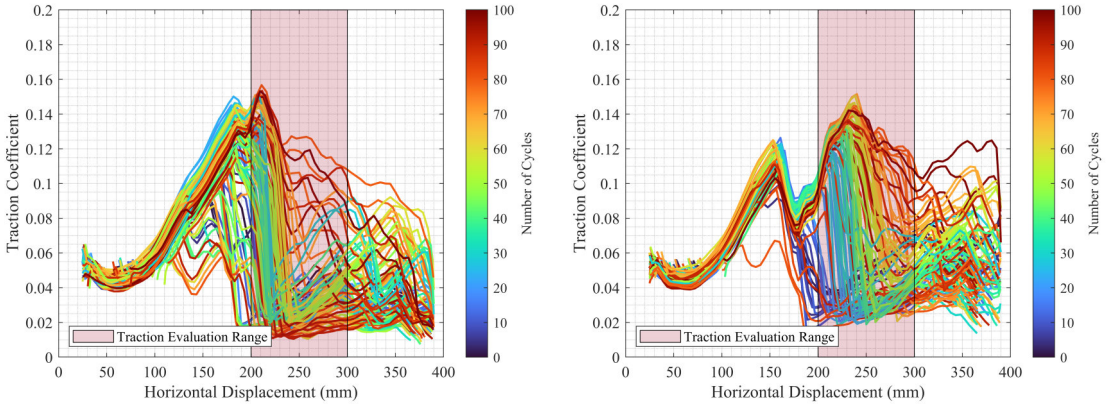

(a) LIR *(b) HIR*

Figure 6.70: FSR leaf traction coefficient evolution

The average traction coefficients were obtained by averaging the traction coefficient over a 100mm stretch of rail insert. The traction coefficient averages can be seen in Figure 6.71.

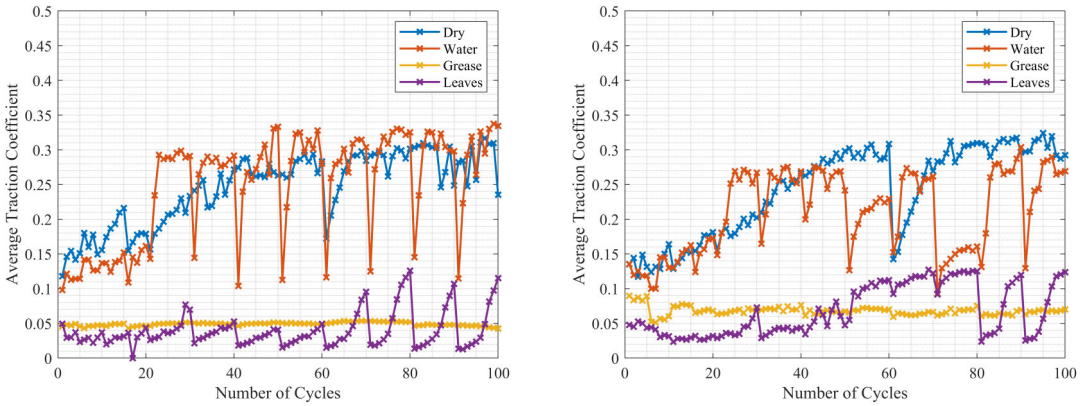

(a) LIR *(b) HIR*

Figure 6.71: FSR average traction coefficient evolution

Dry and water tests showed a similar traction response with the exception that the application of water reduced the traction coefficient significantly for a short period. This was less noticeable for the HIR tests whereby the troughs allowed the water to be removed from the contacting asperities. This water was quickly expelled from

the interface and the traction coefficient returned to those of dry levels after just a few cycles. The levels to which the traction coefficient dropped when water was applied were similar to those found for wet contacts in other work [7]. The traction coefficients for dry tests were lower than expected, possibly due to contamination at the interface and incorrect chain settings. Both grease and leaf tests showed much lower traction coefficients than the dry and water tests as expected. The application of water to the leaf layer reduced the traction coefficient, but as these dried the traction coefficient returned to high levels. The HIR tests provided troughs for grease to sit in during early cycles which resulted in higher traction coefficients. As these surfaces were run-in, these troughs became shallower and therefore had less effect; the traction coefficients more closely mirrored the LIR tests at higher cycles.

6.3.3 Laser Scanning

In addition to the highly accurate surface roughness scans, laser scans were made of the FSR specimens using a Creaform Handyscan and VXscan. This was done to assess how the wheel interacted with the specimens and how the specimens deformed over the course of a test. A reference scan was made before testing and another scan was made after 100 cycles. The scans were then processed using VXmodel and VXinspect. The 'before' and 'after' scans were then laid on top of one another and colormaps were created to see how the specimens had changed. This was used to inform decisions on contact patch size and where on the specimens to measure roughness and friction. Figure 6.72 shows the colour map for the HIR dry test. Green represents surface with little change from the reference scan, blue represents surface below the reference scan and red represents surface above the reference scan. In this way the material flow can be seen. A clear running band is visible along the top of the specimen. Another running band is evident at the very edge of the top of the specimen. This was most likely caused by a double contact due to the wear on the wheel. Either side of these running bands material is deformed upwards.

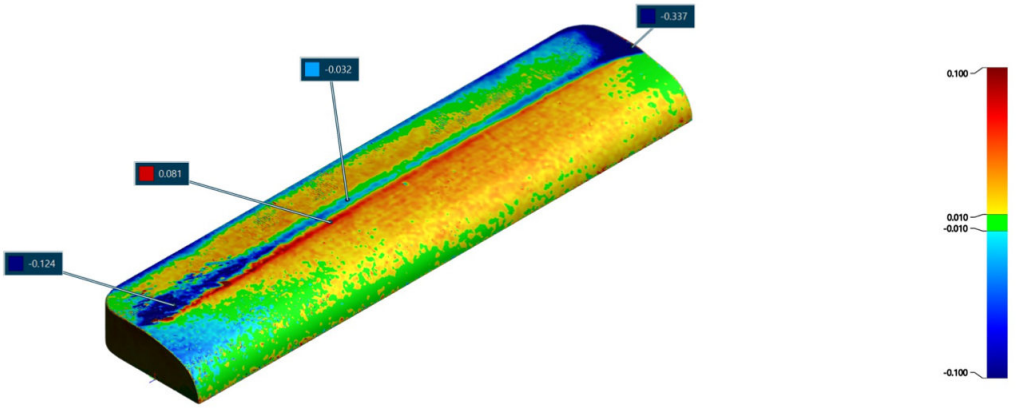

Figure 6.72: FSR specimen scan colourmap (Test: 900MPa HIR Dry)

Due to manufacturing tolerances, the specimens were made to be slightly smaller than the pockets they were inserted into. This meant there was a small gap between the rail and the insert. As the wheel rolls onto the unconstrained specimen, the specimen deformed by up to 0.5mm which was not representative of the entire specimen (see Figure 6.73). To avoid this, the roughness measurement locations were set back by 10mm from the edge. The traction coefficients were averaged over the central 100mm of the specimens as this was when the VTI was most consistent.

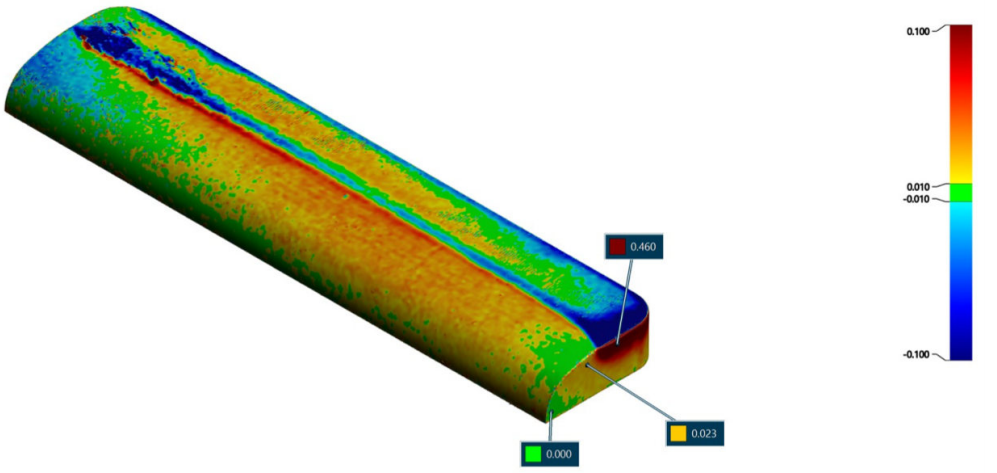

Figure 6.73: FSR specimen scan colourmap (Test: 900MPa HIR Dry)

6.4 HPT vs FSR

The HPT test results are compared to the FSR test results in the following section. The FSR tests were conducted at a fixed normal load of 110kN which equated to roughly 900MPa, therefore only the 900MPa HPT tests were compared to the FSR results.

6.4.1 Roughness

The roughness evolutions for the LIR and HIR tests for both the HPT and FSR test procedures were compared in this section. There were a few immediately obvious differences. The first being the initial roughness applied from the fly cutting processes. This was due to the curved geometry of the FSR specimens. As the surface dropped away, the tool cut less deeply into the specimen. Roughness was measured at three locations across the running band. The central roughness measurement was consistently the higher than the two outer measurements. The FSR initial roughness was lower than for the HPT tests. Another distinguishing factor was the nature of the wheel material. The FSR wheel and HPT wheel specimens had similar initial roughnesses, however the FSR wheel was already run-in as it was used repeatedly (this is shown in Figure 6.74). As a result, the wheel was probably much harder than the rail specimen although this was not measured.

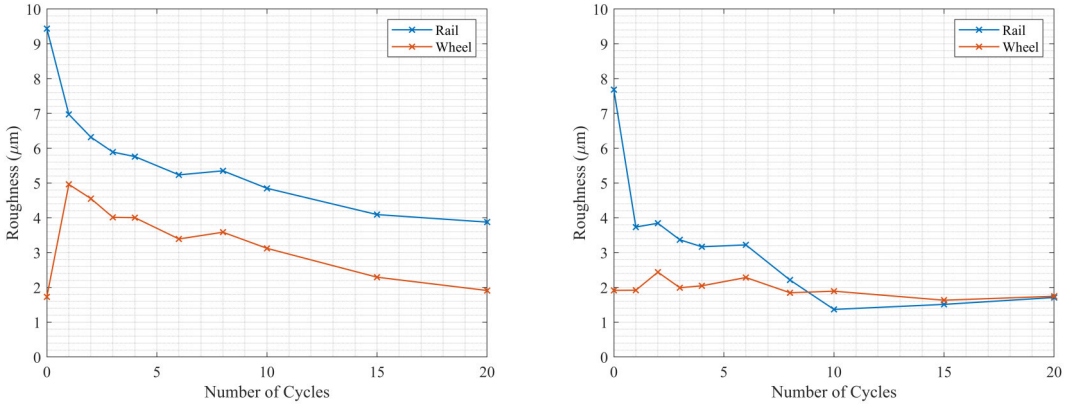

(a) HPT *(b) FSR*

Figure 6.74: Roughness transfer comparison between soft HPT specimen and hard FSR wheel

Roughness was transferred from one specimen to the other on the HPT tests as the

rougher material was pressed into the smoother material. The FSR tests show no such transfer: wheel roughness remains low and constant. The result is a steep initial decline in roughness and greater overall reduction in roughness. This is evident in every FSR test. Another observation from Figure 6.74 was the surface conformity after the first cycle. Surface conformity is defined in Equation 3.9 in Section 3.2.2. HPT test surfaces conform to one another quickly then remain relatively conformed. FSR test surfaces conform more slowly but ultimately have extremely similar roughnesses (see Figure 6.75). The more conformal surfaces are, the greater the true contact area.

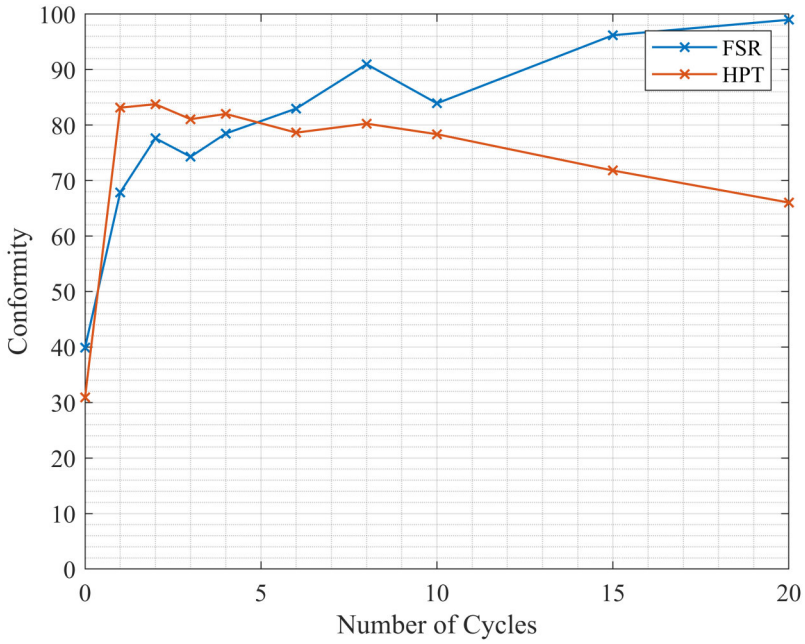

Figure 6.75: Surface conformity (Test: Dry HIR)

6.4.1.1 Dry

The combined roughness evolution for HIR dry tests is compared in Figure 6.76b. This shows that for the FSR tests, the roughness decreased twice as much as during the HPT tests after just the first cycle. The combined roughness reduces quicker at higher pressures as shown in the HPT results (see Figure 6.5). It is possible that there were slight differences in the contact pressures between the HPT and FSR tests which may have contributed to this. However, the large differences in roughness reductions are more likely to have been caused by the differences of the wheel specimen material. Whilst the hardness of the FSR wheel was not able to be measured, run-in surfaces are harder than surfaces that have not been run-in. This

hard surface is able to reduce the roughness of the softer material more effectively.

Figure 6.76a shows the combined roughness evolution for the LIR tests. For the HPT tests, roughness increases as material is removed and then entrained in the contacting surfaces. This third-body abrasive wear acts to increase the combined roughness. This increase happens gradually as more and more scratches are applied to the surfaces. Sudden large material removal is not seen at least in the roughness measurements. For the FSR tests, the combined roughness remained low. The geometry and the relative speeds of the contacting surfaces may act to eject any loose material or else the differing material properties may not have been conducive to this kind of wear.

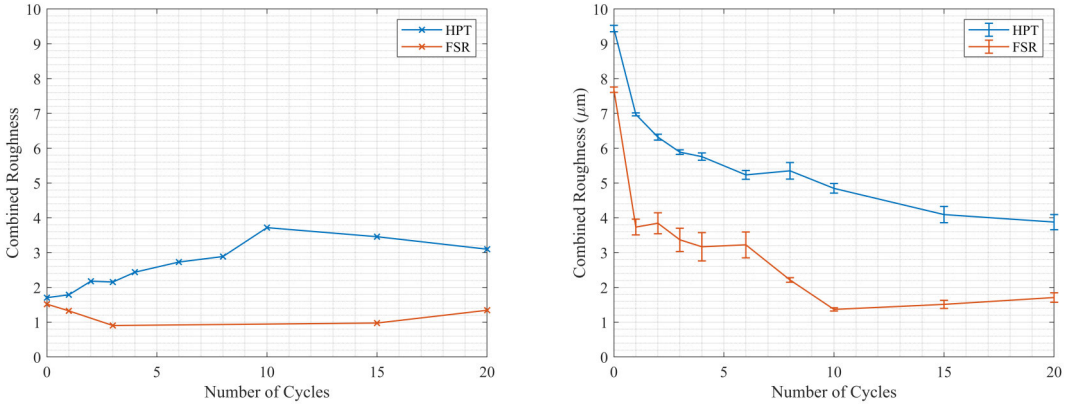

(a) LIR *(b) HIR*

Figure 6.76: HPT vs FSR wheel and rail roughness evolution (Test: 900MPa Dry)

6.4.1.2 Water

The combined roughness evolution for the HIR water tests is compared in Figure 6.77b. We see a similar pattern for both the HPT and the FSR tests: like the dry tests, larger roughness reductions are seen in the FSR tests. The majority of the roughness reduction occurs over just the first few cycles for both tests. Figure 6.77a shows the combined roughness evolution for the LIR water tests. The HPT test roughness remains low until cycle 10 at which point it increases. As roughness is only measured every 5 cycles at this point, it is difficult to say whether this happened suddenly (in just a single cycle) or over a number of cycles. It is expected that these roughness increases happened more quickly than those of the dry tests. During these tests, it was evident that the specimens were slipping, and visually the specimens incurred damage quite quickly in between cycles. The FSR roughness remains low

like the dry LIR FSR tests. It is possible that the contamination evident on the FSR may have reduced the wear these specimens incurred.

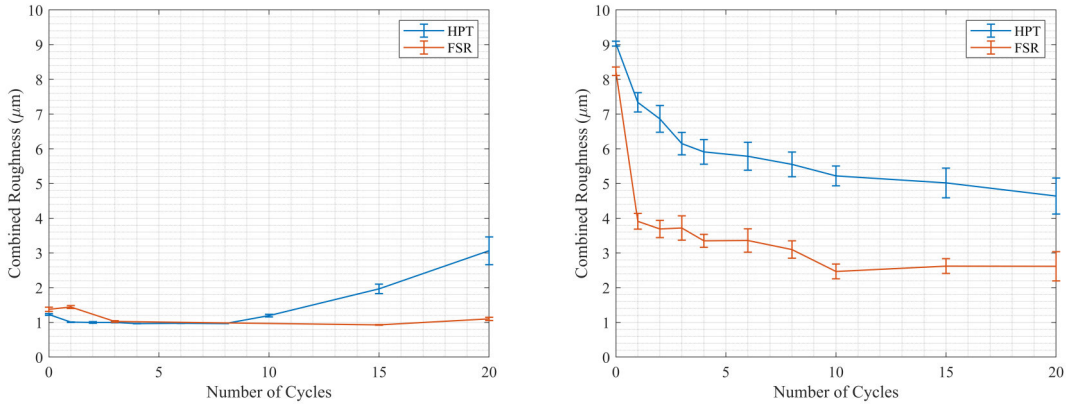

(a) LIR *(b) HIR*

Figure 6.77: HPT vs FSR wheel and rail roughness evolution (Test: 900MPa Water)

6.4.1.3 Grease

The combined roughness evolution for the HIR grease tests are compared in Figure 6.78b. The initial FSR roughness was much lower than the initial HPT roughness. The complex FSR specimen geometry made making consistent initial specimen roughnesses challenging. Despite this, the roughness evolutions look similar for both tests. Figure 6.78a shows the combined roughness evolution for the LIR grease tests. As both tests were purposely covered with grease, they were both well lubricated and so negligible wear was incurred during either test. The resulting roughness evolutions are remarkably similar.

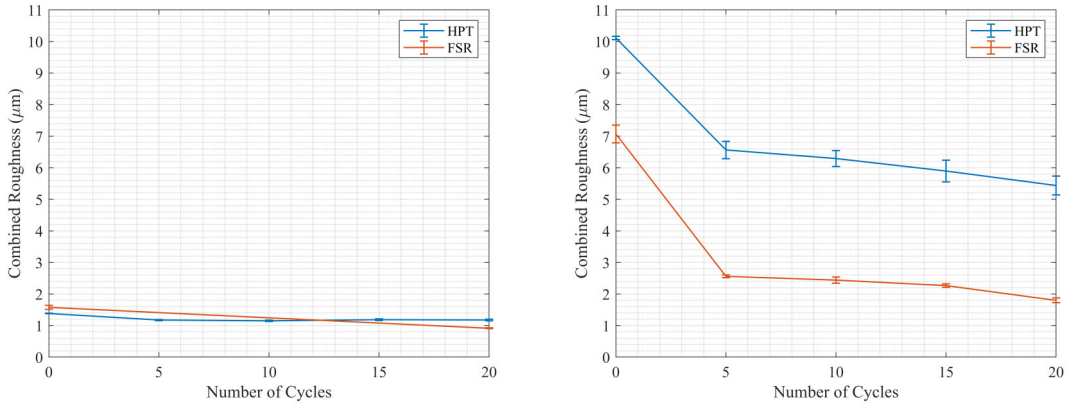

(a) LIR *(b) HIR*

Figure 6.78: HPT vs FSR wheel and rail roughness evolution (Test: 900MPa Grease)

6.4.1.4 Leaves

The combined roughness evolution for the HIR leaf tests is compared in Figure 6.79b. The roughness evolutions appeared similar for both tests, however it is difficult to predict how roughness progressed over 20 cycles for the FSR leaf tests as roughness was only measured at the start and after 100 cycles. It may be that like the other FSR tests, roughness is reduced very quickly. Figure 6.79a shows the combined roughness evolution for the LIR leaf tests. Again the roughness evolution looks similar, but it is difficult to be certain with no FSR roughness data point at 20 cycles.

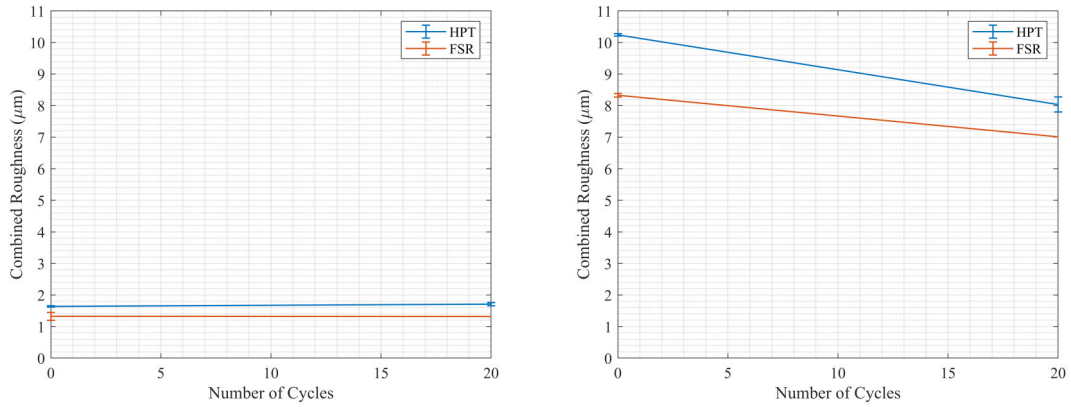

(a) HPT *(b) FSR*

Figure 6.79: HPT vs FSR wheel and rail roughness evolution (Test: 900MPa Leaf)

6.4.2 Friction

The average traction coefficients over the first 20 cycles for both the HPT and the FSR tests are compared in the following section. The 900MPa HPT tests were used as this contact pressure was most similar to that of the FSR tests.

6.4.2.1 Dry

The average traction coefficients for the LIR and HIR dry tests are shown in Figure 6.80. The average traction coefficients for the FSR tests were consistently lower than the HPT tests. HPT specimens were much easier to clean than the FSR specimens, meaning contamination was harder to remove for the FSR tests.

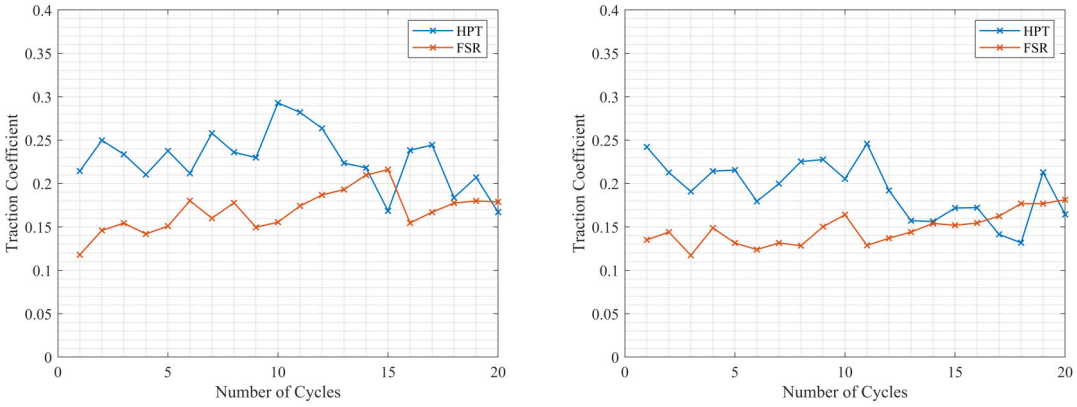

(a) LIR *(b) HIR*

Figure 6.80: HPT vs FSR average traction coefficients over the first 20 cycles (Test: 900MPa Dry)

6.4.2.2 Water

The average traction coefficients for the LIR and HIR water tests are shown in Figure 6.81. In addition to the FSR contamination, large differences in roughness between the HPT and FSR tests could have contributed to the much lower average traction coefficients seen for the FSR tests. Lower roughnesses meant more 3BL was present between the two surfaces, thereby lowering friction.

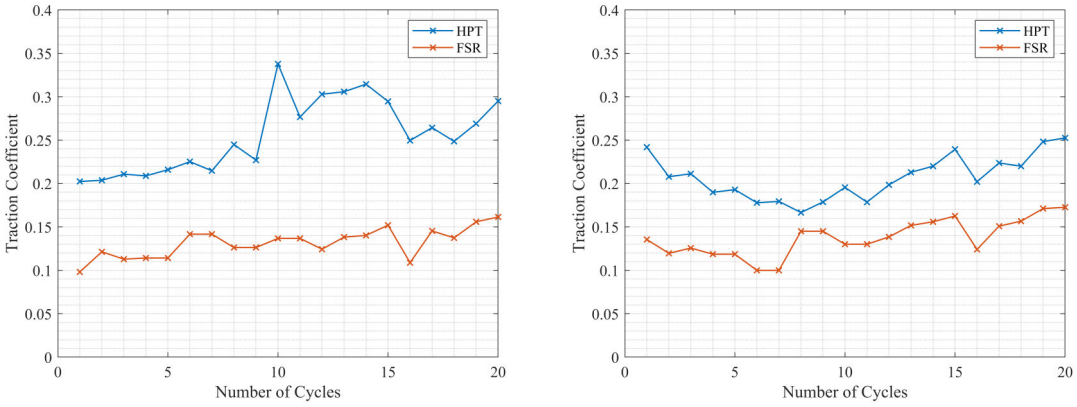

(a) LIR *(b) HIR*

Figure 6.81: HPT vs FSR average traction coefficients over the first 20 cycles (Test: 900MPa Water)

6.4.2.3 Grease

The average traction coefficients for the LIR and HIR grease tests are shown in Figure 6.82. Traction coefficients were similar to levels measured in other studies for grease tests [89]. Like the water tests, large differences in roughness between the HPT and FSR tests could have contributed to the much lower average traction coefficients seen for the FSR tests. Higher roughnesses were found to result in higher traction coefficients when grease was present. Large discrepancies in surface hardness for the FSR tests accelerated the rate at which roughness reduced. Lower roughnesses meant more 3BL was present between the two surfaces, thereby lowering friction.

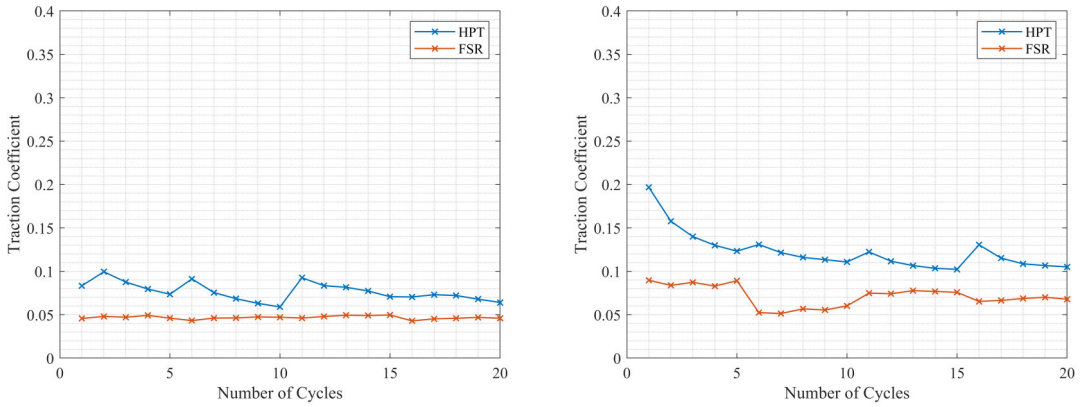

(a) LIR *(b) HIR*

Figure 6.82: HPT vs FSR average traction coefficients over the first 20 cycles (Test: 900MPa Grease)

6.4.2.4 Leaves

The average traction coefficients for the LIR and HIR leaf tests are shown in Figure 6.83. The traction coefficients are similar for both testing methods, however the traction coefficients for the FSR tests tend to decrease whilst the HPT tests increase. Roughness was found to disrupt the formation of leaf layers when analysing the HPT test results. As these tests remained at elevated roughness for longer than the FSR tests, the leaf layers were not able to develop as well for the HIR tests. During this time leaf material is removed from the interface. No additional leaf material was added during the first 20 cycles so the removal of leaf material raises the traction coefficient. The roughness reduction happens too quickly on the FSR tests; leaf layers develop quickly and the traction coefficients remain low.

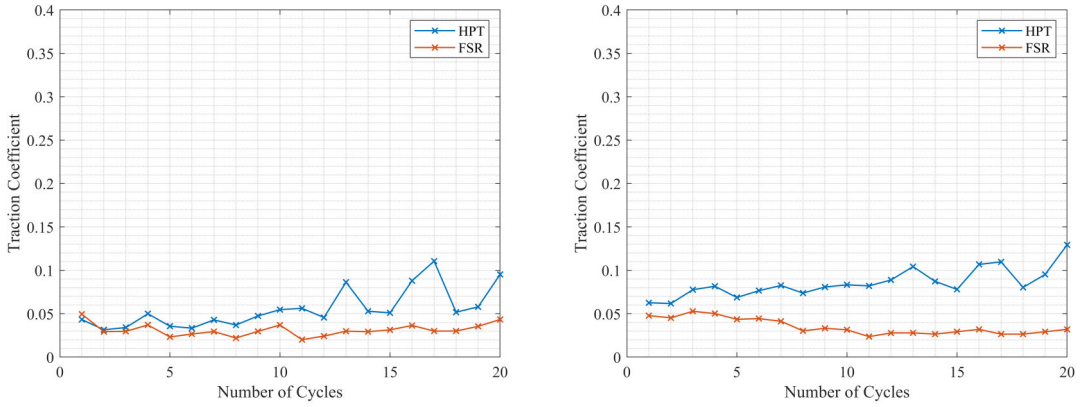

(a) LIR *(b) HIR*

Figure 6.83: HPT vs FSR average traction coefficients over the first 20 cycles (Test: 900MPa Leaf)

6.4.3 Summary

The FSR was used to best mimic a real-world wheel-rail interface. The loads and geometries were that which you would find on a typical rail network. Roughness was applied to rail inserts which were then loaded repeatedly by rolling the wheel over the rail, this was done 100 times for each interfacial condition. Roughness was measured at various intervals. The wheel had no roughness applied to it like the HPT wheel test specimens, however it was already run-in unlike the HPT specimens. The result was an extremely fast run-in, whereby the roughness decreased rapidly over just a few cycles. Very little roughness transfer was seen unlike the HPT tests due to the hardness of the FSR wheel. Issues with the FSR chain settings and frequent contamination from the taking of replicas produced lower, more erratic traction coefficients which made studying the effect of roughness challenging. The application of water temporarily lowered the traction coefficient, but soon returned to dry levels. Grease and leaves were retained throughout the tests maintaining very low traction coefficients.

7 Extended Creep-Force (ECF) Modelling

The following section reviews the ECF model and presents the outcomes from the modelling phase. The ECF model was selected from the range of creep-force models

outlined in Section 3.6 as it has the ability to reproduce features of real world creep curves: these include friction decrease at high creep rates, temperature dependency and the smooth transition from low to medium creep rates. The HPT small-scale test outputs were used to parameterise this model which can then be used to predict the full-scale outcomes. This has been done in previous work by Evans et al. [92].

7.1 Model Overview

The extended creep-force (ECF) model was developed by Meierhofer as part of their thesis [61]. Since then it has been used in a number of studies conducted by Meierhofer et al. and Six et al. [93] [94]. The ECF differs from its predecessors due to the inclusion of a third-body layer (3BL) sub-model. The 3BL within this sub-model consists of fluids and solid particles in between the wheel and rail, as well as the surface layers of wheel and rail, including asperities and micro-cracks. The wheel and rail either side of this 3BL are homogeneous, isotropic and ideally elastic.

When considering this 3BL at a macroscopic scale, it can be assumed to be homogeneous and isotropic. Elasto-plastic material characteristics apply within this 3BL which depend on the normal stress distribution and the local temperature. Normal stresses are Hertzian and local temperatures are calculated using an additional Erzt-based sub-model; these sub-models are time dependent, thereby allowing transient effects to be studied.

A brush model is used to describe the 3BL: a schematic of which can be seen in Figure 7.1. The 3BL consists of many independent bristles that are normal to the contact plane: B1 and B2 represent two bristles of the brush which are displaced by a distance u through the 3BL which has height h. A stress τ acts on each bristle. As each bristle moves through the contact, its respective displacement and stress increase [95].

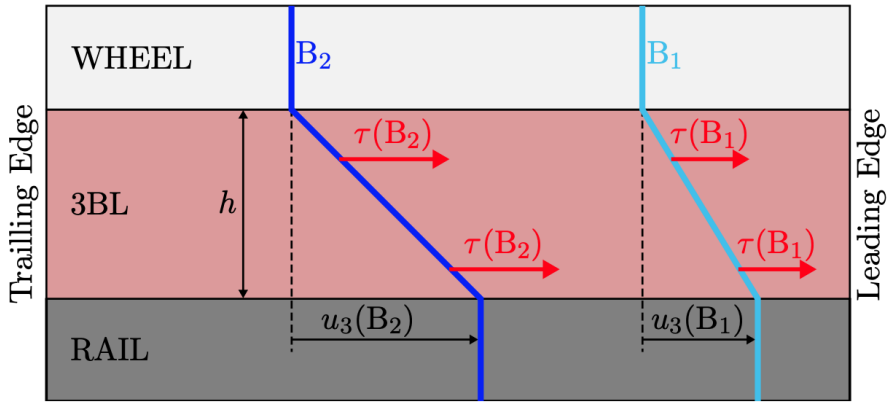

Figure 7.1: 3BL brush model schematic [61]

Each bristle behaves elastically when the tangential stresses $\vec{\tau} = (\tau_x, \tau_y)$ acting upon it are below a critical limit τ_{c1}. When this is the case, the resulting displacements of the bristles u_3 are calculated by using the flexibility coefficient (inverted stiffness) of the 3BL L_e (see Equation 7.1):

$$\vec{\tau} = \frac{u}{L_e} \; for \; |\vec{\tau}| < \tau_{c1} \tag{7.1}$$

When considering higher stresses, the bristles deform plastically. The resulting stresses are based on the Voce strain-hardening law [96] (see Equation 7.2):

$$|\tau| = \tau_{c1} + (\tau_{c2} + \tau_{c1}) \left[\frac{-|\vec{u}| + \Delta u}{L_p} \right] \; for \; \tau_{c1} < |\vec{\tau}| < \tau_{c2} \tag{7.2}$$

where L_p is the plasticity factor and τ_{c2} is the second critical shear stress. τ_{c2} cannot be exceeded due to the exponential nature of this law. To ensure a continuous transition from elastic to plastic behaviour $\Delta u = \tau_{c1} L_e$.

The resulting tangential stresses depend therefore on four parameters: L_e, L_p, τ_{c1} and τ_{c2}. These parameters describe the elasto-plastic material behaviour of each independent bristle. An example of their effects can be seen in Figure 7.2 whereby L_e influences the initial gradient for stresses lower than τ_{c1}, while L_p adjusts the shape of the strain hardening for stresses between τ_{c1} and τ_{c2}.

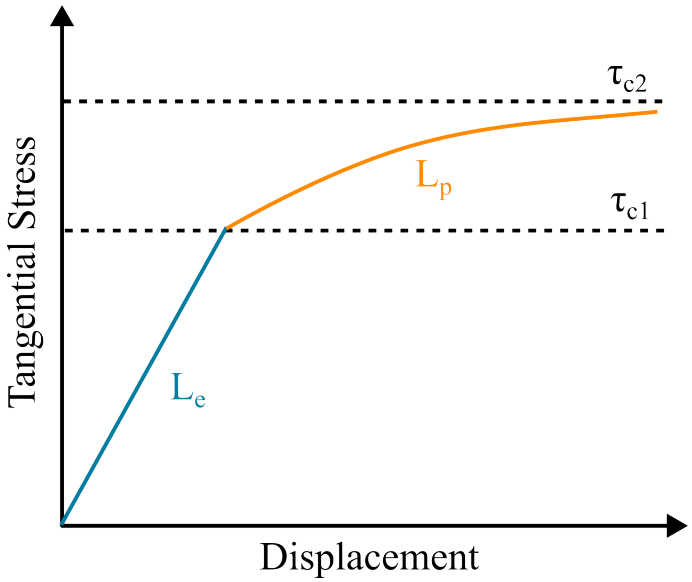

Figure 7.2: ECF model material parameters and their physical influence

These four material parameters are known to depend on both the normal stress p and localised temperature T. Both critical shear stresses are described in Equations 7.3 and 7.4:

$$\tau_{c1}(p,T) = \tau_{c1}^{0}\left[1 - exp(-p\tau_{c1}^{p})\right]\left[exp(-(T-T_0)\tau_{c1}^{T})\right] \tag{7.3}$$

$$\tau_{c2}(p,T) = \tau_{c2}^{0}\left[1 - exp(-p\tau_{c2}^{p})\right]\left[exp(-(T-T_0)\tau_{c2}^{T})\right] \tag{7.4}$$

where T_0 is the ambient temperature and τ_e^0, τ_e^p, τ_e^T, τ_p^0, τ_p^p, τ_p^T are constants. The critical shear stresses τ_{c1} and τ_{c2} are therefore characterised by nominal values τ_e^0 and τ_p^0, the pressure dependent values τ_e^p and τ_p^p and temperature dependent values τ_e^T and τ_p^T. Similarly the inverted stiffness and plasticity factor of the 3BL can be made dependent on the normal pressure and local temperature (see Equations 7.5 and 7.6):

$$L_e(p,T) = L_e^{0}\left[1 - exp(-pL_e^{p})\right]^{-1}\left[exp(-(T-T_0)L_e^{T})\right]^{-1} \tag{7.5}$$

$$L_p(p,T) = L_p^{0}\left[1 - exp(-pL_p^{p})\right]^{-1}\left[exp(-(T-T_0)L_p^{T})\right]^{-1} \tag{7.6}$$

where T_0 is the ambient temperature and L_e^0, L_e^p, L_e^T, L_p^0, L_p^p, L_p^T are constants. The inverted stiffness and plasticity (L_e and L_p respectively) are therefore characterised by nominal values Le^0 and Lp^0, the pressure dependent values Le^p and Lp^p and

temperature dependent values Le^T and Lp^T. It can be deduced from Equations 7.5 and 7.6 that L_e and L_p will increase with decreasing normal stress or increasing temperature.

These 12 constants can be identified experimentally. High pressure torsion (HPT) outputs were used to parameterise nominal and pressure dependent values by conducting HPT tests at three different normal pressures (600, 750 and 900MPa). The temperature dependent constant values were obtained by Meierhofer [61] from vehicle tests which enable the prediction of full-scale behaviour [82]. HPT tests were unable to parameterise these values as the temperature in which the HPT rig is situated was not controllable.

7.2 Parameterisation

As mentioned in Section 7.1, the ECF model is parameterised using outputs from the HPT tests. This involved an iterative process whereby the gradient and elasto-plastic limits of the tangential stress are found by inputting three HPT tests at different pressures into the ECF model parameterisation software and running the program over a number of numerical steps. To accomplish this, another parameter must be considered: the inverse shear stiffness of the HPT rig L_x. This is because the stiffness of the HPT rig is significant when compared to the stiffness of the 3BL. L_x was estimated when fitting the ECF model to the dry HPT data and was then kept constant for all the other test cases. In the previous work of Skipper, L_x was optimised for the HPT rig and calculated to be 80 $\frac{\mu m}{GPa}$ [83]. L_x was used and kept constant for all the parameterisation conditions. L_e^0 can be calculated using Equation 7.7 where G_{3BL} and h_{3BL} are the shear modulus and thickness of the 3BL respectively.

$$L_e^0 = \frac{h_{3BL}}{G_{3BL}} \tag{7.7}$$

For the dry, water and grease tests, the shear modulus can be considered to be that of steel ($G_s = 79.3GPa$). The average 3BL thickness found by Meierhofer [61] ($h_{3BL} = 20\mu m$) was used for all test conditions, therefore the nominal inverted stress $L_e^0 = 0.252\frac{\mu m}{GPa}$. For the LIR leaf and grease tests, the 3BL stiffness is significantly less so L_e^0 was re-parameterised for this test condition. It was assumed that for the HIR leaf and grease tests there would be enough metal-metal contact to assume that

$L_e^0 = 0.252 \frac{\mu m}{GPa}$ as for the dry and water tests.

The pressure dependent and temperature inverted stresses were kept constant as $L_e^p = \infty \frac{\mu m}{GPa}$ and $L_e^T = 0 \frac{1}{0^{\circ}C}$ respectively. Parameterisation of nominal and pressure dependent constants were conducted for 16 HPT test conditions: dry, water, grease and leaf for varying states of roughness. For the high initial roughness tests, the ECF model was parameterised with HPT data from cycles 1, 11 and 20. In addition, for low initial roughnesses tests, the ECF model was parameterised with HPT data from cycle 1. These are outlined in their respective parameterisation sections.

7.2.1 Dry Condition Parameterisation

The ECF model for the dry data has been included in Figures 7.3 and 7.4. These represent high initial roughness (HIR) and low initial roughness (LIR) respectively. As mentioned in Section 7.2, three pressures are included in the parameterisation step (600, 750 and 900MPa). This is to ensure that the parameterisation works over a range of pressures. τ_{c1} and τ_{c2} are found using the ECF model parameterisation software for each pressure. This defines the elasto-plastic limits for the modelled ECF curves at each pressure. The ECF model for the HIR dry data has been included in Figure 7.3. The overall error is outputted by the ECF model and uses the difference between the true value and the modelled value at each numerical step. For the HIR model fit, the error was calculated to be 5.65%. L_e^0, L_e^T and L_e^p were not optimised, but remained the values calculated by Meierhofer [61]. The model appears to fit well for all contact pressures, however the stiffness was consistently overestimated. The critical stresses appear to fit well to the HPT data at all pressures.

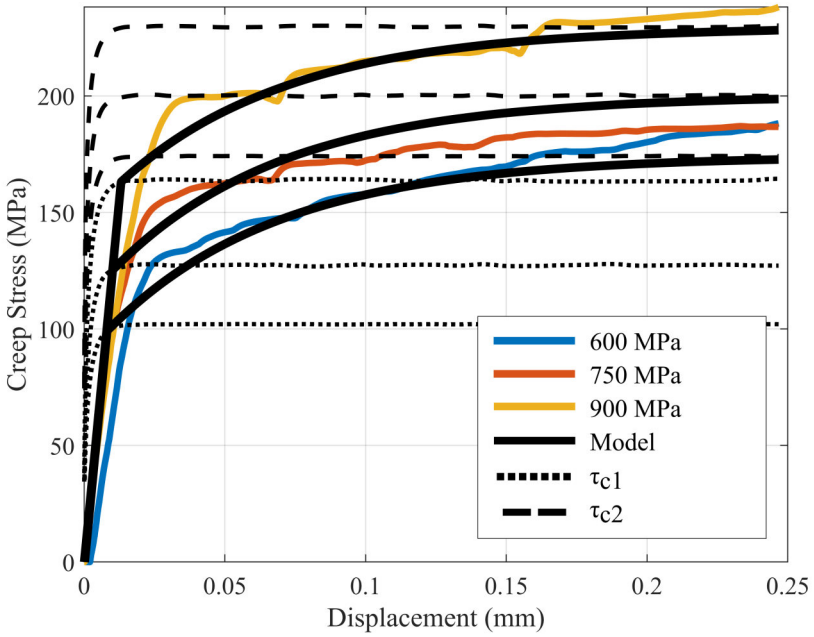

Figure 7.3: ECF parameterisation (Test: Dry - HIR - Cycle 1)

The parameterisation of the HIR dry cycle 1 test produced the input parameters included in Table 7.1.

Material Parameter	**Nominal**	**Units**	**Pressure Dependency**	**Units**
L_e	0.252	$\mu m/GPa$	∞	GPa^{-1}
L_p	0.0606	mm	14.8	GPa^{-1}
τ_{c1}	26.2	GPa	0.00651	GPa^{-1}
τ_{c2}	0.321	GPa	1.3	GPa^{-1}

Table 7.1: ECF input parameters (Test: Dry - HIR - Cycle 1)

The ECF model for the LIR dry data has been included in Figure 7.4. The overall error for the LIR model fit was calculated to be 8.52%. L_e^0, L_e^T and L_e^p were not optimised.

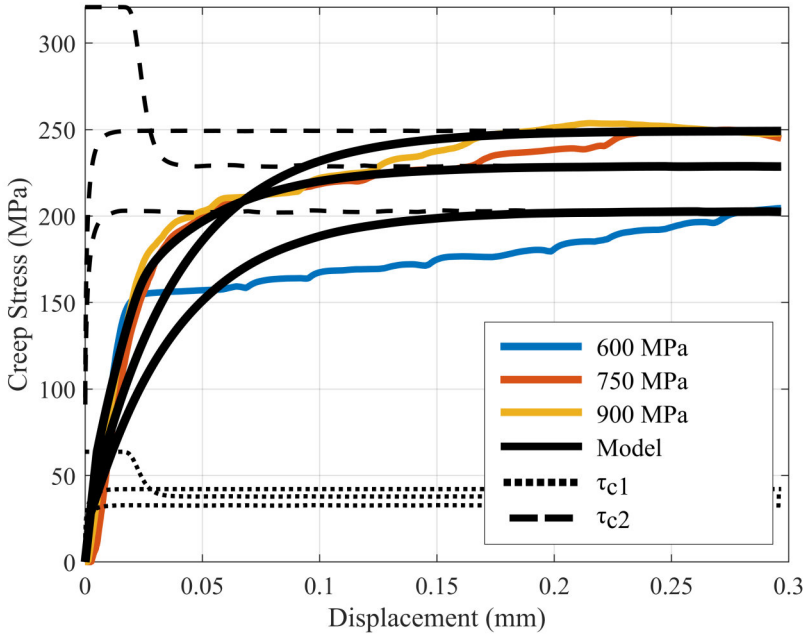

Figure 7.4: ECF parameterisation (Test: Dry - LIR - Cycle 1)

The parameterisation of the LIR dry cycle 1 test produced the input parameters included in Table 7.2.

Material Parameter	**Nominal**	**Units**	**Pressure Dependency**	**Units**
L_e	0.252	$\mu m/GPa$	∞	GPa^{-1}
L_p	0.0388	mm	123	GPa^{-1}
τ_{c1}	0.0638	GPa	1.20	GPa^{-1}
τ_{c2}	0.321	GPa	1.68	GPa^{-1}

Table 7.2: ECF Input parameters (Test: Dry - LIR - Cycle 1)

7.2.2 Water Condition Parameterisation

The ECF model for the water data has been included in Figures 7.5 and 7.6. The ECF model for the HIR water data has been included in Figure 7.5. The overall error for the HIR model fit was calculated to be 7.34%. L_e^0, L_e^T and L_e^p were not optimised.

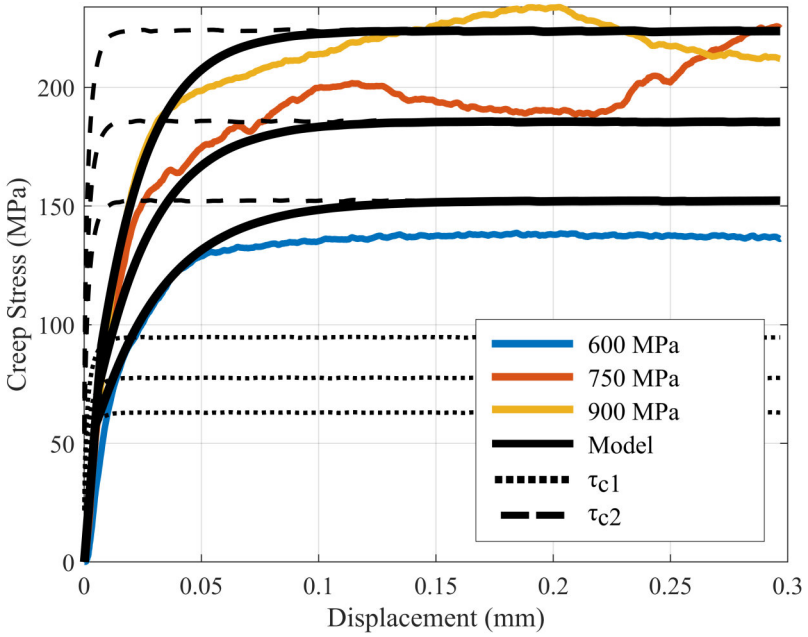

Figure 7.5: ECF parameterisation (Test: Water - HIR - Cycle 1)

The parameterisation of the HIR water cycle 1 test produced the input parameters included in Table 7.3.

Material Parameter	**Nominal**	**Units**	**Pressure Dependency**	**Units**
L_e	0.252	$\mu m/GPa$	∞	GPa^{-1}
L_p	0.00410	mm	0.250	GPa^{-1}
τ_{c1}	0	GPa	0	GPa^{-1}
τ_{c2}	1.97	GPa	0.134	GPa^{-1}

Table 7.3: ECF input parameters (Test: Water - HIR - Cycle 1)

The ECF model for the LIR water data has been included in Figure 7.6. The overall error for the LIR model fit was calculated to be 8.12%. L_e^0, L_e^T and L_e^p were not optimised.

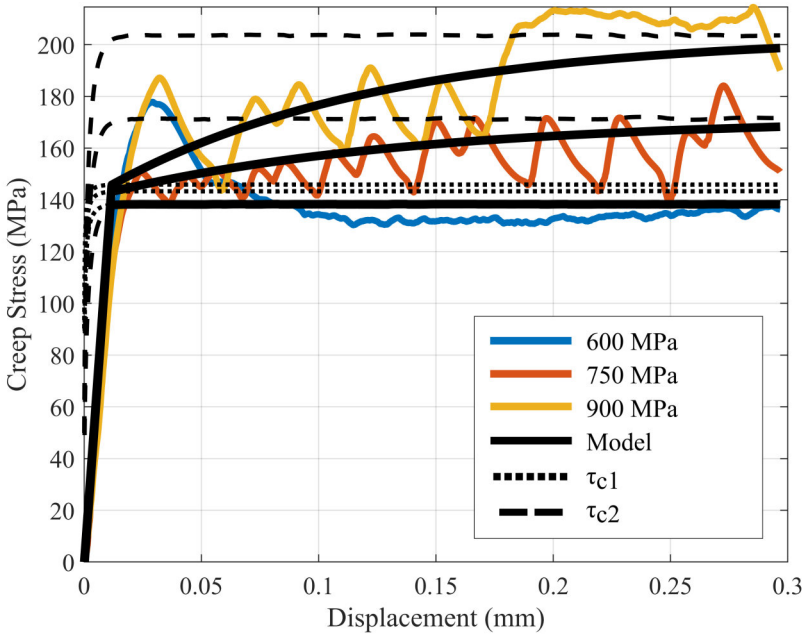

Figure 7.6: ECF parameterisation (Test: Water - LIR - Cycle 1)

The parameterisation of the LIR water cycle 1 test produced the input parameters included in Table 7.4.

Material Parameter	**Nominal**	**Units**	**Pressure Dependency**	**Units**
L_e	0.252	$\mu m/GPa$	∞	GPa^{-1}
L_p	0.122	mm	6.23	GPa^{-1}
τ_{c1}	0.160	GPa	3.30	GPa^{-1}
τ_{c2}	1.25	GPa	0.195	GPa^{-1}

Table 7.4: ECF input parameters (Test: Water - LIR - Cycle 1)

7.2.3 Grease Condition Parameterisation

The ECF model for the grease data has been included in Figures 7.7 and 7.8. The ECF model for the HIR grease data has been included in Figure 7.7. The overall error for the HIR model fit was calculated to be 3.99%. L_e^0, L_e^T and L_e^p were not optimised.

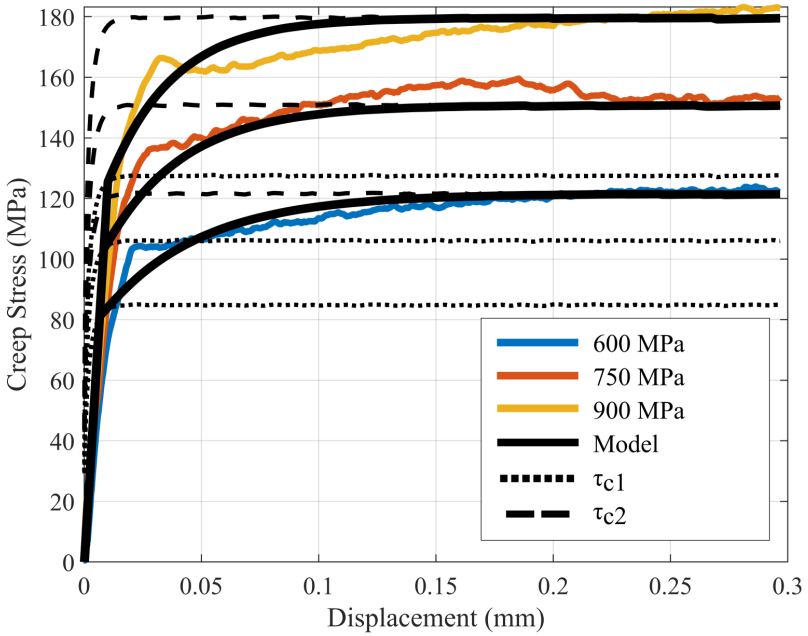

Figure 7.7: ECF parameterisation (Test: Grease - HIR - Cycle 1)

The parameterisation of the HIR grease cycle 1 test produced the input parameters included in Table 7.5.

Material Parameter	**Nominal**	**Units**	**Pressure Dependency**	**Units**
L_e	0.252	$\mu m/GPa$	∞	GPa^{-1}
L_p	0.0000825	mm	0.00333	GPa^{-1}
τ_{c1}	0	GPa	0	GPa^{-1}
τ_{c2}	2.04	GPa	0.103	GPa^{-1}

Table 7.5: ECF input parameters (Test: Grease - HIR - Cycle 1)

The ECF model for LIR grease data has been included in Figure 7.8. The overall error for the LIR model fit was calculated to be 21.2%. L_e^0 was optimised to be 57.1 $\mu m/GPa$. L_e^T and L_e^p were not optimised.

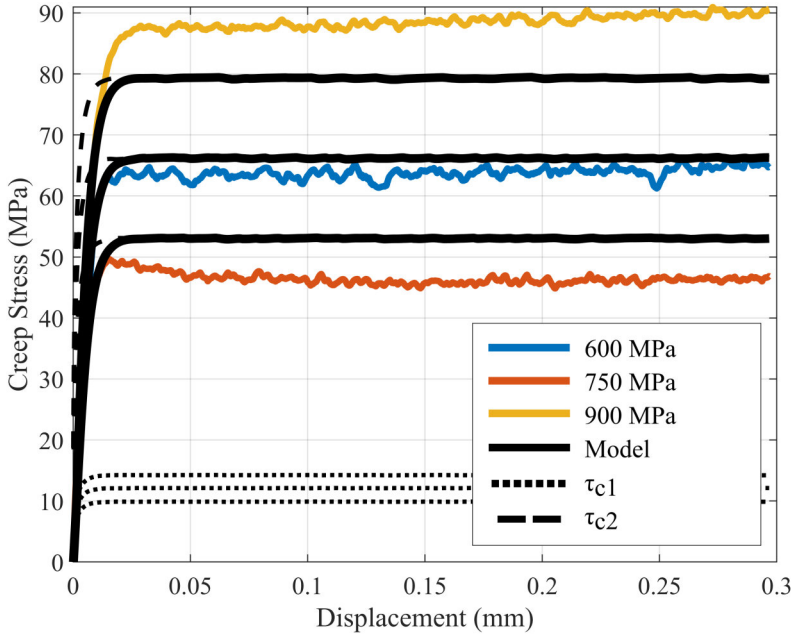

Figure 7.8: ECF parameterisation (Test: Grease - LIR - Cycle 1)

The parameterisation of the LIR grease cycle 1 test produced the input parameters included in Table 7.6.

Material Parameter	**Nominal**	**Units**	**Pressure Dependency**	**Units**
L_e	57.1	$\mu m/GPa$	∞	GPa^{-1}
L_p	0.00369	mm	291.9	GPa^{-1}
τ_{c1}	0.06422	GPa	0.279	GPa^{-1}
τ_{c2}	4.14	GPa	0.0215	GPa^{-1}

Table 7.6: ECF input parameters (Test: Grease - LIR - Cycle 1)

7.2.4 Leaf Condition Parameterisation

The ECF model for the leaf data has been included in Figures 7.9 and 7.10. The ECF model for the HIR leaf data has been included in Figure 7.9. The overall error for the HIR model fit was calculated to be 6.25%. L_e^0, L_e^T and L_e^p were not optimised.

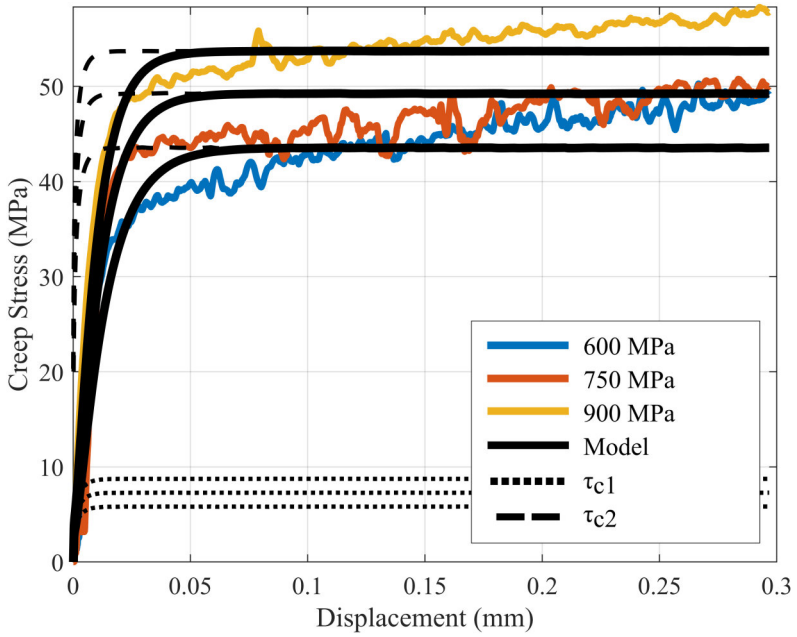

Figure 7.9: ECF parameterisation (Test: Leaves - HIR - Cycle 1)

The parameterisation of the HIR leaf cycle 1 test produced the input parameters included in Table 7.7.

Material Parameter	**Nominal**	**Units**	**Pressure Dependency**	**Units**
L_e	0.252	$\mu m/GPa$	∞	GPa^{-1}
L_p	0.00277	mm	0.415	GPa^{-1}
τ_{c1}	0	GPa	0	GPa^{-1}
τ_{c2}	0.0697	GPa	1.63	GPa^{-1}

Table 7.7: ECF input parameters (Test: Leaves - HIR - Cycle 1)

The ECF model for LIR leaf data has been included in Figure 7.10. The overall error for the LIR model fit was calculated to be 6.81%. L_e^0 was optimised to be 57.1 $\mu m/GPa$. L_e^T and L_e^p were not optimised.

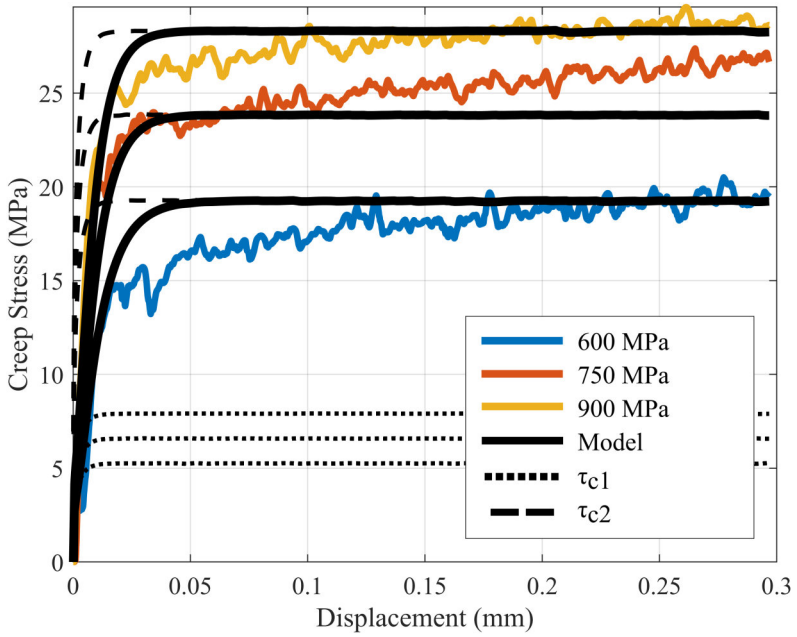

Figure 7.10: ECF parameterisation (Test: Leaves - LIR - Cycle 1)

The parameterisation of the LIR leaf cycle 1 test produced the input parameters included in Table 7.8.

Material Parameter	**Nominal**	**Units**	**Pressure Dependency**	**Units**
L_e	57.1	$\mu m/GPa$	∞	GPa^{-1}
L_p	0.00220	mm	0.431	GPa^{-1}
τ_{c1}	0	GPa	0	GPa^{-1}
τ_{c2}	0.238	GPa	0.141	GPa^{-1}

Table 7.8: ECF input parameters (Test: Leaves - LIR - Cycle 1)

7.2.5 Parameterisation Error

The errors measured in these parameterisation steps are broadly similar to those found in the work of Skipper and Meierhofer, although these parameterisation steps were predominantly done with the addition of sand [61] [83]. It should be be noted that these errors are the errors associated with the parameterisation step, not the error associated with traction prediction. These are studied in Section 7.3.5.

7.3 ECF Predictions

Upon completion of the parameterisation step, the settings tabulated in Section 7.2 can be inputted into the ECF model. The ECF model user interface is shown in Figure 7.11 (access to this model was granted by Virtual Vehicle Research GmBH). This allows for the specific 3BL conditions to be inputted, the number of numerical steps and range of creepages to be altered. The dimensions of the contact, speed of the train and the normal load can be changed. Altering these to the exact conditions that were used on the FSR formed the basis of the modelling for this work. When creepage was evaluated up to 10% with 100 numerical steps, the resultant creep curve was smooth. The FSR wheel and rail dimensions were inputted as well as 110kN of normal load and a wheel speed of 0.1m/s: the same as was used in the FSR tests. Fully 'saturated' slip is generally observed to occur between 1 and 2% creepage. At this point the traction coefficient is also called the friction coefficient. The two things that define the tribology of a system are the creepage at which full slip occurs and the resulting friction coefficient at this point. These two values are compared in the following section.

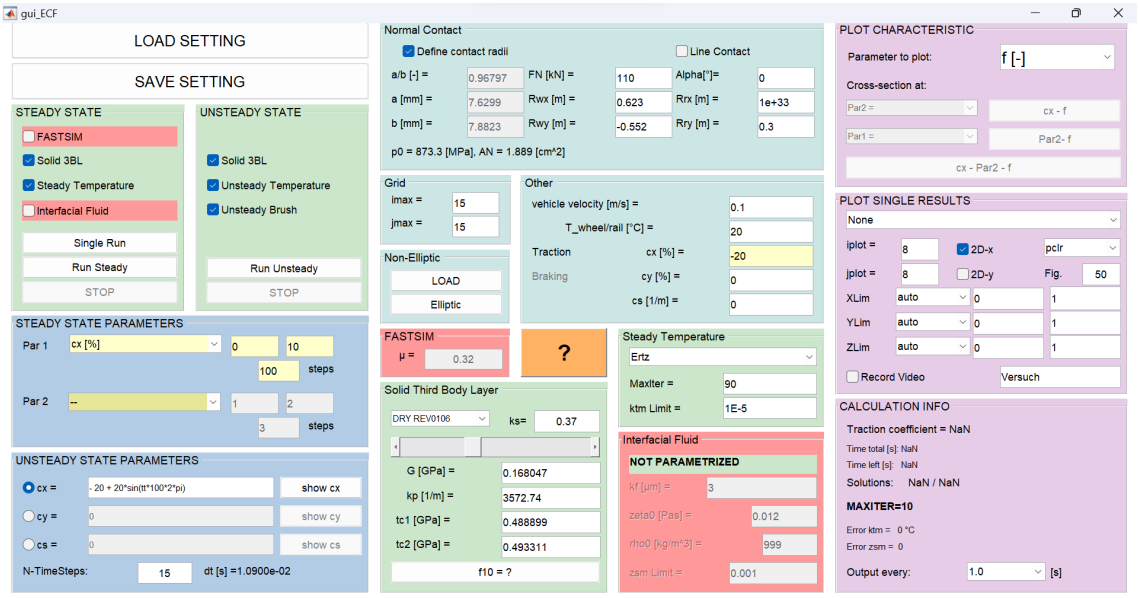

Figure 7.11: ECF model user interface courtesy of Virtual Vehicle Research GmBH [61]

7.3.1 Dry

The ECF predictions for the FSR dry tests are shown in Figure 7.12. The friction coefficient predictions are similar for both the HIR tests and the LIR tests at around

0.25 to 0.3. This is low for dry conditions, but as it was parameterised by the HPT tests which in themselves showed low traction coefficients, this value is a sensible prediction.

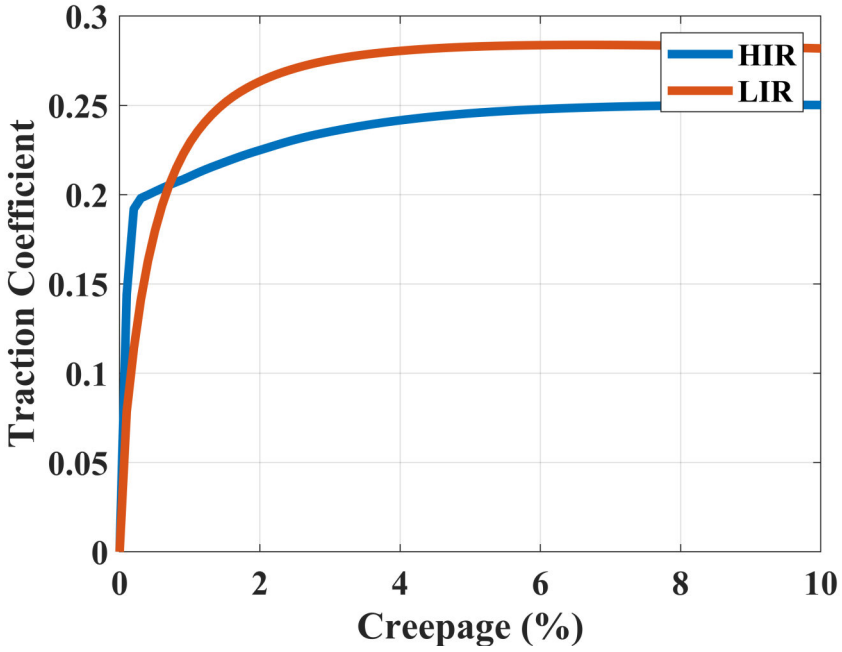

Figure 7.12: FSR creep curve predictions using the ECF model (Tests: Dry)

Fully saturated slip occurs much more quickly on the HIR tests. The true contact area is known to influence friction whereby a greater contact area between two surfaces increases friction. Two dry ideally smooth surfaces when placed together will have a large true contact area and therefore friction will be higher at that interface. A dry rough surface placed against a dry ideally smooth surface will have a small true contact area and therefore friction will be lower at that interface (see Figure 7.13).

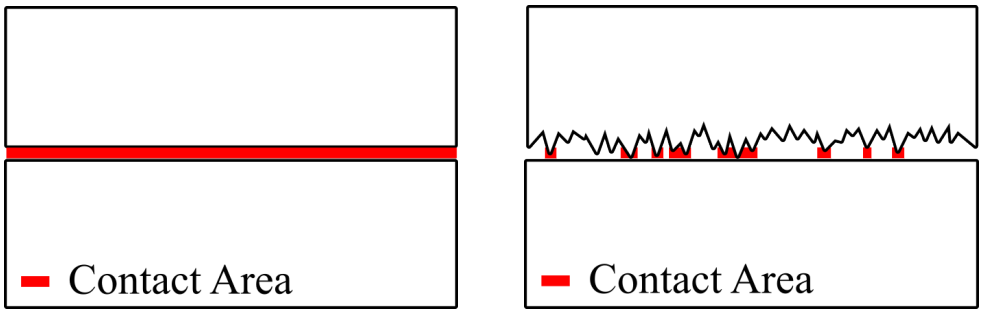

(a) Smooth - Smooth *(b) Rough - Smooth*

Figure 7.13: Schematic showing true contact area reduction when introducing a rough surface to a smooth surface

As these two surfaces are loaded, plastic deformation occurs and the asperities are either entrained into the other surface or reduced in size depending on the hardness of the two surfaces. Both these instances increase the true contact area and raise friction at the interface for dry contacts (see Figure 7.14). When the asperities are entrained, the shear force also increases as the hard rough surface must 'plough' through the softer counter-face. There was a fair amount of roughness transfer between the surfaces for the HPT tests as the surfaces were not run-in and relatively similar in hardness (see Figure 7.14a). The FSR wheel had been used multiple times and was run-in (very hard). This resulted in very little roughness transfer for the FSR tests. Instead asperities were squashed flat (see Figure 7.14b). This also increased the true contact area at the interface. At high loads, this process happens extremely quickly.

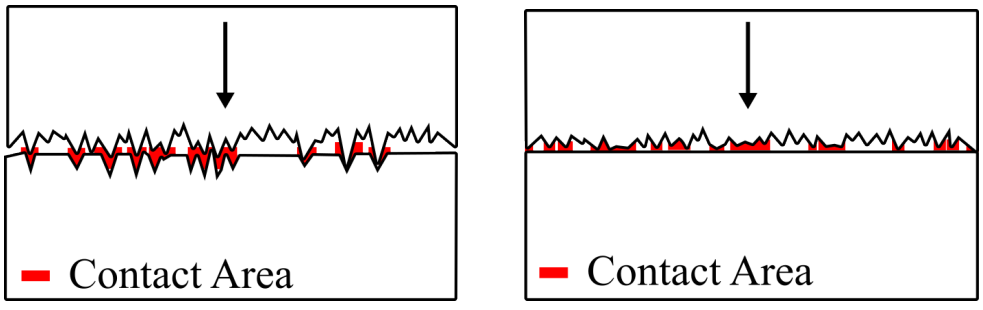

(a) Softer smooth surface *(b) Harder smooth surface*

Figure 7.14: Schematic showing true contact area increase when loading rough surfaces into smooth surface with varying hardnesses

7.3.2 Water

The ECF predictions for the water tests are shown in Figure 7.15. Unlike the dry tests, the LIR tests reach full slip at lower creepages than the HIR tests where the asperities offer gaps for the water to sit recessed from the interface. The gradients of these creep curves with varying roughness have not been extensively studied, especially when paired with 3BLs. Some work has been conducted on wet contacts by Chang et al., but these were at high speeds where lubrication regimes change [97]. Additionally, these were conducted at lower roughnesses ($R_a = 0.1 - 1\mu m$). Such smooth surfaces contacting at high speeds are likely to be fully separated and so are not particularly comparable to this work. The higher roughnesses in this work meant an increased likelihood of boundary lubrication, therefore the characteristics of the initial creep-curve slope and level of friction are different..

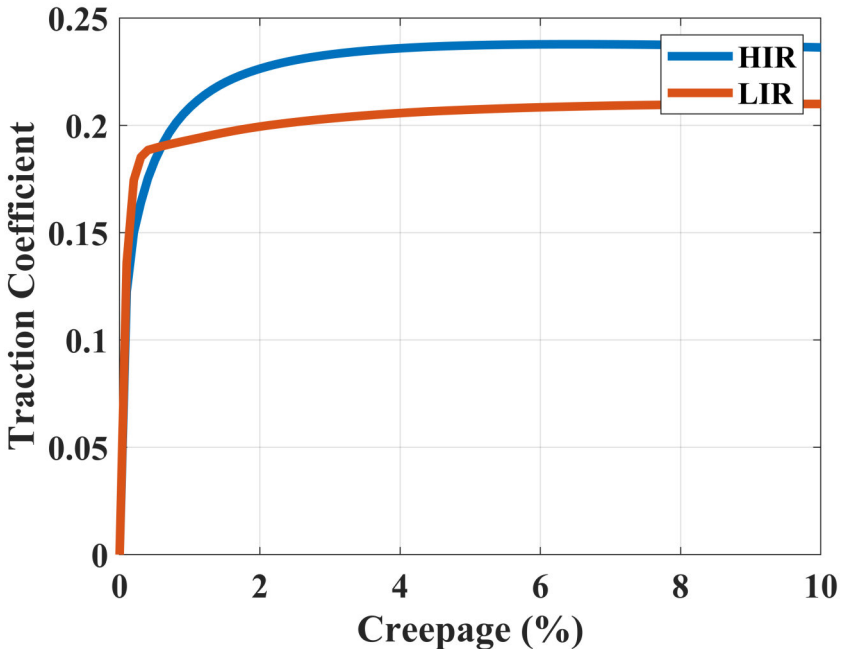

Figure 7.15: FSR creep curve predictions using the ECF model (Tests: Water)

7.3.3 Grease

The ECF predictions for the grease tests are shown in Figure 7.16. The ECF predicts much lower friction coefficients for the LIR tests, whereby a lubricant film is more easily established between the two smooth surfaces. Like the water tests, the HIR tests offer spaces for the grease to sit without influencing the traction coefficient as

severely. Full-slip is achieved much sooner for the LIR test as expected.

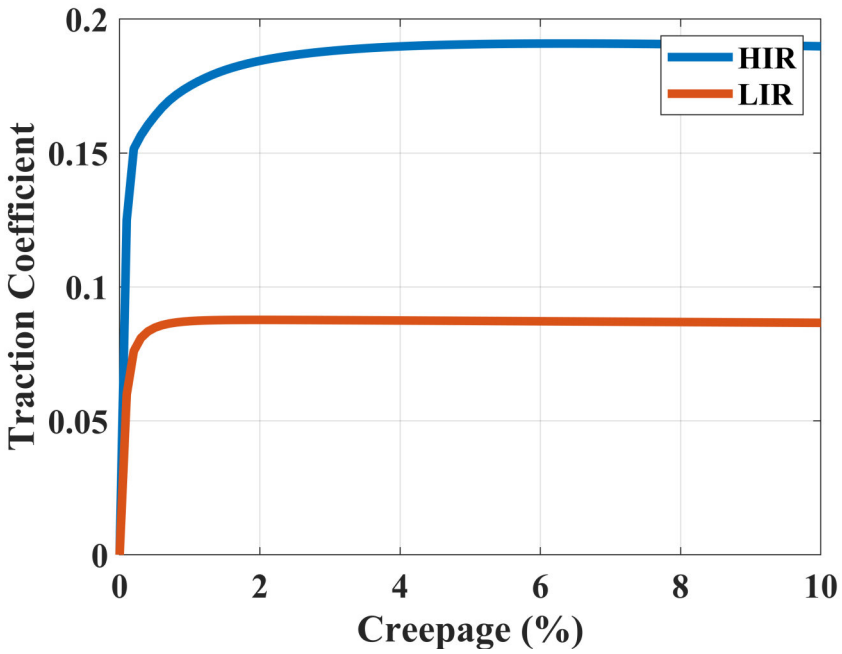

Figure 7.16: FSR creep curve predictions using the ECF model (Tests: Grease)

7.3.4 Leaves

The ECF predictions for the leaf tests are shown in Figure 7.17. As expected, the resultant friction coefficients are extremely low. The LIR tests show lower friction coefficients than the HIR tests, this mirrors what was seen visually on the HPT specimens, whereby leaf layers were disrupted by high roughnesses. Full-slip occurred at similar low creepages.

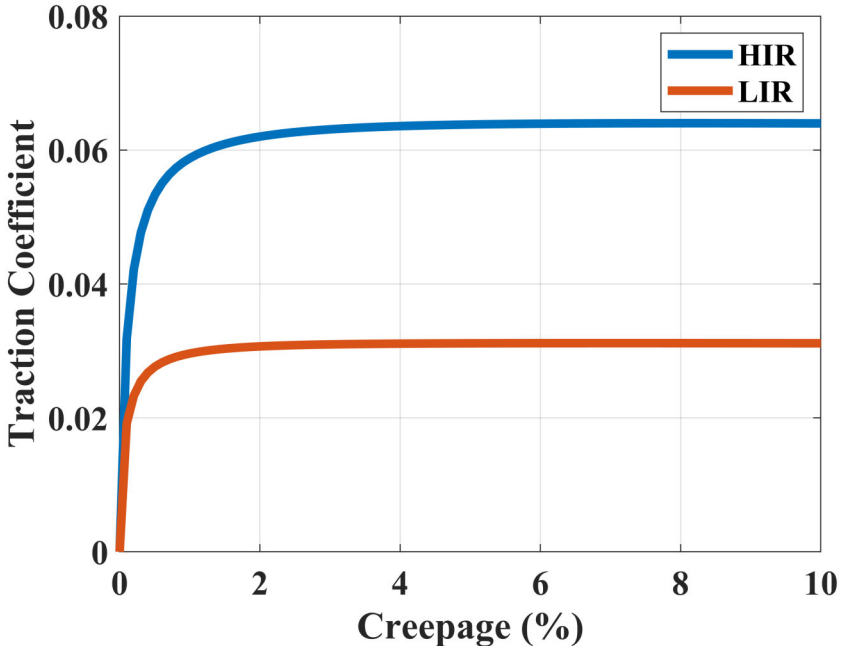

Figure 7.17: FSR creep curve predictions using the ECF model (Tests: Leaf)

7.3.5 ECF Prediction Error

The ECF model predicted the following tribological responses outlined in Figure 7.18 for both the HIR and the LIR tests. As these predictions were parameterised by the HPT tests, it is unsurprising that both the dry and water tests predicted higher friction coefficients whilst predicting lower friction coefficients for the grease tests and still lower friction coefficients for the leaf tests.

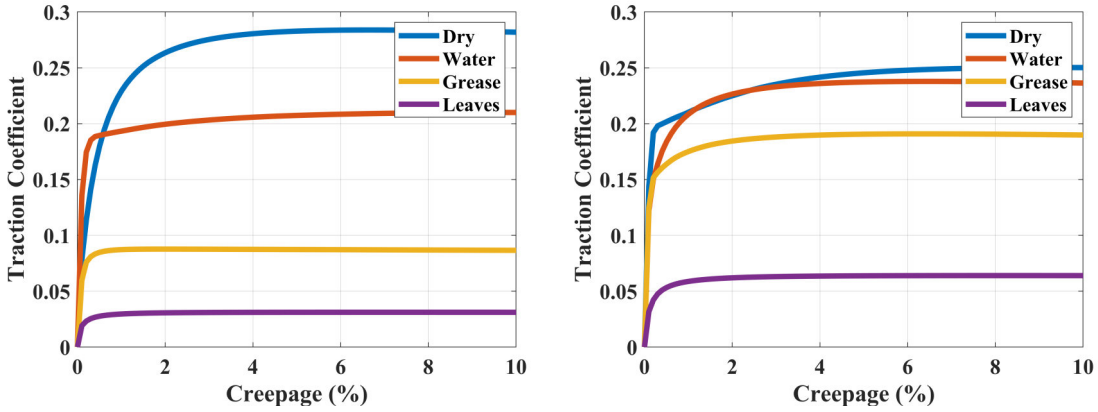

(a) LIR ECF *(b) HIR ECF*

Figure 7.18: ECF model creep curve predictions

These predictions could then be compared with the FSR outputs by selecting the correct FSR settings as previously stated in Section 7.3. The average traction coefficients were calculated from the FSR data and were compared to the ECF predictions at 2% creepage (see Figure 7.19).

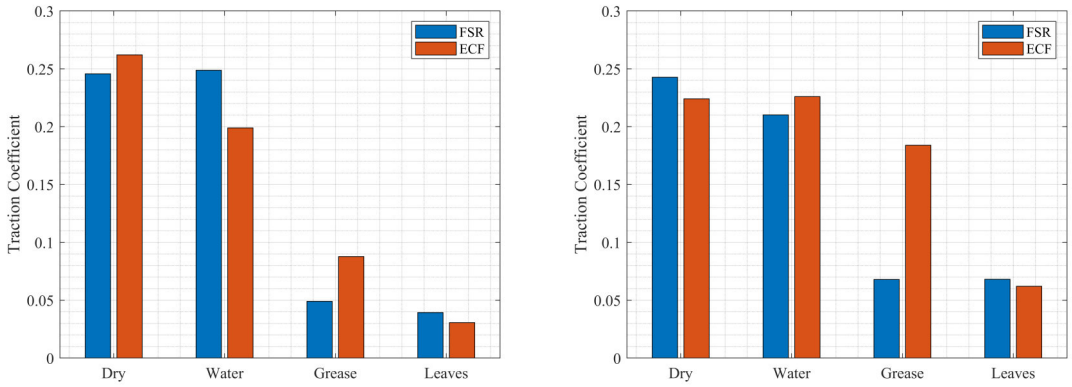

(a) LIR *(b) HIR*

Figure 7.19: Average measured traction coefficients vs the ECF prediction (Test: 110kN)

On the whole, the ECF model was able to predict the FSR outcomes with a fair degree of accuracy, the exception being the grease tests (see Table 7.9).

Test Case	**LIR % Error**	**HIR % Error**
Dry	6.64	7.70
Water	20.0	7.54
Grease	78.8	165
Leaves	22.3	11.6

Table 7.9: ECF prediction error (Test: 900MPa)

The ECF model over-predicted the friction coefficient for both the LIR and the HIR grease tests. As the ECF model was parameterised by the HPT tests, the lack of accurate predictions may stem from differences in the HPT and FSR tests. Small-scale testing is a valuable tool for researchers, but ultimately it is different from the full-scale system. Models such as the ECF model can predict full-scale outcomes, but if they are parameterised by test results produced by tests that do not accurately mimic the full-scale test, then they will be unable to do this. Traction coefficients from the HPT grease tests were higher than for the FSR tests, which explains why the ECF overpredicted the friction. This was most likely caused by the differences in roughness and their evolutions between the two tests. Roughness was consistently lower during the LIR FSR tests, and dropped extremely quickly during HIR FSR tests due to the elevated wheel hardness. This meant that the gaps created by asperities were generally smaller and were quickly reduced in size for the HIR tests. It is hypothesised that the lack of asperity gaps meant more grease occupied the interface, thereby lowering friction for the FSR tests and causing the ECF to overestimate friction for the grease tests. To assess this, the ECF was also parameterised at a higher cycle number for the grease tests. Figure 7.20 shows the comparative ECF predictions based on changing the parameterisation cycle from 1 to 11.

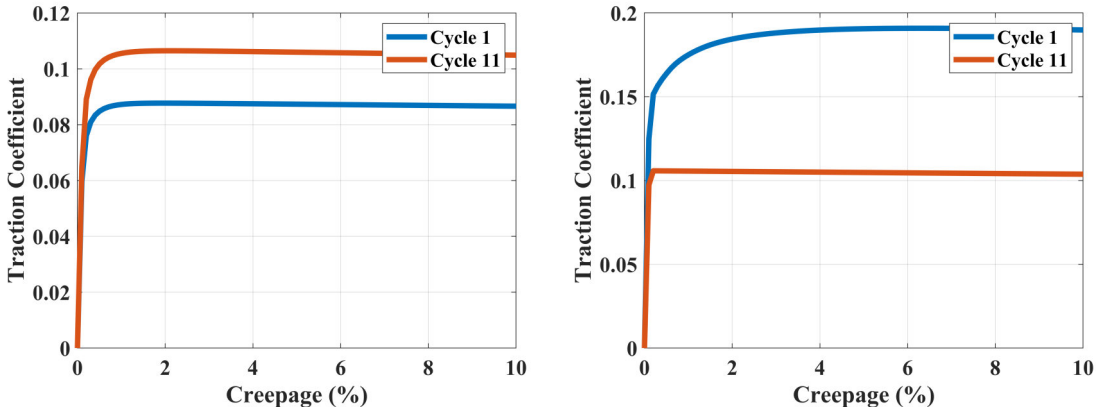

(a) LIR ECF *(b) HIR ECF*

Figure 7.20: Comparative ECF model creep curve predictions for grease at cycles 1 and 11

By altering the parameterisation cycle number, the ECF is parameterised with different surface conditions which included a higher hardness for both the HIR and LIR tests, and a lower surface roughness for the HIR tests. The traction coefficient predictions for the LIR tests are relatively similar for the differing cycles. The traction coefficient predictions for the HIR tests varied considerably when evaluated at a higher cycle number. The predictions at cycle 11 for both the LIR and HIR tests were remarkably similar.

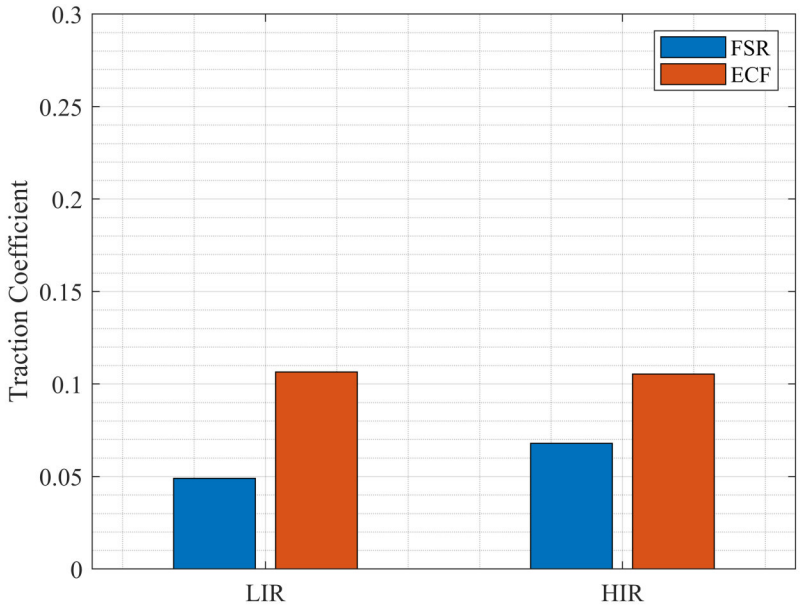

Figure 7.21: Average measured traction coefficients vs the ECF prediction at cycle 11 (Test: 110kN)

The errors were reevaluated at this alternative parameterisation cycle number and it was found that the LIR grease traction coefficient predictions were less accurate than when parameterised at cycle 1. The HIR grease traction coefficient predictions however were more accurate.

Test Case	**LIR % Error**	**HIR % Error**
Grease	117	55.2

Table 7.10: ECF prediction error when parameterised at cycle 11 (Test: 900MPa)

7.4 Summary

The ECF model was used to parameterise the HPT outputs and predict full-scale traction coefficients. This was achieved with a fair degree of accuracy. It was able to predict dry conditions with just 7% error. The ECF model was less accurate at predicting the frictional behaviour of smoother surfaces and when 3BLs were applied, especially grease. It is expected that these errors were introduced due to

the difference between the HPT and FSR specimens, namely the hardness of the wheel specimen: the FSR wheel was run-in whereas the HPT wheel specimen was not. Further work to make the HPT specimens more similar to the FSR specimens in terms of hardness and roughness may eliminate some of this error. With exception to the grease tests, the ECF model was able to predict the traction coefficients for the HIR tests with around 7-9% accuracy. This could indicate that the ECF may be an effective tool when predicting traction coefficients post grinding on track with and without 3BLs present. In addition, the HPT rig has proved to be a quick and inexpensive way to parameterise the ECF with and without 3BLs present, thereby reducing the need for extensive and expensive full-scale testing.

8 Conclusions

The aim of this thesis was to better understand how roughness and 3BLs affect the traction coefficient at the wheel-rail interface. To achieve this, an extensive literature review was undertaken to identify gaps in the existing theory. Small-scale, full-scale, ultrasonic and creep-force model testing methodologies were created. These four methodologies were used to conduct tribological tests and attempt to relate roughness, traction coefficient and interfacial stiffness with and without 3BLs present. Statistical analysis was conducted in an attempt to verify these links. As the work covered in this thesis was quite broad, the conclusions have been grouped into HPT, FSR and ECF based results.

8.1 HPT Conclusions

The HPT testing conclusions are listed below:

- Traction coefficients were measured for dry, water, grease and leaf interfacial conditions at 600, 750 and 900MPa and at two initial roughnesses: HIR ($S_{q\sigma} \approx 8 - 10\mu m$) and LIR ($S_{q\sigma} \approx 1 - 2\mu m$). Pressure was found to not significantly affect the traction coefficient for any of the interfacial conditions or initial roughnesses. Dry conditions produced the highest traction coefficients as expected ($\mu \approx 0.3$), water conditions the next highest ($\mu \approx 0.25$), grease the next highest ($\mu \approx 0.1$) and the lowest were the leaf conditions ($\mu \approx 0.05$). The traction coefficient for the dry conditions was lower than on previous HPT and twin disc testing, possibly due to some contamination, however they tally very well with available on-track data where wheels and rails are not perfectly clean.

- A range of test pressures were applied to the HPT specimens from 600-900MPa. Higher pressures resulted in greater roughness reductions for the HIR specimens for all interfacial conditions.

- The material hardness was found to increase for both specimens the LIR tests after just 20 cycles.

- For the dry HIR tests, the higher initial roughnesses raised traction coefficients for all contact pressures. These traction coefficients then reduced as the

surfaces were run-in and made smoother. It was unclear what effect roughness had on the traction coefficient with the addition of 3BLs. Some significant statistical relationships were found, but further work is required to understand the statistical impact of roughness on the traction coefficient when paired with 3BLs. 3BLs affect tribological conditions so significantly that it was difficult to decouple these independent interfacial conditions and their effects.

- For the water HIR tests, large amounts of wear were visible. The traction coefficient increased in later cycles whilst measured roughness decreased. It is uncertain to what extent this wear had on friction as it was not included in the roughness measurements due to it being highly localised.

- Across all pressures, the application of leaves slowed roughness evolution for the HIR tests. For the LIR tests, leaves lubricated the surfaces well. Roughness remained low for the LIR tests. Visually very little wear was incurred during the leaf tests.

- Across all pressures, grease lowered the traction coefficient significantly from dry conditions. For the HIR tests, this effect was less prevalent as asperity gaps provided space for the grease to sit dormant. The traction coefficients for these HIR tests was therefore higher than the equivalent LIR tests. For the LIR tests, grease lubricated the surfaces well, traction coefficients were low and roughness remained low. Visually no wear was incurred during the grease tests.

- When roughness was elevated, it reduced the traction coefficient lowering capabilities of 3BLs. Large asperity gaps provided a refuge for 3BL material. Asperity peaks are possibly less able to host 3BL material.

- The application of grease was found to increase the traction coefficient temporarily. Excess lubricant may have disrupted the established lubricant films, thereby increasing shear stresses and lowering temperatures at the interface. The resultant viscosity increase and opposition to rotation increased the traction coefficient until the lubricant layer was reestablished.

- During the HIR leaf tests, the roughness reduced leaf layer build-up. Smooth surfaces were able to more readily host leaf layers whilst the larger asperities present of rougher surfaces act to break these layers.

- K_L was higher for dry smooth surfaces than for dry rough surfaces. The large asperity gaps present on rough surfaces reduced metal-to-metal contact and

presented a greater barrier to ultrasound.

- Interfacial stiffness increased when roughness decreased for dry contacts. There was a clear relationship found between surface roughness and K_L for dry contacts.

- The presence of 3BLs lowered K_L. This was most prevalent for the grease tests and when roughness was lower. Higher roughnesses increased the metal-to-metal contact for most 3BLs, however the higher viscosity of grease increased its coverage even when roughness was high. This meant grease was detectable with ultrasonics even when roughness was high.

- When roughness was low, K_L was lower for the 3BL tests than the dry tests. For run-in rail where roughness is low, 3BLs impacted the measured K_L so much so that they were detectable given a dry condition reference measurement.

- K_C and K_R were found to not reliably link to either the traction coefficient or surface roughness for all interfacial conditions and both initial roughnesses.

- A reduction in K_L was often seen during slip events for all roughness levels and interfacial conditions. It is suspected that as material is removed from the interface, this created temporary air gaps that reduces the interfacial stiffness. From these drops in interfacial stiffness, slip could be detected.

The aforementioned conclusions led to the following implications for the rail industry:

- Reprofiling procedures that increase surface roughness both increase the traction coefficient and reduce the impact of 3BLs. This includes applied friction modifiers.

- Roughness is measurable with ultrasonics for dry contacts, however further work needs to be done to find a mathematical link between the two. Reprofiling procedures could be monitored with ultrasonics in-situ to ensure consistent material removal.

- As 3BLs lowered the interfacial stiffness significantly from dry smooth conditions, ultrasound could be used to detect 3BLs in-situ on the rail network. Characterising the type of 3BL still needs further work.

- Slip events were detected by ultrasonics. Ultrasonics could therefore be used to detect slip in-situ, meaning traction systems could be optimised.

8.2 FSR Conclusions

The FSR testing conclusions are listed below:

- Traction coefficients were measured for dry, water, grease and leaf interfacial conditions at 110kN and at two initial roughnesses: HIR ($S_{q\sigma} \approx 7-9\mu m$) and LIR ($S_{q\sigma} \approx 2\mu m$). Dry conditions produced the highest traction coefficients as expected ($\mu \approx 0.3$), water conditions the next highest ($\mu \approx 0.25$), grease the next highest ($\mu \approx 0.075$) and the lowest were the leaf conditions ($\mu \approx 0.05$).

- Roughness reduced to near run-in levels after just 20 wheel passes for the dry, water and grease HIR tests. It is not known if the leaf test roughness decreased this fast, as roughness was not measured until cycle 100. The increased hardness of the FSR wheel was able to plastically deform asperities quicker. After 100 cycles, the leaf test roughness was nearly as low as the other conditions. It is expected that leaf layer still slowed the roughness evolution even at the full-scale.

- Water lowered the traction coefficient temporarily from dry conditions. When this occurred, the traction coefficient dropped as low as 0.1. This occurred more for the LIR tests; higher roughnesses reduced this effect. Traction coefficients increase back to their dehydrated levels after just 3 cycles as the water evaporated or was expelled from the interface.

- Grease lowered the traction coefficient significantly from dry conditions. For the LIR tests, the traction coefficients were stable at just 0.05, the interface was well lubricated and roughness remained low. For the HIR, tests the traction coefficient was higher at around 0.075 and less stable. The traction coefficient reduced as the roughness reduced.

- Leaves lowered the traction coefficient significantly from dry conditions. This was most prevalent on the LIR tests and after hydration. The leaf layers produced a cyclical traction response following hydration with traction coefficients starting at 0.01 and ending at 0.1. The amount of leaf material and the amount of water greatly impact the levels of traction. For the HIR tests, this

effect was less prevalent but still significant. Leaves were applied to the rail specimen, but large amounts of leaf material were transferred to the wheel. The lower roughness of the wheel allowed the material to adhere more readily.

The aforementioned conclusions led to the following implications for the rail industry:

- A single train pass is able to reduce reprofiling roughness levels to near run-in roughness levels.

8.3 ECF Conclusions

The ECF testing conclusions are listed below:

- The ECF model was able to accurately predict dry conditions on the FSR. Errors for both the HIR and LIR test were lower than 10%.
- The ECF model was able to predict FSR water and leaf tests with a fair degree of accuracy (around $10 - 20\%$ error). It performed better for the HIR tests.
- The ECF was unable to accurately predict grease conditions. This was probably due to differences in HPT and FSR specimen material prosperities (most likely the wheel specimen hardness). Tmeant roughness reduced more quickly for the FSR tests. The lack of asperity gaps meant a better established lubricant film and lower traction coefficients. It is unclear why this only occurred for the grease tests and not the other lubricated interfaces.

The aforementioned conclusions led to the following implications for the rail industry:

- The ECF model can be used to predict rough-surface full-scale tribological outcomes with and without 3BLs present. However, further work needs to be done to parameterise grease interfaces.

9 Future Work

Whilst much was covered in this thesis, there were inevitably parts of the work that could have been done more thoroughly and others that were simply not possible in the time allowed. A few areas that would benefit from further study are listed below:

- The number of variables and cycles during the HPT testing campaign meant that conducting repeats was not possible in the time allowed. By conducting additional HPT repeats, the statistical analysis could be improved.
- Whilst surface skewness and kurtosis were measured from the Alicona scans, these were not examined in detail due to time constraints. Whilst statistical analysis showed no link between these parameters and the traction coefficient, this work was not extensive and this subject would benefit from further work.
- Damage to the ultrasonic sensors was incurred for the 750MPa and 900MPa tests. By redesigning the HPT specimens, higher pressure interfacial stiffness measurements may be obtained.
- The time dependent interfacial stiffness data was complex. By analysing this data in more detail, further conclusions may be drawn.
- The FSR rig tests were unstable as the chain was not applying the correct level of slip. The FSR specimens were expensive so no repeats could be made. Repeating these tests with a recalibrated FSR would be beneficial. By cutting specimens from ground pieces of rail, costs could be reduced to allow for a more extensive test campaign.
- The FSR specimens were not instrumented with ultrasonic sensors. By obtaining FSR interfacial stiffness measurements, these could validate the HPT outputs.

References

[1] J. Edgley, "Managing low adhesion," *Adhes. Work. Gr.*, 2018.

[2] R. Lewis, R. S. Dwyer-Joyce, U. Olofsson, J. Pombo, J. Ambrósio, M. Pereira, C. Ariaudo, and N. Kuka, "Mapping railway wheel material wear mechanisms and transitions," *Proceedings of the Institution of Mechanical Engineers, Part F: Journal of Rail and Rapid Transit*, vol. 224, no. 3, pp. 125–137, 2010. [Online]. Available: https://doi.org/10.1243/09544097JRRT328

[3] U. Olofsson and T. Telliskivi, "Wear, plastic deformation and friction of two rail steels—a full-scale test and a laboratory study," *Wear*, vol. 254, no. 1, pp. 80–93, 2003. [Online]. Available: https://www.sciencedirect.com/science/article/pii/S0043164802002910

[4] S. Kumar, G. Yu, and A. Witte, "Wheel-rail resistance and energy consumption analysis of cars on tangent track with different lubrication strategies," in *Proceedings of the 1995 IEEE/ASME Joint Railroad Conference*, 1995, pp. 129–136.

[5] W. Shust and J. Elkins, "Wheel forces during flange climb. i. track loading vehicle tests," in *Proceedings of the 1997 IEEE/ASME Joint Railroad Conference*, 1997, pp. 137–147.

[6] A. Matsumoto, Y. Sato, H. Ohno, M. Tomeoka, K. Matsumoto, J. Kurihara, T. Ogino, M. Tanimoto, Y. Kishimoto, Y. Sato, and T. Nakai, "A new measuring method of wheel–rail contact forces and related considerations," *Wear*, vol. 265, no. 9, pp. 1518–1525, 2008, contact Mechanics and Wear of Rail/Wheel Systems - CM2006. [Online]. Available: https://www.sciencedirect.com/science/article/pii/S0043164808001749

[7] R. Lewis, R. Dwyer-Joyce, S. Lewis, C. Hardwick, and G.-H. E.A., "Tribology of the wheel/rail contact: The effect of third body materials," *International Journal of Railway Technology*, vol. 1, no. 1, pp. 167–194, 2012.

[8] A. Keropyan, S. Gorbatyuk, P. Bibikov, and A. Bardovski, "Influence of roughness of working surfaces of the wheel–rail system of open-pit locomotives with an implementable adhesion coefficient," *Journal of friction and wear*, vol. 40, no. 1, pp. 73–79, 2019.

[9] J. Lundmark, E. Höglund, and B. Prakash, "Running-in behaviour of rail and wheel contacting surfaces," *International Conference on Tribology*, September 2006.

[10] B. Drinkwater, R. Dwyer-Joyce, and P. Cawley, "A study of the interaction between ultrasound and a partially contacting solid-solid interface," *Proceedings of the Royal Society Series A*, vol. 452, pp. 2613– 2628, 1996.

[11] M. B. Marshall, R. Lewis, R. S. Dwyer-Joyce, U. Olofsson, and S. Björklund, "Experimental characterization of wheel-rail contact patch evolution," *Journal of Tribology*, no. 128, pp. 493–504, July 2006.

[12] R. Dwyer-Joyce, C. Yao, J. Zhang, R. Lewis, and B. Drinkwater, "Feasibility study for real time measurement of wheel-rail contact using an ultrasonic array," *Journal of Tribology*, vol. 131, October 2009.

[13] H. Brunskill, A. Hunter, L. Zhou, R. Dwyer-Joyce, and R. Lewis, "An evaluation of ultrasonic arrays for the static and dynamic measurement of wheel/rail contact pressure and area," *Journal of Engineering Tribology, Proceedings of the IMechE, Part J.*, 2020.

[14] K. Holmberg and A. Erdemir, "Influence of tribology on global energy consumption, costs and emissions," *Friction*, vol. 5, no. 3, pp. 263–284, 2017. [Online]. Available: https://doi.org/10.1007/s40544-017-0183-5

[15] H. Hertz, "Über die berührung fester elastischer körper," *Journal für die reine und angewandte Mathematik*, no. 92, pp. 156–171, 1881.

[16] F. P. Bowden and D. Tabor, *The friction and lubrication of solids.* Oxford: Oxford : Clarendon Press, 1950.

[17] J. Williams, *Engineering Tribology.* Cambridge University Press, April 2005.

[18] E. Gadelmawla, M. Koura, T. Maksoud, I. Elewa, and H. Soliman, "Roughness parameters," *Journal of Materials Processing Technology*, vol. 123, no. 1, pp. 133–145, 2002.

[19] M. Sedlaček, B. Podgornik, and J. Vižintin, "Correlation between standard roughness parameters skewness and kurtosis and tribological behaviour of contact surfaces," *Tribology International*, vol. 48, pp. 102–112, 2012, 14th Nordic Symposium on Tribology, NORDTRIB 2010.

[20] E. C. T. Ba, M. R. Dumont, P. S. Martins, R. M. Drumond, M. P. M. da Cruz, and V. F. Vieira, "Investigation of the effects of skewness rsk and kurtosis rku on tribological behavior in a pin-on-disc test of surfaces machined by conventional milling and turning processes," *Materials research (São Carlos, São Paulo, Brazil)*, vol. 24, no. 2, 2021.

[21] F.-X. Wang, P. Lacey, R. S. Gates, and S. M. Hsu, "A study of the relative surface conformity between two surfaces in sliding contact," *Journal of tribology*, vol. 113, no. 4, pp. 755–761, 1991.

[22] M. A. Corporation, *Quick guide to surface roughness measurement*, Mitutoyo, December 2016.

[23] A. Paepegaey, M. L. Barker, D. W. Bartlett, M. Mistry, N. X. West, N. Hellin, L. J. Brown, and P. G. Bellamy, "Measuring enamel erosion: A comparative study of contact profilometry, non-contact profilometry and confocal laser scanning microscopy," *Dental Materials*, vol. 29, pp. 1265–1272, December 2013.

[24] X. Shuman, P. Zhipeng, and Z. Jingwen, "Optical microscope for three-dimensional surface displacement and shape measurements at the microscale," *Optics Letters*, vol. 39, pp. 4267–4270, 2014.

[25] G. Binnig, C. Quate, and C. Gerber, "The atomic force microscope," *Physical Review Letters*, vol. 56, pp. 930–933, 03 1986.

[26] O. Marti, *Handbook of Micro/Nano Tribology*, 2nd ed. CRC Press, 1999, ch. AFM Instrumentation and Tips.

[27] L. Nilsson and R. Ohlsson, "Accuracy of replica materials when measuring engineering surfaces," *International Journal of Machine Tools and Manufacture*, vol. 41, no. 13, pp. 2139–2145, 2001. [Online]. Available: https://www.sciencedirect.com/science/article/pii/S0890695501000803

[28] M. Broster, "An evaluation of replica methods used in roughness measurements," *Brotish Railways Research Department Process Technology Group*, May 1972.

[29] F. Baruffi, P. Parenti, F. Cacciatore, M. Annoni, and G. Tosello, "On the application of replica molding technology for the indirect measurement of surface and geometry of micromilled components," *Micromachines*, vol. 8, no. 6, p. 195, 2017.

[30] R. Lewis and U. Olofsson, *Wheel-Rail Interface Handbook*, January 2009.

[31] A. Rovira, A. Roda, M. Marshall, H. Brunskill, and R. Lewis, "Experimental and numerical modelling of wheel/rail contact and wear," *Wear*, vol. 271, pp. 911–924, 2011.

[32] D. Fletcher, "Combined rolling and sliding," January 2020, taken from the MEC448 lecture notes at the University of Sheffield.

[33] M. Spiryagina, O. Polach, and C. Cole, "Creep force modelling for rail traction vehicles based on the fastsim algorithm," *Vehicle System Dynamics*, vol. 51, no. 11, July 2013.

[34] U. Olofsson, Y. Zhu, S. Abbasi, R. Lewis, and S. Lewis, "Tribology of the wheel/rail contact: Aspects of wear, particle emission and adhesion," *Vehicle System Dynamics*, vol. 51, pp. 1091–1120, 09 2013.

[35] A. Ghidini, M. Diener, A. Gianni, and J. Schneider, "Innovative steel by lucchini rs for high-speed wheel application," *LucchiniRS*, 2012.

[36] K. Mädler, A. Zoll, R. Heyder, and M. Brehmer, "Rail materials - alternatives and limits," *Zeitschrift fuer Eisenbahnwesen und Verkehrstechnik*, vol. 132, pp. 496–503, 2008.

[37] "The art and science of rail grinding," *Scitech Book News*, vol. 30, no. 4, 2006.

[38] H. Tournay and J. Mulder, "The transition from the wear to the stress regime," *Wear*, vol. 191, no. 1, pp. 107–112, 1996.

[39] T. E. Tallian, *Failure atlas for Hertz contact machine elements*. New York: ASME Press, 1992.

[40] T. Makino, T. Kato, and K. Hirakawa, "The effect of slip ratio on the rolling contact fatigue property of railway wheel steel," *International journal of fatigue*, vol. 36, no. 1, pp. 68–79, 2012.

[41] A. Kapoor, F. Franklin, S. Wong, and M. Ishida, "Surface roughness and plastic flow in rail wheel contact," *Wear*, vol. 253, pp. 257–264, 2002.

[42] T. Harris and M. Kotzalas, *Essential Concepts of Bearing Technology*, 5th ed. Taylor and Francis, October 2006.

[43] I. U. Wickramasinghe, D. J. Hargreaves, and D. V. De Pellegrin, "Predicting crack initiation due to ratchetting in rail heads using critical element analysis," *International Journal of Mechanical, Aerospace, Industrial, Mechatronic and Manufacturing Engineering*, vol. 7, no. 5, pp. 945–950, 2013.

[44] R. Lewis and R. S. Dwyer-Joyce, "Wear mechanisms and transitions in railway wheel steels," *Proceedings of the Institution of Mechanical Engineers. Part J, Journal of engineering tribology*, vol. 218, no. 6, pp. 467–478, 2004.

[45] T. Beagley, "Severe wear of rolling/sliding contacts," *Wear*, vol. 36, no. 3, pp. 317–335, 1976.

[46] P. Bolton and P. Clayton, "Rolling—sliding wear damage in rail and tyre steels," *Wear*, vol. 93, no. 2, pp. 145–165, 1984.

[47] F. W. Carter, "On the action of a locomotive driving wheel," *Proceedings of the Royal Society of London. Series A, Containing papers of a mathematical and physical character*, vol. 112, no. 760, pp. 151–157, 1926.

[48] (2020, February). [Online]. Available: https://www.loram.com/products/friction-management/friction-modifiers-grease/top-of-rail-friction-modifiers/

[49] P. M. Cann, "The "leaves on the line"problem—a study of leaf residue film formation and lubricity under laboratory test conditions," *Tribology Letters*, vol. 24, no. 2, pp. 151–158, 11 2006. [Online]. Available: https://www.proquest.com/scholarly-journals/leaves-on-line-problem-study-leaf-residue-film/docview/2281374218/se-2?accountid=13828

[50] Y. Zhu, U. Olofsson, and R. Nilsson, "A field test study of leaf contamination on railhead surfaces," *Proceedings of the Institution of Mechanical Engineers, Part F: Journal of Rail and Rapid Transit*, vol. 228, no. 1, pp. 71–84, 2014. [Online]. Available: https://doi.org/10.1177/0954409712464860

[51] J. L. Lanigan, P. Krier, L. B. Johnstone, B. White, P. Ferriday, and R. Lewis, "Field trials of a methodology for locomotive brake testing to assess friction enhancement in the wheel/rail interface using a representative leaf layer," *Proceedings of the Institution of Mechanical Engineers, Part F: Journal of Rail and Rapid Transit*, vol. 235, no. 9, pp. 1053–1064, 2021. [Online]. Available: https://doi.org/10.1177/0954409720973135

[52] Z. Li, O. Arias-Cuevas, R. Lewis, and E. A. Gallardo-Hernández, "Rolling–sliding laboratory tests of friction modifiers in leaf contaminated wheel–rail

contacts," *Tribology Letters*, vol. 33, no. 2, p. 97, 2008. [Online]. Available: https://doi.org/10.1007/s11249-008-9393-3

[53] B. White, R. Nilsson, U. Olofsson, A. Arnall, M. Evans, T. Armitage, J. Fisk, D. Fletcher, and R. Lewis, "Effect of the presence of moisture at the wheel–rail interface during dew and damp conditions," *Proceedings of the Institution of Mechanical Engineers, Part F: Journal of Rail and Rapid Transit*, vol. 232, no. 4, pp. 979–989, 2018. [Online]. Available: https://doi.org/10.1177/0954409717706251

[54] W. Yan, N. O'Dowd, and E. Busso, "Numerical study of sliding wear caused by a loaded pin on a rotating disc," *Journal of the Mechanics and Physics of Solids*, vol. 50, no. 3, pp. 449–470, March 2002.

[55] B. White and R. Lewis, "Simulation and understanding the wet-rail phenomenon using twin disc testing," *Tribology International*, vol. 136, pp. 475–486, August 2019.

[56] L. Buckley-Johnstone, G. Trummer, P. Voltr, A. Meierhofer, K. Six, D. Fletcher, and R. Lewis, "Assessing the impact of small amounts of water and iron oxides on adhesion in the wheel/rail interface using high pressure torsion testing," *Tribology International*, vol. 135, pp. 55–64, July 2015.

[57] M. Evans, R. Lewis, C. Hardwick, A. Meierhofer, and K. Six, "High pressure torsion testing of the wheel/rail interface," *10th International Conference on Contact Mechanics of Wheel / Rail Systems*, September 2015.

[58] R. Stock, D. Eadie, D. Elvidge, and K. Oldknow, "Influencing rolling contact fatigue through top of rail friction modifier application – a full scale wheel–rail test rig study," *Wear*, vol. 271, pp. 134–142, 2011.

[59] J. Kalker, "Wheel-rail rolling contact theory," *Wear*, vol. 144, pp. 243–261, April 1991.

[60] J. J. Kalker, "A fast algorithm for the simplified theory of rolling contact," *Vehicle System Dynamics*, vol. 11, no. 1, pp. 1–13, 1982. [Online]. Available: https://doi.org/10.1080/00423118208968684

[61] A. Meierhofer, "A new wheel-rail creep force model based on elasto-plastic third body layers," Ph.D. dissertation, TU Graz, 2015.

[62] R. Dwyer-Joyce and B. Drinkwater, "Analysis of contact pressure using ultrasonic reflection," in *Experimental Mechanics*, ser. Proceedings of 11th Annual Conference on Experimental Mechanics, Balkema, Roterdam, 1998, pp. 747–754.

[63] M. Pau, F. Aymerich, and F. Ginesu, "Ultrasonic measurement of nominal contact area and contact pressure in a wheel/rail system," *Journal of Rail and Rapid Transit*, vol. 214, pp. 231–243, 2000.

[64] O. Marshall, R. Lewis, and R. Dwyer-Joyce, "Measuring wheel/rail contact stresses using ultrasound," *14th International Wheelset Congress*, 2004.

[65] R. S. Dwyer-Joyce, B. W. Drinkwater, and A. M. Quinn, "The use of ultrasound in the investigation of rough surface interfaces," *ASME Journal of Tribology*, vol. 123, pp. 8–16, January 2001.

[66] R. S. Dwyer-Joyce, B. W. Drinkwater, and C. J. Donohoe, "The measurement of lubricant-film thickness using ultrasound," *Proc. R. Soc. Lond.*, vol. 459, 2002.

[67] L. Zhou, H. Brunskill, M. Pletz, W. Daves, S. Scheriau, and R. Lewis, "Real time measurement of dynamic wheel-rail contacts using ultrasonic reflectometry," *ASME Journal of Tribology*, vol. 141, no. 6, 2019.

[68] H. Reda, J. Carlier, M. Toubal, P. Campistron, P. Tilmant, and B. Nongaillard, "Interface characterization at nanometer scale using very high frequency ultrasounds," *Composite Interfaces*, vol. 26, no. 4, pp. 325–337, 2019.

[69] T. HECKEL, G. BREKOW, and H. MRASEK, "Ultrasonic testing with matrix arrays, applications in non-destructive testing," *ECNDT*, 2006.

[70] (2010, December). [Online]. Available: https://ewi.org/inspecting-rails-using-matrix-phased-array/

[71] J. Kräutkramer and H. Kräutkramer, *The ultrasonic testing of materials.* Berlin, Germany: Springer-Verlag, 1969.

[72] Engineering-ToolBox. (2020, February) Velocity of sound in solids and metals. [Online]. Available: https://www.engineeringtoolbox.com/sound-speed-solids-d_713.html

[73] Olympus, *Ultrasonic Transducers Technical Notes*, Olympus, 2006.

[74] J. Park, Y. Je, H. Lee, and W. Moon, "Design of an ultrasonic sensor for measuring distance and detecting obstacles," *Ultrasonics*, vol. 50, no. 3, pp. 340–346, March 2010.

[75] S. W. L. C. Xue, "Design and application of distance measure ultrasonic sensor," *Advances in Mechanical and Electronic Engineering*, vol. 178, pp. 109–114, 2013.

[76] J. L. Ferrando Chacon, "Fault detection in rotating machinery using acoustic emission," 2015.

[77] (2020). [Online]. Available: https://www.piceramic.com/en/piezo-technology/fundamentals/

[78] J. Blitz, *Fundamentals of Ultrasonics*. London, England: Butterworths, 1963.

[79] A. Tattersall, "The ultrasonic pulse-echo technique as applied to adhesion testing," vol. 6, pp. 819–832, 1973.

[80] A. Bush, R. Gibson, and T. Thomas, "The elastic contact of a rough surface," *Wear*, vol. 35, no. 1, pp. 87–111, 1975.

[81] S. Fukagaia, H. P. Brunskill, A. K. Hunter, and R. Lewis, "In-situ evaluation of the sliding interface with different roughness conditions using ultrasound reflectometry," *Provisional report not yet published*, 2020.

[82] M. Evans, W. Skipper, L. Buckley-Johnstone, A. Meierhofer, K. Six, and R. Lewis, "The development of a high pressure torsion test methodology for simulating wheel/rail contacts," *Tribology International*, vol. 156, p. 106842, 2021. [Online]. Available: https://www.sciencedirect.com/science/article/pii/S0301679X20306678

[83] W. Skipper, "Sand particle entrainment and its effects on the wheel/rail interface," Ph.D. dissertation, Universiy of Sheffield, September 2021.

[84] B. White, R. Nilsson, U. Olofsson, A. Arnall, M. Evans, T. Armitage, J. Fisk, D. Fletcher, and R. Lewis, "Effect of the presence of moisture at the wheel–rail interface during dew and damp conditions," *Proceedings of the Institution of Mechanical Engineers, Part F: Journal of Rail and Rapid Transit*, vol. 232, no. 4, pp. 979–989, 2018. [Online]. Available: https://doi.org/10.1177/0954409717706251

[85] R. Lewis, E. A. Gallardo-Hernandez, T. Hilton, and T. Armitage, "Effect of oil and water mixtures on adhesion in the wheel/rail contact," *Proceedings of the Institution of Mechanical Engineers. Part F, Journal of rail and rapid transit*, vol. 223, no. 3, pp. 275–283, 2009.

[86] S. Fukagai, M. Marshall, and R. Lewis, "Transition of the friction behaviour and contact stiffness due to repeated high-pressure contact and slip," *Tribology International*, 2022.

[87] T. M. Beagley, "The rheological properties of solid rail contaminants and their effect on wheel/rail adhesion," *Proceedings / Institution of Mechanical Engineers*, vol. 190, no. 1, pp. 419–428, 1976.

[88] P. J. Blau, "On the nature of running-in," *Tribology international*, vol. 38, no. 11, pp. 1007–1012, 2005.

[89] S. Lewis, R. Lewis, G. Evans, and L. Buckley-Johnstone, "Assessment of railway curve lubricant performance using a twin-disc tester," *Wear*, vol. 314, no. 1-2, pp. 205–212, 2014.

[90] D. Hill, P. J. Holliman, J. McGettrick, M. Appelman, P. Chatterjee, T. M. Watson, and D. Worsley, "Study of the tribological properties and ageing of alkyphosphonic acid films on galvanized steel," *Tribology international*, vol. 119, pp. 337–344, 2018.

[91] D. F. Moore and J. F. Booker, "Principles and applications of tribology," *Journal of lubrication technology*, vol. 98, no. 4, pp. 635–635, 1976.

[92] M. Evans, Z. Lee, M. Harmon, K. Six, A. Meierhofer, R. Stock, D. Gutsulyak, and R. Lewis, "Top-of-rail friction modifier performance assessment: High pressure torsion testing; creep force modelling and field validation," *Wear*, vol. 532-533, p. 205073, 2023.

[93] A. Meierhofer, C. Hardwick, R. Lewis, K. Six, and P. Dietmaier, "Third body layer—experimental results and a model describing its influence on the traction coefficient," *Wear*, vol. 314, no. 1-2, pp. 148–154, 2014.

[94] K. Six, A. Meierhofer, G. Müller, and P. Dietmaier, "Physical processes in wheel-rail contact and its implications on vehicle-track interaction," *Vehicle system dynamics*, vol. 53, no. 5, pp. 635–650, 2015.

[95] I. Goryacheva and F. Sadeghi, "Contact characteristics of a rolling/sliding cylinder and a viscoelastic layer bonded to an elastic substrate," *Wear*, vol. 184, no. 2, pp. 125–132, 1995.

[96] S. Alexandrov, "A property of equations of rigid/plastic material obeying a voce-type hardening law," *Meccanica (Milan)*, vol. 34, no. 5, pp. 349–356, 1999.

[97] C. Chang, B. Chen, Y. Cai, and J. Wang, "An experimental study of high speed wheel-rail adhesion characteristics in wet condition on full scale roller rig," *Wear*, vol. 440-441, p. 203092, 2019.

Appendices

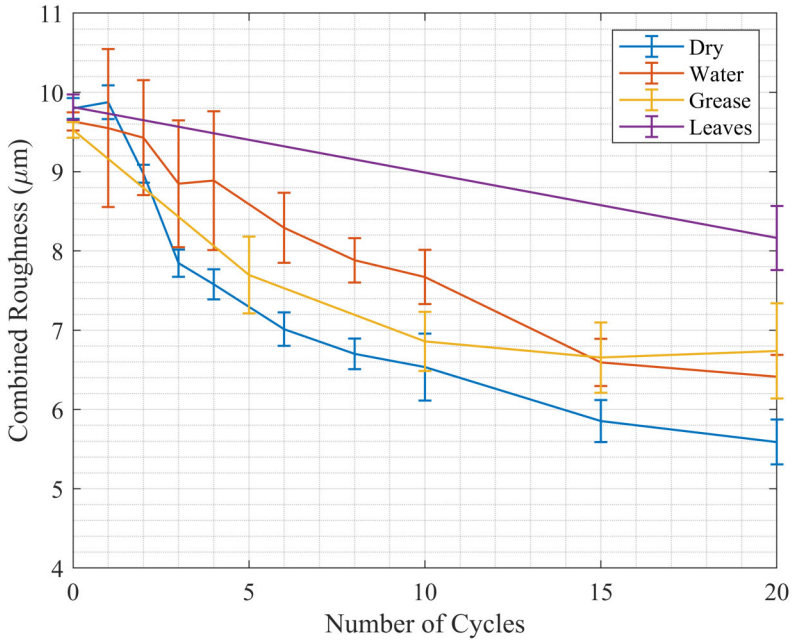

Figure 9.1: Combined roughness ($S_{q\sigma}$) evolution (Test: HPT - HIR - 750MPa)

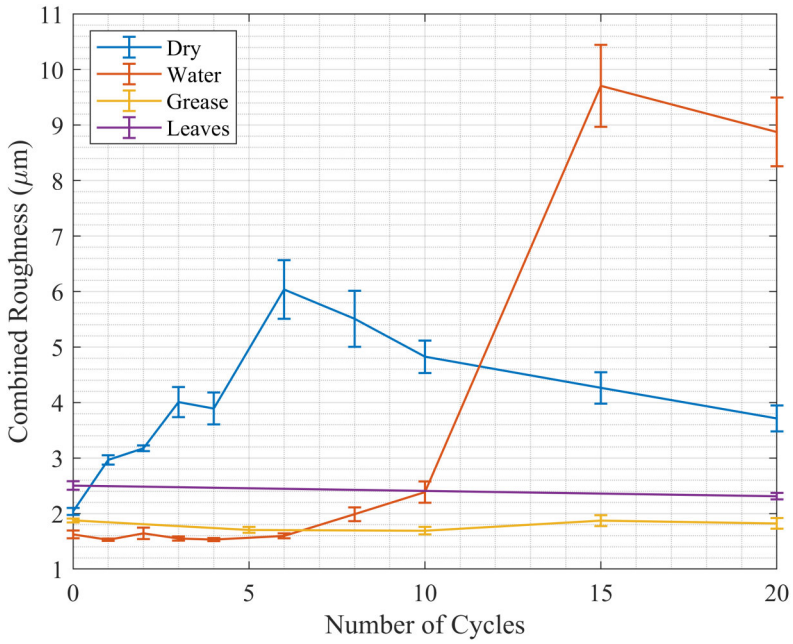

Figure 9.2: Combined roughness ($S_{q\sigma}$) evolution (Test: HPT - LIR - 750MPa)

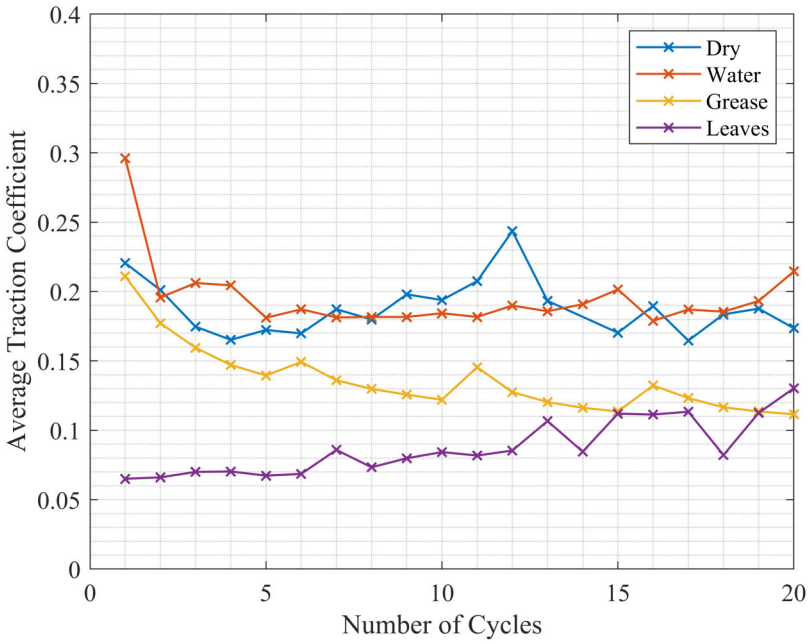

Figure 9.3: Traction coefficient evolution (Tests: HPT - HIR - 750MPa)

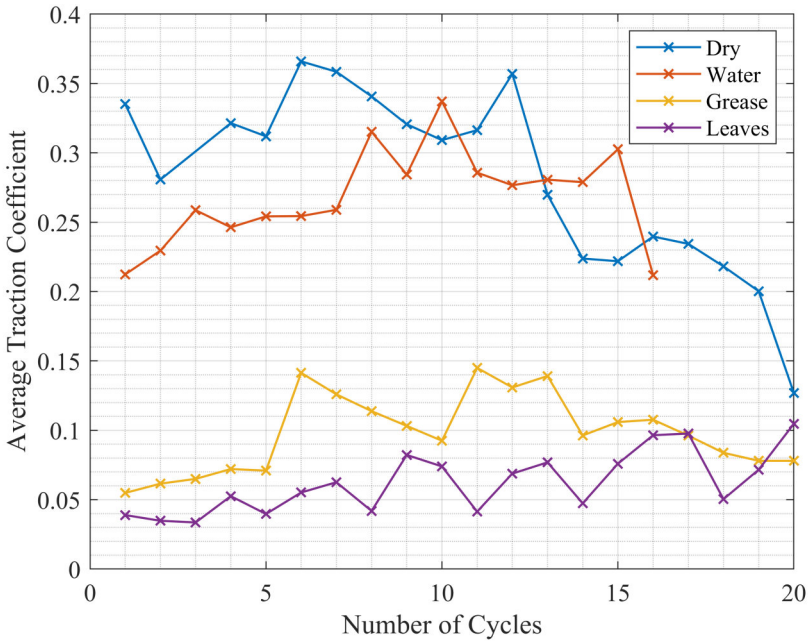

Figure 9.4: Traction coefficient evolution (Tests: HPT - LIR - 750MPa)